Rheological characterisation of bubble suspensions: insights for complex oral health formulations

Stamatina Mitrou

Department of Chemical Engineering

University College London

A thesis submitted for the degree of

Doctor of Philosophy of University College London

May 2025

I, Stamatina Mitrou confirm that the work presented in this thesis is my own. Where information has been derived from other sources, I confirm that this has been indicated in the thesis.

To my family and husband

Abstract

Bubble suspensions are complex systems with applications across various industries. Despite their prevalence, experimental data for understanding their rheology and validating existing models remain sparse. This thesis aims to provide a detailed experimental characterisation of the rheological behaviour of bubble suspensions, particularly to aid the oral care industry in understanding how bubbles influence the rheological properties of their formulations. The dissertation begins by examining the effect of bubbles on the rheology of a Newtonian matrix, progressing to explore their impact on more complex matrices. Alongside conventional rheological tests, a novel rheo-optical set up was employed to visualise the suspension behaviour under shear. First, the steady shear viscosity of bubble suspensions in Newtonian media was investigated. Rheo-optical experiments revealed the shear-induced formation of bubble clusters and threads, suggesting that the shear-thinning behaviour of bubble suspensions originates from both bubble clustering and deformation, rather than solely deformation. The research then delved into the linear viscoelastic properties of bubble suspensions in Newtonian media, crucial for various industrial applications. SAOS results showed that bubble fluid dynamic interactions affected suspension elasticity by introducing additional relaxation modes at low oscillation frequencies. Building on the results obtained in Newtonian media, the final part of the research focused on the influence of bubbles on more intricate matrices typically used in oral care formulations. This study examined the steady shear viscosity of bubble suspensions in a shear thinning Carbopol dispersion, followed by the addition of surfactant to increase matrix complexity. Bubbles induced additional shear-thinning effects in both matrices. In the pure Carbopol matrix, significant bubble coalescence resulted in the formation of bubble clusters and threads as larger bubbles, confined by the flow, aligned with the fluid streamlines. Adding surfactant mitigated bubble coalescence, showing less pronounced bubble clustering compared to both the pure Carbopol and the Newtonian matrices.

Acknowledgements

I would like to thank my supervisors Prof Luca Mazzei and Prof Panagiota Angeli for their endless support and scientific guidance throughout this PhD project. I am deeply grateful for their mentoring, their constant encouragement to explore new ideas and all their efforts to maintain financial support for my research.

I would also like to express my sincere gratitude to Dr Simona Migliozzi for the numerous brainstorming hours we spent together, her invaluable scientific support and her friendship. I wish to thank Dr Loïc Chagot for his help with the image analysis and the talks we shared during long hours in the lab, Dr Victoria Phakoukaki for welcoming me in the group and Mr Kristo Kotsi who spent many hours keeping me company during my experiments. A special thanks to all the members of the ThAMeS group for their willingness to help at any moment and to my ‘‘MechEng crew’’, Anestis, Theofilos and Antonis for letting me borrow their equipment and for our fun Friday evenings after work.

I would also like to thank my parents, Evgenia and Fotis, and my brother Panagiotis for being a constant source of love and support at every step of my life. Last, but definitely not least, I would like to thank my partner Manios who has been my biggest supporter in this journey. We’ve been together through all the ups and downs and I could not have imagined it any other way.

I would like to acknowledge financial support from GlaxoSmithKline (UK) and the Engineering Physical Science Research Council (EPSRC).

Impact Statement

In today's landscape, the demand for increasingly sophisticated formulated products, combined with the need to maintain unwavering product quality, presents a manufacturing challenge in developing novel complex formulations. This challenge is especially significant in the development of personal care products like toothpaste, where multiple functional ingredients must be combined effectively, while maintaining a reliable manufacturing process and key sensory attributes, such as texture, appearance, and mouthfeel, that are critical for consumer satisfaction. During the development of a new toothpaste formulation, the interactions between individual components are not always clear. Moreover, the already intricate and variable rheological properties of such formulations are further complicated by the entrapment of air during the mixing process. The presence of air bubbles significantly impacts the rheological behaviour of these formulations, leading to inconsistencies in subsequent manufacturing steps, such as tube filling, and affecting the final product properties.

The motivation for this work stemmed from the industrial interest in understanding the effect of bubbles on the rheological properties of novel oral non-aqueous formulations, currently produced by GlaxoSmithKline to treat dental hypersensitivity. Comprehending the influence of bubbles allows the oral care industry to efficiently control the rheological properties of their formulations, leading to enhanced manufacturing efficiency and consistently high-quality products. Following this interest, the main scope of this research was to provide a systematic experimental characterisation of the rheological behaviour of bubble suspensions in matrices of increasing complexity. These matrices ranged from simple Newtonian fluids to more complex shear-thinning fluids, typically used in the GSK formulations. The key findings of this thesis offer insights into two critical areas: (i) the effect of bubbles in Newtonian matrices, including their behaviour and interactions under different flow conditions, and the complex rheological phenomena they induce, and (ii) the physical interactions between bubbles and non-Newtonian matrices and their influence on the suspension rheological properties.

The experimental data generated and analysed in this thesis are fundamental for understanding the interplay between bubbles and fluid matrices in different contexts, facilitating the development of novel formulations with consistent rheological properties. Moreover, these findings are valuable for validating existing rheological models proposed for the rheology of bubble suspensions, and can be of great interest to other industries, such as food, oil and gas, and personal care products. In these industries, air is incorporated in the

formulations to improve various product properties, including texture and flavour release (e.g., chocolate), structural integrity and flow properties (e.g., aerated cement), and spreadability and cleansing properties (e.g., foam cleansers).

Highlights

1. The steady shear rheology of semi-dilute polydisperse bubble suspensions in a Newtonian ambient fluid was investigated to elucidate the role of polydispersity on the steady-shear viscosity of such systems. Detailed theoretical calculations revealed that the effect of polydispersity on suspension viscosity becomes apparent only if the bubble size distribution is bimodal, with very small and very large bubbles having similar volume fractions. In any other case, the polydisperse suspension can be considered as monodisperse, with a diameter equal to the volume-weighted average diameter. Steady-shear rheological tests showed an unexpected double power-law decay in suspension relative viscosity, while subsequent novel rheo-optical experiments linked the first decay to the shear-induced formation of bubble clusters and threads and the second to bubble deformation. Despite numerous experimental studies on the steady-shear properties of bubble suspensions, this investigation represents the first study to clearly reveal the shear-induced formation of bubble clusters and threads, which contribute to additional shear-thinning effects, and to clarify the influence of polydispersity without relying on system-dependent empirical approaches.
2. The linear viscoelastic properties of semi-dilute polydisperse bubble suspensions were investigated experimentally through small amplitude oscillatory shear (SAOS) tests performed in a rheo-optical set up. This coupled approach offered a higher confidence in the experimental measurements, because it allowed investigating the effects of bubble size distribution and various SAOS measurement artifacts, including bubble rise, coalescence, and changes in bubble spatial organisation over time, which can influence the rheological measurements of bubble suspensions. The study produced reliable experimental results for validating existing models proposed for the linear viscoelastic behaviour of bubble suspensions and shed light on the rather unexplored effect of bubble fluid dynamic interactions on suspension elasticity. It also clarified the conditions under which pre-shearing can effectively mitigate these effects. Understanding the linear viscoelastic properties of such systems and the influence of pre-shearing conditions is paramount for efficiently designing and controlling manufacturing processes to achieve desired final product properties.

3. The physical interplay between bubbles and a shear-thinning Carbopol dispersion, both with and without the addition of a surfactant (Sodium Dodecyl Sulphate, SDS), was studied via steady shear experiments. This study provided valuable insights into the influence of bubbles on more complex matrices typically found in oral care formulations. The results highlighted how matrix composition affects the interactions between individual components in these suspensions, leading to phenomena such as bubble coalescence and clustering, which directly impact the rheological behaviour of these systems. This study paves the way to further exploration of the intricate interplay between bubbles and shear-thinning matrices in complex formulations.

List of Publications and International Dissemination

This research led to the following publications in peer-reviewed academic journals:

- Mitrou, S., Migliozzi, S., Angeli, P., Mazzei, L., Effect of polydispersity and bubble clustering on the steady-shear viscosity of semi-dilute bubble suspensions in Newtonian media. Journal of Rheology 67, 635–646 (2023).
- Mitrou, S., Migliozzi, S., Mazzei, L., Angeli, P., On the linear viscoelastic behaviour of semi-dilute polydisperse bubble suspensions in Newtonian media. Journal of Rheology 68, 539–552 (2024). (featured article in Journal of Rheology homepage, May 2024)

Additionally, I was able to disseminate this work in the following international conferences:

- Mitrou, S., Migliozzi, S., Mazzei, L., Angeli, P., Study of the linear viscoelastic properties of semi-dilute polydisperse bubble suspensions in Newtonian media, Annual Meeting APS Division of Fluid Dynamics, 19 – 21 November 2023, Washington DC, USA (oral presentation).
- Mitrou, S., Migliozzi, S., Mazzei, L., Angeli, P., Polydispersity and bubble interactions: unravelling the viscoelastic nature of semi-dilute bubble suspensions in Newtonian media, International Conference of Rheology, 29 July – 4 August 2023, Athens, Greece (poster).
- Mitrou, S., Migliozzi, Angeli, P., S., Mazzei, L., Effect of bubble clustering on the steady shear viscosity of semi-dilute polydisperse bubble suspensions, International Conference on Multiphase Flow, 2 – 8 April 2023, Kobe, Japan (oral presentation).
- Mitrou, S., Migliozzi, Angeli, P., S., Mazzei, L., Bubble suspensions: insights into the effects of polydispersity and bubble clustering on their steady shear viscosity, 10th

International conference of the Hellenic Society of Rheology, 29 June – 2 July 2022, Skiathos, Greece (oral presentation).

- Mitrou, S., Migliozzi, Angeli, P., S., Mazzei, L., Rheological behaviour of dilute polydisperse bubble suspensions under steady shear, Early Career International Particle Technology Forum, 26 – 27 May 2022 (virtual meeting) (best poster award).

Table of Contents

List of Figures

List of Tables

List of Symbols and Abbreviations

The following list includes the main symbols and abbreviations used within the thesis.

Abbreviations

Ca	Capillary number
Cd	Dynamic capillary number
$< Ca >$	Volume-weighted average capillary number
$< Cd >$	Volume-weighted average dynamic capillary number
Ca_{elast}	Elastic capillary number
De	Deborah number
Wi	Weissenberg number
SAOS	Small Amplitude Oscillatory Shear

Greek symbols

η	Shear viscosity
η_0	Zero-shear viscosity
η_∞	Infinite Shear viscosity
η_r	Relative viscosity
η_s	Viscosity of the solvent (ambient fluid)
$\boldsymbol{\sigma}$	Stress tensor
τ	Shear stress
τ^*	Dimensionless shear stress
τ_0	Stress amplitude of the sinusoidal stress response
γ	Strain
γ_0	Strain amplitude of the sinusoidal deformation
$\dot{\gamma}$	Strain rate
$\dot{\gamma}_{eff}$	Effective strain rate (i.e., at the edge of the rheometer parallel plate)
φ	Bubble volume fraction
ζ	Volume fraction of swollen Carbopol microgels
σ	Surface tension
λ	Relaxation time
λ_2	Retardation time (Jeffreys mode)
ω	Frequency of oscillation
δ	Phase angle
Ψ_1	First normal stress coefficient
Ψ_2	Second normal stress coefficient

Symbols

G^*	Complex shear modulus
G'	Storage/Elastic modulus
$\overline{G'}$	Dimensionless elastic modulus
G''	Loss/Viscous modulus
G_e	Elastic modulus (Hooke's law)
$G(t)$	Relaxation modulus

$H(\lambda)$	Continuous relaxation spectrum
t_d	Bubble deformation time
R	Radius of an undeformed bubble
$< R >$	Volume-weighted average bubble radius
d_{43}	De Brouckere mean diameter
C	Coverage parameter
N_1	First normal stress difference
N_2	Second normal stress difference

Chapter 1

Introduction

1.1 Scope of the research

The scope of this work is to provide a comprehensive understanding of how bubbles affect the rheological properties of matrices with increasing complexity, ranging from simple Newtonian fluids to complex shear-thinning fluids commonly used in oral health formulations. The research is part of the EPSRC Future Formulations grant CORAL, a collaboration between the Departments of Chemical Engineering, Mechanical Engineering and Mathematics at UCL, and is partly sponsored by the industrial partner GlaxoSmithKline. The overall aim is to introduce new fundamental insights into complex formulations, contributing to enhanced control over their final rheological properties, improved manufacturing efficiency, and consistent product quality.

1.2 Motivation

In today's diverse industries, the development of complex formulated products is essential to meet the ever-evolving needs of consumers. Products such as personal care items, construction materials, food products, and inks rely on the precise combination of multiple phases and active ingredients to achieve specific textures, functionalities, and benefits. This intricate process presents significant manufacturing challenges, requiring a deep understanding of how different components interact and how these interactions influence the overall performance and stability of the product. The oral care industry exemplifies this complexity, with toothpaste serving as a prime example. Integrating novel functionalities into this daily essential while maintaining consistent quality and a reliable manufacturing process is crucial not only for manufactures but also for consumer health and well-being (WHO, 2020). Typical toothpaste formulations consist of a dense suspension of thickening and abrasive substances, flavours, surfactants, and therapeutic agents such as fluoride, all within a liquid matrix of humectants and water (Liu et al., 2015).

The complexity of toothpaste formulations increases when addressing specific oral health issues, such as dental hypersensitivity. This led to the development of novel non-aqueous

formulations incorporating bioactive glass. In the presence of saliva, this biocompatible material reacts rapidly with the surrounding tissue, forming a mineral layer of hydroxycarbonate apatite that protects exposed dentin and relieves pain (Petrović et al., 2023). The absence of water in these new formulations significantly alters the interplay between ingredients, leading to significant changes in the product's microstructure and flow properties. The behaviour of these formulations can vary dramatically with slight alterations in process conditions, ingredient concentrations, or the sequence in which they are added to the formulation.

The introduction of bubbles during the high shear-mixing of the various components adds yet another layer of complexity to an already challenging formulation. Bubbles have been shown to significantly influence the rheological properties of a system, with their impact being highly dependent on factors such as the bubble volume fraction, the matrix composition, the interactions between bubbles and other formulation components, and the applied flow conditions. This variability introduces additional manufacturing challenges and complicates control over the final product's properties, making it difficult to achieve consistent product quality and a reliable manufacturing process. Therefore, comprehensive rheological characterisation that clarifies the effect of bubbles on the flow properties of such systems is paramount for developing high-quality products with reliable and predictable properties.

1.3 Research objectives

This research aims to investigate how bubbles generated during the manufacturing process of novel oral non-aqueous formulations developed by GlaxoSmithKline affect their rheological properties. Toothpaste formulations are inherently complex materials from a rheological perspective, exhibiting distinctive shear-thinning behaviour and often yield stress properties that define their sensory qualities and how consumers perceive them (Ahuja et al., 2020). Understanding and controlling their intricate rheological behaviour is essential for processes such as dispensing, pumping and end usage, as well as for ensuring stable formulations with consumer-preferred sensory attributes. From a manufacturing standpoint, this knowledge is also critical for optimising processing conditions, minimising downtime, and reducing wasted material (Ahuja and Potanin, 2018).

The challenge of controlling the rheological properties of these formulations is further complicated by the entrapment of air bubbles during the initial manufacturing stage. This stage involves the production of a non-aqueous matrix composed of a liquid phase (i.e., glycerol)

and a polymer gel phase (formed with a carbomer and polyethylene glycol (PEG)), to which the solid phase and various additives are subsequently added. The process is conducted in large batch mixers where the polymer gel phase is mixed with the liquid phase. The final properties of the toothpaste heavily depend on the homogeneity of the non-aqueous matrix, highlighting the crucial role of high-shear mixing during this stage. However, this intense mixing also causes air to get entrapped in the mixture, which, due to the mixture's high viscosity, becomes difficult to release, effectively creating a bubble suspension.

The presence of bubbles has been recognized in the literature for inducing shear-thinning and other non-Newtonian phenomena even in Newtonian matrices (Llewellin et al., 2002a; Mader et al., 2013; Morini et al., 2019). Hence, the interaction of bubbles with an already rheologically complex non-aqueous matrix complicates matters even more. In this specific case, the entrapment of bubbles in the toothpaste matrix has been associated with stringiness in the formulation, which interferes with consistent filling, slowing down the line operation, and ultimately reducing manufacturing efficiency. These significant manufacturing challenges coupled with the need to ensure final products with consistent sensory properties underscore the need for studying and characterising the effect of bubbles on the rheology of toothpaste formulations.

This study presents significant challenges because bubble suspensions, even in Newtonian media, remain relatively unexplored compared to emulsions and particle suspensions. This is primarily due to two factors: a) bubble suspensions are inherently less stable systems, making it difficult to generate and maintain them for long enough to enable experimental investigation, and b) the rheological models generated for emulsions and particle suspensions cannot be directly applied to bubble suspensions due to the different nature of the dispersed phase, as bubbles are inviscid and incompressible. Therefore, there are still unexplored aspects of the rheology of bubble suspensions in Newtonian ambient fluids.

One such aspect is the effect of polydispersity on the viscosity of bubble suspensions, an issue that has been scarcely addressed in the literature and mostly through empirical approaches, despite the widespread presence of polydisperse systems in industrial applications. To address this gap, the influence of different bubble sizes on the viscosity of bubble suspensions is investigated through a combination of theoretical analysis and rheological testing with the aim of deriving system-independent insights. Furthermore, this research provides a deeper understanding of the shear-thinning behaviour of bubble suspensions, with

rheo-optical experiments revealing the role of shear-induced phenomena, such as bubble clustering and threading, in this process.

Another aspect requiring investigation in bubble suspensions with Newtonian ambient fluids regards their linear viscoelastic properties, for which there is a distinct lack of experimental data in the literature. Obtaining reliable experimental data to better understand these properties is of paramount importance for effectively controlling manufacturing processes and achieving products with desired texture and spreadability. Therefore, a systematic experimental characterisation of the linear viscoelastic properties of bubble suspensions in Newtonian matrices is conducted through SAOS rheological tests performed in a rheo-optical setup. This study produces reliable experimental data that elucidate the effect of bubbles in suspension elasticity, providing a foundation for similar investigations in more complex non-Newtonian matrices.

Following the study of bubble suspensions in Newtonian media, the steady-shear viscosity of bubble suspensions with a shear-thinning ambient fluid is investigated experimentally with the aim of evaluating the impact of bubbles on the rheology of more complex matrices. The shear-thinning matrix used in this study consists of a Carbopol dispersion in a mixture of PEG and glycerol, simulating the composition used in the initial manufacturing stage of the non-aqueous formulations of interest. To examine how matrix composition influences the way bubbles behave and interact with the matrix, surfactant (SDS) was introduced in the mixture to increase matrix complexity, and the steady-shear viscosities of bubble suspensions with and without surfactant were compared. This study focuses on the interplay between bubbles and matrix components in more complex matrices and how these interactions affect the suspension flow properties. These findings aim to provide the oral care industry with valuable insights on how to control and optimise the rheological properties of their products by fine-tuning the matrix composition. Hence, the objectives of this work can be summarized as follows:

- Investigate the impact of different bubble sizes on the steady-shear viscosity of semi-dilute bubble suspensions in Newtonian media via theoretical analysis and rheological tests;
- Elucidate the effect of shear-induced phenomena, such as bubble clustering and threading, on the steady-shear viscosity of semi-dilute bubble suspensions in Newtonian media;

- Provide a systematic experimental characterisation of the linear viscoelastic behaviour of semi-dilute bubble suspensions in Newtonian media, using a combination of SAOS tests and rheo-optical experiments to ensure greater reliability of experimental results;
- Examine the effect of bubble-fluid dynamic interactions on the elasticity of bubble suspension in Newtonian media, and clarify the conditions under which pre-shearing can mitigate these effects;
- Investigate experimentally the steady-shear viscosity of semi-dilute bubble suspensions in shear-thinning matrices of increasing complexity, and elucidate the interplay between bubbles and matrix components and its impact on the suspension viscosity.

1.4 Thesis outline

The dissertation is organised into six chapters. A brief introduction to the motivation and background for this research has been given in this chapter, along with the primary objectives of the work. Chapter 2 provides a literature review, laying the theoretical groundwork essential for interpreting the results presented in the following chapters. First, general concepts on the rheology of complex fluids are introduced, followed by a more detailed analysis of the rheological properties of bubble suspensions in Newtonian media. Finally, the chapter provides some key literature insights on the rheology of bubble suspensions in non-Newtonian media, focusing specifically on (i) shear-thinning and (ii) yield stress ambient fluids.

The results are presented across Chapters 3 to 5, with each chapter including a small introduction, its individual methodology, results and conclusion subsections. Chapter 3 discusses the steady-shear viscosity of semi-dilute polydisperse bubble suspensions in Newtonian media. The study combines theoretical analysis, steady-shear rheological tests and rheo-optical experiments to elucidate how different bubble sizes and shear-induced phenomena, such as the formation of bubble clusters and threads, influence the suspension relative viscosity. The findings of this chapter clarify the role of polydispersity without relying on system-dependent empirical approaches and highlight the complex shear-thinning nature of bubble suspensions, driven not only by bubble deformation, as previously understood, but also by the shear-induced clustering and alignment of bubbles.

Chapter 4 examines the linear viscoelastic behaviour of semi-dilute polydisperse bubble suspensions in Newtonian media through SAOS rheological tests. A rheo-optical setup was employed to visualise the behaviour of the suspensions during these tests, aiming to investigate how bubble size distribution and various SAOS measurement artifacts – such as bubble rise,

coalescence, and changes in bubble spatial organisation over time – affect the obtained viscoelastic trends. The combination of SAOS rheological data, image analysis, and experimental data fitting provided valuable insights into bubble fluid dynamic interactions, their impact on the suspension elasticity, and the role of pre-shearing in mitigating these effects.

Chapter 5 explores the impact of a shear-thinning matrix on the steady-shear viscosity of bubble suspensions, focusing on the interactions between the bubbles and matrix components. The study examines the steady-shear viscosity of bubble suspensions in two shear-thinning matrices: (i) a Carbopol dispersion, and (ii) a Carbopol dispersion with added surfactant, Sodium Dodecyl Sulphate (SDS), to increase matrix complexity. Rheo-optical experiments are conducted to visualise the phenomena taking place during shearing and to investigate how the interplay between bubbles and matrix components drives the rheological response. The results highlight the critical role of matrix composition, demonstrating that the rheological behaviour of more complex formulations is significantly shaped by the intricate interactions among their individual components.

Finally, Chapter 6 summarises the key findings of this research and outlines future perspectives.

Chapter 2

Theoretical Background and Literature Review

This chapter aims to provide a comprehensive overview of the theoretical background required to understand the research results. First, general concepts on the rheology of complex fluids are introduced, focusing on the material functions that are most pertinent to the subsequent results chapters. Next, a detailed analysis of the rheological properties of bubble suspensions in Newtonian media is presented, along with a discussion on existing rheological models and their limitations. Lastly, the rheology of bubble suspensions with non-Newtonian ambient fluids is discussed, particularly in the context of shear-thinning and yield stress matrices.

2.1 Rheology of complex fluids

Fluid rheology is a vast field of study, essential for addressing fluid dynamics problems involving complex fluids and for gaining insight into the microscopic interactions within new complex formulations. Due to the extensive nature of the subject, a wealth of literature has been dedicated to examining different types and properties of fluids and materials. This section aims to present fundamental concepts pertinent to this research, outlining the primary material functions used throughout the thesis to describe the rheological behaviour of the systems under investigation.

Incompressible fluids are generally characterised by their stress response to externally applied deformations. The kind and extent of this response are closely tied to the material's internal microstructure. Thus, rheological testing is used to correlate the flow behaviour of a complex fluid to its underlying microstructure by subjecting the fluid to simple flow fields. The two primary types of flow used in rheological measurements are (i) shear flows and (ii) shear-free flows, each producing unique material functions that offer different insights into the fluid’s properties.

In shear flows, deformation is exerted tangentially to each element of the fluid. A basic way to represent this type of flow in a two-dimensional space is through the parallel-plate paradigm, depicted in Fig. 2.1.

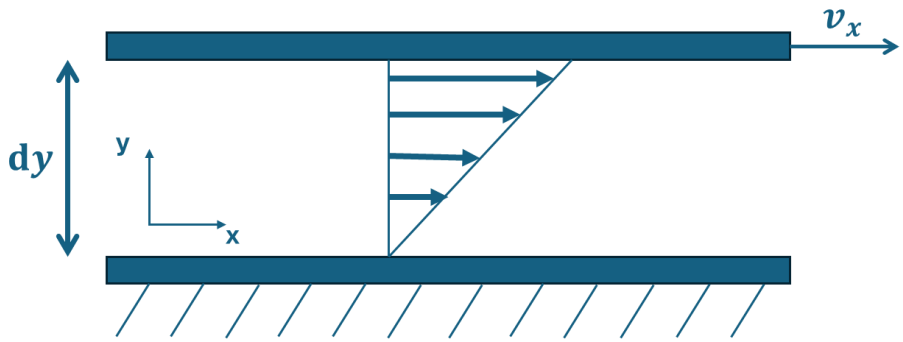

Figure 2.1: Schematic of a shear flow in a parallel plate configuration.

In this case, a fluid is placed between two parallel plates separated by a small distance, and the top plate is moved in the x-direction with a velocity v_x. The resulting strain, or deformation γ, experienced by a fluid element with a differential thickness dy can be described at every point within the fluid domain as follows:

$$\gamma = \frac{ds}{dy} \tag{2.1}$$

where ds is the differential distance covered by a fixed fluid element over a differential time interval dt. The *shear strain* γ is the only non-zero element of the deformation tensor. The absolute value of the rate at which this strain changes over time, specifically due to shear forces, is known as the *shear rate* $\dot{\gamma}$ and is expressed as:

$$\dot{\gamma} = \frac{1}{dt}\frac{ds}{dy} = \frac{dv_x}{dy} \tag{2.2}$$

where dv_x (m/s) is the velocity of the upper plate. The correlation of the shear deformation γ and the shear rate $\dot{\gamma}$ with the force per unit area (N/m²), or *shear stress* τ, applied to induce deformation, is strictly fluid-dependent and represents the most common way to classify fluids.

In shear-free flows, the applied deformation consists only of normal components, with all shear components of the velocity gradient being equal to zero (i.e., $\dot{\gamma}_{ij} = 0, i \neq j$). A typical example of shear-free flow is the extensional flow, which in a three-dimensional space is defined by the *elongational rate* $\dot{\varepsilon}$ as follows:

$$v_x = -\frac{1}{2}\dot{\varepsilon}x; v_y = -\frac{1}{2}\dot{\varepsilon}y; v_z = \dot{\varepsilon}z \quad \text{where} \quad \dot{\varepsilon} = \frac{dv_z}{dz} \tag{2.3}$$

In an extensional flow, every fluid element experiences extension in one direction and contraction in the other two, due to the fluid being incompressible. Unlike shear flow, where surfaces slide relative to each other, here one can observe rigid areas that either approach or

move away from each other in the direction of motion. From a dynamic perspective, an extensional deformation is possible only when there is a difference in the normal stresses acting on two orthogonal surfaces of the material (Macosko, 1994):

$$\tau = \tau_N - \tau_L = -\eta_e(\dot{\varepsilon})\dot{\varepsilon} \tag{2.4}$$

where τ_N and τ_L represent the normal stresses applied to the perpendicular and longitudinal surfaces of the fluid element, respectively, and $\eta_e(\dot{\varepsilon})$ is the extensional viscosity, which is different from the shear viscosity η. Note that certain materials, such as polymer blends, exhibit normal stress differences also in simple shear flows. This phenomenon is linked with the inherent elastic component of these materials.

In the present work, only shear rheology techniques were employed. Therefore, the following sections concentrate solely on the material functions that can be derived from shear flow and the corresponding classifications of complex fluids.

2.1.1. Newtonian fluid behaviour

Following what was stated in the section above, it is then possible to classify fluids depending on their response to an external shear stress. Considering the parallel plate paradigm illustrated in Fig. 2.1, for a Newtonian fluid, the velocity gradient induced in the fluid layer along the y component (shear rate $\dot{\gamma}_{xy}$ (s^{-1})) is directly proportional to the applied shear stress (τ_{xy} (N m^{-2})). The constant of proportionality is the viscosity of the fluid η (Pa s), leading to the following equation, commonly known as Newton's law (Bird et al., 2002):

$$\frac{F}{A} = \tau_{xy} = -\eta\left(\frac{\vartheta v_x}{\vartheta y}\right) = -\eta\dot{\gamma}_{xy} \tag{2.5}$$

The Newtonian viscosity, as defined in the equation above, does not depend on the shear rate and is solely determined by the material's unique properties, including its temperature and pressure (Chhabra and Richardson, 2011).

To extend Eq. 2.5 to the more complex case of three-dimensional flows, one must consider all nine components of the stress tensor acting on a single fluid element (Fig. 2.2). The normal components of the stress tensor σ_{ii} are the sum of two distinct contributions: one related to the pressure exerted by the fluid on the external environment, and the other to the flow as shown below (Bird et al., 2002):

$$\sigma_{ii} = p + \tau_{ii} \text{ with } i = x, y, z \tag{2.6}$$

where the pressure contribution is defined as follows:

$$p \equiv \frac{1}{3}\left(\sigma_{xx} + \sigma_{yy} + \sigma_{zz}\right) \tag{2.7}$$

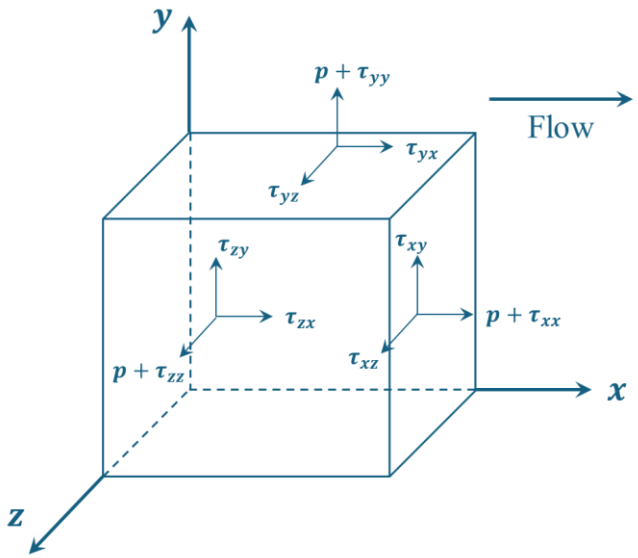

Figure 2.2: Stress components in the three-dimensional flow.

From Eqs. 2.5 and 2.6, one obtains:

$$\tau_{xx} + \tau_{yy} + \tau_{zz} = 0 \tag{2.8}$$

For a Newtonian fluid under simple shear flow, the deviatoric normal stress components are all zero:

$$\tau_{xx} = \tau_{yy} = \tau_{zz} = 0 \tag{2.9}$$

Thus, a fluid can be classified as Newtonian if it meets two conditions: (i) its viscosity remains constant with shear, and (ii) it demonstrates zero normal stresses. Hence, in a three-dimensional space, the Newtonian stress tensor can be expressed as follows (Macosko, 1994):

$$\boldsymbol{\sigma} = p\boldsymbol{I} - \mu\dot{\boldsymbol{\gamma}} \tag{2.10}$$

where $\dot{\boldsymbol{\gamma}} \equiv \left[\boldsymbol{\nabla v} + (\boldsymbol{\nabla v})^T\right]$ is twice the rate of deformation tensor.

2.1.2. Generalised Newtonian fluid behaviour

Fluids that do not meet the conditions presented above are commonly known as 'non-Newtonian' fluids. The simplest deviation from Newtonian behaviour is described by the

generalised Newtonian fluid model, which treats the fluid viscosity as a function of the shear rate rather than a constant:

$$\boldsymbol{\tau} = -\eta[\boldsymbol{\nabla v} + (\boldsymbol{\nabla v})^{T}] = -\eta\dot{\boldsymbol{\gamma}} \tag{2.11}$$

$$\eta = \eta(\dot{\gamma}) \tag{2.12}$$

where $\boldsymbol{\tau}$ is the stress tensor including only the flow contributions and $\dot{\gamma}$ is the shear rate. In a three-dimensional space, the shear rate is defined as the magnitude of the rate of deformation tensor (Bird et al., 1987):

$$\dot{\gamma} \equiv \sqrt{\frac{1}{2}(\dot{\boldsymbol{\gamma}}:\dot{\boldsymbol{\gamma}})} \tag{2.13}$$

The generalised Newtonian model describes only how viscosity changes with shear rate, without accounting for any characteristics related to viscoelasticity. Therefore, it is applicable only to purely viscous (inelastic) non-Newtonian fluids. Figure 2.3 depicts the qualitative relationship between shear stress and shear rate when the fluid behavior deviates from the Newtonian case. Shear-thinning is the most frequently observed non-Newtonian behavior in industrial applications and is typically associated with polymer blends.

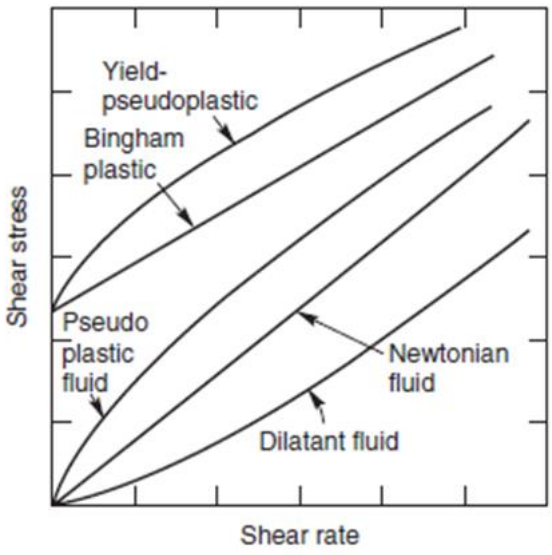

Figure 2.3: Types of generalised Newtonian fluids (Chhabra and Richardson, 2011).

Figure 2.4 illustrates the key characteristics of shear-thinning fluids, primarily showing that the measured viscosity decreases with increasing shear rate. At very low and very high shear rates, shear-thinning materials typically display Newtonian behavior, leading to a *zero-shear viscosity* η_0 plateau at low shear rates and an *infinite-shear viscosity* η_∞ plateau at high shear

rates. The specific features of any flow curve are largely determined by the material's microstructure. For instance, in polymer solutions, the extent of the zero-shear plateau grows as the polymer's molecular weight decreases, as their molecular weight distribution becomes narrower, and as the polymer concentration in the solution reduces (Bird et al., 1987).

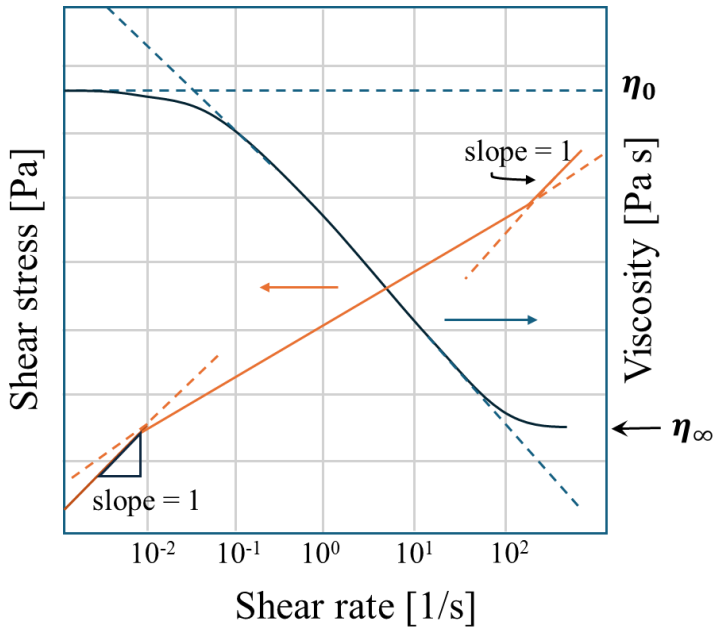

Figure 2.4: Qualitative representation of shear-thinning behaviour.

Throughout the years, various empirical models have been developed to represent viscosity as a function of shear rate, with the *power law model* being the simplest:

$$\eta = \mathrm{K}\,\dot{\gamma}^{n-1} \tag{2.14}$$

where K and n are empirical fitting parameters, known as the *fluid consistency* and *flow index*, respectively.

The power law model is applicable to both shear-thinning and shear-thickening fluids. In the case of shear-thinning fluids, n falls between 0 and 1, while for shear-thickening fluids, n exceeds 1. The further the flow index deviates from 1, which corresponds to the Newtonian behaviour, the more pronounced the non-Newtonian effects become. Despite its widespread application in process engineering, the power law model has limitations, particularly in capturing the zero-shear and infinite-shear Newtonian plateaus. To address these shortcomings, more sophisticated models have been developed, based on assumptions about how the material's molecular network evolves under simple shear stress (Cross, 1965). A characteristic example is the *Carreau-Yasuda* constitutive equation, which effectively captures both the zero-shear and high-shear viscosity plateaus:

$$\eta = \eta_\infty + (\eta_\infty - \eta_0)[1 + (\lambda_c \dot{\gamma})^a]^{\frac{n-1}{a}} \quad (2.15)$$

where λ_c is the *Carreau characteristic time* which is linked to the inverse of the shear rate at which the shear-thinning behaviour begins, n is the flow index, and a is a fitting parameter associated with the smoothness of the transition from zero-shear plateau to the shear-thinning region. Other common generalised Newtonian constitutive equations are outlined below:

$$\text{Ellis model} \quad \eta = \frac{\eta_0}{1+\left(\frac{\sigma}{\sigma_{1/2}}\right)^{\alpha-1}} \quad (2.16a)$$

$$\text{Cross model} \quad \frac{\eta-\eta_0}{\eta-\eta_\infty} = \frac{1}{1+K\dot{\gamma}^n} \quad (2.16b)$$

$$\text{Carreau model} \quad \frac{\eta-\eta_0}{\eta-\eta_\infty} = [1 + (\lambda_c \dot{\gamma})^2]^{\frac{n-1}{2}} \quad (2.16c)$$

$$\text{Herschel-Bulkley model} \quad \sigma = \sigma_y + K\dot{\gamma}^n \; \sigma > \sigma_0 \quad (2.16d)$$

Note that in Eq. 2.16a, α and $\sigma_{1/2}$ are the two fitting parameters of the Ellis model, with α being the equivalent of the flow index and $\sigma_{1/2}$ representing a stress threshold. For $\sigma_{1/2} \to \infty$ the model simplifies to the Newtonian case, while for $\sigma/\sigma_{1/2} \gg 1$, it reduces to the power law model (Eq. 2.14). Eq. 2.16d is known as the Herschel-Bulkley model and is presented in a different format compared to the rest. This model applies to *viscoplastic fluids*, which are characterised by the presence of a yield stress σ_y. Typical examples of viscoplastic materials include emulsions, suspensions and polymeric gels (Larson, 1999). Though yield stress is theoretically impossible to determine for a real fluid, as by definition it is the stress value at shear rate equal to zero, it practically refers to the minimum stress required to break down the material's internal microstructure and cause viscous deformation. Below this threshold, the material can be considered as an elastic solid with infinite viscosity.

All the models presented above can be fitted to rheological data obtained from steady-shear tests, where a constant shear rate is applied, and the corresponding stress is measured once steady-state conditions are reached. This is repeated across a wide range of shear rates, typically between 10^{-3} and 10^3 s^{-1}, to obtain the material's characteristic flow curve.

2.1.3. Viscoelastic fluid behaviour

The types of complex fluid behaviour discussed so far have been associated solely with the presence of viscous stresses in response to a material's deformation or flow. However, many materials of practical significance, such as gels, pastes, and polymer blends, present also an elastic component, forming another important class of complex fluids, known as *viscoelastic*

fluids. The rheological properties of these fluids lie between viscous liquids and elastic solids, meaning that part of the applied shear stress is used to generate a velocity gradient ($\frac{du_x}{dy}$) and part of it gets stored in the material as shear energy (Ferry, 1980). Thus, suggesting that the material may partially recover its original structure once the stress is removed. This response depends on both the material's distinct microstructure and the shear conditions it has undergone (Bird et al., 1987). Therefore, by measuring the viscoelastic properties of a material, one can gain valuable insights into its specific characteristics and the time needed for its internal microstructure to rearrange, which is closely connected to the material's inherent nature and physicochemical properties (Ferry, 1980).

In the context of this research, the investigation of viscoelasticity becomes particularly relevant, as the presence of bubbles has been shown to induce viscoelastic phenomena even in Newtonian ambient fluids. Consequently, the viscoelastic properties of bubble suspensions have been studied with the aim of gaining insights into their unique microstructure and understanding how this influences their macroscopic flow behaviour. This section presents the material functions typically used to describe viscoelasticity, along with fundamental models proposed in the literature to characterise the behaviour of viscoelastic fluids. The application of these models to bubble suspensions is discussed in Section 2.2.

Viscoelastic material functions

The material functions used to describe the viscoelastic nature of a material can be categorised based on the applied flow field. In simple steady shear flows, elastic effects are indicated by the presence of non-zero normal stresses (τ_{ii}), which arise from the material's inherent nature rather than the imposed flow conditions. In this context, elastic effects are not determined by the specific values of the three normal stress components but by the differences between them. Thus, for an incompressible fluid subjected to steady shear flow, the elastic behaviour is typically quantified by measuring the *first* and *second normal stress differences*:

$$N_1 = \tau_{xx} - \tau_{yy} = -\Psi_1(\dot{\gamma})\,\dot{\gamma}_{yx}^2 \tag{2.17a}$$

$$N_2 = \tau_{yy} - \tau_{zz} = -\Psi_2(\dot{\gamma})\,\dot{\gamma}_{yx}^2 \tag{2.17b}$$

where x is the flow direction, y is the velocity gradient direction and z is the neutral direction. Here, N_1, N_2 are the first and second normal stress differences and Ψ_1, Ψ_2 are known as the *first* and *second normal stress coefficients*, respectively. Eq. 2.17 demonstrates that the normal stress differences have a non-linear relationship with the applied shear rate. The behaviour of

the normal stress coefficients in response to shear rate varies based on the type of viscoelastic fluid.

The first normal stress coefficient can be experimentally determined via simple steady-shear tests in a cone-plate rotational rheometer as follows:

$$\Psi_1 = \frac{2F}{\pi R_{c-p}^2 \dot{\gamma}^2} \tag{2.18}$$

where F is the measured normal force exerted by the fluid on the rheometer plates, R_{c-p} is the radius of the cone-plate geometry and $\dot{\gamma}$ is the applied shear rate, which remains uniform across the gap in this specific setup.

For polymer solutions, Ψ_1 typically demonstrates a zero-shear plateau, followed by a shear-thinning behaviour. The second normal stress coefficient is more difficult to measure, as it requires the measurement of the local stress distribution across the plate surface. Limited experimental studies suggest that Ψ_2 is negative and smaller in magnitude compared to Ψ_1 (Bird et al., 1987).

In this work, the viscoelasticity of the tested bubble suspensions was not described through normal stress differences and coefficients due to difficulties associated with their experimental measurement. Specifically, instead of a cone-plate geometry typically used for measuring Ψ_1, a parallel plate geometry was employed to prevent bubble confinement issues that could arise from the smaller gap in cone-plate configurations. The viscoelastic properties of the bubble suspensions were assessed through material functions obtained in unsteady shear flow, and specifically, through small amplitude oscillatory shear (SAOS) tests.

SAOS tests provide useful insight into the relaxation processes occurring within a material's microstructure after the application of a linear sinusoidal shear deformation, as follows:

$$\gamma_{yx}(t) = \gamma_0 \sin \omega t \, ; \gamma_{ij} = 0 \;\; i,j \neq x,y \tag{2.21}$$

where γ_0 represents the infinitesimal amplitude of the sinusoidal deformation and ω is the oscillation frequency. The corresponding shear rate can then be expressed as:

$$\dot{\gamma}_{yx}(t) = \omega\gamma_0 \cos \omega t \, ; \gamma_{ij} = 0 \;\; i,j \neq x,y \tag{2.22}$$

According to the Boltzmann superposition principle, the effects of small sequential strain changes are additive (Ferry, 1980). Hence, the corresponding shear stress τ_{yx} is defined as:

$$\tau_{yx}(t) \equiv \int_{-\infty}^{t} G(t-t')\dot{\gamma}_{yx}(t')dt' \tag{2.23}$$

Eq. 2.23 can be used to define the *relaxation modulus* $G(t)$, which describes how a material recovers, or relaxes, from being deformed, essentially by reflecting how much stress remains in the material as time passes after deformation. $G(t)$ is expressed as a decreasing function because, as time passes, the material adjusts and reduces the residual stress. Thus, more recent deformations have a greater impact on the material's response than older ones, since the stress from earlier deformations has already had time to relax. $G(t)$ can be expressed as a single or multi-mode exponential function as follows:

$$G(t) = \sum_{i=1}^{N} G_i \exp\left(-t/\lambda_i\right) \tag{2.24}$$

where N represents the number of relaxation modes, with each relaxation mode corresponding to a distinct relaxation process occurring over a specific time scale λ_i. For an infinite number of relaxation modes, $G(t)$ can be described using a *continuous relaxation spectrum* $H(\lambda)$ (Bird et al., 1987), as shown below:

$$G(t) \equiv \int_{0}^{\infty} H(\lambda) \exp(-t/\lambda)\, d\ln\lambda \tag{2.25}$$

By substituting Eq. 2.22 into Eq. 2.23 and replacing $t - t'$ with s, one obtains the following expression for the shear stress:

$$\tau_{yx}(t) = -\int_{0}^{\infty} G(s)\,\omega\gamma_0 \cos[\omega(t-s)]\, ds$$

$$= \gamma_0\left[\omega \int_{0}^{\infty} G(s) \sin\omega s\, ds\right] \sin\omega t + \gamma_0\left[\omega \int_{0}^{\infty} G(s) \cos\omega s\, ds\right] \cos\omega t \tag{2.26}$$

As observed, the two terms in brackets are independent of the elapsed time, with the first term being in phase with the deformation and the second being in phase with the shear rate. Consequently, Eq. 2.26 can be expressed as follows:

$$\tau_{yx}(t) = -\gamma_0\,(G' \sin\omega t + G'' \cos\omega t) \tag{2.27}$$

where G' is the *storage modulus*, which describes the material's elastic character, and G'' is the *loss modulus*, which represents its viscous character. Considering the stress amplitude τ_0, Eq. 2.27 can be rewritten as:

$$\tau_{yx}(t) = -\tau_0 \sin(\omega t + \delta) = -\tau_0 \cos\delta \sin\omega t - \tau_0 \sin\delta \cos\omega t \tag{2.28}$$

Thus, the linear viscoelastic material functions can be defined as follows:

$$G' \equiv \frac{\tau_0}{\gamma_0}\cos\delta \tag{2.29a}$$

$$G'' \equiv \frac{\tau_0}{\gamma_0}\sin\delta \tag{2.29b}$$

$$\delta \equiv G''/\,G' \tag{2.29c}$$

The phase angle δ represents the relative importance of the viscous and elastic components of a material. For a purely viscous material, the storage modulus equals zero and δ equals $\pi/2$. On the other hand, for a purely elastic material, the loss modulus is equal to zero, leading to a zero phase angle as well (Larson, 1999). Like normal stress differences, the trends of the linear viscoelastic material functions depend on the specific properties of the fluid. Several viscoelastic models of different complexity have been proposed to describe these material functions. The simplest, but still the most fundamental, is the Maxwell model.

Maxwell model

The Maxwell model considers both the viscous and the elastic character of a material by representing its rheological properties with a spring and a dashpot connected in series (Fig. 2.5). In this configuration, the spring models the elastic component of the material, governed by Hooke's law, while the dashpot represents the viscous component, described by Newton's law. In the Maxwell model the stress contributions from both components are equal, and the total strain of the system is the sum of the individual strains, thus yielding the following constitutive equation:

$$\boldsymbol{\tau} + \lambda\frac{\partial\boldsymbol{\tau}}{\partial t} = -\,\eta_0\dot{\boldsymbol{\gamma}} \tag{2.30}$$

where $\boldsymbol{\tau}$ is the deviatoric stress tensor, η_0 represents the fluid's zero-shear viscosity, λ is the fluid's relaxation time (defined as the ratio of η_0 to the spring's elastic modulus G_e), and $\dot{\boldsymbol{\gamma}}$ is the rate of deformation tensor.

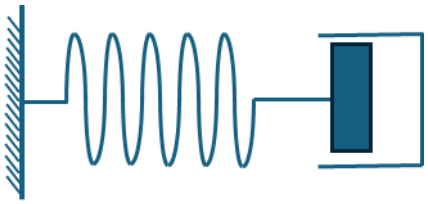

Figure 2.5: Schematic of a Maxwell unit.

Eq. 2.30 is written in terms of material coordinates; thus, the partial time derivative ($\partial/\partial t$) is essentially a material derivative. For a steady-shear flow from a Lagrangian perspective (i.e., from the viewpoint of an observer moving along with a fluid element as it flows), $\dot{\boldsymbol{\gamma}}$ remains constant with time. Consequently, Eq. 2.30 can be treated as a first order differential equation, resulting in:

$$\boldsymbol{\tau} + \eta_0 \dot{\boldsymbol{\gamma}} = A \exp(-t/\lambda);\ A = \boldsymbol{\tau}_{t=0} + \eta_0 \dot{\boldsymbol{\gamma}}_{t=0} \tag{2.31}$$

From Eq. 2.31, it can be concluded that over a time of order of magnitude λ, $\boldsymbol{\tau} \sim \eta_0 \dot{\boldsymbol{\gamma}}$, i.e., the material behaves like a Newtonian fluid with viscosity η_0. For transient flows, $\dot{\boldsymbol{\gamma}}$ varies in time, with $t_{\dot{\gamma}}$ denoting the timescale of its variation, thus Eq. 2.31 no longer applies. However, in this case the fluid behaviour can be interpreted using a scaling approach, for which the following dimensionless variables are introduced:

$$\bar{\boldsymbol{\tau}} \equiv \frac{\boldsymbol{\tau}}{\boldsymbol{\tau}_c};\ \dot{\bar{\boldsymbol{\gamma}}} \equiv \frac{\dot{\gamma}}{\dot{\gamma}_c};\ \bar{t} \equiv \frac{t}{t_{\dot{\gamma}}} \tag{2.32}$$

where for each variable, the scalar appearing at the denominator is the scale of that variable. In terms of these variables, Eq. 2.30 reads:

$$\bar{\boldsymbol{\tau}} + (\lambda/t_{\dot{\gamma}}) \frac{\partial \bar{\boldsymbol{\tau}}}{\partial \bar{t}} = -(\eta_0 \dot{\gamma}_c/\tau_c)\, \dot{\bar{\boldsymbol{\gamma}}} \tag{2.33}$$

The ratio $\lambda/t_{\dot{\gamma}}$ is referred to as the *Deborah number* (De). It appears in the Maxwell constitutive equation for unsteady states and serves as an indicator of whether the material will behave as a Newtonian fluid or as a Hookean solid (Larson, 1999). For $De \ll 1$, the timescale over which the rate of deformation changes significantly is much longer than the material's relaxation time. As a result, the material relaxes before experiencing significant variation in $\dot{\bar{\boldsymbol{\gamma}}}$. In this case, $\bar{\boldsymbol{\tau}} \sim -(\eta_0 \dot{\gamma}_c/\tau_c)\, \dot{\bar{\boldsymbol{\gamma}}}$, leading $\tau_c \sim \eta_0 \dot{\gamma}_c$. Hence, the material behaves like a Newtonian fluid. Conversely, when $De \gg 1$, $(\lambda/t_{\dot{\gamma}}) \frac{\partial \bar{\boldsymbol{\tau}}}{\partial \bar{t}}$ dominates over $\bar{\boldsymbol{\tau}}$, and Eq. 2.33 yields $(\lambda/t_{\dot{\gamma}}) \frac{\partial \bar{\boldsymbol{\tau}}}{\partial \bar{t}} \sim -(\eta_0 \dot{\gamma}_c/\tau_c)\, \dot{\bar{\boldsymbol{\gamma}}}$. In this case, the material behaves as a Hookean solid, where $\tau_c \sim G_e \gamma_c$, with $G_e \equiv \eta_0/\lambda$ and $\gamma_c \equiv \dot{\gamma}_c t_{\dot{\gamma}}$ (γ_c being the deformation scale).

At this point, it is important to note that the Maxwell equation is linear, and therefore it cannot predict non-linear viscoelastic effects, such as normal stress differences. To account for such phenomena, one should use the *upper-convected Maxwell model*, which will be discussed in more detail in the following section. However, the classic Maxwell model remains useful

for describing the linear viscoelastic material functions derived from SAOS tests. The relaxation modulus for a Maxwell fluid can be written in terms of the relaxation time λ and zero-shear viscosity η_0 as follows:

$$\tau_{yx} \equiv \int_{-\infty}^{t} \frac{\eta_0}{\lambda} e^{-(t-t')/\lambda} \dot{\gamma}_{yx}(t')dt' \tag{2.34}$$

By substituting the expression for τ_{yx} (Eq. 2.21) into Eq. 2.34, the shape of the G', G'' curves for a Maxwell fluid can be predicted as follows:

$$G' = \frac{\eta_0 \lambda \omega^2}{1+\lambda^2\omega^2} \tag{2.35a}$$

$$G'' = \frac{\eta_0 \omega}{1+\lambda^2\omega^2} \tag{2.35b}$$

By normalizing Eq. 2.35 with the Hooke's elastic modulus $G_e = \eta_0/\lambda$, and considering the characteristic timescale for the variation of shear rate in an oscillatory shear flow, which is directly linked to the oscillation frequency ($t_{\dot{\gamma}} \sim 1/\omega$), Eq. 2.35 can be expressed in terms of the Deborah number as follows:

$$G' = \frac{De^2}{1+De^2} \tag{2.36a}$$

$$G'' = \frac{De}{1+De^2} \tag{2.36b}$$

Observing Eq. 2.36, it becomes evident that at low oscillation frequencies, i.e., for $De \ll 1$, $G' \sim De^2$ and $G'' \sim De$. In this regime, known as the *terminal viscous regime*, both viscoelastic moduli increase with De but at different rates. Specifically, G' follows a power law with a slope of 2, while G'' increases linearly with De. At higher oscillation frequencies, i.e., for $De \gg 1$, Eq. 2.36 yields $G' \sim 1$ and $G'' \sim 1/De$, indicating that the storage modulus reaches a constant value (i.e., G_e), while the loss modulus gradually decreases toward zero. For $De = 1$, the two moduli intersect, marking the transition from a viscous to an elastic regime, where G' stabilises to a plateau and G'' approaches zero. The relaxation time of the material can be determined from the inverse of the oscillation frequency at which the two moduli intersect. Fig. 2.6 (black lines) illustrates typical G', G'' curves for a Maxwell fluid.

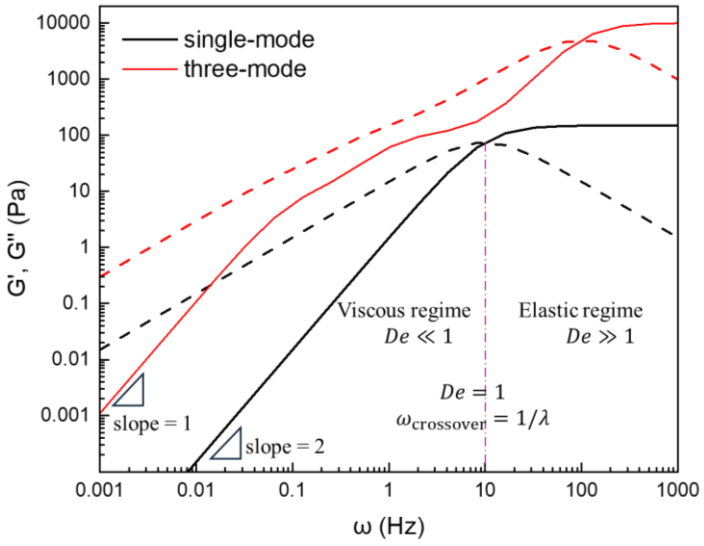

Figure 2.6: Example of G' (solid lines) and G'' (dashed lines) for a single-mode and a three-mode Maxwell fluid.

For more complex relaxation behaviours, the shapes of $G'(\omega)$ and $G''(\omega)$ may differ from the patterns previously described. In such cases, a *generalised Maxwell model* can be used to better capture the fluid's response. This approach models the fluid as consisting of N Maxwell elements arranged in series. Following the linear superposition principle, the total stress is calculated as the sum of the stresses from each individual element. Consequently, Eq. 2.35 can be written more generally as follows:

$$G' = \sum_{i=1}^{N} \frac{\eta_i \lambda_i \omega^2}{1+\lambda_i^2 \omega^2} \tag{2.37a}$$

$$G'' = \sum_{i=1}^{N} \frac{\eta_i \omega}{1+\lambda_i^2 \omega^2} \tag{2.37b}$$

For comparison purposes, Fig. 2.6 also displays an example of G' and G'' curves corresponding to a generalised Maxwell fluid with three relaxation modes (red lines).

Upper-convected Maxwell model

As mentioned earlier, the classic Maxwell model is linear and so cannot predict non-linear viscoelastic phenomena such as normal stress differences. To address this limitation, non-linear models were developed, with the *upper-convected Maxwell model* being the simplest among them. In this model, the material time derivative of the deviatoric stress tensor is replaced by the convected time derivative, resulting in a modified form of Eq. 2.30. This version, scaled and expressed using dimensionless variables, reads:

$$\bar{\boldsymbol{\tau}} + (\lambda/t_{\dot{\gamma}})\frac{\partial\bar{\boldsymbol{\tau}}}{\partial\bar{t}} - (\lambda\dot{\gamma}_c)[\left(\frac{\partial\bar{\boldsymbol{v}}}{\partial\bar{\boldsymbol{x}}}\right)^{\dagger}\cdot\bar{\boldsymbol{\tau}} + \bar{\boldsymbol{\tau}}\cdot\left(\frac{\partial\bar{\boldsymbol{v}}}{\partial\bar{\boldsymbol{x}}}\right)] = -(\eta_0\dot{\gamma}_c/\tau_c)\,\dot{\bar{\boldsymbol{\gamma}}} \tag{2.38}$$

where $\partial/\partial\bar{t}$ is the material time derivative, $\partial\bar{\boldsymbol{v}}/\partial\bar{\boldsymbol{x}}$ is the dimensionless velocity gradient tensor, and $(\partial\bar{\boldsymbol{v}}/\partial\bar{\boldsymbol{x}})^{\dagger}$ is its transpose. On the left-hand side of Eq. 2.38, two dimensionless numbers are present: one is the Deborah number ($De \equiv \lambda/t_{\dot{\gamma}}$) and the other is the *Weissenberg number*, defined as $Wi \equiv \lambda\dot{\gamma}_c$ (Larson, 1999). This number is associated with the non-linear part of Eq. 2.38 – the part that in shear flows results into normal stress differences.

Analysing the different regimes of the Deborah and Weissenberg numbers provides valuable insights into the material behaviour. When $De \ll 1$ and $Wi \ll 1$, Eq. 2.38 yields $\bar{\boldsymbol{\tau}} \sim (\frac{\eta_0\dot{\gamma}_c}{\tau_c})\dot{\bar{\boldsymbol{\gamma}}}$, so that $\tau_c \sim \eta_0\dot{\gamma}_c$, indicating a Newtonian fluid-like behaviour. When $De \ll 1$ and $Wi \gg 1$, the non-linear term of Eq. 2.38 becomes important, while $(\lambda/t_{\dot{\gamma}})\partial_t\bar{\boldsymbol{\tau}}$ is still negligible compared to $\bar{\boldsymbol{\tau}}$. Considering the dimensional variables, Eq. 2.38 can be approximated with:

$$\boldsymbol{\tau} - \lambda[\left(\frac{\partial\boldsymbol{u}}{\partial\boldsymbol{x}}\right)^{\dagger}\cdot\boldsymbol{\tau} + \boldsymbol{\tau}\cdot\left(\frac{\partial\boldsymbol{u}}{\partial\boldsymbol{x}}\right)] = -\eta_0\dot{\boldsymbol{\gamma}} \tag{2.39}$$

For a simple shear flow, this yields $\tau_{xx} = -2\lambda\eta_0\dot{\gamma}^2$, $\tau_{xy} = -\eta_0\dot{\gamma}$, $\tau_{yy} = 0$, showing that the first normal stress difference is not zero and is related to Wi, highlighting the influence of nonlinear effects. For $De \gg 1$ and $Wi \ll 1$, Eq. 2.38 simplifies to $(\lambda/t_{\dot{\gamma}})\partial_t\bar{\boldsymbol{\tau}} \sim (\eta_0\dot{\gamma}_c/\tau_c)\dot{\bar{\boldsymbol{\gamma}}}$, indicating behaviour similar to that of a Hookean solid with $\tau_c \sim G_e\gamma_c$. In cases where both $De \gg 1$ and $Wi \gg 1$, the material exhibits characteristics of a nonlinear solid.

In essence, the Deborah number determines whether the material behaves like a Newtonian fluid or an elastic Hookean solid, while the Weissenberg number reflects the importance of nonlinear effects, such as normal stress differences, relative to viscous stresses (Dealy, 2010; Poole, 2012).

Jeffreys model

The Maxwell and upper-convected Maxwell models previously discussed provide fundamental insights into the viscoelastic behaviour of materials and form the basis for more advanced models. While essential for understanding simpler systems, these models cannot fully capture the behaviour of more complex, multiphase systems. The Jeffreys model extends the Maxwell framework, offering a more comprehensive description of the viscoelastic behaviour in dilute suspensions consisting of viscoelastic particles dispersed in a Newtonian fluid. These particles can be solid particles, droplets, polymeric molecules or bubbles. The

Jeffreys model suggests that the total stress in the suspension is the sum of the stress contributions of the solvent and the dispersed phase (Bird et al., 1987). The solvent is a Newtonian fluid, and the particles obey the Maxwell equation as follows:

$$\boldsymbol{\tau} = \boldsymbol{\tau}_p + \boldsymbol{\tau}_s \; ; \boldsymbol{\tau_s} = -\eta_s \dot{\boldsymbol{\gamma}} \; ; \boldsymbol{\tau}_p + \lambda \frac{\partial \boldsymbol{\tau}_p}{\partial t} = -\eta_p \dot{\boldsymbol{\gamma}} \tag{2.40}$$

where $\boldsymbol{\tau}$ is the deviatoric stress tensor of the mixture, subscripts s and p denote the solvent and the particles, respectively, η_s is the Newtonian viscosity of the solvent (constant), and $\partial/\partial t$ is the material time derivative. The Jeffreys constitutive equations is then given by:

$$\boldsymbol{\tau} + \lambda \frac{\partial \boldsymbol{\tau}}{\partial t} = -\eta_0 (\dot{\boldsymbol{\gamma}} + \lambda_2 \frac{\partial \dot{\boldsymbol{\gamma}}}{\partial t}) \tag{2.41}$$

In Eq. 2.41, $\eta_0 \equiv \eta_s + \eta_p$ is the zero-shear viscosity of the suspension, λ is the relaxation time of the viscoelastic particles, and $\lambda_2 \equiv \lambda \eta_s / \eta_0$ is known as the retardation time. The relaxation time for a single fluid droplet in simple shear is given by the expression $\lambda \equiv (1+\beta)(\eta_s R)/\sigma$, where β is the viscosity ratio between the dispersed and continuous phases, R is the radius of the relaxed droplets, assumed to be all identical, and σ is the interfacial tension between the two phases (Loewenberg and Hinch, 1996). In the case of inviscid bubbles, where $\beta = 0$, this expression reduces to $\lambda \equiv (\eta_s R)/\sigma$.

As seen, Eq. 2.41 is linear and, similarly to the Maxwell equation, cannot predict non-linear effects, such as normal stress differences. The Jeffreys constitutive equation features an additional term compared to the Maxwell equation, and a scaling analysis can be used to understand how this term affects the rheological behaviour of the mixture. Using the scales given in Eq. 2.32, the following expression is obtained:

$$\bar{\boldsymbol{\tau}} + (\lambda / t_{\dot{\gamma}}) \frac{\partial \bar{\boldsymbol{\tau}}}{\partial \bar{t}} = -(\eta_0 \dot{\gamma}_c / \tau_c) \, [\dot{\bar{\boldsymbol{\gamma}}} + (\lambda_2 / t_{\dot{\gamma}}) \frac{\partial \dot{\bar{\boldsymbol{\gamma}}}}{\partial \bar{t}}] \tag{2.42}$$

If $De \ll 1$, then $t_{\dot{\gamma}} \gg \lambda$, and since $\lambda > \lambda_2$, it follows that $t_{\dot{\gamma}} \gg \lambda_2$. Consequently, the terms containing the time derivative become negligible, reducing Eq. 2.42 to $\boldsymbol{\tau} = -\eta_0 \dot{\boldsymbol{\gamma}}$. In this flow regime, the mixture behaves as a Newtonian fluid with viscosity η_0 and, as anticipated, normal stress differences are absent. For $De \gg 1$, two scenarios arise. If $\lambda_2 / t_{\dot{\gamma}} \ll 1$, a condition that holds only if $\eta_0 / \eta_s \gg 1$, $\boldsymbol{\tau}$ is negligible compared to $\lambda \, \partial_\tau \boldsymbol{\tau}$, and $\lambda_2 \, \partial_t \dot{\boldsymbol{\gamma}}$ is negligible compared to $\dot{\boldsymbol{\gamma}}$. In this case, the mixture behaves as a Hookean solid with an elastic modulus G_e. On the other hand, when $\lambda_2 / t_{\dot{\gamma}} \gg 1$, the time derivatives dominate, leading to $\tau_c \sim (\lambda_2/\lambda)\eta_0 \dot{\gamma}_c \sim \eta_s \dot{\gamma}_c$.

Therefore, the mixture behaves as a Newtonian fluid, but in this case the viscosity coincides with the viscosity of the solvent, the particle contribution being negligible.

It is important to note that the Jeffreys model is designed for dilute suspensions, where the interactions among particles are considered negligible. In this case, the total stress can be determined using the linear superposition of the individual stress contributions. However, for more concentrated systems, where the particle-particle interactions become significant, the Jeffreys model may not fully capture the complexities of the system, and more sophisticated models are often required (Ponce-Torres et al., 2018).

2.2 Rheology of bubble suspensions in Newtonian media

Having provided the necessary context for the rheology of complex fluids, this section focuses on the rheological properties of bubble suspensions in Newtonian media, reviewing key studies and their findings. Bubble suspensions, composed of gas bubbles dispersed in a liquid medium, exhibit rheological properties that differ significantly from those of the continuous phase alone. The presence of bubbles has been shown to alter the flow properties of the suspension, introducing non-Newtonian phenomena such as shear-thinning behaviour and viscoelastic effects (Llewellin et al., 2002a; Rust and Manga, 2002). This complex rheological behaviour is influenced by several key parameters, including the properties of the continuous phase, such as viscosity and surface tension, the volume fraction of the bubbles φ, their size distribution, and their interactions with the surrounding fluid (Pal, 2003).

To effectively analyse these systems, it is essential to consider dimensionless numbers that correlate the bubble relaxation time with the characteristic flow time, elucidating the deformation and relaxation processes that affect the overall rheological response of the suspension. Similar to the use of the Deborah and Weissenberg numbers in the broader study of complex fluids, the *capillary number* Ca and the *dynamic capillary number* Cd, which are specific to bubble suspensions, provide critical insights into the behaviour of these systems across different flow regimes (Llewellin and Manga, 2005). A detailed discussion of these important dimensionless parameters is presented in the following section.

2.2.1. Capillary and dynamic capillary numbers

In every sheared bubble suspension, two opposite forces act on the dispersed bubbles: shear stress and surface tension. Shear stress tends to deform and elongate the bubbles, while surface tension tends to restore the bubbles to their initial spherical shape, preventing deformation. Under steady shear, bubbles elongate until they reach an equilibrium configuration in which

their deformation is constant, and their shape remains stable. Llewellin et al. (2002a), Rust and Manga (2002) and several subsequent studies have used a dimensionless parameter called *capillary number* Ca to describe the ratio between the deforming viscous shear stress and the restoring surface tension. In terms of characteristic times, Ca is the ratio between two time scales, namely λ and t_d. The latter represents the time required by the flow to deform the bubble significantly, essentially the time *required* by the deformation process, and is equal to $1/\dot{\gamma}$. The former, as previously mentioned, is the relaxation time, representing the time that the bubble takes to attain a new equilibrium condition after a change of $\dot{\gamma}$. Once a time of order λ has elapsed, the bubble reaches equilibrium again. Therefore, λ can be understood as the time *available* to the deformation process, and the capillary number is defined as follows:

$$Ca \equiv \frac{\lambda}{t_d} \tag{2.43}$$

The relaxation time of uniform-sized bubbles suspended in a Newtonian solvent is given by the following equation (Llewellin et al., 2002a):

$$\lambda \equiv \frac{k(\varphi)\eta_s R}{\sigma} \tag{2.44}$$

where η_s is the constant viscosity of the solvent, R is the radius of the relaxed, undeformed bubbles, σ is the surface tension of the ambient fluid, and $k(\varphi)$ is a parameter, which describes the bubble interactions and increases with the volume fraction of the dispersed phase. For dilute suspensions where interactions are considered negligible, $k \approx 1$ and Eq. 2.44 reduces to the expression for the relaxation time of a single bubble, i.e., $\lambda \equiv \eta_s R/\sigma$. Substituting this expression for λ and the expression for t_d in Eq. 2.43, one obtains the following equivalent expression for Ca, defined as the ratio between the deforming shear stress and the restoring surface tension:

$$Ca \equiv \frac{\lambda}{t_d} = \frac{\frac{\eta_s R}{\sigma}}{\frac{1}{\dot{\gamma}}} = \frac{\eta_s R \dot{\gamma}}{\sigma} \tag{2.45}$$

Eq. 2.43 shows that for small capillary numbers ($Ca \ll 1$), the time available for deformation is much shorter than the time required, resulting in negligible bubble deformation. In this case, the suspended bubbles remain spherical and act as obstacles to the flow, distorting the fluid streamlines around them. Therefore, the relative viscosity of the suspension ($\eta_r \equiv \eta_{suspension}/\eta_{solvent}$) increases with bubble volume fraction. Conversely, for large capillary numbers ($Ca \gg 1$), the time available for deformation is much longer than the time required.

Hence, the bubbles deform significantly, introducing larger free-slip surfaces that align with the fluid streamlines and leading to a decrease in suspension viscosity. In other words, as the shear rate, and in turn the capillary number, increases, bubbles elongate more, and the flow resistance decreases, indicating that the suspension behaves as a shear-thinning fluid. For monodisperse bubble suspensions, the onset of the shear-thinning behaviour occurs at capillary number values of unit order magnitude ($Ca \sim 1$), as illustrated in Fig. 2.7.

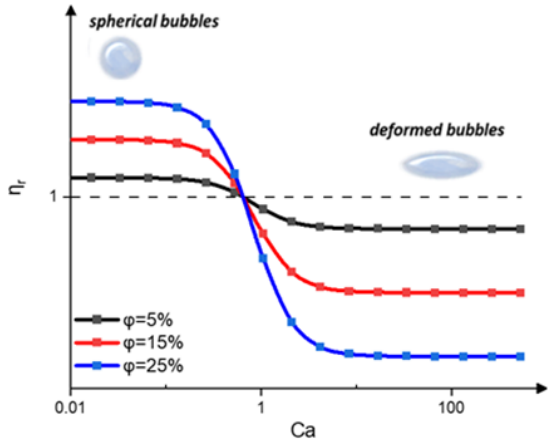

Figure 2.7: Relative viscosity as a function of the capillary number (Ca) and the bubble volume fraction (φ) for a monodisperse bubble suspension.

Shear-thinning behaviour is a non-linear effect and is predicted by the capillary number. Therefore, Ca can be considered the equivalent of the Weissenberg number for bubble suspensions. For unsteady flows from a Lagrangian standpoint, Llewellin et al. (2002a) introduced another dimensionless parameter, called *dynamic capillary number*, Cd, which is equivalent to the Deborah number. In an unsteady flow, bubble suspensions are subjected to a varying shear rate, and thus the deforming (viscous) and restoring (surface tension) forces acting on a bubble are not in equilibrium. As mentioned earlier, λ can be regarded as the time required by the bubbles to attain an equilibrium configuration after a change in $\dot{\gamma}$. The bubble can attain this configuration only if, over a time of order λ, the shear rate is constant. If this condition is not met, the bubble always lags, never being able to reach equilibrium.

Hence, to gauge whether equilibrium is attained, one must compare the relaxation time to the time scale characterising the rate of change of the shear rate. The latter is the time required to make the shear rate change significantly, meaning that the order of magnitude of the change needs to be equal with the order of magnitude of the shear rate. Therefore, the timescale over which the shear rate changes significantly is given by $\dot{\gamma}/\ddot{\gamma}$, and the dynamic capillary number is defined as follows:

$$Cd \equiv \frac{\lambda}{t_{\dot{\gamma}}} = \frac{\lambda}{\frac{\dot{\gamma}}{\ddot{\gamma}}} = \frac{\lambda\ddot{\gamma}}{\dot{\gamma}} \tag{2.46}$$

As shown in Eq. 2.46, for $Cd \ll 1$, the time necessary to reach equilibrium is much shorter than the time over which the shear rate changes significantly, and consequently the bubble relaxes and reaches equilibrium. On the contrary, for $Cd \gg 1$, the bubble is always far from equilibrium. For an oscillatory, simple shear flow, the timescale over which the shear rate changes significantly is equal to the inverse of the oscillation frequency ω, and Eq. 2.46 becomes:

$$Cd = \lambda\omega \tag{2.47}$$

To gain a deeper understanding of the viscoelasticity of bubble suspensions, the Jeffreys constitutive equation (Eq. 2.41) can be employed. Since the Jeffreys equation is linear, it holds only when $Ca \ll 1$, a condition that implies that the bubbles are spherical. Eq. 2.41 can be integrated as a first-order differential equation, using the initial condition that $\boldsymbol{\tau}$ be finite at $t = -\infty$, and reads:

$$\boldsymbol{\tau}(t) = -\int_{-\infty}^{t} \frac{\eta_0}{\lambda}\left(1 - \frac{\lambda_2}{\lambda}\right) e^{-\frac{t-t'}{\lambda}} \dot{\boldsymbol{\gamma}}(t')dt' - \frac{\eta_0\lambda_2}{\lambda}\dot{\boldsymbol{\gamma}}(t) \tag{2.48}$$

where t' is a past time relative to the configuration of the suspension at the present time t. Considering a sinusoidal deformation $\gamma(t) = \gamma_0 \sin\omega t \Longrightarrow \dot{\gamma}(t) = \gamma_0\omega\cos\omega t$, under small amplitude conditions Eq. 2.48 becomes:

$$\boldsymbol{\tau}(t) = G'(\omega)\gamma_0 \sin\omega t + G''(\omega)\gamma_0 \cos\omega t \tag{2.49}$$

where G' and G'' are given by:

$$G'(\omega) = \frac{\eta_0(\lambda-\lambda_2)\omega^2}{1+(\lambda\omega)^2} \tag{2.50a}$$

$$G''(\omega) = \frac{\eta_0\omega(\lambda-\lambda_2)}{\lambda(1+(\lambda\omega)^2)} + \frac{\eta_0\lambda_2\omega}{\lambda} \tag{2.50b}$$

For $Cd \ll 1$ (i.e., when $\omega \sim 0$), Eq. 2.50 yields $G'(\omega) \sim 0$ and $G''(\omega) \sim \eta_0\omega$. Hence, bubbles behave as a Newtonian fluid with zero elasticity, and the total deviatoric stress is given by the sum of the contributions of the liquid and of the bubbles, both of which are significant, so that the mixture viscosity is equal to $\eta_0 \equiv \eta_s + \eta_p$. When $Cd = \lambda\omega \sim 1$, Eq. 2.50 gives $G'(\omega) \sim \frac{\eta_0(\lambda-\lambda_2)}{2\lambda^2}$ and $G''(\omega) \sim \frac{\eta_0(\lambda+\lambda_2)}{2\lambda^2}$. In this case, both the viscous and the elastic parts of the

material's response are important, but in very dilute systems, the elastic part is not appreciable, as $\lambda \approx \lambda_2$.

For $Cd \gg 1$ (i.e., when $\omega \sim \infty$), two scenarios arise. If $Cd \gg 1$ and $\frac{\lambda_2}{t_{\dot{\gamma}}} \ll 1 \rightarrow \lambda_2 \omega \ll 1$, Eq. 2.50 yields $G'(\omega) \sim G_e = \eta_0/\lambda$ and $G''(\omega) \sim 0$, respectively. This means that the bubbles behave like a Hookean solid, their stress contribution being equal to:

$$\tau_{c,bubbles} \sim G_e \gamma_c \sim \left(\frac{\eta_0}{\lambda}\right)\left(\dot{\gamma}_c t_{\dot{\gamma}}\right) \sim \left(\frac{1}{\lambda_2 \omega}\right)\left(\eta_s \dot{\gamma}_c\right) \sim \left(\frac{1}{\lambda_2 \omega}\right)\tau_{c,solvent} \gg \tau_{c,solvent} \qquad (2.51)$$

In this case, the contribution of the bubbles is dominant, so the mixture behaves like a Hookean solid. However, it is important to note that this is possible only if $\lambda_2 \sim 0$, i.e., when the viscosity of the dispersed phase diverges. This can only happen in extremely dense conditions, which are probably not feasible. Therefore, in practise, $G'(\omega) \sim G_e = \eta_0/\lambda$, but $G''(\omega)$ will not vanish, meaning the suspension will behave as a viscoelastic fluid.

On the other hand, for $Cd \gg 1$ and $\frac{\lambda_2}{t_{\dot{\gamma}}} \gg 1 \rightarrow \lambda_2 \omega \gg 1$, Eq. 2.50 giveσ $G'(\omega) \sim 0$ and $G''(\omega) \sim \eta_s \omega$, indicating that the mixture behaves like a Newtonian fluid with viscosity equal to that of the solvent (η_s). The stress contribution from the bubbles is negligible compared to that from the fluid, which dominates the mixture behaviour. This is because the stress coming from the bubbles is proportional to the deformation, and this is very small, whereas the stress from the ambient liquid is proportional to the deformation rate, and this is very large.

The viscoelastic behaviour of bubble suspensions was investigated experimentally in the study of Llewellin et al. (2002a) and the results are shown in Fig. 2.8. As illustrated, for all tested bubble volume fractions, the phase shift decreases up to a minimum and then increases again. The minimum in phase shift indicates a maximum in the elastic deformation of the suspension. The experimental results of Llewellin et al. (2002a) confirm the general viscoelastic behaviour derived from the scaling analysis of the Jeffreys model. At low frequencies and, hence, at $Cd \ll 1$, the suspension behaves as a Newtonian fluid. As Cd approaches unity the elasticity of the suspension becomes evident, and the system behaves as a viscoelastic fluid. Finally, at $Cd \gg 1$, the suspension returns to Newtonian behaviour.

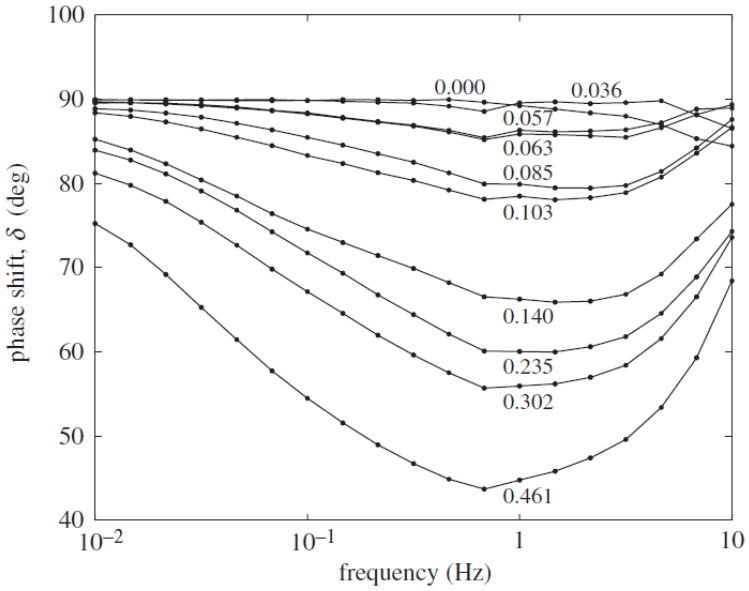

Figure 2.8: Phase shift δ as a function of the oscillation frequency for varying bubble volume fraction (Llewellin et al., 2002a).

2.2.2. Rheological models for bubble suspensions in Newtonian media

After introducing the key dimensionless numbers relevant to the rheology of bubble suspensions, this section provides an overview of the most fundamental rheological models developed for bubble suspensions in Newtonian media. These models describe the rheological properties in both steady and oscillatory shear flows as a function of the bubble volume fraction, the capillary number and the dynamic capillary number, and are essential for validating experimental data and understanding the complex behaviour of bubble suspensions, including shear-thinning and viscoelastic effects. The more intricate rheology of bubble suspensions in non-Newtonian media, along with the associated main models, will be addressed in more detail in a subsequent section.

One of the most fundamental studies on the rheology of bubble suspensions is that of Llewellin et al. (2002a). In this work, the authors prepared bubble suspensions in Newtonian corn syrup, with bubble volume fraction ranging between 3.6% and 46.1%, and performed SAOS tests to investigate their viscoelastic behaviour. To model the observed behaviour, they proposed a semi-empirical rheological model (Eq. 2.52) in the form of the linear Jeffreys model, based on the analysis of Frankel and Acrivos (1970), on the rheology of dilute monodisperse emulsions with nearly spherical droplets ($Ca \ll 1$):

$$\tau_{ij} + \frac{6}{5}\lambda\dot{\tau}_{ij} = \eta_s(1+\varphi)\dot{\gamma}_{ij} + \eta_s\frac{6}{5}\lambda\left(1-\frac{5}{3}\varphi\right)\ddot{\gamma}_{ij} \tag{2.52}$$

where η_s is the viscosity of the solvent (i.e., ambient fluid), φ is the bubble volume fraction and $\dot{\tau}_{ij}$ and $\ddot{\gamma}_{ij}$ are the partial time derivative of the shear stress and the shear rate, respectively.

Although Eq. 2.52 is linear, it is a reduction of the more general and non-linear model developed by Frankel and Acrivos (1970). Before discussing Llewellin et al.'s constitutive equation in more detail, it is worth providing context on this foundational work. Frankel and Acrivos developed a constitutive equation to describe the rheology of a dilute emulsion, where small droplets suspended in an incompressible Newtonian fluid undergo small deformations (i.e., $Ca \ll 1$) under time-dependent (transient) shear flow. The authors employed a perturbation approach to describe the stress response of the droplets, and since the equation is developed under the assumption of small deformations, it allowed for a first-order approximation. It is important to note that despite assuming small deformations, the proposed equation is not linear; non-linearities arise due to the way droplet deformation affects the stress distribution in the surrounding fluid. Specifically, the interaction between the deformed droplets and the surrounding flow introduces quadratic terms in the strain rate. Furthermore, the use of the Jaumann derivative ($\overset{\circ}{A}_{ij} = \frac{\partial A_{ij}}{\partial t} + u_k \frac{\partial A_{ij}}{\partial x_k} + \varpi_{ik} A_{kj} - A_{ik} \varpi_{kj}$, where A_{ij} is an arbitrary tensor, u_i is the velocity vector, and ϖ_{ij} is the vorticity tensor), which accounts for rotational effects, adds further non-linear corrections. Thus, even within the small deformation framework, the model captures a non-linear relationship between stress and strain rate.

Llewellin et al. (2002a) simplified the constitutive equation proposed by Frankel and Acrivos (1970), considering that in a simple oscillatory shear flow the vorticity is zero. Thus, they replaced the Jaumann derivative with the material derivative. Additionally, they considered that bubbles are inviscid, meaning the viscosity ratio between the interior of the bubble and the surrounding fluid is zero, resulting in Eq. 2.52. Llewellin et al. (2002a) proposed that this equation holds for $Ca \ll 1$, Cd varying up to at least 10, and $\varphi \leq 0.5$. However, their statement regarding the validity of the equation at such high bubble volume fractions deserves closer examination, as it conflicts with the theoretical framework of Frankel and Acrivos (1970), which was specifically developed for dilute emulsions and forms the foundation of Llewellin et al.'s work.

Another aspect of Eq. 2.52 that requires careful consideration regards the predicted behaviour when $Cd \gg 1$. For $Cd \ll 1$, Eq. 2.52 simplifies to $\tau_{ij} = \eta_s(1 + \varphi)\dot{\gamma}_{ij}$, indicating that the suspension behaves as a Newtonian fluid with an effective viscosity $\eta_0 = \eta_s(1 + \varphi) = \eta_s + \eta_s\varphi = \eta_s + \eta_b$ (η_b being the viscosity contribution coming from the bubbles). This aligns with the predictions of the Jeffreys model for low Cd values. However, when $Cd \gg 1$, the time derivative terms dominate, leading to:

$$\dot{\tau}_{ij} = \eta_s \left(1 - \frac{5}{3}\varphi\right) \ddot{\gamma}_{ij} \Longrightarrow \tau_{ij} = \eta_s \left(1 - \frac{5}{3}\varphi\right) \dot{\gamma}_{ij} \tag{2.53}$$

This implies that for $Cd \gg 1$ and $Ca \ll 1$, the fluid behaves as a Newtonian fluid with viscosity $\eta_\infty = \eta_s \left(1 - \frac{5}{3}\varphi\right)$, i.e., the viscosity of the suspension decreases with bubble volume fraction. This conclusion contradicts what has been earlier derived from the scaling analysis of the Jeffreys model, which suggested that for $Cd \gg 1$, the viscosity of the suspension coincides with the viscosity of the solvent.

This discrepancy between the predictions of the Jeffreys model and those of the Llewellin et al. (2002a) model in the high Cd regime most likely stems from the different theoretical frameworks underlying the two models. The Jeffreys model is a macroscopic viscoelastic model that describes the overall stress in a suspension by linearly combining elastic and viscous components. In contrast, the Frankel and Acrivos model (which forms the basis of the Llewellin et al. model) accounts for non-linearities in the flow caused by even minimal bubble deformation, which the linear Jeffreys model does not consider. Determining which model is more appropriate for describing the behaviour of bubble suspensions in the $Ca \ll 1$ and $Cd \gg 1$ regime remains an uncertainty and necessitates further experimental data for clarification.

The physical explanation provided by Llewellin et al. (2002a) with regard to the suspension behaviour in this regime requires further examination. They propose that at very high ω, and, thus, Cd, the flow around the bubbles changes very rapidly and the bubbles do not have enough time to relax and attain a new equilibrium configuration. As a result, they oscillate around a fixed shape, which is close to spherical ($Ca \ll 1$). While the ambient Newtonian fluid relaxes instantly, the bubbles are always stressed and this stress leads to internal bubble deformation. Since the bubbles are essentially inviscid, the dissipation per unit volume and, hence, the relative viscosity of the suspension decrease as the bubble volume fraction increases. However, this approach accounts only for the stress inside the bubble and not for what happens on the surface of the bubble and in the ambient fluid. In other words, this reasoning does not consider the surface tension and the distortion of the fluid streamlines, both of which are crucial for shaping the viscoelastic response of the system.

As continuation to their first study, Llewellin et al. (2002b) solved analytically the original constitutive equation of Frankel and Acrivos (1970), i.e., the one featuring the non-linear terms, to obtain a constitutive equation for the steady-shear viscosity of monodisperse bubble suspensions, i.e., for $Cd \sim 0$ and varying Ca. The equation reads:

$$\eta_r = \begin{cases} 1+\varphi, for\ \ Ca \ll 1 \\ 1-\frac{5}{3}\varphi, for\ \ Ca \gg 1 \end{cases} \tag{2.54}$$

and can be recast in the form of Cross model as follows:

$$\eta_r = \eta_{r,\infty} + \frac{\eta_{r,0}-\eta_{r,\infty}}{1+(KCa)^m}\text{ , with } K = 6/5 \text{ and } m = 2 \tag{2.55a}$$

$$\eta_{r,0} = 1+\varphi \tag{2.55b}$$

$$\eta_{r,\infty} = 1-\frac{5}{3}\varphi \tag{2.55c}$$

where $\eta_r \equiv \eta_{suspension}/\eta_{solvent}$ is the relative viscosity of the suspension. Eq. 2.55b is essentially the Taylor equation (Taylor, 1932) for the relative zero-shear viscosity of dilute bubble suspensions, and it is derived as follows:

$$\eta_r = 1+\frac{2+5b}{2+2b}\varphi \tag{2.56}$$

where b is the ratio of inclusion material viscosity to matrix liquid viscosity. For solid particles, $b \to \infty$ and Eq. 2.56 reduces to the Einstein equation (Einstein, 1911). For bubbles, $b \to 0$ and Eq. 2.56 becomes equal to $1+\varphi$. Eq. 2.55c is known as the Mackenzie equation ((Mackenzie, 1950)), proposed for the infinite-shear viscosity of bubble suspensions under steady shear.

Rust & Manga (2002) found good agreement between their steady-shear experimental data and Eq. 2.55 with $K = 0.72$ and $m = 1.43$. In this case, rather than using the Taylor and Mackenzie equations, they suggested that the zero-shear relative viscosity is given by the Krieger–Dougherty equation for solid particles ($\eta_{r,0} = \left(1-\frac{\varphi}{\varphi_m}\right)^{-B\varphi_m}$) with empirically defined parameters $\varphi_m = 0.6$ and $B = 1$, while the infinite-shear viscosity follows an empirical correlation with the volume fraction: $\eta_{r,\infty} = 1+c_1\varphi+c_2\varphi^2$, with $c_1 = -1.14$ and $c_2 = -9.8$. Morini et al. (2019) also reported good agreement between their experimental data and the predictions of Eq. 2.55.

Tasaka et al. (2015) investigated the magnitude of the complex viscosity of dilute bubble suspensions subjected to oscillatory shear flows using ultrasonic spinning rheometry. This technique enables measurement of this quantity at different radial positions within a rotating cylinder by using spatio-temporal velocity data obtained via ultrasonic velocity profiling (UVP). The oscillatory rotation induces an unsteady shear flow with continuous non-equilibrium bubble deformations. The authors found that the extent of bubble deformation, and consequently the magnitude of the complex viscosity of the suspension, varied depending on the radial position within the cylinder, with bubbles near the wall experiencing significant deformation due to higher shear stress, while those closer to the centre remained relatively

undeformed (i.e., $Ca \ll 1$). The degree of deformation was also influenced by the imposed oscillation frequency, with higher frequencies leading to increased deformations.

At the highest tested frequency, the relative viscosity of the suspension (defined as the ratio of the magnitude of the complex viscosity of the suspension to the viscosity of the Newtonian ambient fluid) dropped below unity near the wall, where bubbles were most deformed. This suggests that under conditions where both $Cd \gg 1$ and $Ca \gg 1$, the presence of bubbles reduces the suspension viscosity. However, it is important to note that the observed drop in relative viscosity did not follow the predictions of Eq.2.55c, which also refers to large bubble deformations but under steady shear flow. For the same frequency, the relative viscosity at the centre of the cylinder, where the bubbles remained undeformed, increased above unity. These findings suggest that under unsteady conditions with large deformations, the presence of bubbles reduces the suspension viscosity, similarly to steady-state conditions and large deformations, although the reductions do not follow the same trend. In contrast, for unsteady flows with minimal deformation ($Cd \gg 1$ and $Ca \ll 1$), the results show an increase to viscosity due to bubbles, deviating from the predictions of Llewellin's et al. (2002a) model for this regime (Eq.2.53). While these findings offer valuable insights, they are limited to a single volume fraction and do not cover a wide range of increasing oscillation frequencies, thus highlighting the need for further experimental studies to clarify how the suspension viscosity behaves with bubble volume fraction under conditions where both Cd and Ca vary simultaneously.

In a recent study, Ohie et al. (2024) also employed ultrasonic spinning rheometry to investigate the viscoelasticity of bubble suspensions under conditions involving bubble deformation, i.e., when Ca and Cd vary simultaneously and arbitrarily. Their results showed that for $Cd = 1.4$ and Ca varying from 0 to 2.2, the mean suspension viscosity (i.e., the average viscosity across experimental repetitions) was very close to that of the solvent and decreased as the capillary number increased, agreeing with the findings of Tasaka et al. (2015). However, their raw data was highly scattered, leading the authors to conclude that further experimental data over a wider range of Ca and Cd values are necessary to draw reliable conclusions about the suspension viscosity at $Cd \gg 1$ and varying extents of deformation (Ca). Additionally, the authors concurred with earlier studies (Llewellin et al., 2002b; Llewellin & Manga, 2005; Mader et al., 2013) that the maximum of viscoelasticity, corresponding to the minimum of the phase shift δ between shear stress and shear rate, occurs at $Cd \sim 1$ and in the limit of zero Ca, but also suggested that the transition from viscoelastic behaviour to purely viscous response is

determined by the condition $Cd/Ca = 1$, regardless of the values of the dimensionless parameters. When the ratio of the dynamic capillary to capillary number exceeds the threshold of unity, the suspension loses its viscoelastic properties and behaves as a Newtonian fluid.

The rheological models discussed thus far describe dilute and monodisperse bubble suspensions. Although polydispersity is common in industrial applications, it has mostly been addressed through empirical approaches that have not thoroughly investigated the effect of different bubble sizes on suspension rheology. This issue is examined in Chapter 3, which also provides a detailed review of the relevant studies that have addressed polydispersity. In the case of more concentrated bubble suspensions, Pal (2004) proposed a constitutive equation, based on the framework of the viscoelastic Oldroyd B model (Oldroyd, 1953), for the steady-shear rheology of these systems, which are characterised by hydrodynamic interactions among bubbles. The proposed expressions for the relative viscosity and the reduced first and second normal stress differences read:

$$\eta_r = \frac{1+\frac{3}{5}\varphi}{1-\frac{2}{5}\varphi}\left[\frac{1+\left(\frac{1+\frac{2}{3}\varphi}{1-\frac{2}{5}\varphi}\right)\left(\frac{1-\varphi}{1+\frac{3}{5}\varphi}\right)^2\left(\frac{6}{5}Ca\right)^2}{1+\left(\frac{1-\varphi}{1+\frac{3}{5}\varphi}\right)^2\left(\frac{6}{5}Ca\right)^2}\right] \tag{2.57a}$$

$$N_{1r} = 2\left[\frac{\left(\frac{1+\frac{3}{5}\varphi}{1-\frac{2}{5}\varphi}\right)\left(\frac{16}{15}\varphi+\frac{2}{5}\varphi^2\right)Ca}{1+\left(\frac{1-\varphi}{1+\frac{5}{3}\varphi}\right)^2\left(\frac{6}{5}Ca\right)^2}\right] \tag{2.57b}$$

$$N_{2r} = -\left[\frac{\left(\frac{1+\frac{3}{5}\varphi}{1-\frac{2}{5}\varphi}\right)\left(\frac{16}{15}\varphi+\frac{2}{5}\varphi^2\right)Ca}{1+\left(\frac{1-\varphi}{1+\frac{5}{3}\varphi}\right)^2\left(\frac{6}{5}Ca\right)^2}\right] \tag{2.57c}$$

where η_r is the relative viscosity of the suspension, and N_{1r} and N_{2r} are the reduced first and second normal stress differences, defined as $N_1/\eta_s\dot{\gamma}$ and $N_2/\eta_s\dot{\gamma}$, respectively.

Upon comparing their viscosity predictions with experimental data (Pal, 1992, 1996; Stein and Spera, 2002), the authors found good agreement for bubble volume fractions of approximately 20%. However, the experimental results deviated significantly from the predictions for bubble volume fractions higher than that. Additionally, the authors highlighted the need for further experimental data to validate the constitutive equations for the two normal stress differences. The viscoelastic behaviour of concentrated bubble suspensions and liquid foams (φ up to ~90%) is more complex due to the strong bubble interactions and the tight packing that affect the microstructure and, in turn, the stress relaxation process. Lavergne et al.

(2022) observed that liquid foams exhibit a non-Maxwellian rheological behaviour with G'' increasing in a non-standard manner at high oscillation frequencies. This behaviour is attributed to the nonaffine motion of bubbles, which deform irregularly along random slip planes. Additionally, deviation from the Maxwel behaviour was observed in the low frequency region, where G' demonstrated a gradual decay. This suggests that the foam's elastic response diminishes more slowly with decreasing frequency than would be expected for a Maxwell fluid, indicating more complex viscoelastic behaviour, likely due to the interactions and rearrangements of the bubbles.

The rheology of concentrated bubble suspensions falls outside the scope of the current research, and the findings discussed in Chapters 3, 4, and 5 pertain to dilute and semi-dilute suspensions.

2.3 Rheology of bubble suspensions in non-Newtonian media

Building upon the findings presented in Section 2.2 regarding the rheological behaviour of bubble suspensions in Newtonian media, this section extends the analysis to non-Newtonian ambient fluids. These fluids exhibit more complex flow behaviours, such as shear-thinning or viscoelasticity, which are highly sensitive to the addition of bubbles. In this context, the presence of bubbles not only influences the flow properties but may also introduce interactions between the bubbles and the matrix that are absent in simpler systems. Despite the broad industrial relevance of bubble suspensions with non-Newtonian ambient fluids, the rheology of these systems has been sparsely studied; hence, fundamental knowledge is still missing. This section presents key literature findings on their rheology, providing context for understanding how the interplay between bubbles and non-Newtonian matrices affects the overall rheological properties of the suspension.

Torres et al. (2013) compared the steady-shear rheology of bubble suspensions in two different ambient fluids: a shear-thinning guar gum solution and a Newtonian fluid. They also examined the effect of surfactant, adding varying amounts of Tween 20 in the guar gum solution to assess its impact on the bubble size distribution and the suspension viscosity. Bubbles generated in the guar gum solution were twice the size of those generated in the Newtonian ambient fluid, and paradoxically, the addition of surfactant further increased the bubble size. The authors generated bubble suspensions with volume fractions ranging from 11% to 24% in both the Newtonian matrix and the guar gum matrix without surfactant, and up to 39% in the guar gum matrix with surfactant. Instead of using the capillary number, which is

commonly employed for bubble suspension with Newtonian matrices, the authors chose to correlate their viscosity data with the *dimensionless shear stress* τ^*:

$$\tau^* = \frac{\tau}{\sigma/R} \tag{2.58}$$

where τ denotes the product of the shear-dependent solvent viscosity and the amplitude of the shear rate ($\eta_s\dot{\gamma}$). In their subsequent study, Torres et al. (2015) clarified that their use of τ^* instead of the capillary number was a convention intended to reflect the fact that, unlike in Newtonian fluids, the viscosity of the solvent and the shear rate in their shear-thinning matrix are not known a priori, meaning they're not independent quantities. Since τ^* in this context is equivalent in nature to Ca, Ca will be used for nomenclature consistency when referring to the findings of Torres et al. in this thesis.

According to their results, the presence of bubbles enhanced the shear-thinning character of the ambient fluid, making it more pronounced compared to its unaerated state. Moreover, the shear-thinning behaviour observed for the bubble suspensions with the guar gum matrix, both with and without surfactant, began at much lower Ca values, between 0.01 and 0.1- an order of magnitude lower than the Ca values at which shear-thinning started for the Newtonian ambient fluid. Although the bubbles in the shear-thinning ambient fluid were larger than those in the Newtonian matrix, the size difference could not account for the earlier onset of shear-thinning, as the corresponding capillary numbers were still well below unity—the regime where bubble deformation typically becomes significant. The authors attributed this behaviour to the lower shear stresses required to deform bubbles in a shear-thinning viscoelastic medium compared to a Newtonian fluid. Specifically, the guar gum solution exhibited significant normal stress differences even in its unaerated state, and the addition of bubbles further enhanced these effects. The presence of significant normal stress differences likely led to bubble deformation and shear-thinning behaviour occurring at lower shear rates, and consequently Ca values, in the guar gum solution compared to the Newtonian matrix.

While this study offers useful insights into the interaction between the rheology of the matrix and the presence of bubbles, several aspects require more careful consideration. Specifically, the authors subjected the bubble suspensions to very high shear rates, up to 300 s^{-1}, and images of the samples taken at the end of the tests revealed significant changes in bubble size distribution and volume fraction during the measurements. Although polymers can typically withstand such high shear rates without issue, bubble suspensions are more sensitive and prone to bubble coalescence and burst under these conditions. These changes in bubble size and

volume fraction are expected to influence suspension rheology, a factor the authors did not fully address. Therefore, the microstructural changes occurring during the shearing of the samples in the rheometer require further investigation, as they may offer useful insights into the observed rheological trends. Additionally, the authors acknowledge the need for further investigation in the role of surfactant, particularly in understanding how it influences bubble formation and size in shear-thinning fluids, and in turn, how this affects the rheological properties of the suspension.

In a subsequent study, Torres et al. (2015) generated bubble suspensions in a different shear-thinning ambient fluid, specifically a κ/ι-hybrid carrageenan gum solution with varying polymer concentrations and bubble volume fractions ranging between 5% and 25%. They observed a similar rheological behaviour to that in the guar gum solution, with significant normal stress differences and shear-thinning starting at lower shear rates compared to Newtonian ambient fluids. The authors proposed that the viscoelastic behaviour of both the ambient fluid and the bubble suspensions could be accurately modelled using a single-mode Giesekus model:

$$\eta(\dot{\gamma}) = \frac{\eta_0(1-n_2)}{1+(2-\alpha)n_2} + \eta_\infty \tag{2.59a}$$

$$N_1 = 2\lambda\eta_0 \frac{n_2(1-\alpha n_2)}{\lambda^2\alpha(1-n_2)} \tag{2.59b}$$

$$N_2 = -\alpha \frac{N_1}{2} \frac{(1-n_2)}{(1-\alpha n_2)} \tag{2.59c}$$

where $0 < \alpha < 1$ is the mobility parameter, representing the anisotropy in the fluid's response to shear forces, and the dimensionless parameter n_2 is given by:

$$n_2 = \frac{1-\Lambda}{1+(2-\alpha)\Lambda} \text{ with } \Lambda = \sqrt{\frac{\sqrt{1+(16\alpha(1-\alpha)\lambda^2\dot{\gamma}^2}-1}{8\alpha(1-\alpha)\lambda^2\dot{\gamma}^2}} \tag{2.59d}$$

where λ is the relaxation time.

For dilute bubble suspensions, the experimental zero-shear viscosities exhibited a linear dependence on bubble volume faction, described by a modified Taylor equation: $\eta_{r,0} = 1 + 1.5\varphi$. At higher bubble volume fractions, the dependence of the measured zero-shear viscosities on φ became non-linear, aligning closely with the predictions of the (Choi and Schowalter, 1975) model for emulsions:

$$\eta_{r,0} = 1 + I(\psi)\varphi \text{ with } \psi = \varphi^{\frac{1}{3}} \tag{2.60a}$$

$$I(\psi) = \frac{2[(5k+2)-5(k-1)\psi^7]}{[4(k+1)-5(5k+2)\psi^3+42\psi^5-5(5k-2)\psi^7+4(k-1)\psi^{10}} \quad (2.60b)$$

where, in the case of droplets, k denotes the ratio of the viscosity of the internal fluid to that of the continuous phase. For bubbles k equals zero.

The study also provided valuable insights into how the bubble volume fraction influences the parameters of the Giesekus model, particularly the relaxation time λ and the mobility parameter α. As the bubble volume fraction (φ) increased, λ also increased following a linear dependence on φ, with $\lambda/\lambda(\varphi = 0) \approx 1 + 2.5\varphi$, which is reminiscent of the Einstein equation for shear viscosity. This finding aligns with the observed increase in normal stress differences in the presence of bubbles, confirming that bubbles enhance the suspension's viscoelastic response, causing the fluid to take longer to return to equilibrium after deformation.

In terms of the effect of φ on the mobility parameter, the authors observed that α increased linearly with φ in the suspensions with a lower concentration of the κ/ι-hybrid carrageenan gum, suggesting that the presence of bubbles increases the system's anisotropy as more bubbles deform under flow. On the contrary, in bubble suspensions with higher polymer concentration in the matrix, α remained relatively constant as φ increased. The authors argued that this may be because at higher polymer concentrations, the fluid matrix was more structured, which could limit the ability of the bubbles to deform as easily under flow as in the lower concentration solution. While the Giesekus model was effective in describing the rheological behaviour of both aerated and unaerated fluids, the authors noted that the mechanisms by which bubbles influence the model's parameters require further investigation in order to understand the interactions between the bubbles and the rheology of the matrix and refine the model's applicability to complex multiphase systems.

Several studies (Sikorski et al., 2009; Lopez et al., 2018; Daneshi and Frigaard, 2023) have also focused on bubbles in yield stress fluids, exploring how the presence of a yield stress affects bubble formation and rise. In terms of rheology, Kogan et al. (2013) investigated the effect of bubbles on the elastic behaviour of yield stress fluids, using an O/W emulsion as the yield stress matrix and incorporating varying amounts of an aqueous foam to generate bubble suspensions with different bubble volume fractions. SAOS rheological tests revealed that for a given bubble size, there is a critical bubble volume fraction φ_c below which the dimensionless elastic modulus, $\bar{G}(\varphi)$ (defined as the suspension elastic modulus normalized by the elastic modulus of the continuous phase), decreases linearly with φ, indicating that the bubbles deform

and soften the material. When the bubble volume fraction exceeds this critical value, bubbles become confined and less deformable, behaving like rigid inclusions in the suspension, which causes the dimensionless elastic modulus to increase with φ. This behaviour is illustrated in Fig. 2.9a.

To gain a better understanding of the deformability of bubbles and the behaviour of $\bar{G}(\varphi)$, the authors introduced a dimensionless number called *elastic capillary number* Ca_{elast}, which compares the elastic modulus of the matrix with the bubble capillary pressure as follows:

$$Ca_{elast} \equiv \frac{G'_{matrix}}{\frac{\sigma}{R}} = \frac{RG'_{matrix}}{\sigma} \tag{2.61}$$

where σ is the surface tension and R is the bubble radius. When $Ca_{elast} \gg 1$, the elastic stresses in the matrix are significantly larger than the bubble surface tension, thus the bubbles get deformed, and $\bar{G}(\varphi)$ decreases with bubble volume fraction. When Ca_{elast}~1, bubbles start to become stiffer, transitioning into the undeformed regime, which is reflected as a change in the trend of $\bar{G}(\varphi)$. As mentioned above, the critical volume fraction beyond which the bubbles behave as rigid inclusions depends on the bubble size. This can be justified as follows: as the bubble volume fraction increases, the elastic modulus of the matrix decreases due to its dilution by the surfactant solution brought in by the foam. However, large bubble sizes counteract this reduction in G'_{matrix}, delaying the point at which Ca_{elast}~1. Consequently, larger bubble sizes require a higher bubble volume fraction that will achieve such a drop at G'_{matrix}, so that Ca_{elast}~1. This is the critical bubble volume fraction, over which $\bar{G}(\varphi)$ increases with φ.

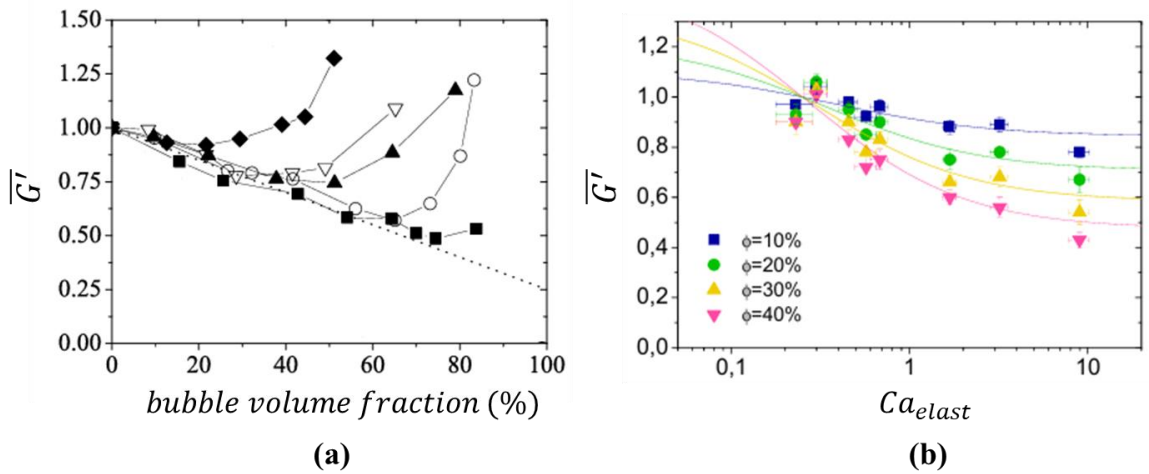

Figure 2.9: (a) Dimensionless elastic modulus as function of the bubble volume fraction for bubble suspensions with a yield stress ambient fluid and bubble diameter $d = 320\ \mu m$ (squares), $260\ \mu m$ (empty circles), $230\ \mu m$ (filled triangles), $210\ \mu m$ (empty triangles), and $110\ \mu m$ (diamonds) (adapted from Kogan et al., 2013), (b) Dimensionless elastic modulus as function of the elastic capillary number

for varying bubble volume fraction. The solid lines correspond to micromechanical computations while the markers to experimental data (Ducloué et al., 2015).

In terms of the effect of bubbles on the yield stress of the suspension, the authors align with earlier findings (Larson, 1999), which suggest that the impact depends on whether the bubbles are deformed. Deformed bubbles tend to decrease the suspension yield stress, acting like soft inclusions that make it easier for the material to yield under stress. For undeformed bubbles, the yield stress of the suspension is approximately equal to that of the matrix, unless the bubble volume fraction is very large (such as in foams). In this case, the suspension behaves as a packed system of rigid inclusions, and the yield stress increases with the presence of bubbles.

Similar findings have been reported by Ducloué et al. (2015) who also studied the effect of bubble presence in a simple yield stress fluid. Their experimental results came to a good agreement with the predictions of a micromechanical model developed for soft, porous materials (Eq. 2.62) (Thuy Linh et al., 2013), which takes into account both bubble volume fraction and elastic capillary number. As shown in Fig. 2.9b, at low Ca_{elast}, the model predicts an increase of the dimensionless elastic modulus with increasing bubble volume fraction, while above a Ca_{elast} threshold of unit order of magnitude, the elastic modulus decreases with φ.

$$\overline{G'}(\varphi, Ca_{elast}) = 1 - \frac{\varphi(4Ca_{elast}-1)}{1+\frac{12}{5}Ca_{elast}-\frac{2}{5}\varphi(1-4Ca_{elast})} \tag{2.62}$$

As evidenced, there are limited studies focusing on the rheology of bubble suspensions with non-Newtonian ambient fluids, with these highlighting the need for further experimental data to better understand the interaction between bubbles and matrices with more complex rheological behaviours. The intricacies of non-Newtonian ambient fluids, combined with the shear-thinning and viscoelastic effects induced by the bubbles, result in suspensions with rheological properties that vary significantly depending on the matrix composition, its inherent rheology, and the bubble size and volume fraction. The presence of surfactants further complicates the prediction of these systems' rheological behaviour, as the interactions between the different phases remain largely uncharacterised in the literature. Chapter 5 aims to offer insights into the rather unexplored rheology of bubble suspensions in non-Newtonian matrices, in particular shear-thinning Carbopol dispersions, to contribute to a better understanding of the interplay between bubbles and more complex matrices.

Chapter 3

Investigation of the steady-shear viscosity of semi-dilute bubble suspensions in Newtonian media

This chapter explores the steady shear viscosity of semi-dilute polydisperse bubble suspensions with Newtonian ambient fluids, in the limit of $Cd \to 0$ and for varying Ca. The study involves a theoretical analysis of how different bubble sizes affect the suspension relative viscosity, complemented by steady-shear rheological tests to validate these theoretical findings. An unexpected double power law decay of the suspension relative viscosity was observed at average capillary numbers between 0.01 and 1. This behaviour was further examined through novel rheo-optical experiments, which revealed the shear-induced formation of bubble clusters and threads.

The main aim of this investigation is to characterise the steady-shear viscosity of bubble suspensions by (i) clarifying the influence of polydispersity without relying on system-dependent empirical approaches, and (ii) elucidating the effect of shear-induced phenomena, such as bubble clustering and alignment. The results highlight the complex shear-thinning nature of bubble suspensions, which is related not only to bubble deformation, but also to the shear-induced clustering and alignment of bubbles.

The results of this chapter have been published:

Mitrou, S., S. Migliozzi, P. Angeli, and L. Mazzei, "Effect of polydispersity and bubble clustering on the steady shear viscosity of semi-dilute bubble suspensions in Newtonian media," J. Rheol. 67, 635–646 (2023).

3.1 Introduction

Suspensions of bubbles in a liquid are often encountered in nature in the form of magmas (Manga and Loewenberg, 2001), while they find wide applications in industry, e.g. in aerated

food products (Campbell and Mougeot, 1999), cement (Ahmed et al., 2009) and personal care products (Malysa and Lunkenheimer, 2008). The gas volume fraction, φ, can range from almost zero for very dilute suspensions to more than 0.9 for foams, with most suspensions of practical interest lying in the intermediate range (Llewellin et al., 2002a). As also reported in Chapter 2, the presence of bubbles has been shown to change the viscosity of the suspension, inducing shear-thinning and other viscoelastic phenomena, even in Newtonian ambient fluids (Llewellin et al., 2002a, 2002b; Mader et al., 2013; Rust & Manga, 2002). Consequently, it is important to characterise the rheology of bubble suspensions, providing industry with useful insight into how aeration affects the viscosity and flowability of various formulations.

For steady-shear flows, the effect of bubble volume fraction on the suspension viscosity has been unclear for some time. According to Sibree (1934) and Stein and Spera (1992), the relative viscosity of a suspension increases with φ, while Sura and Panda (1990), Bagdassarov and Dingwell (1992, 1993) and Lejeune et al. (1999) claimed the opposite. Subsequent studies (e.g. Llewellin et al., 2002a, 2002b; Rust & Manga, 2002; Stein & Spera, 2002) resolved this controversy by identifying two flow regimes, which for simple steady shear flows depend on the capillary number Ca. For $Ca \ll 1$, the bubbles obstruct the flow, leading to an increase in suspension viscosity with increasing volume fraction, while, for $Ca \gg 1$, bubbles deform and facilitate the flow, causing a decrease in suspension viscosity. Between the two extremes, the suspension behaves as a shear-thinning fluid, with the onset of this behaviour occurring at $Ca \sim 1$ for monodisperse suspensions.

To describe the viscosity of bubble suspensions under steady conditions, researchers have proposed various models where the viscosity is a function of the bubble volume fraction and the capillary number. Despite most suspensions of practical significance being polydisperse, the effect of different bubble sizes on the suspension viscosity remains rather unexplored with existing studies focusing mostly on monodisperse suspensions or addressing polydispersity through empirical approaches related to their experimental systems. Given that the bubble size directly affects the capillary number (Eq. 2.45), understanding the effect of polydispersity is critical for characterising the viscosity of bubble suspensions, highlighting an aspect that requires further investigation.

As reported in Chapter 2, Llewellin et al. (2002b) suggested the following equation for the relative viscosity of dilute, *monodisperse* bubble suspensions under steady shear:

$$\eta_r = \eta_{r,\infty} + \frac{\eta_{r,0} - \eta_{r,\infty}}{1 + (K\mathrm{Ca})^m}, \text{ with } K = 6/5 \text{ and } m = 2 \qquad (3.1a)$$

$$\eta_{r,0} = 1 + \varphi \tag{3.1b}$$

$$\eta_{r,\infty} = 1 - \frac{5}{3}\varphi \tag{3.1c}$$

To extend the validity of Eq. 3.1 to polydisperse bubble suspensions above the dilute regime, the authors modified the Taylor equation for the zero-shear viscosity to include a fitting parameter:

$$\eta_{r,0} = 1 + b\varphi \tag{3.2}$$

With this modification, they found good agreement of Eq. 3.1 to their experimental data for polydisperse systems with bubble volume fractions up to 46%, suggesting an optimal value of $b = 9$. Their approach was however purely empirical and strictly related to their experimental system, thus proving to be not conclusive in terms of evaluating how polydispersity affects the viscosity of bubble suspensions.

According to Mendoza and Santamaría-Holek (2009), for dilute suspensions at low capillary numbers, polydispersity does not affect the zero-shear viscosity of the suspension strongly. Mader et al. (2013) confirmed this statement, claiming that the relative zero-shear viscosity of bubble suspensions obeys the Taylor equation, regardless of polydispersity. They further suggested that the coefficient $b = 9$ is most likely related to bubble interactions emerging at the high bubble volume fractions reported by Llewellin et al. (2002a), rather than polydispersity. To account for the effect of polydispersity, Mader et al. (2013) suggested treating the dilute polydisperse suspension as the sum of N monodisperse components with a characteristic radius R_i and bubble volume fraction φ_i. Using Eq. 3.1, one can calculate the relative viscosity for each size class and then sum the individual viscosity contributions $(\eta_{ri} - 1)$ to attain the relative viscosity of the polydisperse suspension. The authors provided a worked example, but without testing it with experimental data.

Rust & Manga (2002) investigated the steady shear viscosity of polydisperse bubble suspensions, considering a surface-weighted average bubble diameter, defined as follows:

$$d_{32} \equiv \frac{M_3}{M_2} \equiv \frac{\int_0^\infty d^3\, f(s)\, ds}{\int_0^\infty d^2\, f(s)\, ds} \tag{3.3}$$

where d is the bubble diameter and $f(d)$ is the number density function (NDF) of the bubbles. Fitting their rheological data to Eq. 3.1, they found good agreement for $K = 0.72$ and $m = 1.43$, using empirically derived expressions for the relative zero-shear and infinite-shear

viscosities. Even though the authors accounted for the effect of polydispersity, their approach is not supported by theory and is strongly system dependent.

Joh et al. (2010) addressed the issue of polydispersity following an approach similar to Mader et al. However, instead of considering a discrete bubble radii distribution, they generalised the linear superposition approach by treating the bubble radius R as a continuous variable. Assuming that bubble sizes typically follow a gamma type distribution, they generalised the model of Seo and Youn (2005) for monodisperse bubble suspensions, by incorporating the *probability distribution function of the gamma distribution* as follows:

$$\eta_r = 1 - \frac{5}{3}\varphi + \frac{8}{3}\varphi \int_0^{\infty} \frac{\frac{\beta^a}{\Gamma(a)} R^{a-1} e^{-\beta R}}{1+\frac{9}{16}(Ca(R))^2} dR \tag{3.4}$$

where a and β are parameters obtained by fitting experimental bubble size data to the gamma distribution. In this case, the viscosity contribution from bubbles of different sizes is weighted by the probability density function, which gives higher weight to bubble sizes that are more likely to occur and lower weight to those that are less likely based on the type of size distribution.

Typically, gamma-type distributions observed in bubble suspensions consist of a higher number of smaller bubbles and fewer larger ones, which however contribute significantly to the total bubble volume fraction. As mentioned earlier, the bubble volume fraction is a key parameter for determining the suspension viscosity. In this context, the approach of Joh et al. (2010) introduces a significant limitation as it underweights the contribution of larger bubbles because of their lower probability density. When comparing their experimental data for polydisperse bubble suspensions in the semi-dilute regime with the predictions of Eq. 3.4, the authors observed that the model underestimated the suspension viscosity starting at capillary number values around unity.

As highlighted above, the effect of polydispersity on the steady shear viscosity of bubble suspensions has been sparsely studied, with existing studies depending mostly on empirical approaches that strongly depend on experimental data. This chapter aims to elucidate the role of polydispersity through theoretical analysis, validated with experimental studies. To this end, semi-dilute polydisperse bubble suspensions were generated, and their steady shear viscosity was measured. The rheological measurements revealed an unexpected double power-law decay of the relative viscosity, a trend that could not be supported by the theoretical analysis on polydispersity. To investigate this behaviour, the produced bubble suspensions were visualised

under shear. The rheo-optical experiments revealed the shear induced formation of bubble threads and clusters, which is considered responsible for the first decay of viscosity.

The chapter is organised as follows. Firstly, theoretical calculations that clarify the effect of polydispersity on the relative viscosity of semi-dilute bubble suspensions are presented. Next, the experimental methods for the generation, rheological characterisation, and visualisation of the produced bubble suspensions are introduced, followed by the discussion of the results.

3.2 Theoretical Calculations on Polydispersity

To investigate theoretically the effect of polydispersity, a bubble suspension in a mixture of mineral oil and 0.57 mol/L span 80 (surfactant) was considered, with bubble volume fraction of 10.4% and different bubble sizes. The relative viscosity of the bubble suspension was calculated following the linear superposition method described by Mader et al. (2013). Eq. 3.1 was used to calculate the relative viscosity for each *i-th* bubble class, where the capillary number Ca of the suspension was replaced with the capillary number Ca_i of the i-th size class, and the total volume fraction of bubbles φ with that of the *i-th* bubble class, φ_i.

To determine φ_i, the bubble volume for each size class (V_i) was first calculated. Then, the bubble volumes for all the different size classes were summed to attain the total bubble volume in the suspension (V_{tot}), and finally the bubble volume fraction for each class (ω_i) was calculated and multiplied with the measured total volume fraction of bubbles in the suspension (φ_{tot}):

$$V_i = N_i * \frac{4}{3}\pi R_i^3 \tag{3.5a}$$

$$\omega_i = \frac{V_i}{V_{tot}} \tag{3.5b}$$

$$\varphi_i = \omega_i * \varphi_{tot} \tag{3.5c}$$

where N_i is the number of bubbles in each bubble class. The relative viscosity of the polydisperse suspension is then obtained by linearly combining the individual viscosities of the different bubble classes η_i with the solvent contribution as follows:

$$\eta_i = \eta_{r_i} - 1 \tag{3.6}$$

$$\eta_{r_{polydisperse}} = 1 + \sum_i^N \eta_i \tag{3.7}$$

For each theoretical example, the relative viscosity of the suspension was plotted as a function of an average capillary number, $\langle Ca \rangle$. This was defined using the volume-weighted average radius of the undeformed bubble, $\langle R \rangle$, obtained from the De Brouckere average diameter d_{43}. $\langle R \rangle$ is the ratio of the fourth to the third moments of the bubble *number* density function, $n(R)$; in terms of *volume fraction* density function, the same average radius is given by the ratio of the moments of order one and zero:

$$\langle R \rangle \equiv \frac{\int_0^\infty R^4\, n(R)\, dR}{\int_0^\infty R^3\, n(R)\, dR} \equiv \frac{\int_0^\infty R\, f(R)\, dR}{\int_0^\infty f(R)\, dR} \quad \text{with} \quad f(R) \equiv \left(\frac{4}{3}\pi R^3\right) n(R) \tag{3.8}$$

Note that using a volume-weighted mean radius, as opposed to other types of mean radii, takes into account the bubble volume fraction, which significantly impacts the rheological properties of the suspension.

It is important to clarify that the linear superposition approach is primarily valid for dilute systems, where bubble interactions are considered negligible. However, when its predictions were compared with the experimental results presented in this chapter, it was found that it can accurately predict the relative viscosity of semi-dilute suspensions as well. Thus, the Mader et al. (2013) model is considered suitable for describing the relative viscosity of the bubble suspensions discussed in this chapter.

3.2.1. Scenario 1 – bimodal distribution ($R_1 = 10\ \mu m$, $R_2 = 500\ \mu m$)

The first scenario concerns a bubble suspension consisting of bubbles with only two radii, 10 and 500 μm. The total bubble volume fraction is equally divided between the small and large bubbles, so that the volume-weighted average radius is equal to 255 μm. Following the procedure explained above, the viscosity curve of Fig. 3.1 was obtained.

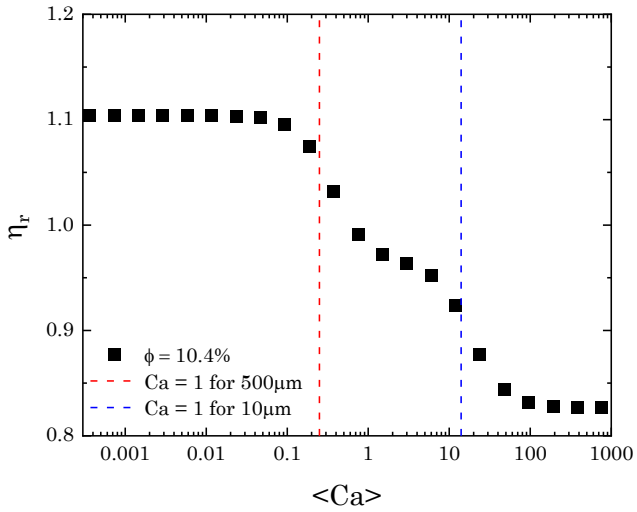

Figure 3.1: Relative viscosity versus average capillary number, for $\varphi = 10.4\%$ and bubble sizes of 10 and 500 microns with $\omega_1 = \omega_2 = 0.5$.

In this example, the shear-thinning behaviour does not occur at $\langle Ca \rangle \sim 1$, as it happens for a monodisperse bubble suspension. Instead, it spans a range of average capillary numbers, between 0.1 and 100. This behaviour is due to polydispersity and can be explained by correlating the average capillary number with the capillary number for each size class, as follows:

$$Ca_i \equiv \frac{\eta_s R_i \dot{\gamma}}{\sigma} = \frac{\eta_s \langle R \rangle \dot{\gamma}}{\sigma} \frac{R_i}{\langle R \rangle} = \langle Ca \rangle \frac{R_i}{\langle R \rangle} \tag{3.9}$$

which gives:

$$\langle Ca \rangle = \frac{\langle R \rangle}{R_i} Ca_i \tag{3.10}$$

Each size class starts deforming when the corresponding capillary number is of order 1, and the average capillary number will be of order:

$$\langle Ca \rangle \sim \frac{\langle R \rangle}{R_i} \tag{3.11}$$

Based on this, the large bubbles with radius equal to 500 μm start deforming when $\langle Ca \rangle \sim 0.1$, where the first drop of the suspension relative viscosity is observed. Likewise, the small bubbles with radius 10 μm start deforming $\langle Ca \rangle \sim 10$, causing the second decay of the relative viscosity. Between the two relative viscosity drops, there is an intermediate plateau, which indicates that the larger bubbles have been fully deformed, while the smaller ones remain almost spherical.

Even though this example is extreme, it demonstrates that polydispersity can cause an extended shear-thinning behaviour that spans a range of average capillary number values, instead of happening at $\langle Ca \rangle \sim 1$. This rheological trend is similar to what is observed in polymer melts, where a polydisperse molecular weight distribution leads to a relaxation time spectrum (Macosko, 1994). Moreover, the viscosity curve has a more complex behaviour, with a plateau between the two viscosity decays. The presence of the intermediate plateau poses a challenge for modelling this behaviour using a constitutive equation for monodisperse suspensions and an average bubble diameter, as the plateau could not appear. In these cases, for dilute and semi-dilute suspensions, one must operate as discussed earlier, considering each bubble class individually, obtaining the viscosity contribution for each class by using the constitutive equation for monodisperse suspensions, and then adding the contributions.

3.2.2. Scenario 2 – bimodal distribution ($R_1 = 10\ \mu m$, $R_2 = 200\ \mu m$)

This scenario concerns another bidisperse bubble suspension, with a smaller difference between the two bubble sizes, these being 10 and 200 μm. As in the previous scenario, the two bubble classes contribute equally to the total bubble volume fraction, and the volume-weighted average radius is equal to 105 μm. Following the same method, the viscosity curve of Fig. 3.2 was obtained. As seen, also in this case the shear-thinning part of the curve spans a wider range of Ca values than that for a monodisperse suspension. However, unlike the first scenario, this range is smaller, between 0.1 and 50. The first decay of the relative viscosity again happens at $\langle Ca \rangle \sim 0.1$ and indicates the deformation of the 200 μm bubbles. The second viscosity drop happens at $\langle Ca \rangle \sim 1$ and is correlated with the deformation of the 10 μm bubbles. The intermediate plateau of viscosity still exists but is less noticeable than in the first example. Thus, the effect of polydispersity becomes more evident when the difference in bubble size increases.

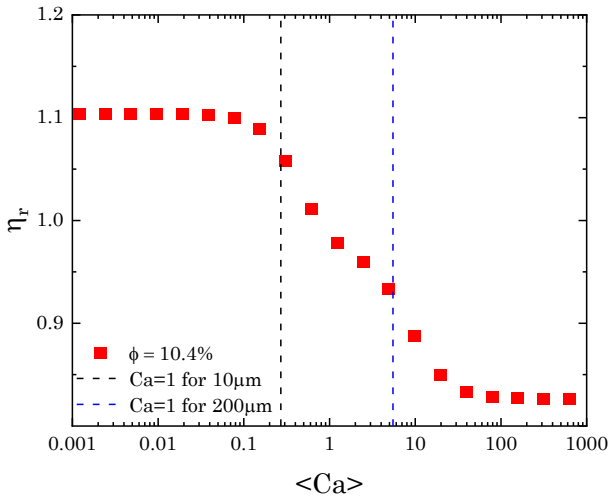

Figure 3.2: Relative viscosity versus average capillary number, for $\varphi = 10.4\%$ and bubble sizes of 10 and 200 microns, with $\omega_1 = \omega_2 = 0.5$.

3.2.3. Scenario 3 – Gamma-type distribution (bubble sizes between 10 and 170 μm)

The last scenario refers to the experimental data presented in this chapter, with bubble radii following a gamma distribution between 10 and 170 μm (Fig. 3.3a), and $\langle R \rangle = 82.5$ μm. The limits of the size distribution are similar to those in scenario 2; however, in this case the total bubble volume fraction is not equally divided between the small and large sizes. Instead, each size class corresponds to a percentage of the total bubble volume fraction. Calculating the relative viscosity of the polydisperse suspension, the viscosity curve of Fig. 3.3b (green points) was obtained.

As seen, the shear-thinning behaviour happens in a range of $\langle Ca \rangle$ across 1 and does not extend further than this, as it happened in the previous scenarios. There is no intermediate plateau, and the viscosity curve closely resembles that of a monodisperse suspension. To validate this, the viscosity curve of a monodisperse suspension with bubble radius equal to 82.5 μm was calculated, using Eq. 3.1 (Fig. 3.3b - red curve). As seen, the two viscosity curves almost coincide. Thus, it can be concluded that polydispersity can significantly affect the suspension viscosity only if the total bubble volume fraction is divided between very small and very large bubbles – a condition that is hard to meet experimentally. Under usual experimental conditions, where the bubble sizes follow the gamma distribution, the effect of polydispersity is not profound, and the polydisperse suspension can be regarded as monodisperse with a volume-weighted average bubble diameter.

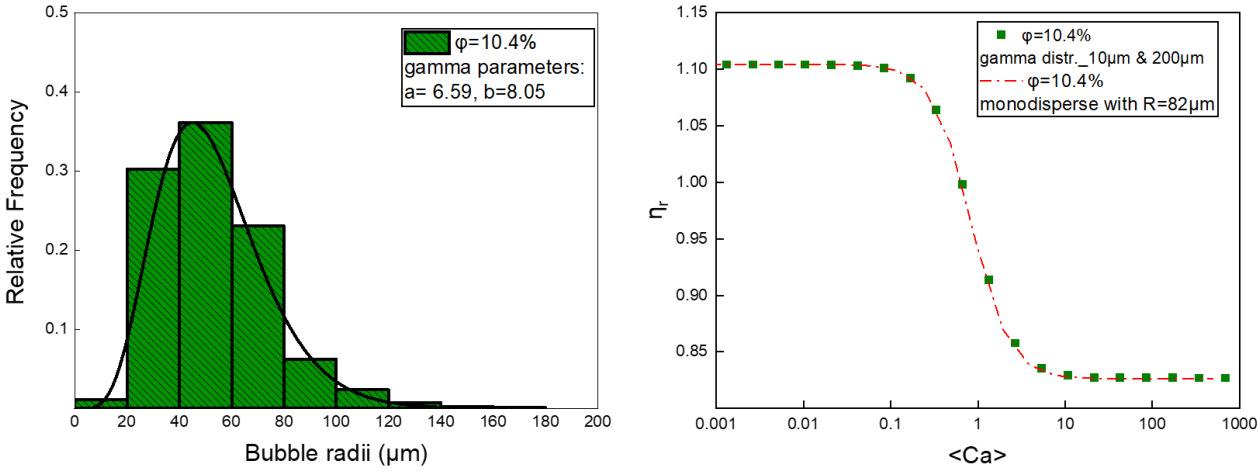

(a) (b)

Figure 3.3: a) Gamma-type bubble size distribution (10-170 μm); b) relative viscosity versus average Capillary number for $\varphi = 10.4\%$ and bubble sizes following a gamma distribution between 10 μm and 170 μm.

3.3 Materials and Methods

3.3.1. Chemicals

RTM32 Mineral Oil Rotational Viscometer Standard (Paragon Scientific, Birkenhead, UK) is a Newtonian oil, with a viscosity of 9.274 Pa s. Span 80 (Sigma Aldrich, St. Louis, USA) is a liquid, non-ionic surfactant (molecular weight: 428.61 g/mol; density at 20 °C: 1 g/cm³). A mixture of the mineral oil and 0.57 mol/L of Span 80 was used to generate the bubble suspensions. This was chosen as ambient fluid because it is Newtonian and it allows generating small bubbles and stable suspensions. The properties of the individual chemicals and the final mixture are summarized in Table 3.1.

Table 3.1: Physical properties of fluids used to prepare the Newtonian ambient fluid.

Name	Viscosity (Pa s)[1]	Density (g/mL)[2]	Surface tension (mN/m)[3]
RTM32 min. oil	9.27±0.09	0.86±0.02	32.36±0.25
Span 80	1.95±0.02	0.99±0.01	29.34±0.25
Mixture	4.23±0.04	0.89±0.01	29.99±0.25

3.3.2. Generation and rheological characterisation of bubble suspensions

An in-house custom aeration device (Fig. 3.4a), designed in collaboration with the UCL Mechanical Workshop (Roberts Building, UCL) for simultaneous aeration and mixing, was used to generate the bubble suspensions. The apparatus consists of a consists of a sealed acrylic tank (internal dimensions approximately 290 × 290 × 306 mm) supported by an aluminium frame. The system is driven by a motor–pulley assembly mounted above the tank, providing a load torque of approximately 0.39 N·m and an acceleration torque of 40 mN·m, transmitted via a 25-tooth, 5 mm pitch, 10 mm wide belt. Inside the tank, a rotating propeller fitted with aeration plates distributes bubbles evenly throughout the fluid. Each plate holds eight 25 mm sintered ceramic discs (2 μm pore size) for bubble generation. Air is introduced through fittings positioned along the propeller shaft, while a waste outlet at the base allows drainage after experiments. The propeller rotation promotes both aeration and mixing, producing homogeneous suspensions. The aeration time was varied depending on the target gas volume fraction: longer aeration times yielded denser suspensions. Detailed design schematics of the custom aeration device are provided in Sec. A1 of Appendix A.

[1] Values are means ± standard deviation (n = 3) measured at 20 °C. The relative standard deviation (RSD = (standard deviation / mean) × 100) was approximately 1%, consistent with the repeatability specification of the MCR 302 rheometer used in the experiments.

[2] Values represent means ± standard deviation (n = 2) measured at 20 °C. Densities were determined gravimetrically by weighing ~60 mL of each sample in a 100 mL Pyrex® beaker using an analytical balance (sensitivity ± 0.001 g). According to the manufacturer, the beaker's nominal capacity is accurate to ± 5 %, with approximate graduations. The observed SDs (0.01–0.02 g mL^{-1}; 1–2.3 % relative standard deviation) reflect the repeatability limits imposed by the volume measurement, with the balance uncertainty negligible in comparison.

[3] Values represent single measurements obtained using a Krüss K100C force tensiometer at 20 °C. The reported uncertainty corresponds to the method sensitivity, which for pendant-drop and force-tensiometer measurements ranges between ± 0.25 and ± 0.30 mN m^{-1} under ideal conditions (Farias et al. (2025)).

After generation, bubble suspensions were subjected to high-shear mixing using a Silverson, L5 Series mixer to effectively reduce the bubble size. Subsequently, the suspensions were left to rest until their temperature reached that of the ambient fluid before the aeration, and the bubble volume fraction was determined gravimetrically, weighting ~60 mL of a representative sample from the batch suspension and using the following equation:

$$\varphi = 1 - \frac{\rho_{suspension}}{\rho_{ambient\ fluid}} \tag{3.12}$$

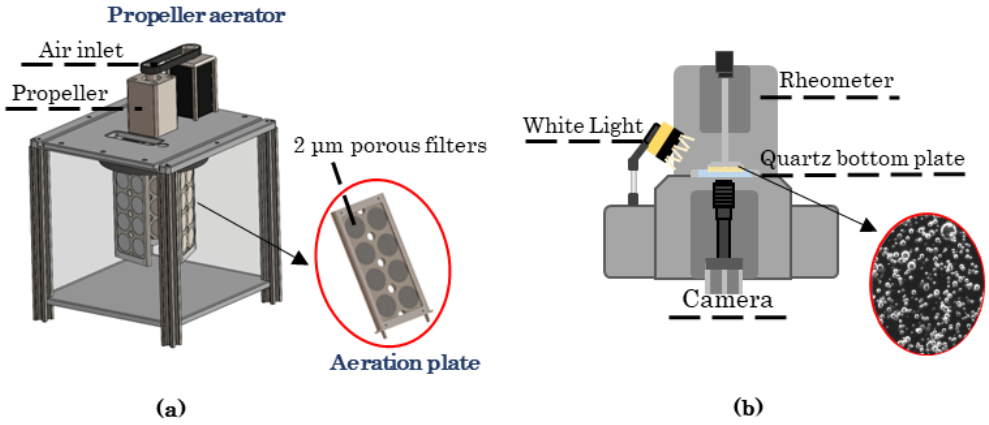

Figure 3.4: (a) Schematic of the aeration device used to generate bubble suspensions; (b) rheo-optical setup.

Images of all generated bubble suspensions were recorded prior to rheological measurements using a bright-field optical microscope (Zeiss Axio Observer 5) equipped with a 10×Plan-Apochromat objective and then analysed with an in-house MATLAB code to determine the bubble size distribution. The obtained microscope images (2752 × 2208 px) corresponded to a scale of 0.91 px/µm, and brightness and contrast were adjusted uniformly across samples to improve bubble edge detection. A characteristic microscope image of a bubble suspension with $\varphi = 4.2\%$ is provided in Section A2 of Appendix A.

The rheological tests were carried out in an Anton Paar MCR302 stress-controlled rotational rheometer, equipped with a Peltier plate to control the operating temperature (20 ˚C) and a sandblasted parallel-plate geometry (R=20 mm) to avoid wall-slip effects. For all measurements, the rheometer gap was set at 1.9 mm to ensure a gap ten times larger than the average bubble diameter, thus avoiding possible wall effects induced by the plates confinement. To obtain the viscosity curves for the bubble suspensions, steady shear measurements were performed in the range 0.05 s^{-1} to 150 s^{-1}, with each test conducted in triplicate to ensure

reproducibility and reliable viscosity data. The limit of 150 s^{-1} was chosen to minimize bubble coalescence and bursting and to keep the bubble volume fraction stable. The samples were carefully analysed by eye after each measurement to ensure that no material was spurted out of the geometry during the rheological experiments. The Weissenberg-Rabinowitsch correction (Macosko, 1994) was applied to account for the non-uniform shear across the parallel plates, and a detailed description of this correction is provided in Section A3 of Appendix A.

As mentioned in Morini et al. (2019), the radial variation of the shear rate in the parallel-plate geometry causes a linear change of the capillary number from zero to its maximum value at the rim of the geometry. Consequently, bubbles deform differently depending on their position in the measuring plate. The Weissenberg-Rabinowitsch method overcomes the problem arising from the radial change of the shear rate, because it considers a value of the shear rate and of the corresponding shear stress in a specific location, namely at the edge of the plates. This ensures that the rheological trends reported in the following sections are not influenced by the radial distribution of shear rates, and in turn of capillary numbers.

3.3.3. Visualisation of bubble suspensions under steady shear

To visualise the bubble suspensions under shear, the setup of the rheometer was modified using a glass bottom plate (Anton Paar Peltier Universal Optical Device - P-PTD 200/GL) to allow optical access. During the shear tests, images of the suspension were recorded using a Zyla 5.5 sCMOS camera (acquisition frequency: 15 Hz, image resolution: 2560x2160 pixels), a Nikon mono zoom lens and a white led light as illumination. To avoid reflections from the metal, the sandblasted parallel plate was coated with black spray-paint. A schematic of the visualisation set up is given in Fig. 3.4b. The recorded images were taken at a plane around 0.6 mm within the gap. To calibrate the plane of focus, transparent laminated sheets of 0.3 mm thickness were sticked together to create a disc of 0.6 mm height. A millimetric scale grid was then placed on top of this disc and the camera was focused on it. All rheo-optical experiments were performed with this focus which, for different samples, was only slightly adjusted.

Steady shear rheological tests were performed in the range 0.1 s^{-1} to 50 s^{-1} for a fixed time of 40 s per shear rate and the rheometer gap was set at 1.9 mm, to be consistent with the previous viscosity measurements. However, with this gap, multiple suspension layers formed, preventing a detailed image analysis. Thus, experiments with a 0.8 mm gap were also conducted. Fig. 3.5 shows two representative images, taken with the 1.9 mm and 0.8 mm gaps. Even if it was difficult to individuate the bubbles accurately in the 1.9 mm images, these still

offered insight into the shear-induced phenomena happening in the entire volume of the tested samples, which is relevant to the final viscosity recorded. The 0.8 mm gap images were only used to investigate the bubble size distributions and identify possible coalescence phenomena during shearing, even though it must be emphasized that bubble coalescence can be enhanced due to the more confined flow.

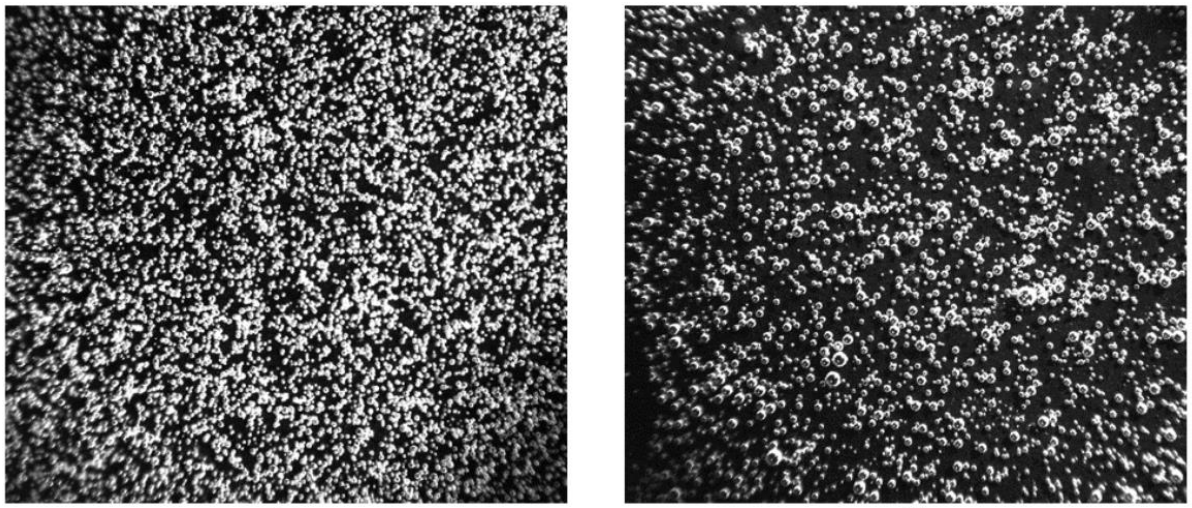

Figure 3.5: Bubble suspension ($\varphi = 5.6\%$) under steady shear (1 s^{-1}) with (a) 1.9 mm gap and (b) 0.8 mm gap.

While the rheo-optical set up enabled real-time visualisation of the suspension microstructure during shear, one of its main limitations was slip at the glass plate, which led to lower torque readings—typically 10–15 % lower than those obtained using the standard sandblasted plates. This deviation, caused by the smoother surface of the transparent plate, affected the accuracy of the rheological data. As a result, the torque and viscosity values obtained under optical conditions were not used quantitatively, and simultaneous bulk rheological measurements and direct visualisation of the same sample were not possible. Instead, separate experiments were performed for rheological and optical characterisation. Despite this limitation, the optical setup proved highly effective for observing microstructural changes under shear.

3.4 Rheological Measurement

In this section, experimental results for bubble suspensions with volume fractions $\varphi_1 =$ 4.7 % and $\varphi_2 = 10.4\%$ are presented.

3.4.1. Bubble size distributions

The tested samples were found to be polydisperse, with bubble radii following the gamma distribution between 10 and 170 μm (Fig. 3.6). This means that the suspensions consisted mostly of small bubbles, with radii ranging up to 100 μm; even though the larger bubbles were fewer in number, they contributed importantly to the total bubble volume fraction. As the suspensions were polydisperse, the De Brouckere average diameter d_{43} was used to characterise them. For the reported bubble volume fractions, $\varphi_1 = 4.7\ \%$ and $\varphi_2 = 10.4\ \%$, d_{43} was equal to 199 μm and 165 μm, respectively.

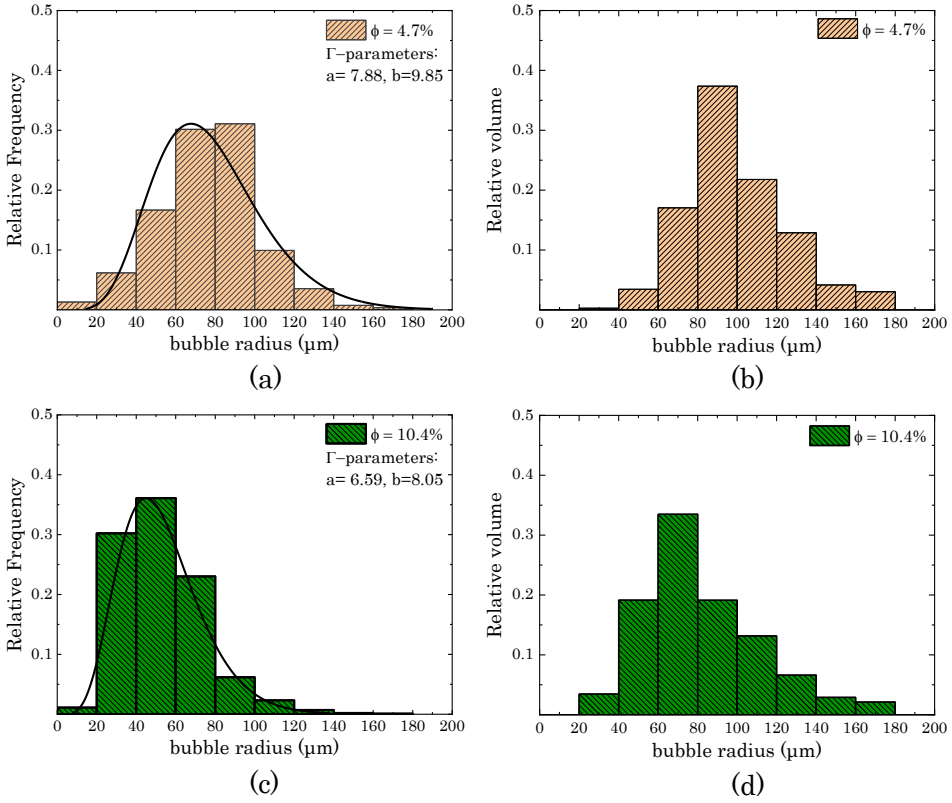

Figure 3.6: Number-weighted bubble size distribution for (a) $\varphi_1 = 4.7\%$ and (c) $\varphi_2 = 10.4\%$; volume-weighted bubble size distribution for (b) $\varphi_1 = 4.7\%$ and (d) $\varphi_1 = 10.4\%$.

3.4.2. Steady shear experiments

As shown in Figure 3.7, all tested suspensions are characterised by a shear-thinning behaviour with a double power law decay of the suspension relative viscosity. Each curve represents the average of three replicate measurements, with the standard deviation among replicates shown as error bars. The measurements were highly repeatable, with the maximum standard deviation on the order of 0.01. The first decay always happened at shear rates around 1 s^{-1}, corresponding to $\langle Ca \rangle \sim 0.01$, while the second started at shear rates around 20 s^{-1}, corresponding to $\langle Ca \rangle \sim 1$. This double decay was unexpected, because it is not predicted by

the rheological models discussed in Section 3.2. As discussed, two decays of the relative viscosity – with a plateau between them – appear only if the bubble size distribution is bimodal, with very small and very large bubbles having similar volume fractions. However, this is not the case in the present experiments, where the bubble sizes follow the gamma distribution. As shown in the theoretical examples, when the bubble sizes follow the gamma distribution, the suspension has a viscosity curve that is quite similar to that of a monodisperse suspension, the only difference being that the viscosity drop spans a larger range of $\langle Ca \rangle$ values. The observation of a different trend suggested that polydispersity may not be the sole factor responsible for this behaviour.

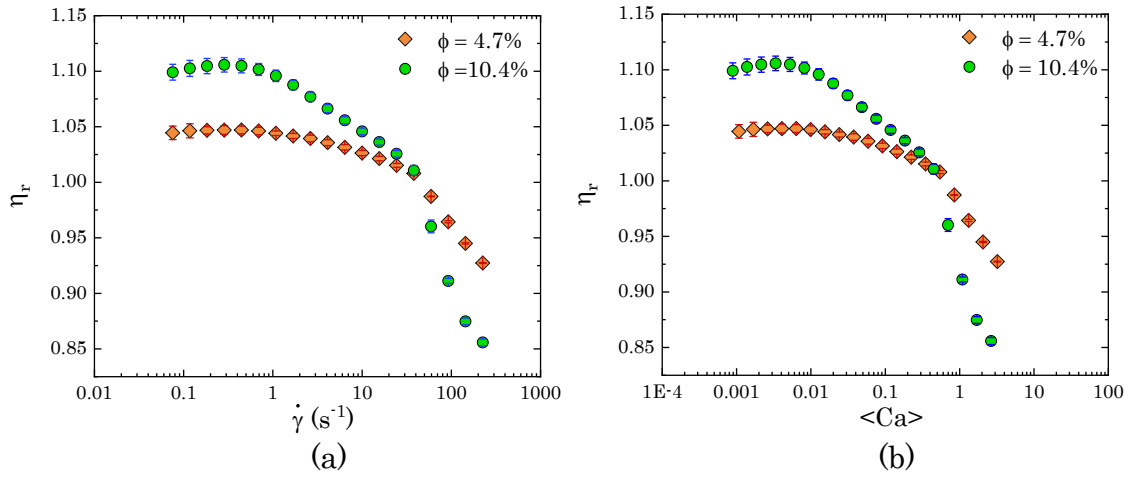

Figure 3.7: (a) Relative viscosity as a function of shear rate for $\varphi_1 = 4.7\%$ and $\varphi_2 = 10.4\%$; (b) relative viscosity as a function of $\langle Ca \rangle$ for $\varphi_1 = 4.7\%$ and $\varphi_2 = 10.4\%$. Error bars represent the variation between three experimental repeats.

To validate the above assumption, the experimental results were compared to the theoretical polydisperse model of Mader et al. (2013). Fig. 3.8 shows the experimental and theoretical relative viscosities as functions of $\langle Ca \rangle$ for the two reported polydisperse suspensions. As seen, there is good agreement between the real and theoretical values in the zero-shear plateau and in the second decay of viscosity. But the polydisperse model does not predict the first decay of viscosity. Therefore, it can be argued that the second decrease in viscosity is due to bubble deformation and polydispersity, but not the first decrease. To eliminate the possibility of elastic instabilities affecting the viscosity at higher shear rates, the suspensions were checked with the criteria described by Mckinley et al. (1991, 1996) and Shaqfeh (1996) for a plate-plate geometry. It was observed that even for the highest tested shear rate, the suspensions do not fulfil the criteria for the onset of elastic instabilities, hence confirming that the second decay of viscosity is not due to this effect.

To ensure that the first decrease of viscosity is not related to a stress overshoot or any other time-dependent phenomena, start-up shear experiments were performed, shearing the suspensions for 40 s at $\dot{\gamma}$ = 0.5 s^{-1}, 5 s^{-1} and 50 s^{-1}. The recorded transient data confirmed that there were no unexpected features in the viscosity trends with time. Further shear tests were performed, during which the shear rate was consecutively ramped up and down, in order to investigate the thixotropic character of the dispersions. However, these tests could not give reliable information about the present samples. This is because the bubble suspensions do not preserve the initial structure after being sheared at medium/high shear rates, where bubble deformation and coalescence become dominant. Thus, to investigate the cause of the first decay of viscosity, the dynamic behaviour of the bubble suspensions was visualised under shear.

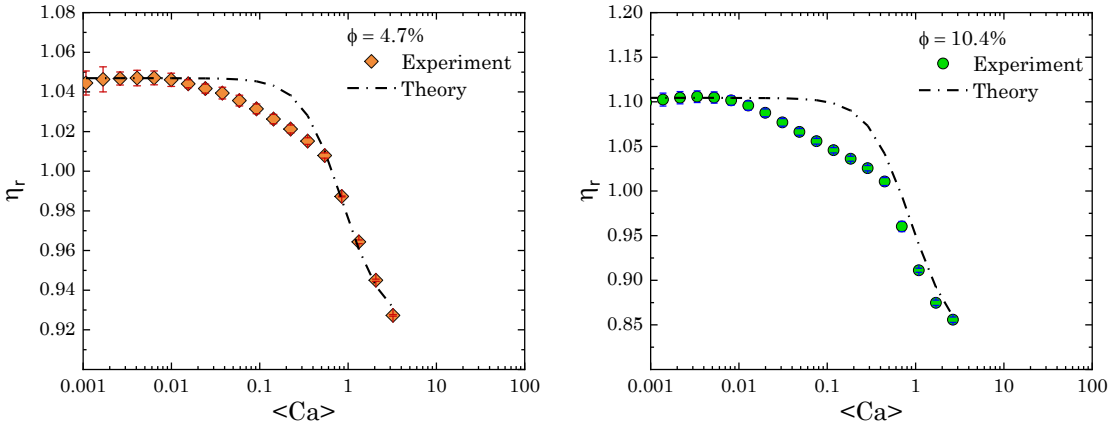

Figure 3.8: Experimental vs theoretical relative viscosity for polydisperse bubble suspensions with (a) $\varphi_1 = 4.7\%$ and (b) $\varphi_2 = 10.4\%$. Error bars represent the variation between three experimental repeats.

3.5 Visualisation of bubbles under shear

3.5.1. Shear induced phenomena

To visualise bubbles under shear, three fresh semi-dilute polydisperse bubble suspensions were prepared. The volume fractions of these new suspensions were $\varphi_1 = 5.6$ %, $\varphi_2 = 7.23$ % and $\varphi_3 = 8.52$ %. Fig. 3.9 presents some representative images for the suspension with bubble volume fraction φ_2, taken with a 1.9 mm gap, at shear rates 0.1 s^{-1} and 23 s^{-1}. At shear rates around 0.1 s^{-1} corresponding to $< Ca > \sim 0.01$, the bubbles are uniformly dispersed. As the average capillary number increases, bubbles start aligning to form bubble threads or getting closer to each other, forming clusters. It was observed that the shear-induced bubble clustering was three-dimensional and dynamic, with threads and clusters breaking and reforming continuously throughout the entire samples. The phenomenon became progressively more evident in the $< Ca >$ range 0.01 to 1, where the first decay of viscosity was also noticed.

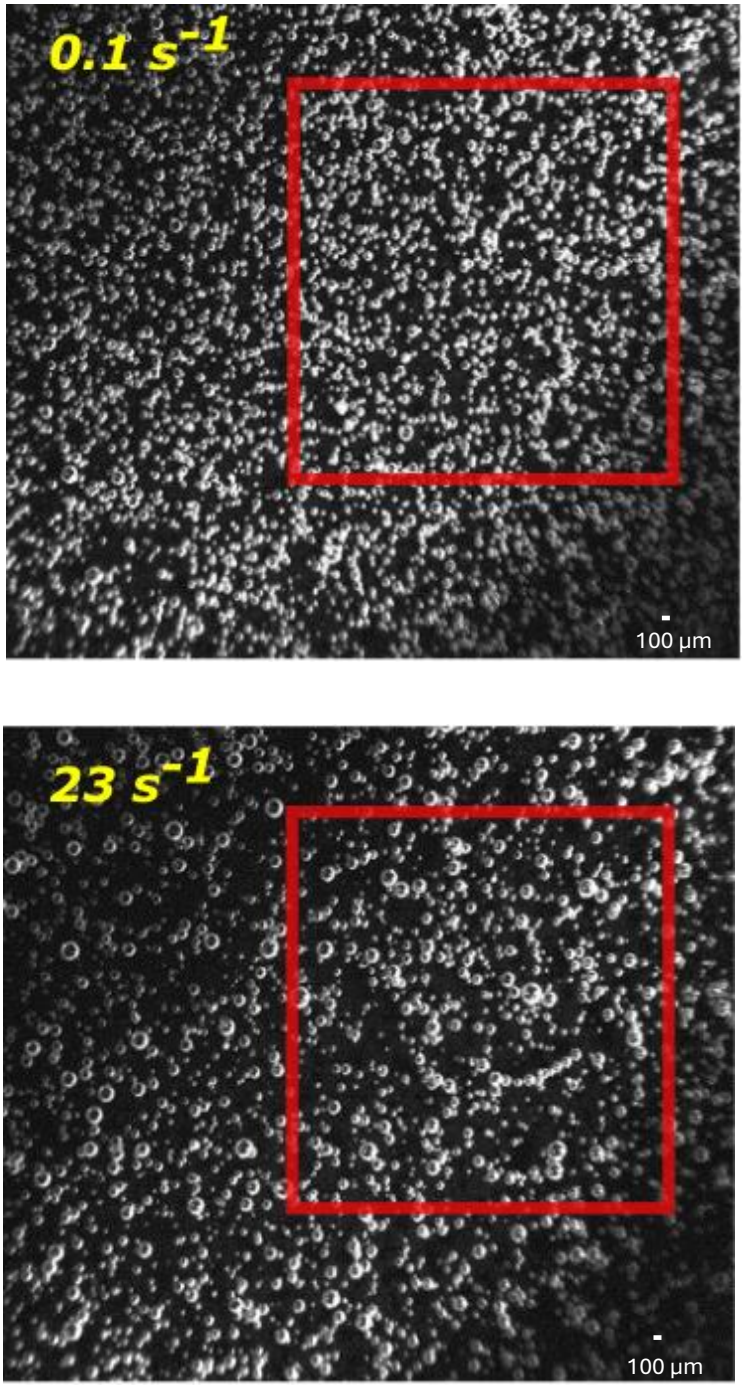

Figure 3.9: Bubble suspension ($\varphi = 7.23\%$) under steady shear at 0.1 s^{-1} and 23 s^{-1} (1.9 mm gap). The red rectangles highlight regions showing the formation of bubble clusters and threads.

Feneuil et al. (2023) confirmed the formation of bubble clusters and threads under steady shear. According to them, the phenomenon is mainly caused due to bubble deformation, and thus, occurs only when the capillary number is large enough; that is $Ca > 0.2$ for their experiments. However, this is not the case in the present suspensions, where the formation of bubble clusters and threads started at average capillary numbers smaller than 0.2. At this point it is worth clarifying that the model of Mader et al. (2013) does not account for bubble clustering and alignment, so the deviation between the experimental and the theoretical values

in the first decay of viscosity is reasonable. The model simply suggests the linear additivity of the contributions of the different bubble classes in a polydisperse system, whose viscosity is calculated with the constitutive equation developed by Llewellin et al. (2002b) for a monodisperse suspension (Eq. 3.1). As discussed, this constitutive equation was derived from the equation of Frankel and Acrivos (1970), which recovers Taylor's (Taylor, 1932) equation for $Ca \ll 1$, and does not contain second or higher orders terms of the dispersed-phase volume fraction, so that it cannot account for complex phenomena arising from bubble interactions, such as bubble clustering and/or alignment.

In addition to bubble clustering, bubble coalescence and deformation were also observed at higher $< Ca >$. Finally, the optical measurements also confirmed the absence of any bubble rise in the duration of the experiments (whose total time was 11 minutes). The issue of bubble rise becomes important in long stationary experiments, where the bubbles experience only buoyancy. However, under steady shear, bubble rise is retarded due to flow in the tangential direction. Moreover, the use of surfactants, as in the experiments discussed in this chapter, can reduce the rising velocity of small bubbles by up to 50% (De Kee' et al., 1990; Tzounakos et al., 2004). For all these reasons, it can be confidently asserted that bubble rise was negligible and did not affect the experimental results.

3.5.2. Statistical analysis

3.5.2a. Coverage

To quantify the shear-induced bubble clustering, a statistical image analysis was performed, defining the following dimensionless parameter, named *coverage*:

$$C \equiv \frac{Total\ bubble\ surface\ (in\ pixels)}{Image\ surface\ (in\ pixels)} \tag{3.13}$$

C represents the percentage of the image covered with bubbles. When bubbles are close enough to form threads and clusters, a greater overlapping of bubbles is expected, resulting in a decrease in the area of the image occupied by bubbles and a consequent decrease in coverage. Thus, a reduction in coverage can be used as a measure for bubble clustering. This can be visually confirmed with the images presented in Fig. 3.9. As seen, for shear rate 23 s^{-1}, where bubble threads and clusters are present, the image seems less covered with bubbles compared to the case with shear rate 0.1 s^{-1}, where the bubbles are uniformly dispersed. To minimise the volume of data, the analysis was conducted using 30 representative images out of the almost 600 obtained for each shear rate. The selected images corresponded to the time interval during

which steady state was accomplished. This happened almost immediately even for the lower shear rates and, thus, apart from some initial images, the rest were equivalent. The images were chosen using mostly a step of 20.

Each image was first converted into a black and white matrix, with the bubbles depicted as white pixels in a black background. Then, all the white pixels were summed and divided by the total number of pixels in the image, as shown in Fig. 3.10. For each shear rate, a mean coverage, $\bar{C}$, was calculated by averaging over the coverage values of the 30 images. Fig. 3.11 presents the average coverage as a function of the shear rate for the tested suspensions. The error bars represent the standard deviation of the coverage values obtained across the analysed images for each shear rate. As seen, $\bar{C}$ always increased up to shear rates around 1 s^{-1} corresponding to $\langle Ca \rangle \sim 0.01$, and then decreased continuously in the range of shear rates observed. Here it must be noted that coverage is a qualitative metric for bubble clustering, meaning that one should focus on the general trend and not the absolute values. The decrease in $\bar{C}$ validates the optical observations, confirming the formation of bubble clusters and threads around 1 s^{-1}. The initial increase is believed to be due to bubble redistribution in the sample. Similar to particle suspensions during pre-shearing, bubbles disperse at low shear rates, removing any nonuniform bubble distribution formed during sample loading in the rheometer. Moreover, the coverage increased with the bubble volume fraction for all shear rates tested. This behaviour is reasonable since larger bubble volume fractions lead to an increase in the total bubble surface and, thus, to larger values of coverage.

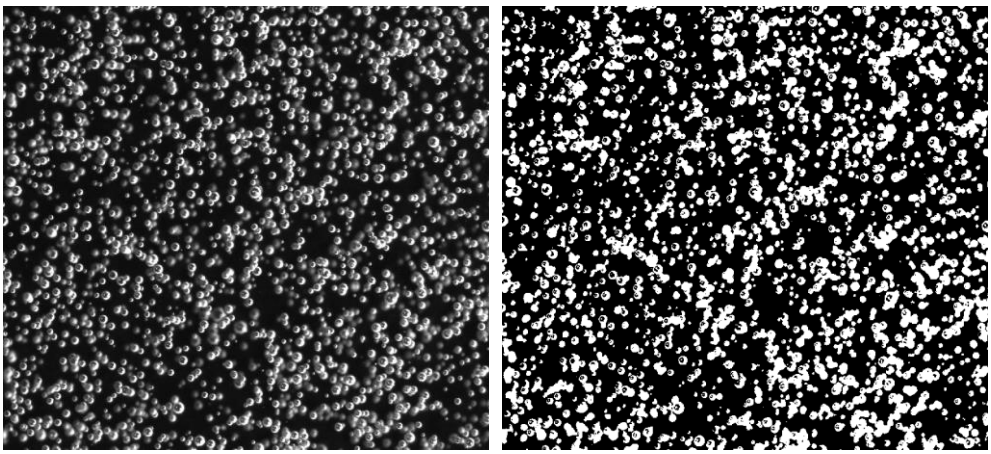

$$Coverage = \frac{sum\ of\ white\ pixels}{total\ image\ pixels}$$

Figure 3.10: Example of an image (left) after black and white conversion (right) and definition of coverage.

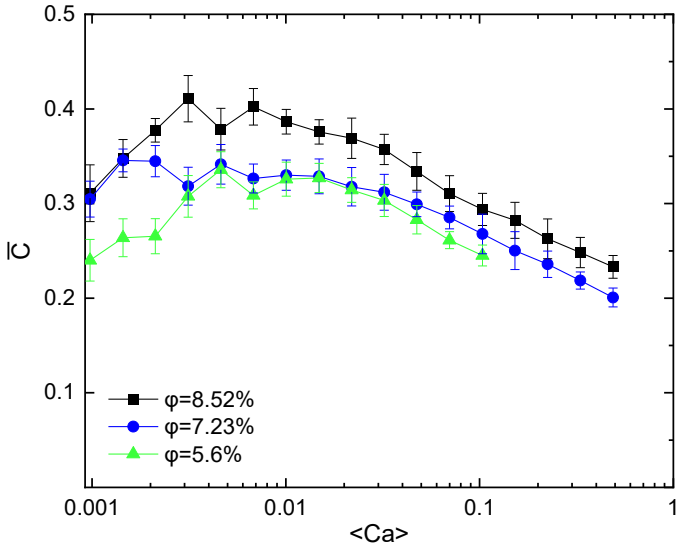

Figure 3.11: Coverage as a function of $\langle Ca \rangle$ for $\varphi_1 = 5.6\%$, $\varphi_2 = 7.23\%$ and $\varphi_3 = 8.52\%$.

3.5.2b. Bubble coalescence

To ensure that the initial bubble size distribution did not change significantly during the rheological tests, an investigation was conducted to observe how bubble sizes changed with shear. To this end, the 0.8 mm gap images were used because they allowed identifying the bubbles more precisely. The bubbles and their respective radii in pixels were identified for each image using MATLAB. To convert pixels into mm, a 1 mm calibration tape was attached on the glass bottom plate. The scale was found to be equal to 306 pixels/mm. For each image, the bubble size distribution was determined and found to consistently follow a gamma type distribution, and the De Brouckere average diameter d_{43} was calculated. Subsequently, for each shear rate, the mean De Brouckere average diameter $\langle d_{43} \rangle$ was evaluated by averaging the d_{43} values obtained for 30 images different images. Fig. 3.12 indicatively presents how $\langle d_{43} \rangle$ changed for the suspension with φ =7.23%. As seen, the bubble size increased by 16.4%. As mentioned earlier, this value might have been slightly enhanced due to the smaller gap used for this analysis. Hence, even with the use of surfactants, there was some bubble coalescence, but this did not affect the average bubble size significantly.

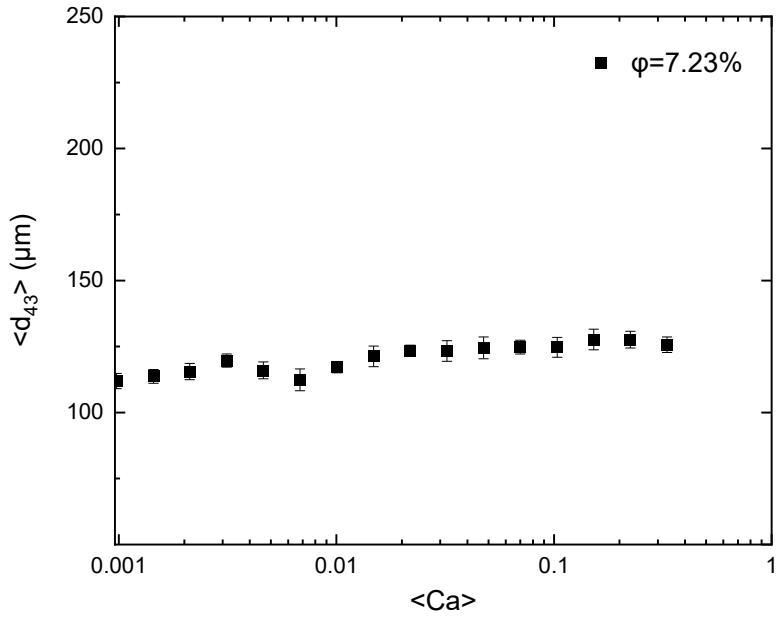

Figure 3.12: Mean De Brouckere average diameter $\langle d_{43} \rangle$ as a function of $\langle Ca \rangle$ for $\varphi = 7.23\%$.

3.5.3. Bubble clustering and shear-thinning

As shown by the statistical image analysis, bubbles started aligning/clustering at shear rates around 1 s^{-1} ($\langle Ca \rangle \sim 0.01$), where the first decay of viscosity was also observed. Therefore, the formation of bubble threads and clusters appears to be responsible for the first shear-thinning trend. Specifically, when bubbles align, the total bubble area exposed to the flow decreases; thus, the distortion of the fluid streamlines due to the presence of the bubbles, and in turn the suspension viscosity, reduces. Ordering in the direction of the fluid streamlines does not apply only to single bubbles but also to the 3-D dynamic bubble clusters, observed during the rheo-optical experiments. Moreover, when bubbles are positioned very close to each other, forming clusters, there is no flow in the interstitial spaces. The fluid streamlines do not distort within the clusters, but only around them. Consequently, the flow resistance is smaller for bubble clusters compared with randomly positioned bubbles.

Microstructure changes and higher order phenomena, such as clustering and alignment, have been associated with shear-thinning behaviour in multiple occasions. Recent works (Yang et al., 2012; Yokozeki et al., 2012; Papadopoulou et al., 2020) showed that the formation of solid particle agglomerations at lower shear rates and their later breakdown and alignment with the fluid streamlines at increasing applied deformations lead to a decrease in suspension viscosity. Comparing bubble and particle suspensions, one can identify both similarities and differences in the mechanism of clustering-induced shear-thinning. The similarity lies in the core of the

shear-thinning mechanism, which is common for both particle and bubble suspensions, and regards the ordering of either individual particles/bubbles or particle/bubble clusters in the direction of the fluid streamlines. However, the way this ordering happens is different for each case. For particle suspensions, the shear-thinning behaviour is observed when the agglomerations break down, while for bubble suspensions in the semi-dilute regime, it was observed that the shear-thinning onset coincided with the formation of bubble clusters and threads. This contrast can be explained considering the different nature of the two systems. Particle agglomerations are usually formed in concentrated systems due to attractive forces between the particles. This results in a highly structured network of clusters with restrained movement and rotation, which, at lower shear rates, opposes the flow and results in higher suspension viscosity. As the shear rate increases, the particle agglomerations break down and start aligning with the fluid streamlines, causing the shear-thinning behaviour. However, for semi-dilute bubble suspensions, the nature of the shear-induced clusters is different. Since the bubble suspensions are not concentrated, the generated dynamic bubble clusters are more free to move and finally align in the direction of the fluid streamlines, causing the first viscosity drop observed in the present rheological experiments.

3.6 Conclusions

In this chapter, the complex shear-thinning behaviour of semi-dilute polydisperse bubble suspensions under steady shear was delineated, by explaining the effect of polydispersity and shear-induced clustering. To this end, semi-dilute polydisperse bubble suspensions were generated using a mixture of mineral oil and 0.57 mol/L Span80 as ambient fluid, and their steady shear viscosity was measured. The bubble sizes of the produced polydisperse suspensions were found to follow the gamma distribution between 10 and 170 μm. It was confirmed that polydispersity can cause an extended shear-thinning behaviour, which spans a larger range of average capillary number values, instead of happening at $\langle Ca \rangle \sim 1$. However, the effect of polydispersity becomes important only if the total bubble volume fraction is evenly divided between very small and very large bubbles. Under real experimental conditions, where the bubble sizes follow the gamma distribution, the polydisperse suspension can be regarded as monodisperse with a diameter equal to the volume-weighted average diameter.

However, the flow curves obtained from the present experimental investigations showed an unexpected double power-law decay in the suspension viscosity, the first decrease happening at $\langle Ca \rangle \sim 0.01$and the second at $\langle Ca \rangle \sim 1$. Comparison of the experimental results with the

polydisperse viscosity model of Mader et al. (2013) showed good agreement in the zero-shear viscosity plateau and in the second decay of viscosity. But the model failed to predict the first viscosity drop. Thus, unlike the second shear-thinning trend, the first appears to be unrelated to bubble deformation and polydispersity.

To investigate further the first decrease of viscosity, the bubble suspensions were visualised under steady shear. Statistical image analysis showed that bubbles started aligning/clustering at $\langle Ca \rangle \sim 0.01$. The image analysis also revealed that at higher shear rates, bubbles deform and coalesce, with the average bubble diameter increasing by 16.4%, an increase that however cannot explain the first decay of viscosity observed. Therefore, it is suggested that the first decrease in viscosity is due to the formation of bubble threads and clusters and their ordering across the direction of the flow, which, in turn, causes less distortion of the fluid streamlines, and, hence, a decrease in suspension viscosity.

Chapter 4

Linear viscoelastic behaviour of semi-dilute polydisperse bubble suspensions in Newtonian media

In Chapter 3, the steady shear viscosity of dilute polydisperse bubble suspensions was investigated in the limit of Cd approaching zero and for varying Ca. To fully characterise the rheology of bubble suspensions in Newtonian ambient fluids, it is essential to also examine the linear viscoelastic regime under conditions of vanishingly small Ca and varying Cd. This chapter aims to provide a systematic experimental characterisation of the linear viscoelastic behaviour of semi-dilute polydisperse bubble suspensions by employing a rheo-optical setup to visualise the behaviour of the suspensions during SAOS rheological tests. For all tested suspensions, the measured viscoelastic moduli (G', G'') aligned with the theoretical predictions of the Jeffreys model for average dynamic capillary numbers ($\langle Cd \rangle$) greater than unity. But at lower $\langle Cd \rangle$ values, experimental G' values exceeded theoretical predictions. Upon investigating and ruling out the effects of potential experimental artifacts – such as bubble rise, coalescence, and changes in suspension microstructure over time – it was determined that the unexpected G' deviation is linked to bubble fluid dynamic interactions. These interactions complicate the relaxation process, introducing multiple relaxation modes. The results of this chapter offer valuable insights on the effect of microstructure on the rheology of bubble suspensions, addressing a significant gap in reliable experimental data in this area.

The results of this chapter have been published and chosen as featured article in the Journal of Rheology homepage:

Mitrou, S., S. Migliozzi, L. Mazzei, and P. Angeli, “On the linear viscoelastic behaviour of semi-dilute polydisperse bubble suspensions in Newtonian media,” J. Rheol. 68, 539–552 (2024).

4.1 Introduction

As discussed in Chapter 3, the steady-shear rheology of bubble suspensions, in the limit of $Cd \to 0$ and for varying Ca, has been investigated for monodisperse (Llewellin et al., 2002a; Lim et al., 2004; Morini et al., 2019) and polydisperse (Llewellin et al., 2002b; Mader at al., 2013; Mitrou et al., 2023; Joh et al., 2010) systems, with studies showing that bubble deformation (Llewellin et al., 2002a; Rust & Manga, 2002; Lejeune et al., 1999) and clustering (Mitrou et al., 2023) are responsible for the characteristic shear-thinning behaviour. Time-dependent flows (from a Lagrangian point of view) with infinitesimal bubble deformation, that is, in the limit of $Ca \to 0$ for varying Cd, have also been investigated to characterise the linear viscoelastic behaviour of bubble suspensions (e.g. Llewellin et al., 2002b; Joh et al., 2010; Mitrias et al., 2017; Seo and Youn, 2005). These flow conditions can be achieved through small amplitude oscillatory shear (SAOS) rheological tests, where a sinusoidal deformation γ_{ij} is applied to the system and the resulting shear stress τ_{ij} is measured:

$$\gamma_{ij} = \gamma_{ij}^0 \sin(\omega t) \tag{4.1a}$$

$$\tau_{ij} = G'(\omega)\, \gamma_{ij}^0 \sin(\omega t) + G''(\omega)\, \gamma_{ij}^0 \cos(\omega t) \tag{4.1b}$$

where γ_{ij}^0 is the amplitude of the applied deformation, ω is the oscillation frequency, G' is the *elastic modulus*, which describes the elastic character of the suspension, and G'' is the *loss modulus*, which describes the viscous character of the suspension. The main models that describe the linear viscoelastic behaviour of bubble suspensions as a function of the bubble volume fraction and dynamic capillary number are presented below.

As reported in Chapter 2, Llewellin et al. (2002a) proposed a constitutive equation (Eq. 2.52) expressed in the form of the linear Jeffreys model (Bird et al., 2002) to characterise the linear viscoelastic behaviour of dilute monodisperse bubble suspensions. This constitutive equation holds for $Ca \ll 1$ and varying Cd, and has its theoretical foundation in the analysis of Frankel and Acrivos (1970) on the time-dependent flow of dilute monodisperse emulsions with infinitesimal droplet deformation. For convenience, the equation is presented again below:

$$\tau_{ij} + \alpha_1 \dot{\tau}_{ij} = 2\eta_s(\beta_1 e_{ij} + \beta_2 \dot{e}_{ij}) \tag{4.2}$$

where τ_{ij} is the deviatoric stress tensor, e_{ij} is the rate-of-strain tensor, η_s is the viscosity of the Newtonian ambient fluid, and the overdot (in $\dot{\tau}_{ij}$ and $\dot{e}_{ij}$) denotes the partial time derivative. The parameters α_1, β_1 and β_2 are functions of the bubble volume fraction φ and the relaxation

time of a single bubble λ. The expressions of these parameters are presented in Table 4.1. Solving Eq. 4.2 for a linear oscillatory shear flow, Llewellin et al. (2002a) obtained the following expressions for G' and G'':

$$\frac{G'(Cd,\varphi)}{\omega\eta_s} = \frac{(\beta_1\alpha_1-\beta_2)\omega}{1+\alpha_1^2\omega^2} = \left(\frac{\frac{16}{5}Cd}{1+\frac{36}{25}Cd^2}\right)\varphi \tag{4.3a}$$

$$\frac{G''(Cd,\varphi)}{\omega\eta_s} = \frac{\beta_1+\alpha_1\beta_2\omega^2}{1+\alpha_1^2\omega^2} = 1 + \frac{G''_{red}(Cd,\varphi)}{\omega\eta_s} \quad \text{with} \quad \frac{G''_{red}(Cd,\varphi)}{\omega\eta_s} \equiv \left(\frac{1}{1+\frac{36}{25}Cd^2}\right)\frac{8}{3}\varphi - \frac{5}{3}\varphi \tag{4.3b}$$

where G''_{red} denotes the loss modulus without the viscous contribution of the solvent (i.e., $\omega\eta_s$). In the limit of large Cd, Eq. 4.3b yields a negative value of G'' for $\varphi > 0.6$; however, this is not a problem, because the model is valid only for *dilute* suspensions. Mitrias et al. (2017) simulated the oscillatory shear flow of dilute monodisperse bubble suspensions to determine their viscoelastic moduli. They then compared their results with the predictions of Eq. 4.3, finding good agreement for bubble volume fractions lower than 0.5%.

Note that Eq. 4.3 rigorously holds for monodisperse bubble suspensions. To account for the effect of polydispersity on the viscoelastic behaviour of dilute and semi-dilute bubble suspensions, the linear superposition method proposed by Mader et al. (2013) is a reasonable approach. This method, analogous to determining the viscosity of a polydisperse suspension, involves calculating the material functions for each bubble size class and then summing the individual contributions. While the authors applied this method to the steady-shear viscosity of a dilute polydisperse bubble suspension, they did not extend it to the case of linear viscoelastic material functions.

Seo and Youn (2005) suggested a phenomenological rheological model for dilute monodisperse bubble suspensions. Their constitutive equation is also expressed in the form of the linear Jeffreys model (i.e., Eq. 4.2) and was based on the analysis of Maffettone and Minale (1998) on the deformation of an ellipsoidal droplet in a simple shear flow. Similar to the model of Doi and Ohta (1991), the model of Seo and Youn (2005) describes the macroscopic stress of the suspension, accounting for the evolution of the bubble size and shape. The parameters α_1, β_1 and β_2 for their model are shown in Table 4.1. Note that the models of Llewellin et al. (2002a) and Seo and Youn (2005) represent modified versions of the Jeffreys model (Bird et al., 2002), the difference in the coefficients α_1, β_1 and β_2 stemming from the analysis in the limit of a single droplet of Frankel and Acrivos (1970) and Maffetone & Minale (1998),

respectively; therefore, these models do not account for fluid dynamic interactions or crowding effects among bubbles.

Joh et al. (2010) solved the constitutive equation proposed by Seo and Youn (2005) for a linear oscillatory shear flow, obtaining the following expressions for G' and G'':

$$\frac{G'(Cd,\varphi)}{\omega\eta_s} = \left[\frac{(\xi_1-\xi_3)\omega}{1+\xi_1^2\omega^2}\right]\xi_2 = \left(\frac{2Cd}{1+\frac{9}{16}Cd^2}\right)\varphi \tag{4.4a}$$

$$\frac{G''(Cd,\varphi)}{\omega\eta_s} = \left(\frac{1+\xi_1\xi_3\omega^2}{1+\xi_1^2\omega^2}\right)\xi_2 = 1+\frac{G''_{red}(Cd,\varphi)}{\omega\eta_s} \quad \text{with} \quad \frac{G''_{red}(Cd,\varphi)}{\omega\eta_s} \equiv \left(\frac{1}{1+\frac{9}{16}Cd^2}\right)\frac{8}{3}\varphi - \frac{5}{3}\varphi \tag{4.4b}$$

To account for their polydisperse experimental data, they modified Eq. 4.4 by applying the same method described in Sec. 3.1 for the relative viscosity. Specifically, they incorporated a probability density fraction $f(R)$ related to the bubble radii distribution. As outlined in Sec. 3.1, this approach is effective only if $f(R)$ is a *volume fraction probability density fraction*, so that $f(R)dR$ yields the volume fraction of bubbles with radius in the range dR around R. Under that assumption, Eq 4.4 can be generalised as follows:

$$\frac{G'_{polydisperse}}{\omega\eta_s} = \int_0^\infty \frac{G'[Cd(R),\varphi]}{\varphi\omega\eta_s} f(R)dR \tag{4.5a}$$

$$\frac{G''_{polydisperse}}{\omega\eta_s} = 1 + \int_0^\infty \frac{G''_{red}(Cd,\varphi)}{\varphi\omega\eta_s} f(R)dR \tag{4.5b}$$

Comparing their experimental data with the predictions of Eq. 4.5, Joh et al. (2010) noted a deviation of G' at low values of ω. They attributed this to bubble fluid dynamic interactions, without however validating this assumption.

As seen, several studies have focused on the time-dependent flow of suspensions with infinitesimally deformed bubbles (i.e., $Ca \ll 1$), advancing constitutive equations to describe their viscoelastic behaviour. However, there are sparse experimental data to validate these equations. This work aims to provide a systematic experimental characterisation of the linear viscoelastic behaviour of semi-dilute bubble suspensions by employing a rheo-optical setup to visualise the behaviour of the suspensions during SAOS rheological tests. This coupled approach offers a higher confidence in the experimental measurements because it allows investigating the effects of bubble size distribution and various SAOS measurement artifacts, including bubble rise, coalescence, and changes in bubble spatial organisation over time, which can influence the rheological measurements of bubble suspensions.

Table 4.1: Parameters α_1, β_1 and β_2 for the different rheological models.

Rheological model	α_1	β_1	β_2
Llewellin et al. (2002a)	$\frac{6}{5}\lambda$	$1+\varphi$	$\left(1-\frac{5}{3}\varphi\right)\alpha_1$
Seo and Youn (2005)	$\frac{3}{4}\lambda$	$1+\varphi$	$\frac{\left(1-\frac{5}{3}\varphi\right)}{1+\varphi}\alpha_1$
Jeffreys	λ	$1+\varphi$	α_1

4.2 Materials and Methods

4.2.1 Chemicals

Bubble suspensions were generated using a Newtonian mixture of mineral oil (RTM38 Mineral Oil Rotational Viscometer Standard – produced by Paragon Scientific, Birkenhead, UK) and 5% w/w of the liquid, non-ionic surfactant Span 80 (Sigma Aldrich, St. Louis, USA). The chosen ambient fluid was viscous enough to ensure time-stable suspensions and minimal bubble rise during the rheological measurements. The properties of the individual materials and the final mixture were measured at 12 °C, in compliance with the rheological tests, and are presented in Table 4.2. Additionally, a detailed rheological characterisation of the used base matrix is provided in Sec. B1 of Appendix B.

Table 4.2: Viscosity η_s, density ρ and surface tension $\sigma_{\alpha,\beta}$ of the fluids constituting the Newtonian ambient fluid.

Fluid	Viscosity (Pa s)	Density (g/mL)	Surface tension (mN/m)
RTM38 Mineral Oil	77.54±0.78	0.93±0.01	36.57±0.25
Span 80	1.95±0.02	0.99±0.01	29.34±0.25
Mixture	53.06±0.53	0.94±0.02	36.03±0.25

4.2.2 Generation and rheological characterisation of the bubble suspensions

Bubble suspensions were produced using the aeration device detailed in Sec. 3.3.2. The bubble volume fraction and size distribution of the generated suspensions were also determined following the methods described in that section. To retrieve the suspension viscoelastic moduli, SAOS rheological tests were performed in an Anton Paar MCR302 stress-controlled rotational rheometer. The tests were carried out with a gap of 1.3 mm at a constant temperature of 12 °C.

The chosen gap was ten times larger than the average bubble diameter to minimize wall effects caused by confinement. Moreover, the operating temperature allowed for minimal bubble rise during the rheological measurements.

To determine the appropriate strain amplitude for the SAOS tests, strain sweep experiments were conducted on a bubble suspension with $\varphi = 9.5\%$. These experiments covered three oscillation frequencies: $\omega_1 = 0.56$ rad/s, $\omega_2 = 1$ rad/s and $\omega_3 = 10$ rad/s, and shear strains ranging from 0.05% to 10%. The results showed that the viscoelastic moduli remained constant across this strain range, indicating that any strain value within this range is suitable for assessing the system's linear viscoelastic properties. Therefore, a shear strain of 5% was selected for the SAOS rheological measurements. The G', G'' curves obtained from the strain sweep experiments are reported in Sec. B2 of Appendix B.

The SAOS measurements were performed by ramping down the oscillation frequency from 50 rad/s to 0.05 rad/s. Operating from higher to lower frequencies, i.e., from shorter to longer characteristic flow times, was chosen to minimize the effect of bubble coalescence and rise on the obtained viscoelastic curves. To validate the accuracy of the experimental data, particularly in terms of low torque and phase angle resolution issues, a dedicated study was performed, which is detailed in Sec. B3 of Appendix B.

Prior to the SAOS measurements, the bubble suspensions were pre-sheared for three minutes at 0.1 s^{-1}. This pre-shearing step was selected to remove potential loading effects without altering the suspension microstructure (as confirmed by the experiments discussed in Sec. 4.3.1).

4.2.3 Visualisation of the bubble suspensions under oscillatory shear

The bubble suspensions were visualised under oscillatory shear, using the rheo-optical setup depicted in Fig. 3.4. SAOS tests were conducted as previously described, with images captured throughout the process using a FLIR GS3-U3-32S4M-C 1/1.8" camera (acquisition frequency: 5 Hz, image resolution: 1536 × 2048 pixels), a Nikon mono zoom lens and a white LED light as illumination. All visualisation experiments were conducted at a focus plane of 600 μm, with minor adjustments for different samples. The pixel-to-mm conversion scale was found equal to 306 pixels/mm. The depth of field for the current visualisation setup was 600 μm.

Note that, although the camera was focused on a pre-calibrated plane, the large depth of field allowed for the visualisation of multiple bubble layers. This enabled the visualisation of

bubbles even when they had risen beyond the calibration plane, effectively covering a visualisation gap of up to 300 μm above the calibration plane.

4.3 Results on bubble size and viscoelastic properties

This section presents experimental results for bubble suspensions with volume fractions $\varphi_1 = 4.2$ %, $\varphi_2 = 13.5\%$ and $\varphi_3 = 19.2\%$.

4.3.1 Bubble size distributions

All tested samples were polydisperse, with bubble radii following the gamma distribution between 20 μm and 120 μm (Fig. 4.1). As in Chapter 3, a volume-weighted average radius, $\langle R \rangle$, was determined for each bubble suspension. For the reported bubble volume fractions, $\varphi_1 = 4.2$ %, 13.5 % and 19.2 %, the respective volume-weighted mean radii were equal to 61 μm, 64 μm and 65 μm.

To ensure that the initial bubble size distribution did not change significantly during the pre-shear stage, bubble sizes computed from the microscope images were compared to those derived from the visualisation experiments. For each sample, the image taken immediately after the end of pre-shearing was analysed using MATLAB to identify bubbles and their radii (in pixels). The radii were then converted to mm using a conversion scale of 306 pixels/mm, determined through the focus plane calibration. The image analysis revealed that after three minutes of pre-shearing at 0.1 s^{-1}, the bubble radii distributions remained essentially the same.

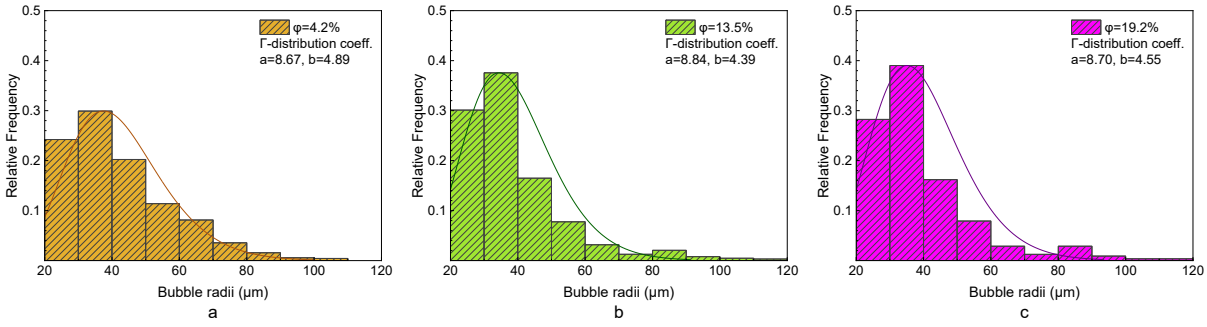

Figure 4.1: Bubble size distribution for (a) $\varphi_1 = 4.2\%$, (b) $\varphi_2 = 13.5\%$ and (c) $\varphi_3 = 19.2\%$ after three minutes of pre-shearing at 0.1 s^{-1}.

4.3.2 SAOS results

To characterise the viscoelastic behaviour of the bubble suspensions, the experimental values of G' and G''_{red} need to be compared to the predictions of an appropriate theoretical model. Since the aim is to use the simplest model that can describe the behaviour correctly, the polydisperse suspension was initially modelled as a monodisperse one, using Eq. 4.2 with the

parameters α_1 and β_2 expressed in terms of the volume-weighted average bubble radius $\langle R \rangle$ and of an average dynamic capillary:

$$\langle Cd \rangle \equiv \langle \lambda \rangle \omega \tag{4.6}$$

where $\langle \lambda \rangle$ is the average relaxation time of the suspension, defined using $\langle R \rangle$.

Next, it was necessary to determine which version of Eq. 4.2 is more appropriate: (i) the original Jeffreys version, (ii) the Llewellin et al. (2002a) modification, or (iii) the Seo and Youn (2005) modification. By observing Eqs. 4.3b and 4.4b, it becomes evident that for large values of $\langle Cd \rangle$, the second term in the expressions for G''_{red} becomes dominant, resulting in negative G''_{red} values. This is not physically reasonable. In particular, for the current experimental system, substituting its physical parameters (i.e., solvent viscosity $\eta_s = 53.063$ Pa s, bubble volume fraction of the tested suspensions $\varphi_1 = 4.2\%$, $\varphi_2 = 13.5\%$ and $\varphi_3 = 19.2\%$, and respective average relaxation times of the bubbles $\langle \lambda \rangle_1 = 0.88$ s, $\langle \lambda \rangle_2 = 0.80$ s and $\langle \lambda \rangle_3 = 0.75$ s) into Eqs. 4.3b and 4.4b leads to negative G''_{red} values for Cd larger than 0.8.

This issue was not addressed in the works of Llewellin et al. (2002a) and Seo and Youn (2005), despite their experimental parameters being similar to those of the present study. It should be noted that both studies accounted for the viscous contribution of the solvent, which for semi-dilute suspensions is dominant. Thus, even if G''_{red} was negative, it was not readily noticeable from the η' and G'' graphs presented in Llewellin et al. (2002a) and Seo and Youn (2005). Therefore, the original Jeffreys model (Bird et al., 2002) (i.e., Eq. 4.2 with $\alpha_1 = \beta_2 = \langle \lambda \rangle$) was selected to describe the linear viscoelastic moduli of the suspensions investigated in this work, because this model does not pose this problem. For an oscillatory shear flow, the original Jeffreys constitutive equation yields the following expressions for G' and G''_{red} in a suspension of identical bubbles:

$$\frac{G'(Cd,\varphi)}{\omega \eta_s} = \left(\frac{Cd}{1+Cd^2}\right)\varphi \tag{4.7a}$$

$$\frac{G''_{red}(Cd,\varphi)}{\omega \eta_s} = \left(\frac{1}{1+Cd^2}\right)\varphi \tag{4.7b}$$

For each of the reported bubble volume fractions, the theoretical G' and G''_{red} values were determined using Eq. 4.7, expressed in terms of $\langle Cd \rangle$. Fig. 4.2 presents the experimental G', G''_{red} curves (black and hollow points), along with the theoretical predictions of the Jeffreys

model for a monodisperse suspension (red and black dashed lines), as functions of the average dynamic capillary number.

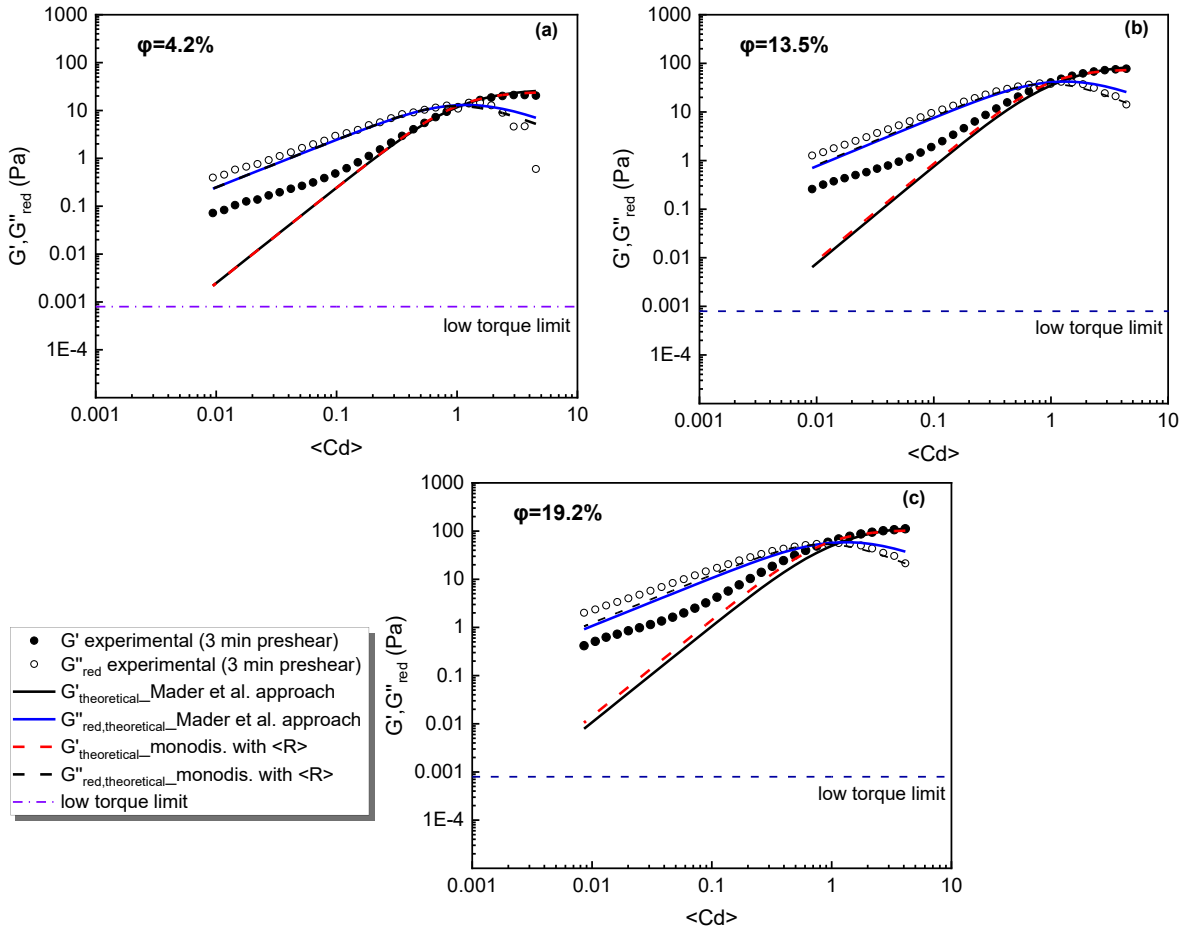

Figure 4.2: Experimental values vs theoretical predictions of G' and G''_{red} for polydisperse bubble suspensions with (a) $\varphi_1 = 4.2\%$, (b) $\varphi_2 = 13.5\%$ and (c) $\varphi_3 = 19.2\%$.

As shown, there is good agreement between the experimental and theoretical values for $\langle Cd \rangle$ larger than unity. But at lower $\langle Cd \rangle$, the experimental values of G' are significantly larger than the theoretical ones. Moreover, the shape of the experimental G' curves is more complex, resembling that of a suspension with multiple relaxation modes. As shown in Fig. 4.3, the onset of the G' deviation is related to the bubble volume fraction, with denser suspensions deviating earlier, that is, at higher $\langle Cd \rangle$ values. Furthermore, within the same low range of $\langle Cd \rangle$, the experimental values of G' deviate more from the theoretical predictions as the bubble volume fraction increases, with the densest suspension deviating almost twice as much compared to the most dilute one. For a dedicated discussion on this, please refer to Sec. B4 of Appendix B.

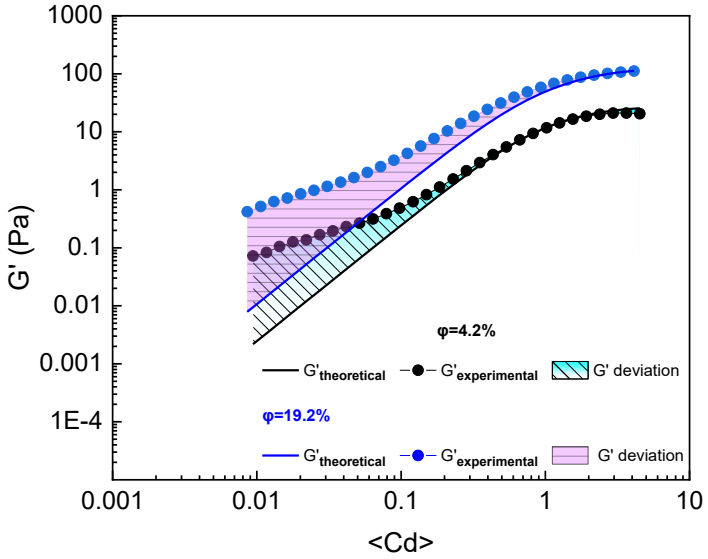

Figure 4.3: Effect of the bubble volume fraction on the onset of the G' deviation from the theoretical predictions of the generalised Jeffreys model.

The observed complex G' trend was unexpected, because it is not predicted by the model. This discrepancy indicates that the considered model may not be appropriate for describing the experimental data. A possible reason for the poor predictions at low $\langle Cd \rangle$ may be the polydisperse character of the studied suspensions. To account for this issue more thoroughly, the linear superposition approach suggested by Mader et al. (2013) was employed. Considering a polydisperse bubble suspension with N discrete bubble radii classes, Eq. 4.7 can be generalised as follows:

$$\frac{G'_{polydisperse}}{\omega\eta_s} = \sum_{i=1}^{N} \frac{G'_i(Cd_i,\varphi_i)}{\omega\eta_s} = \sum_{i=1}^{N} \left(\frac{Cd_i}{1+Cd_i^2}\right)\varphi_i \qquad (4.8a)$$

$$\frac{G''_{red,polydisperse}}{\omega\eta_s} = \sum_{i=1}^{N} \frac{G''_{red,i}(Cd_i,\varphi_i)}{\omega\eta_s} = \sum_{i=1}^{N} \left(\frac{1}{1+Cd_i^2}\right)\varphi_i \qquad (4.8b)$$

where $Cd_i \equiv \lambda_i\omega$, with λ_i and φ_i representing the bubble relaxation time and volume fraction of the *i-th* bubble class, respectively.

Using Eq. 4.8, the theoretical G' and G''_{red} curves for the tested suspensions were derived. These curves are also reported in Fig. 4.2 (black and blue solid lines). As seen, these new curves are almost identical to those derived by modelling the polydisperse suspension as monodisperse with a bubble radius equal to the volume-weighted average radius of the bubble population. This is not unexpected, as one can prove that the theoretical predictions of the simpler Jeffreys model (i.e., Eq. 4.7 expressed in terms of $\langle Cd \rangle$) differ from those of the more refined one (i.e., that based on the summation of the G', G''_{red} contributions of each bubble size class) only if the

suspension bubble size distribution is bimodal, with equal volume fractions of very small and very large bubbles. In any other case, the two versions of the Jeffreys model yield nearly the same predictions. This is discussed in more detail in Sec. B5 of Appendix B.

Because the generalised Jeffreys model, which accounts for polydispersity more accurately, yields almost the same results as its simpler version (that for monodisperse suspensions), it can be concluded that polydispersity is not the root cause for the observed G' deviation at low $\langle Cd \rangle$ values. To investigate this behaviour further, the influence of artifacts potentially induced by the rheological measurements was considered. Specifically, due to their extended duration, SAOS tests can be susceptible to phenomena such as bubble rise, coalescence and, more broadly, changes in the suspension microstructure over time. These phenomena are examined in detail in the following sections.

4.3.2 Effect of bubble rise

To investigate the effect of bubble rise on the obtained G′ curves, the bubble rise velocity was first calculated, using the Hadamard–Rybczynski equation (Hadamard, 1911; Rybczynski, 1911):

$$u_{rise} = \frac{\langle R \rangle^2 \, \rho_s \, g}{3\eta_s} \tag{4.9}$$

where $\langle R \rangle$ is the volume-weighted average bubble radius, ρ_s and η_s are the density and viscosity of the ambient fluid, respectively, and g is the gravitational acceleration. This equation is accurate in the limit of a single bubble rising in a clear liquid. However, the presence of other bubbles and surfactants in a suspension has been shown to retard bubble rise (D. Kee' et al., 1990; Tzounakos et al., 2004), causing Eq. 4.9 to overestimate the rising velocity. It must be noted that while this equation provides the most conservative estimation of bubble rise during the experiments, its use also means that the computed rise velocities may be exaggerated, so that the actual effect of bubble rise may not be as pronounced as these predictions suggest for the experimental system under investigation. The calculated bubble rise velocities for all tested suspensions are presented in Table 4.3.

Table 4.3: Bubble rise velocity for different bubble volume fractions.

Bubble volume fraction (%)	u_{rise} (mm/min)	mm covered during 5 minutes of SAOS	mm covered during 35 minutes of SAOS
4.2	0.013	0.065	0.458
13.5	0.015	0.075	0.525
19.2	0.017	0.084	0.590

Based on the computed bubble rise velocities shown in Table 4.3, bubbles should have risen appreciably by the end of the SAOS measurements, which last about 35 minutes, covering a distance equal to nearly 45% of the rheometer gap. Even if these values are overestimated, they still indicate that the effect of bubble rise may become important towards the end of the SAOS tests. To investigate whether bubble rise is pronounced from the beginning of the SAOS measurements, the distance covered by the rising bubbles during the initial five minutes of the experiment was calculated. This timeframe corresponds to the frequency range 50-10 rad/s, after which the onset of the G' deviation was observed. For all the tested suspensions, this distance was found to be negligible, indicating that bubble rise cannot be responsible for causing the observed G' deviation at low $\langle Cd \rangle$ values.

To validate these calculations, a sample of a suspension with $\varphi = 10.4\%$ was placed on the rheometer plate, and after a 35-minute waiting period to allow the bubbles to rise freely, a SAOS test was initiated. For comparison, a normal SAOS measurement was also conducted on the same suspension without any waiting time. As shown in Fig. 4.4, the G' curves obtained from the two SAOS experiments almost overlap, with the complex G' trends being essentially the same regardless of bubble rise. This indicates that in the present experiments, bubble rise is not the cause for the characteristic G' deviation observed at low $\langle Cd \rangle$ values. Nevertheless, it could potentially amplify this deviation towards the end of the experiments by affecting the mean inter-bubble distance. This observation was confirmed via time sweep experiments and SAOS measurements performed by increasing and decreasing the oscillation frequency. The results of these experiments are presented in Sec. B6 of Appendix B.

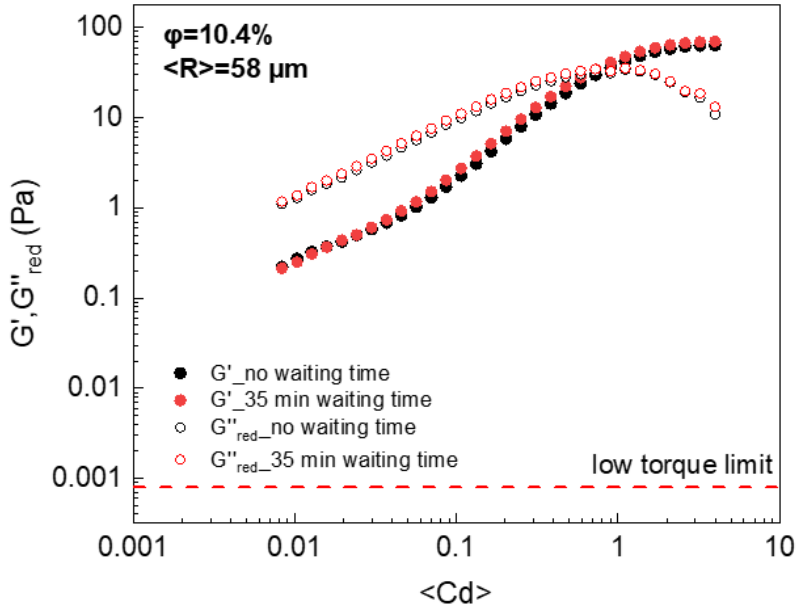

Figure 4.4: Effect of bubble rise on G' and G''_{red} of a polydisperse bubble suspensions with $\varphi = 10.4\%$.

Specifically, Fig. B.13a in Appendix B demonstrates that the G' deviation at lower $\langle Cd \rangle$ values is present even in SAOS measurements performed by ramping up the oscillation frequency, where the influence from bubble rise is minimal. When the measurements are performed inversely, more time elapses before recording the low $\langle Cd \rangle$ viscoelastic data. During this time, bubbles tend to rise, leading to a decrease in the average inter-bubble distance, which evidently amplifies the G' deviation. This observation suggests that there is a correlation between the deviation of G' and the average inter-bubble distance or, more broadly, the overall bubble spatial organisation in the tested samples.

It is worth noting that in dense colloidal suspensions, the presence of clusters has been shown to increase the bulk elasticity of the suspension as the particles come into close proximity and create a network structure (Conrad et al., 2006; Larsen et al., 2010; Whitaker et al., 2019). This network effectively stores elasticity, leading to increased resistance to deformation and larger G' values. Even though the presence of bubble clusters or threads may not result in a network as organised and robust as that in colloidal suspensions, it certainly alters the average inter-bubble distance, influencing the microstructure and, in turn, the rheology of the suspension. From Fig. B.13b in Appendix B, it is evident that bubbles are not uniformly distributed within the tested samples before the initiation of the SAOS measurements. This non-uniform bubble spatial distribution is most likely created upon loading the samples on the rheometer plate and affects the average inter-bubble distance, leading to the characteristic G' deviation at lower $\langle Cd \rangle$ values. This aspect is further investigated in Sec. 4.5.

4.4 Visualisation of bubbles under oscillatory shear

Having examined the effect of bubble rise during the SAOS measurements, the investigation then focused on whether the observed G' trends can be attributed to changes in the suspension microstructure over time. These changes can be related to the general bubble organisation and the bubble size. To this end, the bubble suspensions were visualised under oscillatory shear, and a statistical image analysis was performed. The results are discussed below.

4.4.1 Changes in bubble organisation over time

To examine whether the pre-existing spatial organisation of the bubbles right after the preshear changed significantly as a result of the SAOS measurement, the coverage parameter introduced in Sec. 3.5.2a was utilized. This parameter indicates the percentage of image covered with bubbles, with a reduction in coverage serving as a qualitative metric for bubble clustering and alignment, or more broadly, for changes in the microstructure of the dispersed phase.

To this end, an image analysis was conducted to determine the trend of coverage during a SAOS experiment. To minimize the amount of data, 15 representative images were analysed for each oscillation frequency. Each image was first converted into a black and white matrix, with the bubbles portrayed as white pixels on a black background. Then, all the white pixels were summed and divided by the total number of pixels in the image to obtain a characteristic value of coverage. For each frequency, a mean coverage value, $\bar{C}$, was determined by averaging the coverage values of the corresponding 15 images. Fig. 4.5a presents the mean coverage as a function of the average dynamic capillary number for the three reported bubble volume fractions. As seen, $\bar{C}$ remains constant for all the tested suspensions, suggesting that the general bubble organisation does not change significantly throughout the rheological measurements.

4.4.2 Bubble coalescence

To investigate potential bubble coalescence phenomena that would affect the suspension microstructure, the average bubble radius was evaluated during the rheological tests. To this end, the same images used to calculate the coverage were analysed to measure the bubble size distribution and the corresponding mean radius $\langle R \rangle$ during the oscillatory tests. For each oscillation frequency, an average value for $\langle R \rangle$, denoted as $\overline{\langle R \rangle}$, was obtained by averaging the $\langle R \rangle$ values of the 15 representative images. Fig. 4.5b illustrates how $\overline{\langle R \rangle}$ changed for the three reported bubble suspensions throughout the SAOS tests. As seen, the average bubble size slightly increases throughout the rheological experiments (these tests start at large $\langle Cd \rangle$ values

and then, in time, progress towards lower $\langle Cd \rangle$ values), reaching a maximum of 7% to 9% of the initial size. Therefore, based on the observed trend of coverage and the minimal increase in the average bubble size, it can be concluded that the suspension microstructure remains mostly stable during the rheological tests.

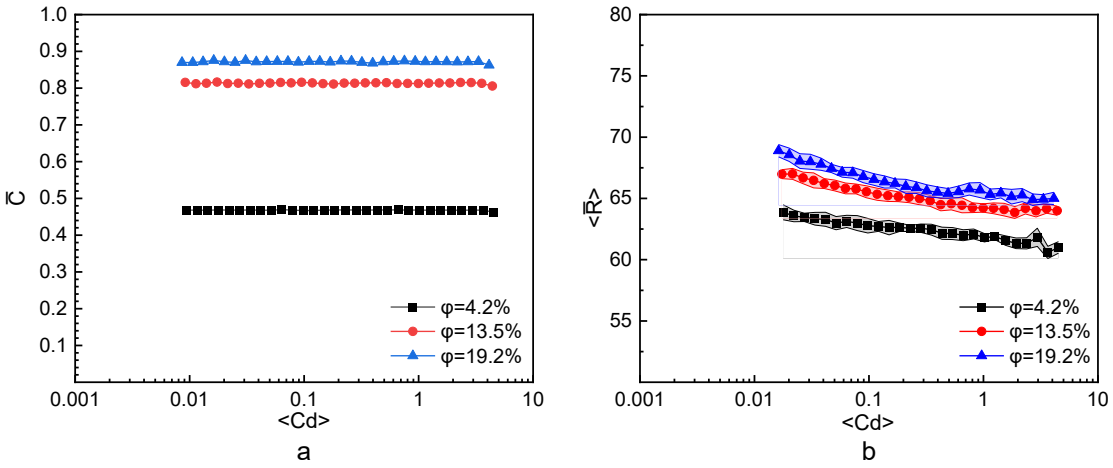

Figure 4.5: a) Coverage and b) mean volume-weighted average bubble radius as functions of $\langle Cd \rangle$ for $\varphi = 4.2\%$, $\varphi = 13.5\%$ and $\varphi = 19.2\%$.

The failure of the linear Jeffreys model, and of other models (e.g., Seo and Youn, 2005) previously used for dilute and semi-dilute bubble suspensions, to predict accurately the G' trends at low $\langle Cd \rangle$ values led to the investigation of other nonlinear phenomena, specifically bubble fluid dynamic interactions, that may affect the experimental data. As suggested by Joh et al. (2010), such interactions may induce phenomena with longer relaxation times, resulting in the characteristic G' deviation at low $\langle Cd \rangle$ values. Specifically, when bubbles are in close proximity or interact with each other, the fluid flow induced by the motion of one bubble can influence the motion and the behaviour of the neighbouring bubbles, leading to groups of bubbles behaving collectively.

In this context, interactions are influenced by two key factors: (i) the bubble volume fraction and (ii) the mean inter-bubble distance. In an idealised system, where bubbles can be considered perfectly distributed, these two parameters are directly related. But in the present experimental system, technical aspects, such as rheometer loading and subsequent pre-shear protocol, can change the average inter-bubble distance for a fixed bubble volume fraction. To investigate this, additional SAOS tests were conducted on the generated suspensions, using different pre-shearing conditions. Specifically, samples were pre-sheared for 33 minutes at 0.9 s^{-1}, and the corresponding SAOS results were then compared to those obtained after three minutes of pre-shearing at 0.1 s^{-1}. The aim was to determine whether a change in the bubble

spatial distribution, induced by longer pre-shear protocols, could mitigate the deviation from the theoretical predictions of G'. At this point, it must noted that the second pre-shearing protocol was found to be the maximum pre-shear that could be applied without causing any significant changes to the bubble size distribution and the total bubble volume fraction of the suspensions. The findings from this investigation are discussed below.

4.5 Bubble fluid dynamic interactions and effect of pre-shear

4.5.1 Rheological results

Following the method described in Sec. 4.3.1, the bubble size distribution at the end of the stronger and more prolonged pre-shearing stage was determined to confirm that the pre-shearing did not alter significantly the initial distribution. Image analysis showed that after 33 minutes of pre-shearing at 0.9 s^{-1}, the bubble radii shifted to slightly higher values, while still following a gamma type distribution (Fig. B.14 in the Appendix). Table 4.4 provides the updated volume-weighted average bubble radii for the reported suspensions. For each of them, the corresponding $\langle Cd \rangle$ value was also calculated. Fig. 4.6 compares the G' and G''_{red} curves of the reported bubble suspensions, obtained after three minutes of pre-shearing at 0.1 s^{-1} and after 33 minutes of pre-shearing at 0.9 s^{-1}.

Table 4.4: Volume-weighted average bubble radius $\langle R \rangle$ for different pre-shearing conditions.

Bubble volume fraction (%)	$\langle R \rangle$ computed through the microscope images (μm)	$\langle R \rangle$ after 3 minutes of pre-shear at 0.1 s^{-1} (μm)	$\langle R \rangle$ after 33 minutes of pre-shear at 0.9 s^{-1} (μm)	% increase of $\langle R \rangle$
4.2	61	61	66	8.2
13.5	64	64	69	7.8
19.2	65	65	72	10.8

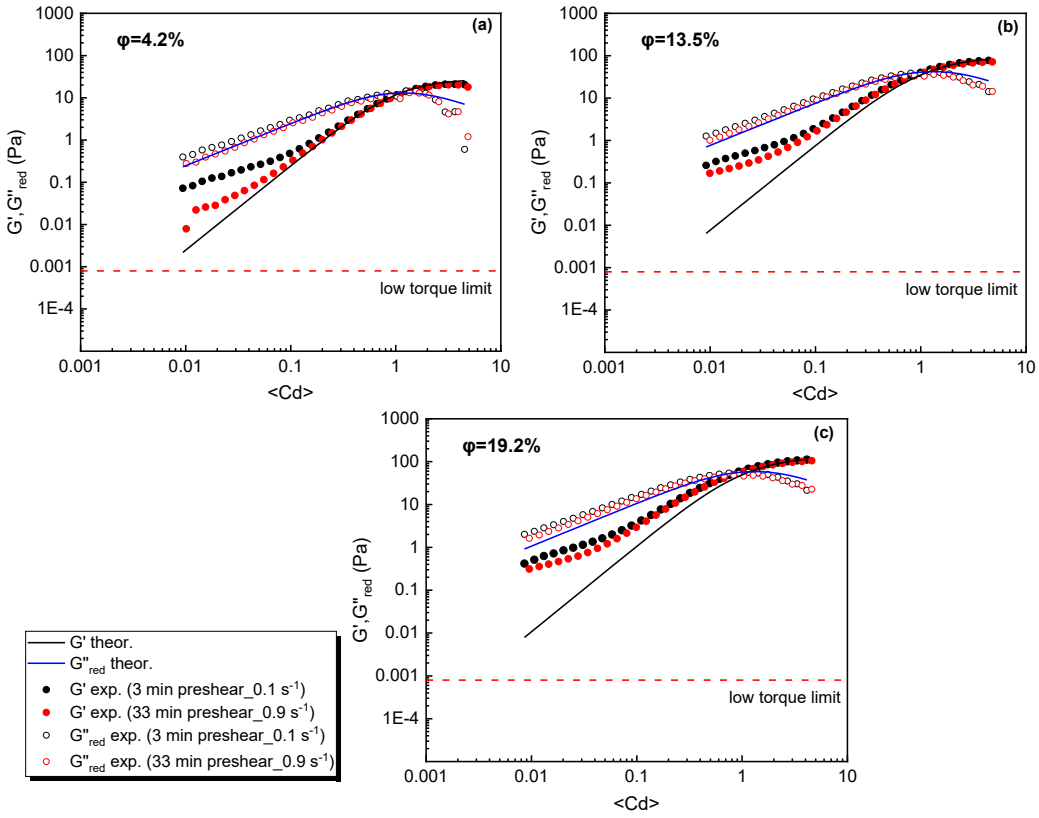

Figure 4.6: Effect of the pre-shearing conditions on G' and G''_{red} of polydisperse bubble suspensions with (a) $\varphi_1 = 4.2\%$, (b) $\varphi_2 = 13.5\%$ and (c) $\varphi_3 = 19.2\%$.

As shown, pre-shearing affects the resulting G' curves only for low bubble volume fraction. For $\varphi = 4.2\%$, stronger and more prolonged pre-shearing leads to G' values closer to the theoretical ones, suggesting a more uniform redistribution of the bubbles, and therefore weaker fluid dynamic interactions among them. There is still a deviation between the experimental and theoretical values for average dynamic capillary numbers lower than 0.1, likely due to bubble rise during the SAOS tests, which directly impacts the average inter-bubble distance and, in turn, the bubble interactions. As the bubble volume fraction increases, the experimental G' curves are almost insensitive to the applied pre-shearing conditions, suggesting that pre-shearing affects the mean inter-bubble distance negligibly when the suspensions are denser. The reported results indicate no significant bubble rise during the longer pre-shearing stage. This is supported by both the rheological and optical findings, which revealed no significant differences in the high frequency plateau of G', and in the bubble size distributions obtained just after the pre-shearing (see Fig. B.14 in Appendix B), respectively.

4.5.2 Local spatial distribution of bubbles

To quantify the fluid dynamic interactions among bubbles due to their local spatial distribution, a statistical image analysis was performed using the method described by

(Kudrolli, Wolpert and Gollub, 1997). In brief, for each of the reported bubble suspensions, an image obtained after the end of the pre-shearing stage was analysed, considering both pre-shearing conditions. Each image was divided into 64 equal squares, and the number of bubbles in each square was identified using MATLAB. The distribution function for the local bubble number (n), i.e., the probability of having a certain number of bubbles in a cell, was then determined. This method allows evaluating bubble interactions based on the assumption that a smaller number of bubbles in a given area indicates a larger average inter-bubble distance and thus weaker fluid dynamic bubble interactions. Fig. 4.7 presents the probability distribution of the local bubble number for the tested bubble volume fractions and pre-shearing conditions. If the bubble suspensions were monodisperse and uniformly distributed, each cell would contain the same number of bubbles, and the probability function would be a narrow peak centered over this specific value of n. However, in this case where the tested suspensions are polydisperse and the bubbles are not uniformly distributed, a wider distribution of local bubble numbers is obtained.

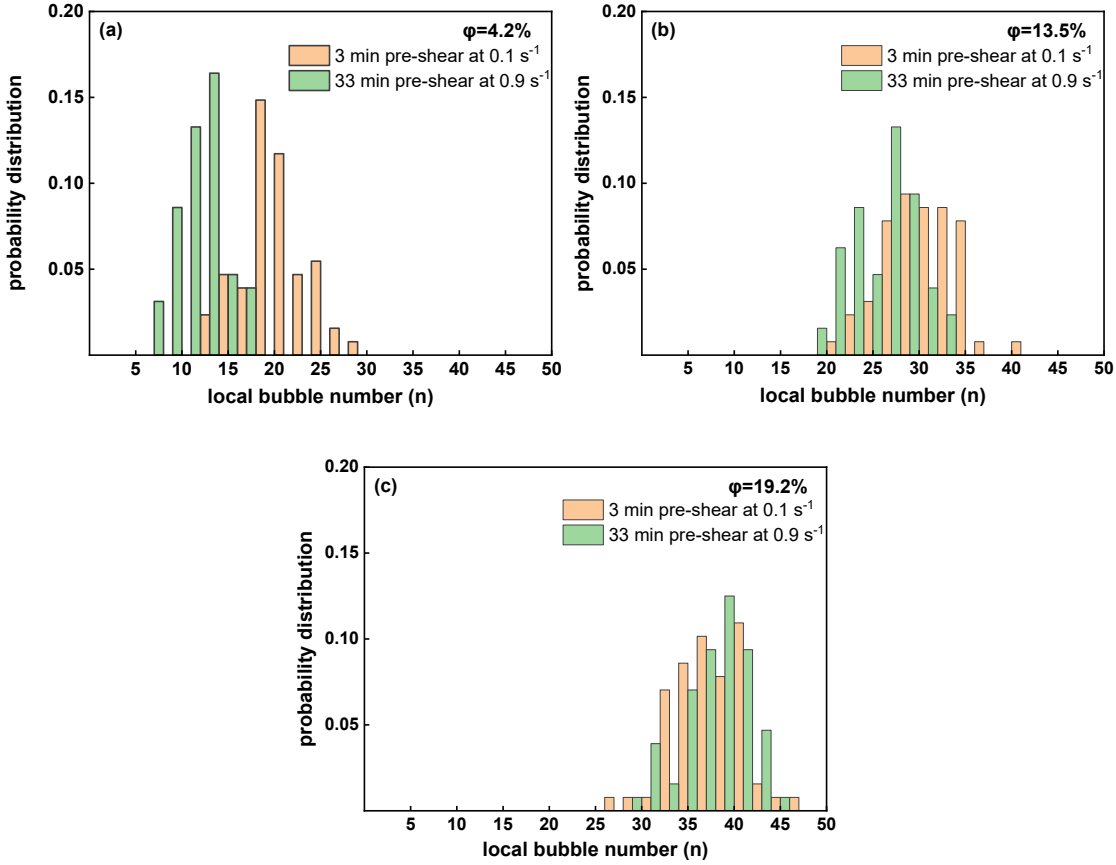

Figure 4.7: Probability distribution of the local bubble number for polydisperse bubble suspensions with (a) $\varphi_1 = 4.2\%$, (b) $\varphi_2 = 13.5\%$ and (c) $\varphi_3 = 19.2\%$.

Comparing between the two different pre-shearing conditions reveals that for the lowest bubble volume fraction, stronger and more prolonged pre-shearing results in narrower local bubble number distributions, which are also shifted towards lower values, meaning that the average inter-bubble distance decreases, resulting in weaker fluid dynamic interactions among the bubbles. However, as the bubble volume fraction increases, the two distributions almost overlap, confirming the rheological measurements of Sec. 4.5.1 and suggesting that in denser suspensions pre-shearing does not reduce the bubble interactions significantly.

It is important to note that for all tested volume fractions, the bubble size distribution, as opposed to the local bubble spatial distribution, is not altered by pre-shearing (as reported in Fig. B.14 in Appendix B), thus indicating that the shift observed in Fig. 4.7(a) can be solely associated to the more effective bubble re-distribution.

4.6 Fitting a multi-mode Jeffreys model

As the rheological measurements indicate, there is an unexpected increase in the suspension elastic modulus at low $\langle Cd \rangle$ values. Based on the statistical image analysis, during the SAOS experiments the microstructure of the suspension remains mostly stable. Therefore, the G' increase is mainly attributed to bubble fluid dynamic interactions caused by the initial spatial distribution of the bubbles after the loading of the samples on the rheometer plate. As shown, these interactions are closely related to the bubble volume fraction and the applied pre-shearing conditions. When the suspension is subjected to high oscillation frequencies, the characteristic flow time is very small; thus, the measured viscoelastic moduli capture the response of the smallest length scale of the suspension microstructure, namely that of an individual bubble. This explains the good agreement between the real and the theoretical values at higher $\langle Cd \rangle$, where the generalised Jeffreys model predicts the viscoelasticity arising solely from the bubble interfaces accurately. As the oscillation frequency decreases, the characteristic flow time increases, enabling more complex relaxation phenomena associated with bubble fluid dynamic interactions. These interactions manifest as an increase in suspension elasticity, with the measured G' reflecting the response of bubbles that behave collectively owing to their proximity and mutual influence.

As previously discussed, the Jeffreys model, as well as the models of Llewellyn et al. (2002a) and Seo and Youn (2005), does not account for bubble fluid dynamic interactions, thus failing to predict the G' deviation at low $\langle Cd \rangle$ values. To address this limitation, a model developed by (Palierne, 1990) was considered, which is designed to describe the rheology of

dilute and semi-dilute emulsions consisting of viscoelastic and Newtonian fluids. This model accounts for droplet fluid dynamic interactions by assuming that the local strain exerted on a single droplet is modified by the deformation of the surrounding droplets, and that the interactions between droplets are of a dipole kind. For emulsions formed by two viscoelastic fluids, the model predicts a G' profile with a double shoulder. This profile typically exhibits a relaxation mode associated with the relaxation of the viscoelastic matrix at high oscillation frequencies and a secondary relaxation mode associated with droplet interface relaxation at low oscillation frequencies.

While the G' profiles observed in this study also present multiple relaxation modes, a fundamental difference must be noted: the suspensions under study consist of two Newtonian fluids, i.e., air as dispersed phase and a mixture of mineral oil and span 80 as the ambient fluid. These fluids relax instantly, unlike for emulsions of two viscoelastic fluids. Therefore, in these systems, the relaxation mode at high oscillation frequencies cannot be attributed to the relaxation of the ambient fluid. To confirm this, the predictions of the Palierne and Jeffreys models are compared with the experimental data in Sec. B8 of Appendix B. As shown, the G' trend predicted by the Palierne model qualitatively resembles that of the Jeffreys model, both featuring only one characteristic relaxation time. This is not surprising, given that the literature ((Graebling, Muller and Palierne, 1993; Lacroix, Aressy and Carreau, 1997)) widely acknowledges the similarity between the two models for emulsions of Newtonian fluids. Similar to the Jeffreys model, the Palierne model fails to predict the second G' shoulder at low $\langle Cd \rangle$ values. In addition, it does not capture the high $\langle Cd \rangle$ plateau as accurately as the Jeffreys model. These shortcomings likely stem from the assumptions of the Palierne model about the type of droplet interactions. Specifically, the model assumes that the interactions are of a fluid dynamic dipole nature and that, within the interaction range, droplets are uniformly dispersed. Palierne (1990), along with subsequent relevant studies (Bousmina and Muller, 1993; Carreau et al., 1994) clearly acknowledges that the model fails to accurately predict experimental results for systems where the aforementioned assumptions are not met.

The interactions responsible for the observed G' deviation in the tested suspensions differ from those considered by the Palierne model. As evidenced by the rheo-optical experiments, bubbles are locally distributed non-uniformly within the tested samples. Consequently, in some regions of the sample, bubbles are closer than they would be if they were uniformly distributed, making their local interactions stronger and causing them to behave and relax collectively. Similar observations were reported by Bousmina and Muller (1993) and by Carreau et al.

(1994), who also noted the failure of the Palierne to predict the low frequency G' shoulder, which they attributed to interactions caused by the presence of aggregates in their systems. Despite the absence of a model that well describes the current experimental data at low $\langle Cd \rangle$ values, the rheo-optical experiments indicate a non-uniform spatial distribution of bubbles within the ambient fluid. Drawing from existing literature and having excluded experimental artifacts related to the performed rheological measurements, it can be inferred that these higher-order interaction phenomena lead to the longer relaxation times observed in the present experiments. To validate this argument and quantify the complex relaxation phenomena arising from the bubble interactions, a multi-mode Jeffreys model was fitted to the experimentally determined values of G' and G''_{red}. The effect of the bubble volume fraction and the applied pre-shearing conditions on the suspension relaxation modes was then examined.

The fitting was performed using the Curve Fitting App of MATLAB. Initially, Eq. 4.8a was fitted to the experimental G' values, using the relaxation times λ_i and the volume fractions φ_i as fitting parameters. In all cases, the fitting process began with a single-mode Jeffreys model, and modes were progressively added until the best fit was achieved. The maximum number of relaxation modes was determined through a simple convergence analysis, assessing whether the addition of an extra relaxation mode resulted in a noticeable reduction is the sum of squared errors (SSE). The determined λ_i and φ_i values were then substituted in Eq. 4.8b to obtain the corresponding G''_{red} curve. Table 4.5 presents the values of the fitting parameters for the various bubble volume fractions and pre-shearing conditions, along with the corresponding R^2 value for each fit.

Table 4.5: Fitting parameters for different bubble volume fractions and pre-shearing conditions.

	3 minutes pre-shearing at 0.1 s^{-1}					**33 minutes pre-shearing at 0.9 s^{-1}**				
Bubble volume fraction (%)	**λ_i (s)**	**φ_i (%)**	**$\varphi_i / \sum \varphi_i$ (%)**	**$\lambda_{single\ bubble}$ (s)**	**R^2**	**λ_i (s)**	**φ_i (%)**	**$\varphi_i / \sum \varphi_i$ (%)**	**$\lambda_{single\ bubble}$ (s)**	**R^2**
4.2	0.093	3.9	55.7	0.090	0.999	0.103	4.0	89.3	0.097	0.995
	2.222	0.8	11.9			6.151	0.5	10.7		
	13.270	2.3	32.4			-	-	-		
		$\Sigma\varphi_i$=7.0					$\Sigma\varphi_i$=4.5			
13.5	0.089	13.5	49.1	0.088	0.999	0.095	12.9	51.4	0.096	0.999
	0.518	3.2	11.5			0.420	3.6	14.3		
	3.782	2.4	8.7			2.818	1.0	3.9		
	15.100	8.5	30.7			25.925	7.6	30.4		
		$\Sigma\varphi_i$=27.6					$\Sigma\varphi_i$=25.1			
19.2	0.081	17.7	38.4	0.083	0.999	0.088	16.9	38.5	0.092	0.995
	0.326	9.2	19.9			0.319	10.5	23.8		
	1.140	1.1	2.5			1.200	0.6	1.3		
	7.975	10.5	22.9			11.975	4.6	10.6		
	15.950	7.6	16.4			25.750	11.3	25.9		
		$\Sigma\varphi_i$=46.1					$\Sigma\varphi_i$=43.9			

As can be observed, the smallest relaxation time was very similar in all cases, closely matching the relaxation time of an individual bubble, as given inthe Jeffreys model (Eq. 2.41), and calculated using the volume-weighted mean bubble radius of each suspension. This finding supports the argument that at higher oscillation frequencies and, in turn, shorter characteristic flow times, SAOS experiments effectively capture the relaxation of a single bubble. The number of relaxation modes increases with the bubble volume fraction, suggesting that bubble interactions, and consequently complex relaxation phenomena, are more pronounced in denser suspensions. This complements the rheological measurements, which revealed that the onset of the G' deviation starts at higher $\langle Cd \rangle$ values for larger bubble volume fractions.

It worth mentioning that the relaxation time given by the Jeffreys model (i.e., $\lambda \equiv \eta_s R/\sigma$) refers to the case of a solitary bubble relaxing independently. In such a scenario, the bubble relaxes to its original undeformed state without the influence of neighbouring bubbles. In the case of emulsions, it has been shown that the presence of neighbouring droplets can influence the shape relaxation process of a single droplet. To further investigate the effect of bubble shape relaxation on the obtained G' trends, the bubble shape relaxation time in the tested suspensions was calculated using the Palierne expression ((Graebling, Muller and Palierne, 1993)), which considers the effect of on the shape relaxation of the single droplet. This expression is a modification of the Jeffreys relaxation time, incorporating a function of the bubble volume fraction. The equation and the calculated bubble shape relaxation times are reported in Sec. B9 of Appendix B. The bubble shape relaxation times were found to be close to the relaxation times given by the Jeffreys model. In fact, comparing the shape relaxation times with the fitting results reported in Table 4.5 shows that they fall between the first and second relaxation times computed through fitting for all tested suspensions. However, the fitting results revealed the presence of additional relaxation times which are at least an order of magnitude larger compared to the computed bubble shape relaxation times. This suggests that even though the relaxation mode associated with the shape relaxation of the bubbles can be influenced by crowding effects, it cannot be considered responsible for the characteristic G' deviation at lower $\langle Cd \rangle$ values, which is clearly associated with longer relaxation times.

It is important to note that the sum of the φ_i values obtained from fitting does not always match the measured total bubble volume fraction of the suspension. This is reasonable considering that, to study the intricate behaviour of the bubble suspensions, an idealized bubble suspension was used. Fig. 4.8 provides a schematic of this idealization. As shown in the

schematic, the tested suspensions are not uniformly distributed the moment the SAOS measurements begin. Due to their spatial distribution, some bubbles are in close proximity, behaving collectively as one group. When fitting the predictions of the model to the experimental results, it was assumed that each group of bubbles behaves like a single bubble with a radius equivalent to an effective (interaction) radius. In this context, it is expected that the sum of the φ_i values computed via fitting may exceed the actual bubble volume fraction of the tested suspension – especially in denser suspensions, where interactions become more pronounced.

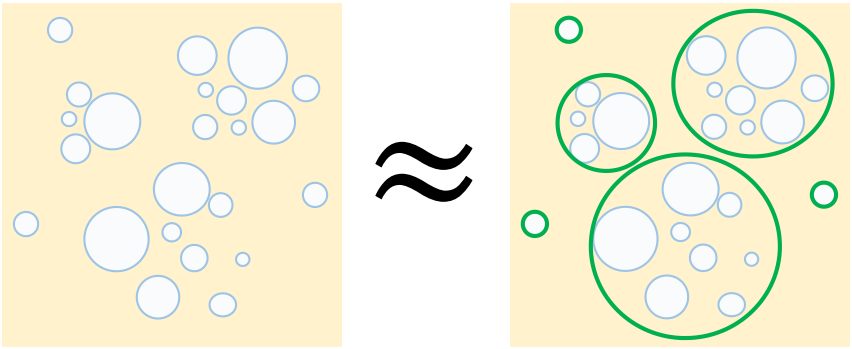

Figure 4.8: Schematic depicting the range of bubble fluid dynamic interactions, as emulated when fitting our experimental G', G''_{red} data using a multi-mode Jeffreys model.

Nevertheless, in the case of the most dilute suspension ($\varphi_1 = 4.2\%$) subjected to stronger and more prolonged pre-shearing, the sum of the φ_i values aligned closely with the bubble volume fraction obtained experimentally. This suggests that the applied pre-shear effectively redistributed the bubbles, causing the range of bubble fluid dynamic interactions to coincide with the volume-weighted radius of a single bubble. In this case, the interactions among bubbles were negligible, causing most bubbles to behave individually, without being influenced by the neighbouring bubbles. This is confirmed by the decrease in the number of relaxation modes and the increase in the relative bubble volume fraction associated with the shortest relaxation time. However, as the overall bubble volume fraction increased, the applied pre-shearing conditions did not alter the number and the characteristics of the relaxation modes significantly. This aligns with the rheological measurements and image analysis results reported earlier, suggesting that in denser suspensions pre-shearing impacts negligibly the bubble fluid dynamic interactions and the associated complex relaxation phenomena.

It is worth mentioning that, in the current study, the effect of bubble fluid dynamic interactions is noticeable due to the applied flow field. In the steady-shear experiments presented in Chapter 3, the Taylor (1932) equation for the zero-shear viscosity was successfully

recovered, a result that indicates that bubble interactions were not appreciable. However, in SAOS experiments, designed to probe the suspension microstructure, interactions, even if mild, become relevant, because they affect the relaxation process of the suspension and, consequently, the observed viscoelastic trends. Additionally, the experiments presented in Chapter 3 involved bubble volume fractions up to 10.4%, while in this study, the range was extended to 19.2%. Although both studies examine semi-dilute suspensions, the current work involves a significantly higher bubble volume fraction, which is expected to cause more pronounced bubble fluid dynamic interactions.

4.7 Conclusions

This study explored the linear viscoelastic behaviour of semi-dilute polydisperse bubble suspensions with a Newtonian ambient fluid. To determine the suspensions viscoelastic moduli, G' and G''_{red}, SAOS rheological tests were performed with a pre-shear stage of three minutes at 0.1 s^{-1}. The experimental G' curves were compared with the theoretical predictions of the original Jeffreys model, showing good agreement for $\langle Cd \rangle$ values larger than unity. But for lower $\langle Cd \rangle$ values, the measured G' was larger than expected, this deviation occurring earlier in more concentrated suspensions. To elucidate this behaviour, various potential contributing factors were systematically investigated, including polydispersity, bubble rise, coalescence and changes in suspension microstructure over time.

The investigation revealed that, for the suspensions studied, the predictions of the generalised Jeffreys model accounting for polydispersity and of the simple Jeffreys model for monodisperse suspensions (used for bubbles with radius equal to the volume-weighted mean bubble radius of the suspension) yield essentially the same results. This indicates that polydispersity in itself is not the reason for the observed deviation between the experimental results and the model predictions.

As the observed trends could not be attributed to polydispersity, the effects of microstructure were examined to determine whether significant changes occurred over time due to artifacts related to the performed rheological measurements. To this end, the generated bubble suspensions were visualised under linear oscillatory shear, and a statistical image analysis was performed to examine the effects of bubble rise, coalescence and spatial organisation. The findings indicated that in general the suspension microstructure was preserved during the SAOS measurements, suggesting that the observed viscoelastic trends were not the result of experimental artifacts.

The failure of the Jeffreys model to accurately predict the G' trends at low $\langle Cd \rangle$ values led to further exploration of the impact of bubble fluid dynamic interactions on the experimental data. These interactions appear to be induced by the initial spatial arrangement of the bubbles on the plate of the rheometer, present before the initiation of the SAOS measurements, and lead to complex relaxation phenomena, which become evident at longer characteristic flow times. To see whether a variation in the bubble spatial distribution, induced by longer pre-shearing protocols, could mitigate the deviation from the theoretical predictions of G', additional SAOS experiments were conducted with a pre-shear stage of 33 minutes at 0.9 s^{-1}. The results indicated that, for dilute bubble suspensions, stronger and more prolonged pre-shearing led to G' values closer to the theoretical predictions. But as the bubble volume fraction increased, the applied pre-shearing conditions had no significant impact on the experimental G' values.

To validate this, a multi-mode Jeffreys model was fitted to the viscoelastic moduli obtained experimentally. In line with the rheological measurements and the image analysis results, the findings demonstrated that bubble interactions cause a complex relaxation process, consisting of multiple relaxation modes. The number of relaxation modes increased with the bubble volume fraction, indicating that the effect of bubble interactions amplifies in denser suspensions. Finally, the results overall suggest that stronger and prolonged pre-shearing can effectively reduce the fluid dynamic interactions among bubbles when the bubble volume fraction is low. But as the bubble volume fraction increases and the bubble fluid dynamic interactions start dominating, pre-shearing does not impact the local bubble spatial distribution significantly, leading to the same G' trends independently of the applied pre-shearing conditions.

Chapter 5

Steady-shear viscosity of bubble suspensions in shear-thinning Carbopol matrices: investigating the effects of bubble-matrix interplay

Building on the findings from Chapters 2 and 3 regarding bubble suspensions in Newtonian media, the final phase of this research investigated the influence of bubbles in more intricate matrices typically used in oral care formulations. The study focused on the steady shear viscosity of bubble suspensions in two shear-thinning matrices with no appreciable normal stress differences: (i) a Carbopol dispersion, and (ii) a Carbopol dispersion with added surfactant, Sodium Dodecyl Sulphate (SDS). The composition of the matrices was carefully designed to allow for an ideal soft colloid system with negligible interactions between Carbopol microgels. Moreover, the addition of a strong anionic surfactant such as SDS aimed to systematically increase matrix complexity by altering the extent of microgel swelling and modifying the system's interfacial properties, thereby influencing the overall microstructure and, consequently, the rheological behaviour of the generated bubble suspensions. The steady-shear rheological results showed that the presence of bubbles enhanced the shear-thinning behaviour in both matrices. In bubble suspensions with the pure Carbopol matrix, the flow curves exhibited the characteristic double viscosity decay observed in suspensions with Newtonian ambient fluids but shifted to lower average Capillary number values ($< Ca >$). Additionally, the zero-shear viscosity of these suspensions deviated significantly from the predictions of the Taylor equation but aligned well with the Mooney equation when considering the combined volume fraction of Carbopol microgels and bubbles. This suggests that crowding effects and interactions between the two dispersed phases played a key role in suspension behaviour. Rheo-optical experiments revealed significant bubble coalescence, followed by the alignment and clustering of the coalesced bubbles. This clustering was potentially driven by wall effects arising from the significant increase in bubble size, to the extent that confinement effects within the rheometer gap became observable.

Bubble suspensions in the SDS-containing Carbopol matrix exhibited distinct rheological trends. Instead of a double viscosity decay, a single decay was observed over a range of $< Ca >$ values between 0.01 and 1. Rheo-optical experiments confirmed that SDS effectively

mitigated bubble coalescence. Additionally, shear-induced bubble clustering and alignment phenomena were less pronounced compared to those observed in the suspensions with the Newtonian ambient fluid discussed in Chapter 3, most likely due to electrostatic repulsions introduced by SDS.

The findings of this chapter highlight how variations in the matrix composition influence suspension microstructure under shear and, consequently, the rheological behaviour of these systems. The study provides insights into the complex interplay between bubbles and shear-thinning matrices, laying the groundwork for further research in this area.

5.1 Introduction

As demonstrated in Chapters 3 and 4, the presence of bubbles can significantly influence the rheology of the surrounding fluid. Microstructural changes, such as shear-induced bubble clustering and alignment, as well as bubble-fluid dynamic interactions influenced by the spatial distribution of bubbles, can lead to shear-thinning and other viscoelastic phenomena even in Newtonian matrices. These effects are expected to become even more intricate when the matrix itself exhibits non-Newtonian behaviour. While non-Newtonian fluids are prevalent both in nature and across different industries, the rheology of bubble suspensions in non-Newtonian matrices remains relatively unexplored (Torres et al., 2013, 2015; Kogan et al., 2013; Ducloué et al., 2015). Given the vast diversity of non-Newtonian matrices, this chapter focuses specifically on the steady-shear rheology of bubble suspensions with shear-thinning inelastic ambient fluids, specifically Carbopol solutions.

The choice of a Carbopol solution as ambient fluid is based on its widespread industrial use in various formulations across personal care and pharmaceutical industries (Boulmedarat et al., 2003; Bonacucina et al., 2004), including oral care formulations such as those detailed in Chapter 1. Carbomers, commercially known as Carbopol, are high molecular weight polymeric molecules of polyacrylic acid crosslinked with polyalkenyl ethers or divinyl glycol (Lefrançois et al., 2015). These molecules swell when dispersed in an appropriate solvent creating a microgel suspension, i.e., a suspension consisting of soft elastic particles (Migliozzi et al., 2020). The swelling mechanism of Carbopol depends on the solvent. In aqueous solutions, swelling is driven by the ionisation of carboxyl groups on the polymer backbone, which induces electrostatic repulsion between polymer chains and creates an osmotic pressure gradient, leading to solvent uptake and particle expansion (Carnali and Naser, 1992). In contrast, non-aqueous solvents promote swelling through solvent-polymer interactions rather than

electrostatic effects. Here, the solvent molecules penetrate the polymer network based on their size and affinity with the Carbopol structure, thereby enabling expansion. However, overall swelling remains significantly lower than in water due to the absence of strong ionic repulsions (Migliozzi et al., 2020).

The rheology of both aqueous (Piau, 2007; Bhattacharjee et al., 2018) and non-aqueous (Migliozzi et al., 2020) Carbopol solutions has been extensively studied, mapping their behaviour from dilute to highly concentrated conditions. In brief, in aqueous media, Carbopol microgels in the concentrated regime exhibit a typical soft glass behaviour that can be effectively described by the Herschel–Bulkley model (Piau, 2007; Jofore et al., 2015). For non-aqueous Carbopol suspensions, swelling behaviour and rheological properties depend significantly on the solvent. Migliozzi et al. (2020) investigated the effect of polar solvents—specifically glycerol, polyethylene glycol (PEG), and their combination—on Carbopol swelling and subsequent rheological behaviour. Their findings indicate that the final swollen state of Carbopol is solvent-dependent, with PEG leading to a nearly 50% reduction in swelling compared to glycerol, thereby shifting the jamming transition to higher polymer concentrations. Despite this variation in swelling, once jamming is reached, elastic and yielding behaviours scale similarly with particle volume fraction, suggesting that the solvent primarily affects the final volume of the single Carbopol particles rather than the interactions among them. At low concentrations (<0.8% wt), Carbopol dispersions exhibit purely shear-thinning, inelastic behaviour which can be effectively described using the Carreau – Yasuda constitutive equation. These findings are important to the present work, as they provide a comprehensive characterisation of the Carbopol matrix rheology, which evidently becomes more complex as the Carbopol concentration increases. For this study, dilute Carbopol dispersions will be used aligning with the focus on shear-thinning inelastic matrices.

The interplay between bubbles and shear thinning matrices has been a subject of interest in the literature, particularly in buoyancy-driven bubbly flows. Several studies have explored the rise of a single bubble or a swarm of bubbles in shear-thinning matrices (Vélez-Cordero and Zenit, 2011; Zenit and Feng, 2018; Chen et al., 2022), offering valuable insights into bubble dynamics in such fluids. Vélez-Cordero and Zenit (2011) investigated the rise of bubbles in shear-thinning, inelastic solutions of xanthan gum, finding that bubbles in shear-thinning media tend to form large aggregates as they rise, unlike in Newtonian fluids. This was attributed to the nature of the fluid, which leads to a decrease in viscosity in the wake region of a leading bubble, facilitating the acceleration of trailing bubbles and resulting in the formation of

ascending bubble clusters. Similar clustering phenomena were also reported by Chen et al. (2022) for bubbles rising in shear-thinning, viscoelastic fluids. According to them, in viscoelastic fluids, normal stress differences are also pivotal in the formation of bubble clusters during rising, as they modify the pressure distribution at the bubble surface causing bubbles to attract and form clusters. Although buoyancy-driven flows differ significantly from the steady-shear flows studied in this chapter, these findings highlight the strong influence of shear-thinning ambient fluids on the flow behaviour of bubbles, inducing clustering and microstructural changes that are known to affect suspension viscosity.

To the best of our knowledge, the steady shear rheology of bubble suspensions with shear-thinning ambient fluids remains largely unexplored, with the studies of Torres et al. (2013, 2015) being the most relevant. In their first study, the authors examined the steady-shear rheology of semi-dilute and concentrated bubble suspensions in shear-thinning, elastic guar gum solutions both with and without surfactant and compared their behaviour to bubble suspensions with a Newtonian ambient fluid. The study demonstrated that the presence of bubbles enhanced the shear-thinning behaviour and the normal stress differences of the ambient fluid, making them more pronounced compared to its unaerated state. Furthermore, when plotting the relative viscosity of the bubble suspensions with the guar gum matrix (with and without surfactant) as a function of the Capillary number (Ca), the onset of the shear-thinning behaviour was observed at Ca values in the range 0.01- 0.1, an order of magnitude lower than what is typically observed for bubble suspensions in Newtonian ambient fluids. Since the relative viscosity was calculated by dividing the measured viscosity for the suspension with that of the shear-thinning ambient fluid at each tested shear rate, the obtained flow curve reflected solely phenomena associated with the bubbles. Thus, the earlier onset of shear-thinning could not be attributed to the shear-thinning behaviour of the matrix itself.

Instead, the authors speculated that this behaviour was due to the presence of significant normal stress differences in the guar gum solutions, which may have led to bubble deformation and shear-thinning behaviour occurring at lower shear rates and, consequently, lower Ca values compared to Newtonian matrices. However, this speculation was not further investigated or proved in their study. At this point, it is important to note that the suspensions examined in this study were subjected to high shear rates (up to 300 s^{-1}) and images of the samples taken at the end of the tests revealed significant changes in bubble volume fraction and size distribution. Such alterations in microstructure during rheological measurements could influence the observed trends, an aspect that was not fully addressed in the study.

In their following study, Torres et al. (2015) extended their observations to other shear-thinning fluids and aimed to model the behaviour of bubble suspensions within these matrices. Specifically, they prepared and characterised the steady-shear rheology of bubble suspensions in a κ/ι-hybrid carrageenan gum solution with bubble volume fractions ranging between 5% and 25%. They observed a similar rheological behaviour to that in the guar gum solution, with bubbles enhancing the non-Newtonian behaviour of the matrix and shear-thinning starting earlier compared to bubble suspensions with Newtonian ambient fluids. The authors proposed that the viscoelastic behaviour of both the ambient fluid and the bubble suspensions could be accurately modelled using a single-mode Giesekus model, as discussed in more detail in Chapter 2 (Eq. 2.59).

The study also yielded valuable insights into the zero-shear viscosity of bubble suspensions with shear-thinning matrices. For suspensions with bubble volume fraction up to 15%, the relative zero-shear viscosities exhibited a linear dependence on bubble volume faction, described by a modified Taylor equation:

$$\eta_{r,0} = 1 + b\varphi \quad \text{with} \quad b = 1.5 \tag{5.1}$$

where b is a fitting parameter derived from experimental data. For suspensions with higher bubble volume fractions, the authors found good agreement between their experimental zero-shear viscosity data and the predictions of the Choi and Schowalter (1975) model for emulsions, adjusted for a viscosity ratio equal to 0 (Eq. 5.2). The Choi and Schowalter model was developed to describe the zero-shear viscosity of non-dilute emulsions and accounts for hydrodynamic interactions among droplets, as reflected by the presence of higher-order φ terms. In the limit of $\varphi \to 0$, corresponding to vanishingly small droplet volume fractions, the Choi and Schowalter model reduces to the classic Taylor equation.

$$\eta_{r,0} = 1 + I(\varphi)\varphi \tag{5.2a}$$

$$I(\varphi) = \frac{2+5\varphi^{7/3}}{2-5\varphi+21\varphi^{\frac{5}{3}}+5\varphi^{7/3}-2\varphi^{10/3}} \tag{5.2b}$$

Pal (2024) further highlighted the crucial role of matrix rheology in determining the rheological behaviour of bubble suspensions and emulsions. Specifically, for semi-dilute and concentrated emulsions with Carbopol matrices, the author suggested that microgels can induce droplet bridging, leading to higher zero-shear viscosity and shear-thinning behaviour as the flocculated droplet structure breaks down under shear. Given the rheological similarities

between bubble suspensions and emulsions, it is worth investigating whether—and what type of—clustering phenomena occur in bubble suspensions with Carbopol solutions as ambient fluids, and how these may affect the resulting rheological trends. To this end, this chapter examines the steady-shear viscosity of dilute bubble suspensions in Carbopol matrices, investigating how bubble-matrix interplay affects the rheological behaviour of these systems. Through steady-shear rheological tests and rheo-optical visualisation, this study aims to provide experimental data to address the gap in the literature regarding bubble suspensions with shear-thinning matrices, thereby offering insights for the formulation and processing of complex multiphase systems like toothpaste.

5.2 Experimental Methods

5.2.1. Materials and sample preparation

A shear-thinning polymeric dispersion was prepared using powdered Carbopol 974P NF (C974P NF, Lubrizol Limited) at a 0.5% wt concentration in a 30/70 wt mixture of polyethylene glycol (PEG400, MW=400 g/mol, Sigma-Aldrich, UK) and glycerol (MW=92 g/mol, Sigma-Aldrich, UK). The preparation followed the method described by Migliozzi et al. (2020). Initially, Carbopol was dispersed in PEG400 at 20 °C using a high-shear mixer (Silverson, L5 Series) and operating at 7000 rpm for approximately five minutes. The resulting concentrated stock solution was then diluted with glycerol to reach the desired 30/70 wt PEG400/glycerol composition. After dilution, the solutions were gently mixed with a magnetic stirrer until fully homogenised and placed in a heated ultrasonic bath (SciQuip Ultrasonic bath, heated, 150 W) at 50 °C overnight. This Carbopol dispersion served as the base matrix for generating bubble suspensions, using the aeration device detailed in Section 3.3. The bubble volume fraction and size distribution of the produced suspensions were then determined following the methodology outlined in the same section.

The composition of the Carbopol matrix was inspired by the non-aqueous matrix used in the toothpaste formulations described in Sec. 1.3 but was carefully designed to balance multiple considerations. The system as a whole—including the selected Carbopol concentration and the choice of the PEG/glycerol mixture as the ambient fluid for the dispersion—enabled the formation of an ideal soft colloid system with negligible interactions between Carbopol microgels. As a result, the macroscopic elastic properties of the suspensions were governed solely by the elasticity and thermal energy of individual particles. At intermediate Carbopol volume fractions, this contribution is very small and can hardly be measured, resulting in a

purely viscous shear-thinning behaviour (Migliozzi et al., 2020). Additionally, the PEG/glycerol ratio was chosen to provide a matrix viscosity high enough to maintain stable bubble suspensions throughout rheological tests, while the excess of glycerol also accelerated Carbopol microgel swelling, facilitating the preparation of the dispersions.

To systematically increase the complexity of the matrix composition and examine the impact of surfactant on the rheology of the generated bubble suspensions, a second shear-thinning matrix was prepared. This formulation consisted of a 0.55% wt Carbopol dispersion in a 30/70 wt PEG400/glycerol mixture containing 35mM SDS. For brevity, the pure Carbopol matrix will be referred to as ST1, and the SDS-containing Carbopol matrix as ST2 throughout this thesis. For the preparation of the ST2 matrix, SDS was first dissolved in glycerol. Once fully homogenised, the same preparation process as for ST1 was followed. The SDS concentration was maintained below the CMC (~43 mM) to prevent physical gelation in glycerol, which would otherwise alter its Newtonian rheology (Makri et al., 2019). To achieve comparable viscosities between the two matrices, the Carbopol concentration in the ST2 matrix was slightly increased from 0.5% wt to 0.55 wt to compensate for the viscosity reduction caused by SDS. The addition of SDS has been shown to disrupt the hydrophobic interactions between the solvent and the Carbopol polymer network, leading to molecular deswelling (Milanović et al., 2015). This deswelling decreases the effective volume fraction of Carbopol, thereby lowering the viscosity of the solution. The chosen increase in Carbopol concentration ensured that the matrix remained outside the yield stress regime while maintaining its viscosity within the desired experimental range.

Table 5.1 presents the properties of the fluids comprising the two shear-thinning Carbopol matrices, measured at 20 °C in accordance with the rheological tests. It also includes the volume fraction of the swollen Carbopol microgels in each solvent mixture (PEG400/glycerol for the ST1 matrix and PEG400/glycerol/SDS for ST2), determined using the Mooney (1951) equation:

$$\eta_r = \exp\left(\frac{2.5\zeta}{1-\lambda_M\zeta}\right) \tag{5.3}$$

where $\eta_r \equiv \frac{\eta_{Carbopol\ dispersion}}{\eta solvent}$ represents the relative viscosity of ST1 and ST2, calculated by dividing the zero-shear viscosity of each system (obtained from steady-shear rheological measurements) by the viscosity of the corresponding solvent mixture. Here, ζ denotes the volume fraction of the swollen Carbopol microgels and λ_M is a fitting parameter related to the

maximum packing factor that the system can achieve. Although the Mooney equation was originally developed for hard spheres, it has been widely used for softer colloidal systems such as those described here. According to Migliozzi et al. (2020), λ_M is equal to 1.3 for any PEG400/glycerol ratio.

Table 5. 1: Viscosity η_s, density ρ and surface tension $\sigma_{\alpha,\beta}$ of the fluids comprising the shear-thinning Carbopol matrices. The PEG400/Glycerol mixtures have a 30/70 wt composition and the SDS concentration in the second mixture is 35mM.

Fluid	Viscosity (Pa s)	Density (g/mL)	Surface tension (mN/m)	Swollen Carbopol microgel volume fraction (ζ)
PEG400	0.12±0.01	1.13±0.02	43.61±0.25	-
Glycerol	1.41±0.02	1.25±0.01	62.96±0.25	-
PEG400/Glycerol	0.82±0.01	1.21±0.01	50.15±0.25	0.30
PEG400/Glycerol/SDS	0.84±0.01	1.22±0.02	41.09±0.25	0.24

5.2.2. Rheological characterisation and visualisation of bubble suspensions under steady shear

To obtain the viscosity curves of the generated bubble suspensions, steady-shear rheological tests were performed over a shear rate range of 0.1 s^{-1} to 50 s^{-1} using an Anton Paar MCR302 stress-controlled rotational rheometer. A mild pre-shear stage of 3 min at 0.2 s^{-1} was applied prior to the measurements to minimise potential memory effects in the Carbopol matrix induced by the high-shear mixing during bubble generation. All steady-shear measurements were carried out at an operating temperature of 20 ˚C, using a sandblasted parallel-plate geometry (R=20 mm) to prevent wall-slip effects. The rheometer gap was set at 1.3 mm, ensuring it was at least ten times larger than the average bubble diameter (as determined from bubble size measurements) to avoid any wall effects caused by plate confinement. All rheological measurements were performed in triplicate to ensure reproducibility, and the average viscosity values of both the suspensions and the Carbopol matrices were used for the rheological analysis.

To account for the non-uniform shear distribution across the parallel plates, the Weissenberg-Rabinowitsch correction (Macosko, 1994) was applied to the viscosity data. To accurately determine the relative viscosity of the suspensions ($\eta_r \equiv \eta_{suspension}/\eta_{ambient\ fluid}$), the samples were left to de-aerate overnight after testing, and the viscosity of

the matrix was measured the following day. This step ensured that the measured viscosity reflected the true state of the matrix, as the high-shear mixing used during bubble generation was observed to induce de-swelling of the Carbopol microgels, leading to a reduction in matrix viscosity compared to its initial pre-aeration state (Sec. C1 in Appendix C).

To investigate potential shear-induced phenomena, the generated bubble suspensions were visualised under steady shear, using the rheo-optical set up described in Sec. 4.2.3. Images were captured during steady-shear measurements over a shear rate range of 0.1 s^{-1} to 50 s^{-1}, with a fixed acquisition time of 20 s per shear rate. The rheometer gap was maintained at 1.3 mm, consistent with the viscosity measurements. The images were then analysed to investigate dynamic changes in the suspension microstructure under shear, including changes in bubble size due to coalescence and the formation of bubble clusters and threads.

5.3 Experimental results for dilute bubble suspensions prepared using the ST1 matrix

This section presents the experimental findings for dilute bubble suspensions prepared using ST1 as the ambient fluid. The section is organised as follows: first, the bubble size distributions and the corresponding volume-weighted average bubble radii are presented for each tested bubble volume fraction, followed by the obtained viscosity trends. Next, the results from the rheo-optical experiments are discussed to elucidate the observed rheological behaviour and provide further insights into the microstructure of these complex systems.

5.3.1. Bubble size distributions

Similar to the bubble suspensions described in Chapters 3 and 4, which were generated in Newtonian matrices, the bubble suspensions tested here were also found to be polydisperse, following a gamma-type distribution between 20 μm and 110 μm (Fig. 5.1). Consequently, a volume-weighted average bubble radius, $< R >$, was determined for each suspension. For the reported bubble volume fractions, $\varphi_1 = 3.85\%$, $\varphi_2 = 5.12\%$, $\varphi_3 = 6.4\%$, and $\varphi_4 = 8.7\%$, the corresponding volume-weighted mean radii were found to be 54 μm, 50 μm, 57 μm and 63 μm, respectively.

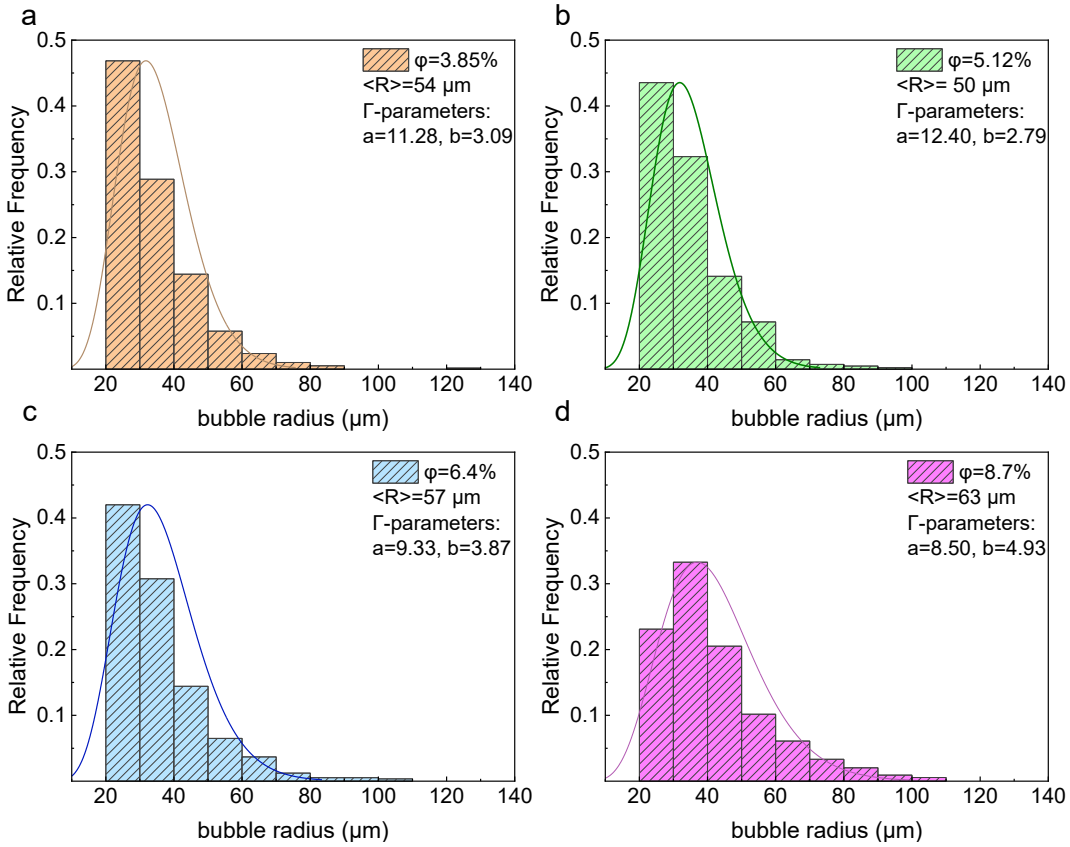

Figure 5.1: Bubble size distributions for suspensions generated using the ST1 matrix as the ambient fluid.

5.3.2. Steady shear rheological measurements

Fig. 5.2 presents the flow curves of the tested bubble suspensions and their corresponding ST1 matrices, plotted as functions of the effective shear rate, which is defined as the shear rate at the edge of the rheometer plate according to the Weissenberg-Rabinowitsch correction. As shown, in all cases the presence of bubbles amplified the shear-thinning behaviour of the matrix. Furthermore, the zero-shear viscosity increased with bubble volume fraction (Fig. 5.3), similar to the behaviour observed in bubble suspensions with Newtonian ambient fluids.

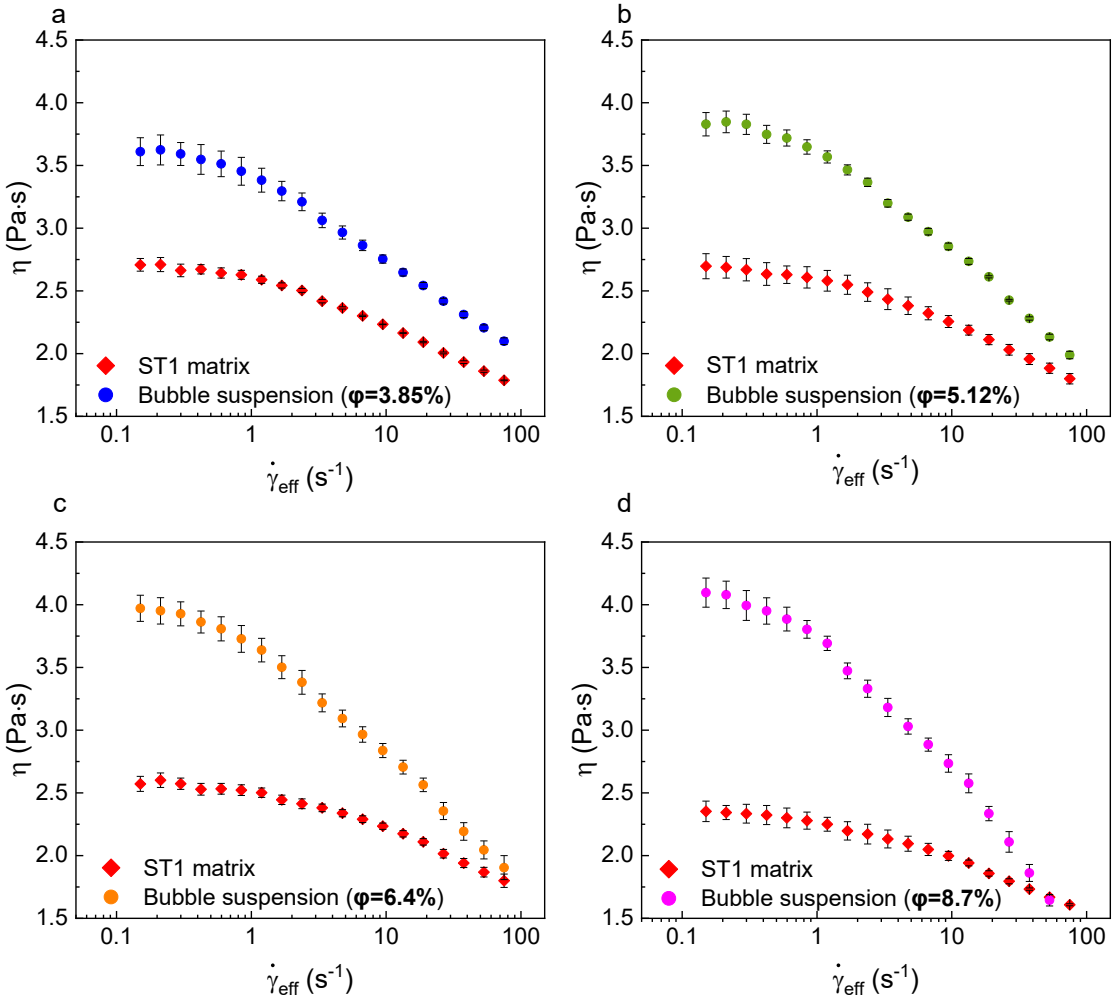

Figure 5.2: Flow curves for the tested bubble suspensions and the corresponding ST1 matrices. Viscosity is plotted as a function of the effective shear rate, i.e., the shear rate at the edge of the parallel plate geometry based on the Weissenberg-Rabinowitsch correction.

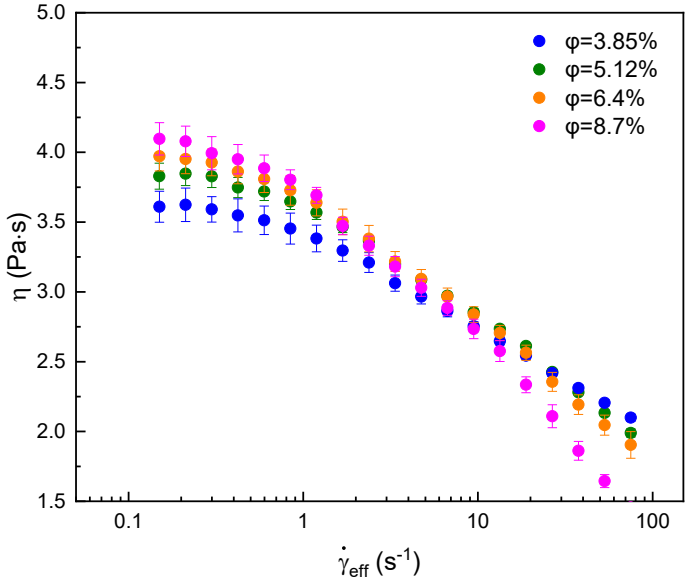

Figure 5.3: Flow curves for $\varphi_1 = 3.85\%$, $\varphi_2 = 5.12\%$, $\varphi_3 = 6.4\%$, and $\varphi_1 = 8.7\%$. The zero-shear viscosity increases with bubble volume fraction.

To further evaluate the effect of bubbles on the shear-thinning behaviour of the matrix, the experimentally determined viscosities for both the bubble suspensions and their corresponding ST1 matrices were fitted to a simplified version of the Carreau-Yasuda equation, considering the infinite viscosity η_∞ equal to zero (Macosko, 1994):

$$\eta = \eta_0[1 + (\lambda_c\dot{\gamma})^a]^{\frac{n-1}{a}} \tag{5.4}$$

The fitting was performed using the Curve Fitting App of MATLAB and treating the zero-shear viscosity η_0, the Carreau relaxation time λ_c, the flow index n and the a-parameter as fitting variables. The simplification of $\eta_\infty = 0$ was made because there were no available experimental data for the infinite-shear region, as bubble suspensions cannot be subjected to very high shear rates without altering their microstructure (i.e., changes in bubble volume fraction and size distribution). The fitted Carreau-Yasuda parameters for each tested bubble volume fraction are presented in Table C.1 (Appendix C). In all cases, the flow index of the suspensions was lower than that of the matrix, confirming the enhanced shear-thinning behaviour observed in the flow curves of Fig. 5.2.

Fig. 5.4 presents the relative viscosities for all tested bubble volume fractions as functions of both the effective shear rate and the average Capillary number, $< Ca >$, calculated using the volume-weighted average bubble radius for each suspension. The flow curves exhibit a characteristic double power–law decay of relative viscosity, a trend previously observed in bubble suspensions with a Newtonian matrix (see Chapter 3). The trend becomes more evident as the bubble volume fraction increases. However, as shown in Fig. 5.5, in this case, the double decay occurs at $< Ca >$ values an order of magnitude lower than the $< Ca >$ values where this trend was observed in bubble suspensions with Newtonian ambient fluids. Specifically, the first viscosity drop begins within the $\langle Ca \rangle$ range of 0.001-0.01, while the second drop occurs around $\langle Ca \rangle \sim 0.1$. In contrast, for bubble suspensions with a Newtonian ambient fluid, the first decay starts at $< Ca >$ values between 0.01 and 0.1, with the second decay occurring at $< Ca > \sim 1$.

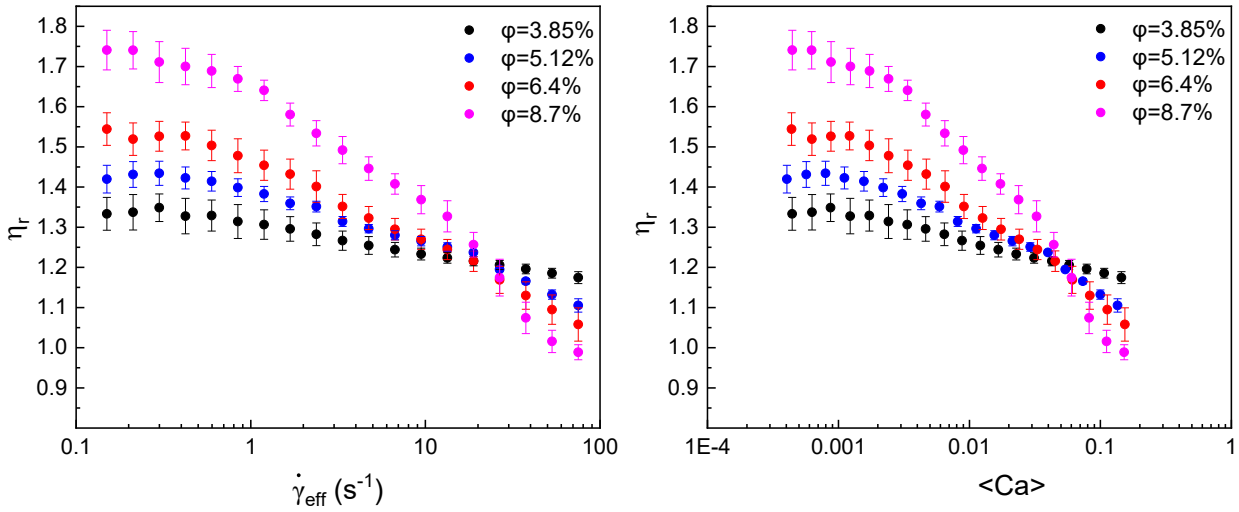

Figure 5.4: Relative viscosity as a function of effective shear rate and average Capillary number for bubble suspensions with the ST1 matrix and bubble volume fractions $\varphi_1 = 3.85\%$, $\varphi_2 = 5.12\%$, $\varphi_3 = 6.4\%$, and $\varphi_4 = 8.7\%$.

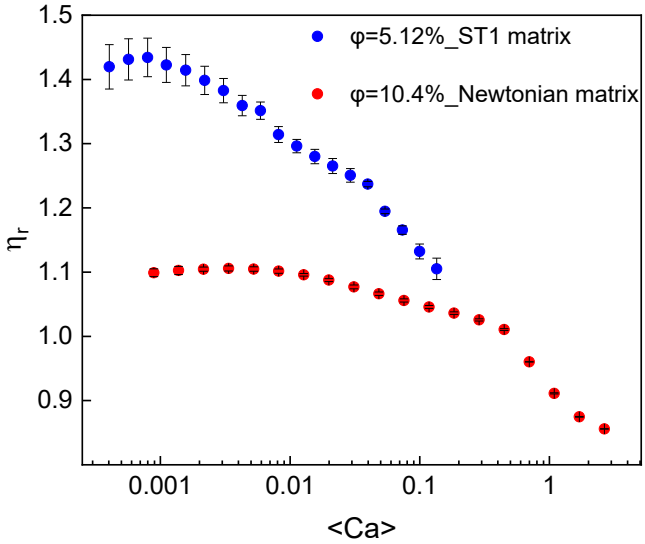

Figure 5.5: Relative viscosity as a function of average capillary number for a bubble suspension with the ST1 matrix ($\varphi = 5.12\%$) and a bubble suspension with the Newtonian matrix from Chapter 3 ($\varphi = 10.4\%$). In the ST1 matrix, the double decay of relative viscosity occurs at $< Ca >$ values an order of magnitude lower than the values at which the same trend is observed in the Newtonian matrix.

This shift in shear-thinning behaviour to lower capillary numbers was also observed by Torres et al. (2013). As mentioned earlier, the authors speculated that this behaviour was driven by significant normal stress differences measured in their shear-thinning solutions, which may have caused bubble deformation at lower shear rates, and consequently, lower Ca values. However, since the Carbopol dispersions used in this study are purely shear-thinning without

appreciable elasticity, this explanation does not apply here, and the observed shift requires further investigation to elucidate its underlying cause.

Another key difference between bubble suspensions with Newtonian ambient fluids and those studied here lies in how the zero-shear viscosity scales with bubble volume fraction. As discussed in Chapter 3, in the case of Newtonian background fluids, the suspension relative viscosities closely matched the predictions of the classic Taylor equation, i.e., $\eta_{r,0} = 1 + \varphi$. However, for the bubble suspensions with the shear-thinning Carbopol matrix studied here, the relative viscosities were found to be significantly higher than the predictions of the Taylor equation. Previous studies by Torres et al. (2015) and Chesterton et al. (2013) suggested that for dilute bubble suspensions with shear-thinning matrices, the relative zero-shear viscosity can instead be described by a modified Taylor equation: $\eta_r = 1 + b\varphi$ (as given in Eq. 5.1). To evaluate whether this equation could better describe the zero-shear relative viscosities obtained here, the experimental data for all tested bubble volume fractions were fitted to Eq. 5.1 using the Curve Fitting App of MATLAB to obtain an appropriate value for the scaling parameter b.

The fitting results indicated that Eq. 5.1 with $b = 8.75$ effectively described the zero-shear viscosity data. However, this b value lacks physical meaning, because it exceeds the Einstein coefficient for hard spheres ($b = 2.5$). Instead, it closely aligns with the coefficient of the modified Taylor equation reported by Llewellin et al. (2002b) for the relative zero-shear viscosity of their polydisperse bubble suspensions in a Newtonian ambient fluid. A subsequent study by Mader et al. (2013) attributed this higher coefficient to interactions among bubbles, insofar as the bubble volume fractions in Llewellin's study extended into the semi-dilute and concentrated regimes, reaching up to 46%. Although the bubble suspensions examined here were dilute, so that interactions among bubbles would not typically be expected, it is important to consider the presence of a second dispersed phase—the Carbopol microgels. These microgel particles occupy nearly 30% of the suspension volume, meaning that the total system composed of bubbles and microgels is effectively crowded, potentially causing interactions between the two dispersed phases. This may explain why the classic Taylor equation, which was developed for dilute emulsions with negligible interactions, fails to accurately predict the zero-shear relative viscosities in these suspensions.

To further investigate the hypothesis regarding crowding effects and their impact on the zero-shear viscosity, the suspensions were treated as having a single dispersed phase with a volume fraction equal to the sum of the Carbopol microgel volume fraction and the bubble

volume fraction. The measured zero-shear viscosities were then compared to the predictions of the Mooney equation, which describes how the zero-shear suspension viscosity varies with the dispersed phase volume fraction, accounting for crowding effects and hydrodynamic interactions among the dispersed particles. As shown in Fig. 5.6, the experimentally determined zero-shear viscosities align well with the predictions of the Mooney equation for both the suspensions with the ST1 matrix and those with the ST2 matrix. This finding confirms that the systems effectively behave as crowded suspensions, where interactions between the two dispersed phases significantly impact the measured zero-shear viscosity.

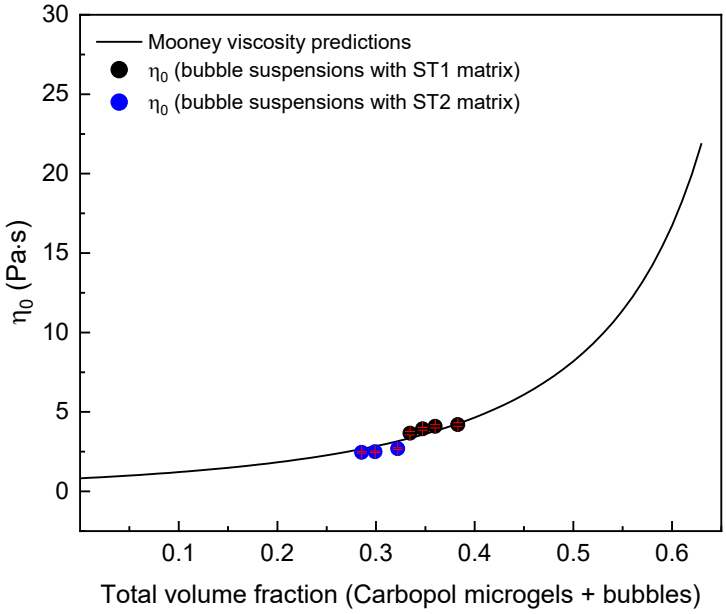

Figure 5.6: Zero-shear viscosity as a function of the total dispersed phase volume fraction for bubble suspensions with the ST1 and ST2 matrices, respectively. The experimentally determined zero-shear viscosities for the different suspensions are compared to predictions of the Mooney equation. Error bars represent the standard deviation of the measured zero-shear viscosities.

5.3.3. Visualisation of bubble suspensions under steady shear

To further examine the shift of the double decay in relative viscosity toward lower $< Ca >$ values and assess potential shear-induced phenomena and microstructural changes influencing the rheological trends, three fresh bubble suspensions with the ST1 matrix and $\varphi_1 = 2.98\%$, $\varphi_2 = 5.8\%$, and $\varphi_3 = 8.2\%$ were prepared and visualised under steady shear using the rheo-optical set up. Fig. 5.7 presents three representative images for the suspension with bubble volume fraction φ_2, taken at shear rates 0.1 s^{-1}, 9 s^{-1} and 35 s^{-1} (corresponding to $< Ca >$ values of approximately 0.001, 0.01, and 0.1), along with their respective bubble size distributions.

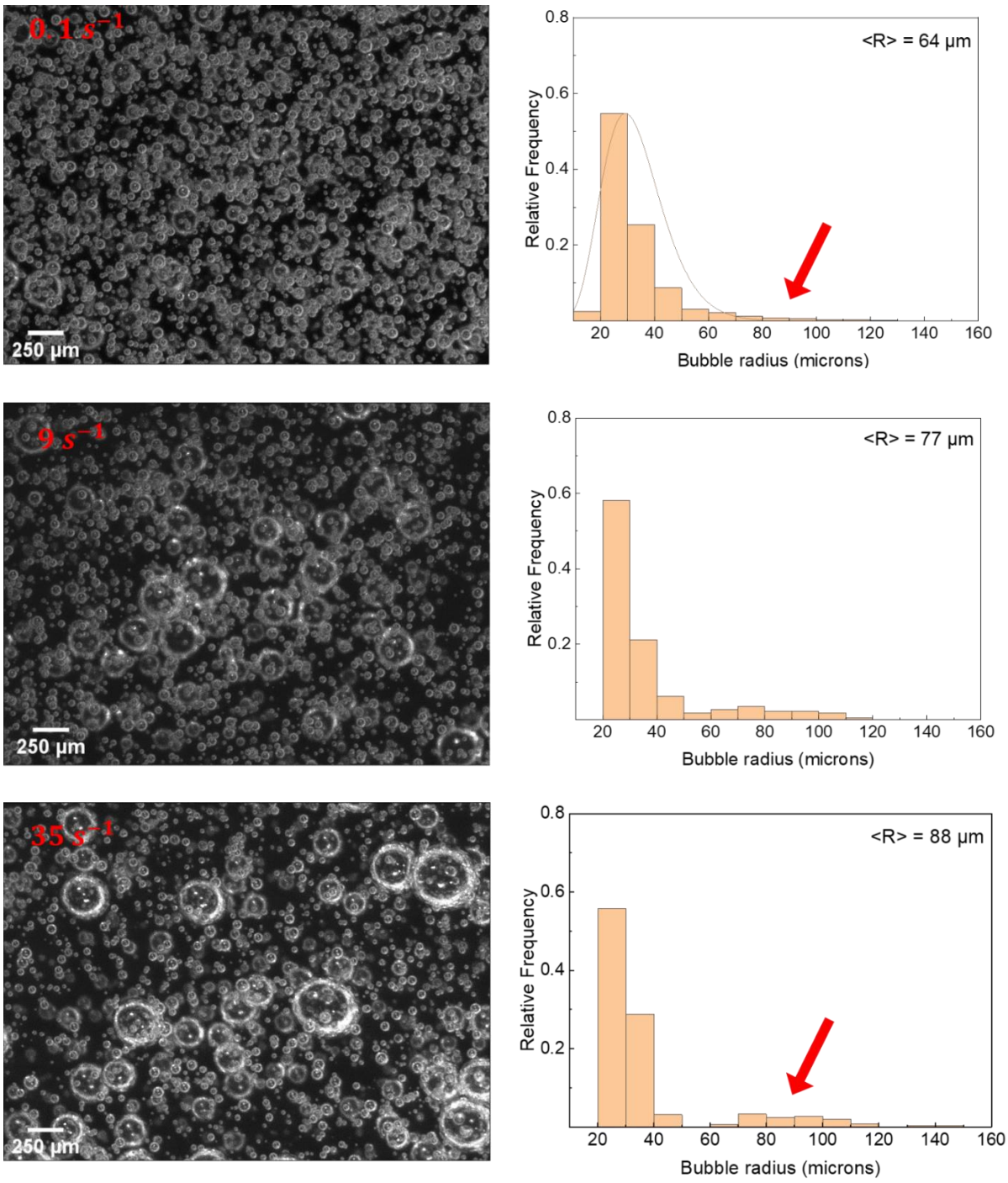

Figure 5.7: Bubble suspension with the ST1 matrix and $\varphi = 5.8\%$, visualised under steady shear at 0.1 s^{-1}, 9 s^{-1}, and 35 s^{-1}. The corresponding bubble size distributions are shown alongside each image.

The images reveal that as the shear rate, and in turn $< Ca >$, increases, bubbles tend to coalesce, leading to deviations from the initial gamma-type size distribution and an increase in the average bubble size. Additionally, as larger bubbles form, they begin to align or move closer together, resulting in the formation of bubble threads and clusters. This is likely due to wall

effects, which become more pronounced as bubbles grow larger and experience greater confinement within the parallel plate gap. These microstructural changes begin to emerge within the shear rate range of 1-10 s^{-1}, coinciding with the first drop in relative viscosity. It is worth noting that at similar shear rates, shear-induced bubble clustering was also observed in Newtonian matrices (as described in Chapter 3), suggesting a potential connection between the two phenomena. As shear brings bubbles into closer proximity, coalescence becomes more likely, leading to the formation of larger bubbles, which in turn begin to aggregate into secondary clusters.

The microstructure continues to evolve significantly across the shear rate range of 10-50 s^{-1}. In this range, bubble coalescence becomes more prominent, and the clustering of the resulting larger bubbles intensifies. These coalesced bubbles form dynamic structures that move collectively under shear (Fig. 5.8), and this behaviour becomes more evident with increasing shear rate. At higher shear rates toward the upper end of the tested range, deformation of these larger bubbles also becomes apparent. Overall, the rheo-optical observations suggest that the observed rheological behaviour is linked to a sequence of interconnected microstructural changes. These include bubble coalescence, the formation of dynamic clusters of coalesced bubbles, and their eventual deformation at higher shear rates. Each of these phenomena emerges progressively with increasing shear, collectively contributing to the complex flow response of the suspension.

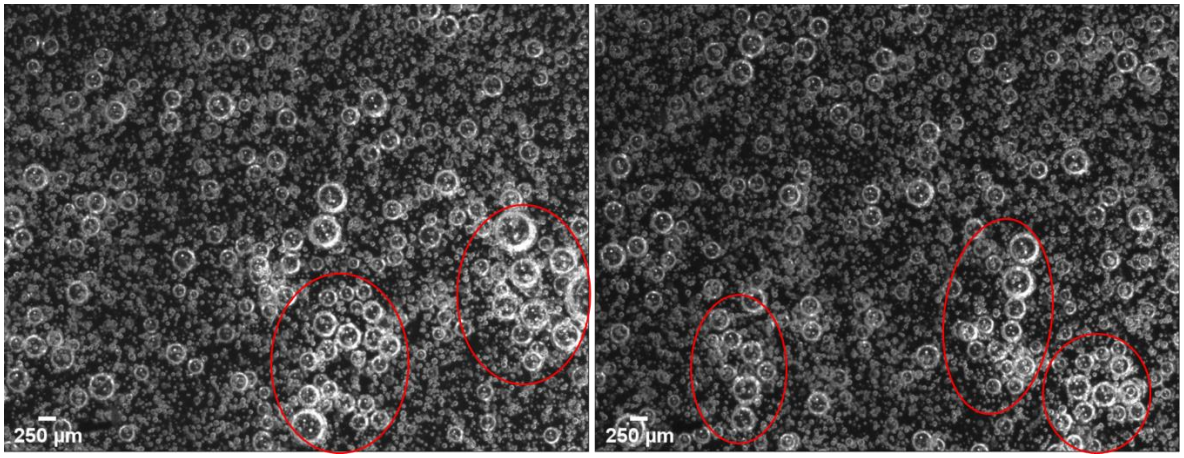

Figure 5.8: Formation of dynamic structures composed of coalesced bubbles moving collectively under shear, corresponding to the bubble suspension with the ST1 matrix and $\varphi = 5.8\%$ at a shear rate of 12.6 s^{-1}.

To further understand how the microstructure of the current suspensions evolves under shear, statistical image analysis was performed to assess how the volume-weighted average

bubble radius ($< R >$) and the coverage (C) metric-introduced in Chapter 3 to qualitatively detect changes in the arrangement of bubbles at the microscale-varied with shear rate. For each shear rate, 20 representative images were analysed using the methodology described in Sec. 3.5.2. The obtained C and $< R >$ values for these images were then averaged to yield representative mean values of coverage ($\bar{C}$) and volume-weighted average radius ($\overline{\langle R \rangle}$) for each shear rate. Fig. 5.9 illustrates the trends of $\bar{C}$ and $\overline{\langle R \rangle}$ as functions of the effective shear rate for the three tested bubble suspensions. The results show a decrease in coverage beginning at shear rates around 1 s^{-1}, which coincides with the onset of the first drop in relative viscosity (see Fig. 5.4). At the same shear rate, the average bubble radius also begins to increase. As the shear rate increases further, coverage continues to decrease, while the volume-weighted average bubble radius grows by 29%, 34% and 38% for $\varphi_1 = 2.98\%$, $\varphi_2 = 5.8\%$, and $\varphi_3 = 8.2\%$, respectively, by the end of measurement. As expected, the increase in average bubble size is larger at higher bubble volume fractions, where the average inter-bubble distance reduces, increasing the probability of coalescence.

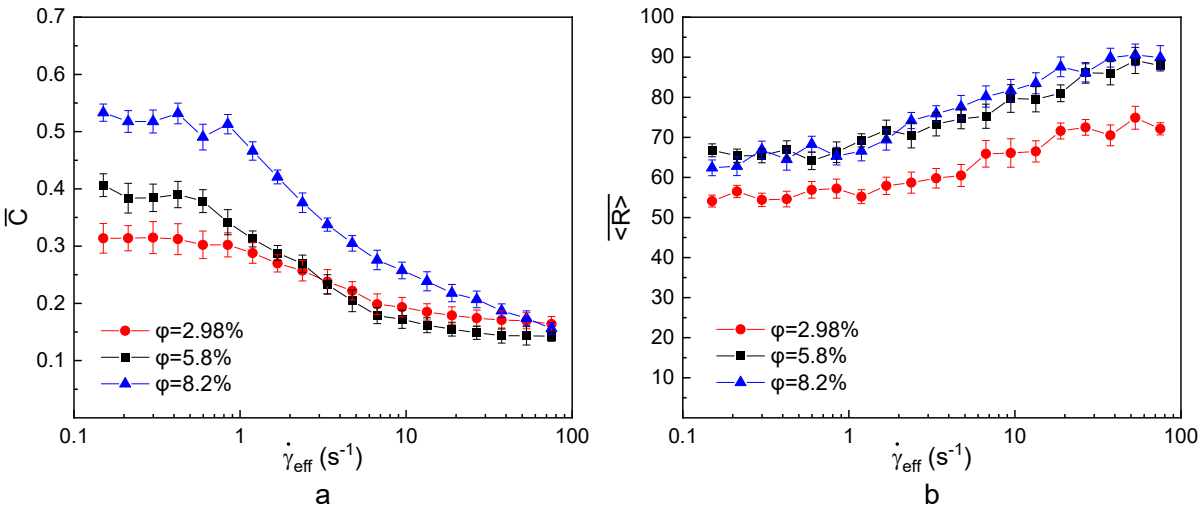

Figure 5.9: a) Mean Coverage and b) Mean volume-weighted average bubble radius as functions of the effective shear rate for $\varphi_1 = 2.98\%$, $\varphi_2 = 5.8\%$ and $\varphi_3 = 8.2\%$.

These results highlight that, in this instance, the decreasing coverage trend reflects both bubble coalescence and microstructural rearrangements under shear. A comparison with the results from the rheo-optical experiments on bubble suspensions in Newtonian media (discussed in Sec. 3.5.2) reveals that the decrease in coverage and the increase in bubble size observed in this first shear-thinning matrix are more pronounced. The greater reduction in coverage is directly influenced by enhanced bubble coalescence; as bubbles coalesce, the number of white pixels in the image decreases, leading to a measurable reduction in coverage. To confirm that coalescence affects the observed coverage trends, the data were normalised by

the initial plateau value to allow for a direct comparison across the different bubble volume fractions. As shown in Fig. 5.10, the drop in coverage increases with bubble volume fraction, indicating that the phenomena captured by the coverage trend are not simply shear-dependent, but rather scale with bubble volume fraction, aligning with coalescence-driven behaviour. It is also worth noting that the coverage trends of the current suspensions exhibit a more complex shape characterised by a two-stage decrease (as seen in Fig. 5.10), whereas the coverage trends observed in Chapter 3 for bubble suspensions with a Newtonian matrix followed a simpler linear trend. This may indicate that different microstructural effects, such as the spatial reorganisation of bubbles into clusters and threads or changes in the local bubble size distribution due to coalescence, occur at different time scales, potentially leading to the multistage decay observed. However, since the coverage parameter represents an overall measure of the microstructural configuration under shear, it inherently lacks the ability to differentiate between distinct microstructural changes, which more advanced statistical measures could capture in greater detail.

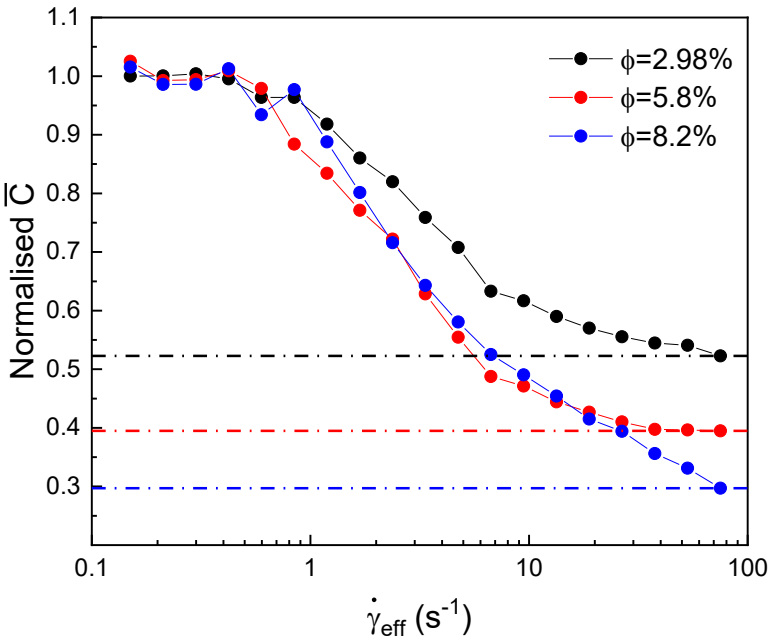

Figure 5.10: Normalised mean coverage as function of effective shear rate for bubble suspensions with the ST1 matrix and $\varphi_1 = 2.98\%$, $\varphi_2 = 5.8\%$, and $\varphi_3 = 8.2\%$, respectively. The dashed lines indicate that the drop in coverage from the initial plateau becomes more pronounced as bubble volume fraction increases.

As shown, bubble coalescence plays a key factor in shaping the microstructure of the current suspensions, and consequently, their rheological behaviour. Although the exact mechanism driving the increased coalescence observed in these systems cannot be elucidated from the obtained images, two factors likely contribute: the shear-thinning nature of the matrix and the

absence of surfactants, which would otherwise stabilise the bubbles. In the literature (Fanebust, Ozan and Jakobsen, 2021; Long, 2024), it is suggested that a shear-thinning matrix enhances bubble coalescence by accelerating fluid film drainage between bubbles. When two bubbles come into close proximity, the thin fluid film separating them is compressed and forced outward. This outward flow creates a velocity gradient, which leads to a localised increase in shear rate. In shear-thinning fluids, viscosity decreases with shear rate, thereby reducing resistance to film drainage. As a result, the thin liquid film between colliding bubbles drains more rapidly than in Newtonian ambient fluids, facilitating bubble coalescence. Although these findings refer to a simplified system, specifically a pair of bubbles rather than a suspension, they still provide a qualitative explanation for the phenomena occurring at the microscale. In addition to the shear-thinning matrix, the absence of surfactant in the present system leaves the bubble interfaces without an interfacial barrier that would otherwise stabilise them, thereby lowering the energy required for coalescence and making them more susceptible to merging.

As previously discussed, bubble coalescence and the associated microstructural changes, evidenced by the increase in average bubble size and the reduction in coverage, began at shear rates around 1 s^{-1}, where shear-induced bubble clustering was also observed in Newtonian matrices. This suggests a similar shear-induced clustering effect in the present system. However, unlike in the Newtonian case-where the presence of surfactants and the Newtonian character of the matrix did not promote coalescence-here, the combined effects of the shear-thinning matrix and the absence of surfactants allowed bubbles to coalesce more readily as they came into closer proximity under shear. This, in turn, led to secondary clustering phenomena, this time involving the larger, coalesced bubbles, which may be driven by wall effects as the bubble size grows significantly larger, and the coalesced bubbles are more confined within the rheometer plates.

Given the increase in the volume-weighted average bubble radius during the rheological measurements, the $< Ca >$ values used to plot the viscosity curves of Fig. 5.4 do not accurately represent the system, as they were calculated using the initial $< R >$ values obtained from microscope images taken before the rheological tests. Since $< Ca >$ depends on the average bubble radius, it is expected to shift to higher values as the bubbles grow larger. Therefore, to assess whether the observed shift of the shear-thinning trend toward lower capillary numbers is an artifact of using the initial $< R >$ values in the calculation of $< Ca >$, updated $< Ca >$ values were calculated to account for the increase in bubble size. To this end, the trend of $\overline{\langle R \rangle}$,

determined through the statistical image analysis, was used to reconstruct the bubble size evolution of the suspensions described in Sec. 5.3.2, and the values of $< Ca >$ were recalculated based on these updated bubble sizes.

Fig. 5.11 indicatively presents the flow curve for the bubble suspension with $\varphi_2 = 5.12\%$, plotted as a function of both the initial and the updated $< Ca >$ values that account for the increasing average bubble radius due to coalescence. As shown, the characteristic double decay in relative viscosity shifts to slightly larger $< Ca >$ values due to the rise in the average bubble radius. Nevertheless, the overall double decay viscosity trend remains distinct from that observed in Newtonian matrices and still corresponds to $< Ca >$ values that are approximately an order of magnitude lower. This shift in $< Ca >$, particularly in relation to the earlier-than-expected bubble deformation, warrants further investigation. Rheo-optical observations confirmed deformation of the coalesced bubbles at $< Ca >$ values around 0.1, instead of $< Ca > \sim 1$, which is typically considered the threshold for noticeable deformation. Even when estimating the capillary number specifically for the larger, coalesced bubbles (rather than relying on the volume-weighted average capillary number for the overall population) these individual bubbles had not reached $Ca \sim 1$ at the shear rates where their deformation became visible, based on their radii obtained from image analysis. This suggests that additional factors may influence bubble deformation and the overall rheological response of bubble suspensions in shear-thinning matrices.

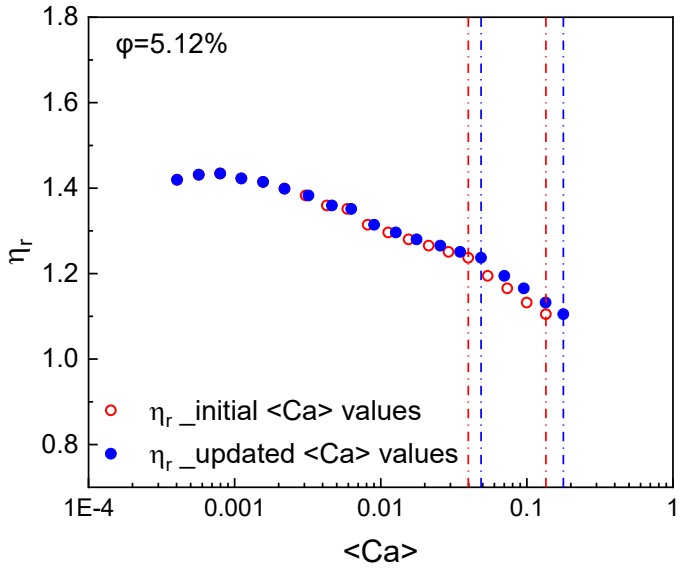

Figure 5.11: Relative viscosity of a bubble suspension ($\varphi = 5.12\%$) as a function of both the initial and the updated average capillary number, recalculated to account for the increasing volume-weighted

average bubble radius due to coalescence. The vertical lines indicate the shift of the second viscosity decay to slightly larger $< Ca >$ values as a result of bubble growth.

Although no appreciable normal stresses were measured during the rheological tests, one must note that the suspensions under investigation are complex crowded systems with interactions among the two dispersed phases, dynamic changes in the microstructure under shear, and potential wall effects emerging as bubbles grow larger. Such phenomena possibly alter the flow field around the bubbles, inducing localised high-stress regions that deform bubbles sooner than expected. While these effects provide a plausible basis for explaining the observed behaviour, the exact underlying mechanisms and their relationship remain unclear, requiring further experimental and theoretical work to fully understand the earlier onset of bubble deformation in shear-thinning inelastic matrices.

As demonstrated, the interplay between bubbles and the matrix significantly influences the steady-shear rheological behaviour of the tested bubble suspensions. The presence of Carbopol microgels led to crowding effects and interactions between the two dispersed phases, directly impacting the zero-shear viscosity of the suspensions. Moreover, the shear-thinning matrix combined with the absence of surfactants in the system resulted in substantial bubble coalescence and subsequent clustering/alignment of the coalesced bubbles, possibly due to wall effects and bubble confinement within the rheometer gap. To further increase matrix complexity and evaluate the impact of matrix composition on the rheological behaviour of bubble suspensions, the following section examines how the addition of SDS as a surfactant in the Carbopol matrix affects viscosity trends, bubble coalescence, and bubble clustering phenomena.

5.4 Experimental results for dilute bubble suspensions prepared using the ST2 matrix

This section presents experimental results from steady-shear rheological tests and rheo-optical experiments performed on bubble suspensions with the ST2 matrix and volume fractions $\varphi_1 = 4.95$ %, $\varphi_2 = 6.3\%$, and $\varphi_3 = 8.6\%$.

5.4.1. Bubble size distributions

Fig. 5.12 presents the bubble size distributions for the tested bubble suspensions with the ST2 matrix, calculated from microscope images taken before the rheological measurements. As shown, the bubble sizes follow a gamma-type distribution ranging from 10 μm to 100 μm. The volume-weighted average bubble radii for the reported bubble volume fractions $\varphi_1 =$

4.95%, $\varphi_2 = 6.30\%$, and $\varphi_3 = 8.60\%$ were found to be 40 μm, 44 μm, and 46 μm, respectively—smaller than those obtained for the ST1 matrix. This is consistent with the lower surface tension measured in the current system.

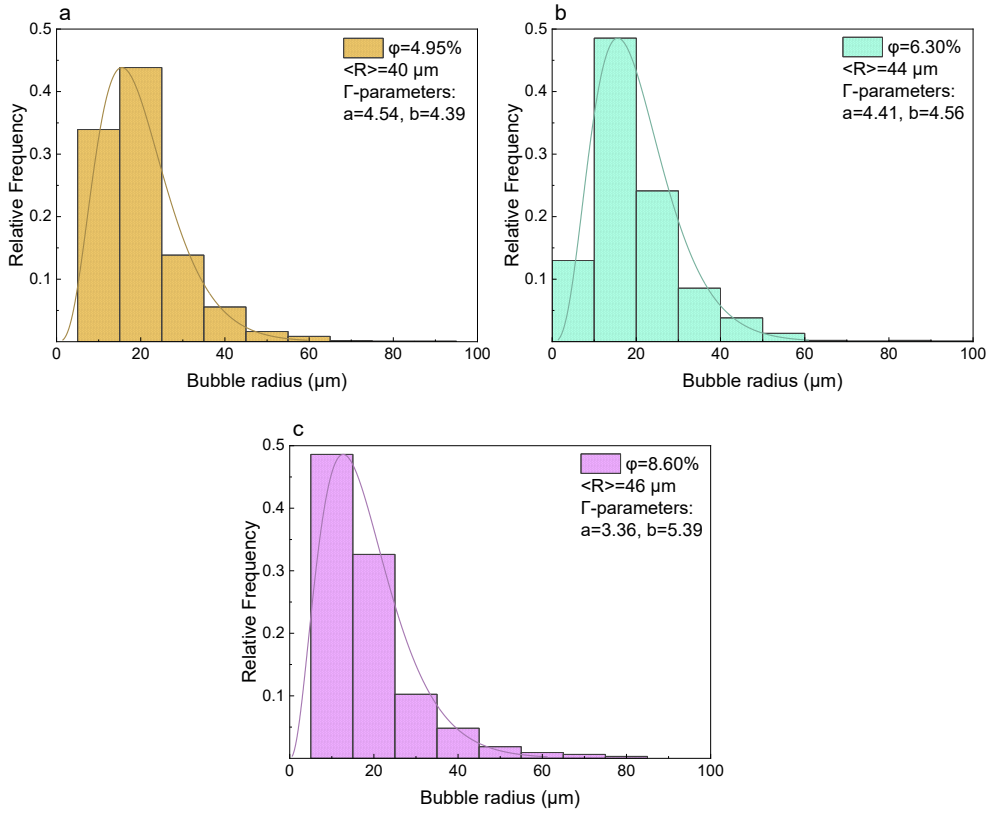

Figure 5.12: Bubble size distributions for suspensions prepared using the ST2 matrix as the ambient fluid.

5.4.2. Steady shear rheological measurements

Given the presence of surfactant, which typically limits coalescence phenomena and stabilises suspensions under high shear, the upper shear rate in the rheological tests was extended from 50 s^{-1} to 200 s^{-1} to assess the rheological behaviour over a broader shear rate range. Fig. 5.13 presents the flow curves of the tested bubble suspensions and their corresponding ST2 matrices, plotted as functions of the effective shear rate. Similar to what was observed in the ST1 matrix, the presence of bubbles induced additional shear-thinning effects. Following the same procedure as in Sec. 4.3.2, the experimental viscosity data for the bubble suspensions and their corresponding ST2 matrices were fitted to the simplified Carreau-Yasuda equation (Eq. 5.4) to further evaluate the effect of bubbles on the shear-thinning behaviour of the matrix. The obtained fitting values for the Carreau-Yasuda parameters are presented in Table C.2 (Appendix C).

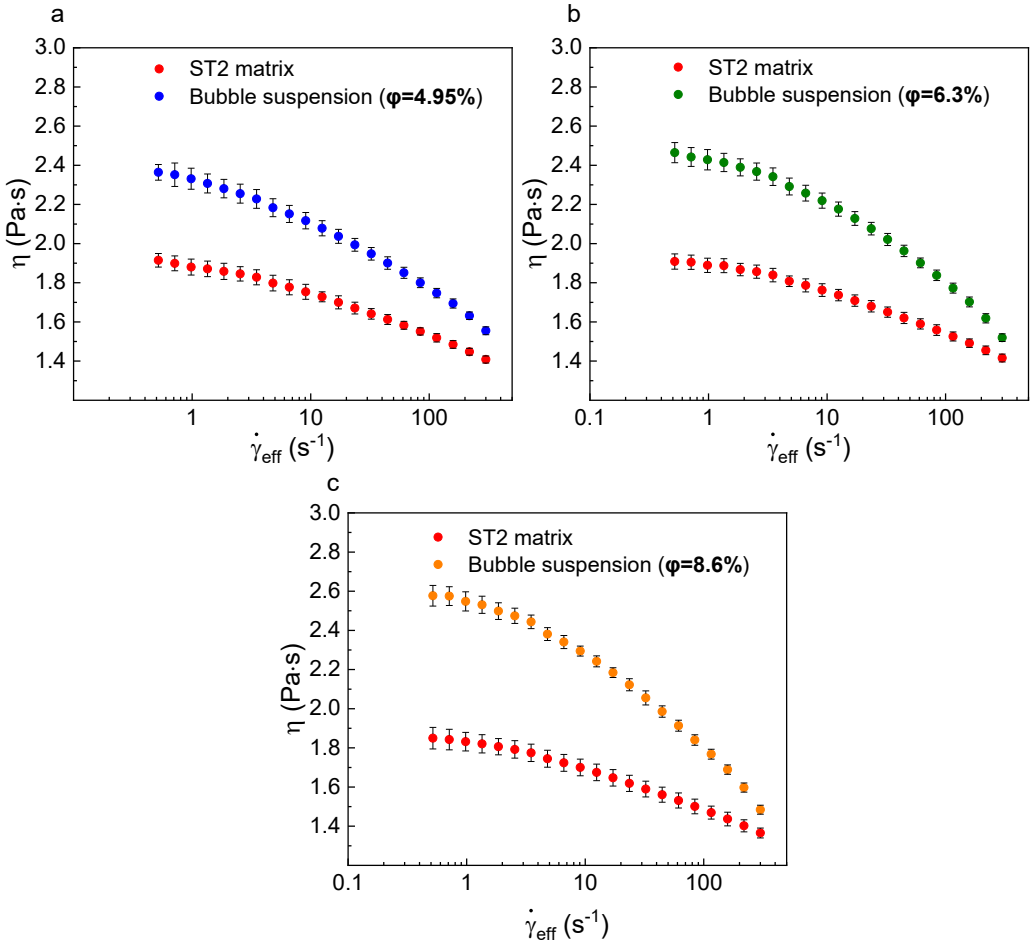

Figure 5.13: Flow curves for bubble suspensions with $\varphi_1 = 4.95\%$, $\varphi_2 = 6.3\%$, and $\varphi_3 = 8.6\%$, and the corresponding ST2 matrices. Viscosity is plotted as a function of the effective shear rate.

In all three cases, the flow index of the suspensions was lower than that of the matrix alone and decreased with increasing bubble volume fraction, indicating that a higher bubble content enhances shear-thinning effects. However, in this case, the reduction in flow index was smaller than in suspensions with the ST1 matrix, suggesting that while the bubbles intensified shear-thinning behaviour, their effect was less pronounced in the SDS-containing system. Additionally, the zero-shear viscosity increased with bubble volume fraction (Fig. C2 in Appendix C) consistent with observations in suspensions with the ST1 or Newtonian matrices.

Another noteworthy observation was that the addition of SDS appeared to stabilise the Carbopol matrix against de-swelling caused by the high-shear mixing used during bubble generation. This is evidenced by the nearly overlapping matrix flow curves presented in Fig. C3 (Appendix C) and the very similar Carreau-Yasuda fitting values obtained for the matrices of the three tested suspensions, regardless of aeration time. In addition to this stabilising effect, SDS also led to a reduction in the final volume of the swollen Carbopol microgels, as reported in Table 5.1. This finding is consistent with the results of Milanovic et al. (2015), who reported

that Carbopol microgels in aqueous solutions tend to swell less in the presence of SDS. The reduction in the volume occupied by the Carbopol microgels is expected to lessen crowding effects in the present suspensions compared to those with the ST2 matrix, and consequently, result in less pronounced interactions between the two dispersed phases.

This hypothesis was assessed by examining the zero-shear viscosity of the suspensions, given its sensitivity to crowding effects. Similar to what was observed in bubble suspensions with the ST1 matrix, the experimental zero-shear viscosities here were also higher than the predictions of the classic Taylor equation, indicating that crowding effects persist. In fact, as shown in Fig. 5.6, the data can be well described by the Mooney equation, which accounts for crowding effects and the resulting dispersed-phase interactions. However, applying the same procedure used for bubble suspensions with the ST1 matrix and fitting the zero-shear viscosity data for the tested bubble volume fractions to a scaled Taylor equation (Eq. 5.1) yields a b coefficient of 4.51—nearly half the value obtained for suspensions with the ST1 matrix. Although b remains well above the Einstein limit of 2.5, confirming that interactions between the two dispersed phases are still present, the reduction from its previous value likely suggests that these effects are less intense in the ST2 matrix compared to ST1.

Fig. 5.14 presents the relative viscosities η_r for the tested bubble volume fractions as functions of both the effective shear rate and the average capillary number. In this case, only a single drop in relative viscosity was observed across a $< Ca >$ range spanning approximately 0.01 to just below 1. This behaviour contrasts with the double decay trend observed for suspensions in the ST1 matrix, where two distinct viscosity drops were already evident within the $< Ca >$ range common to both systems: the first around $< Ca > \sim 0.01$ and the second around $< Ca > \sim 0.1$ (Fig. 5.15). This suggests that the evolution of microstructure under shear, which directly impacts the rheological response, may differ significantly between the two matrices.

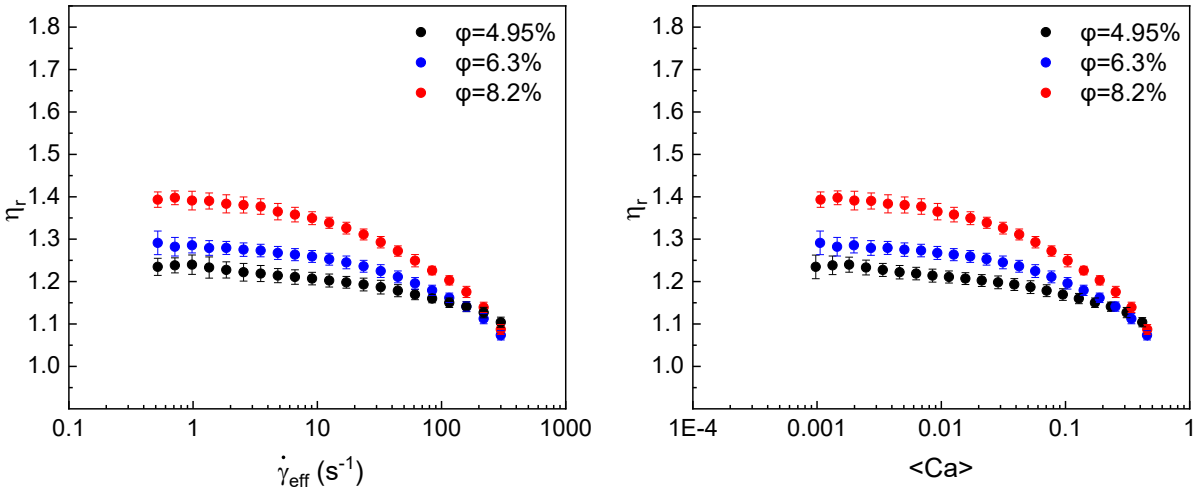

Figure 5.14: Relative viscosity as a function of the effective shear rate and the average capillary number for bubble suspensions with the ST2 matrix and bubble volume fractions $\varphi_1 = 4.95\%$, $\varphi_2 = 6.30\%$, and $\varphi_3 = 8.60\%$.

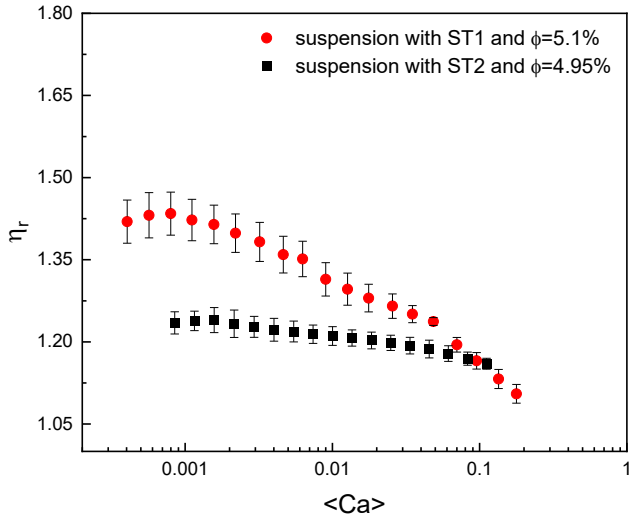

Figure 5. 15: Comparison of the relative viscosities of a bubble suspension with the ST1 matrix and $\varphi = 5.1\%$ versus a bubble suspension with the ST2 matrix and $\varphi = 4.95\%$.

A further comparison with bubble suspensions in Newtonian matrices also reveals a deviation from the double decay trend seen in that case. However, it is important to note that in the ST2 system, $< Ca >$ values only approached order magnitude unity at the upper end of the tested shear rate range. In contrast, in the Newtonian system, $< Ca >$ values well exceeded unity within the same shear rate range. This difference is primarily attributed to the larger bubble sizes in the bubble suspensions with the Newtonian matrix, which led to higher capillary numbers at equivalent shear rates. Therefore, the absence of a second viscosity drop in the ST2 system may simply reflect that bubbles had not fully reached $< Ca > \approx 1$, and the onset of bubble deformation, which in the Newtonian case was associated with the second decay, had not yet occurred. To further investigate these assumptions and examine how the new matrix

composition affected bubble coalescence, alignment and clustering phenomena, three fresh bubble suspensions with $\varphi_1 = 2.5\%$, $\varphi_2 = 4.62\%$, and $\varphi_3 = 7.25\%$ were prepared and visualised under steady shear. The results of the rheo-optical experiments are presented in the following section.

5.4.3. Visualisation of bubble suspensions under steady shear

Fig. 5.16 presents four representative images for the suspension with bubble volume fraction $\varphi_2 = 4.62\%$, taken at shear rates 0.5 s^{-1}, 5 s^{-1}, 50 s^{-1}, and 150 s^{-1}, which correspond to $< Ca >$ values of approximately 0.001, 0.01, 0.1, and 1, respectively. A comparison with Fig. 5.7 highlights the differences between bubble suspensions with the ST1 matrix and those with the ST2 matrix. The most notable distinction is that bubble coalescence is significantly less pronounced in the ST2 system. Consequently, no secondary clustering of coalesced bubbles was observed—a key microstructural phenomenon in the ST1 matrix that strongly influenced its rheological response. Correlating the rheo-optical observations with the flow curves obtained for the bubble suspensions with the ST2 matrix (Fig. 5.14), one can see that at $< Ca >$ values in the range 0.01 to 0.1, where the viscosity starts to drop, bubbles tend to align or move closer together to form clusters. This behaviour resembles the shear-induced clustering observed in Newtonian media, rather than the coalescence-driven clustering seen in the ST1 matrix within the same $< Ca >$ range. At higher $< Ca >$ values, approaching unity, bubbles appear slightly larger, indicating some degree of coalescence (Fig. 5.15d). However, the extent of bubble coalescence remains minimal compared to that observed in the ST1 matrix at significantly lower $< Ca >$ values. Additionally, no appreciable bubble deformation is observed throughout the rheo-optical experiments, aside from mild signs in a few larger bubbles at the upper end of the tested shear rate range, as shown in Fig. 5.15d. This supports the argument that the observed drop in relative viscosity in the ST2 suspensions is associated with shear-induced bubble clustering. The absence of a second viscosity drop in these systems is likely due to the fact that the bubbles had not yet begun to deform, unlike in the suspensions with the Newtonian matrix in Chapter 3, where the bubbles were larger and therefore reached and surpassed the threshold of $< Ca > = 1$ within the same shear rate range, resulting in a second drop in viscosity.

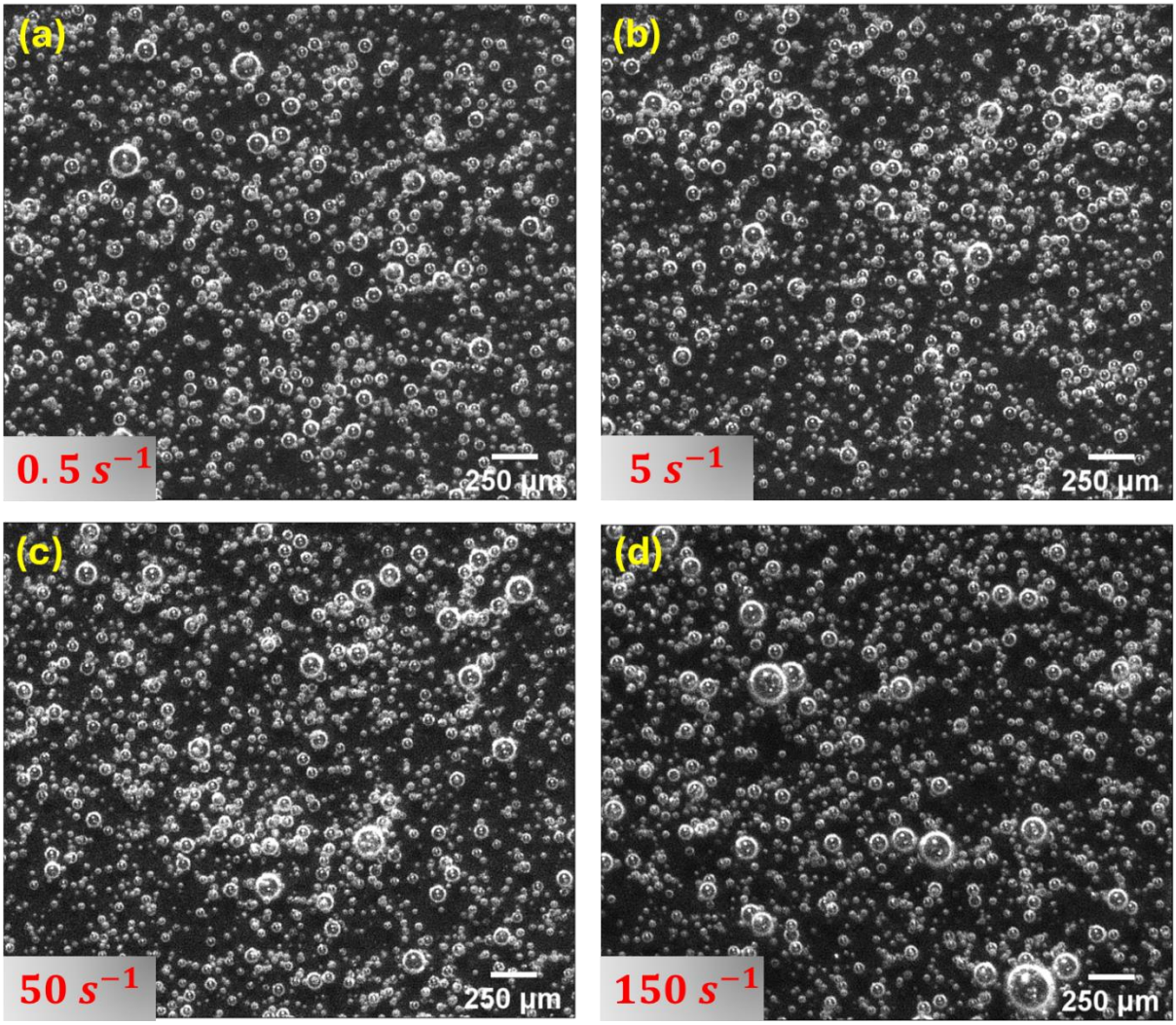

Figure 5.16: Bubble suspension ($\varphi = 4.62\%$) with the ST2 matrix as the ambient fluid, visualised under steady shear at 0.5 s^{-1}, 5 s^{-1}, 50 s^{-1}, and 150 s^{-1}.

Fig. 5.17 compares the variation in the volume-weighted average bubble radius over the same effective shear rate range for a bubble suspension with the ST1 matrix ($\varphi = 4.62\%$) and one with the ST2 matrix ($\varphi = 5.8\%$). As shown, in the ST2 matrix, bubble size remains relatively stable with increasing shear rate, confirming that coalescence is minimal, in contrast to what was observed in the ST1 matrix. This can be attributed to the presence of SDS, which owing to its strong anionic nature, adsorbs on bubble interfaces forming negatively charged monolayers. The presence of these like charges on neighbouring bubbles leads to long-range electrostatic repulsions between them, thereby preventing coalescence phenomena (Sunartio et al., 2007). Furthermore, at the microscale, evidence suggests that SDS at concentrations below or near the CMC can slow thin film drainage between colliding bubbles due to Marangoni stresses arising from surface tension gradients (Bhamla et al., 2017). Specifically, as the fluid film thins, surfactant redistribution creates a restoring force that immobilises the bubble interface and resists further thinning, thereby delaying coalescence.

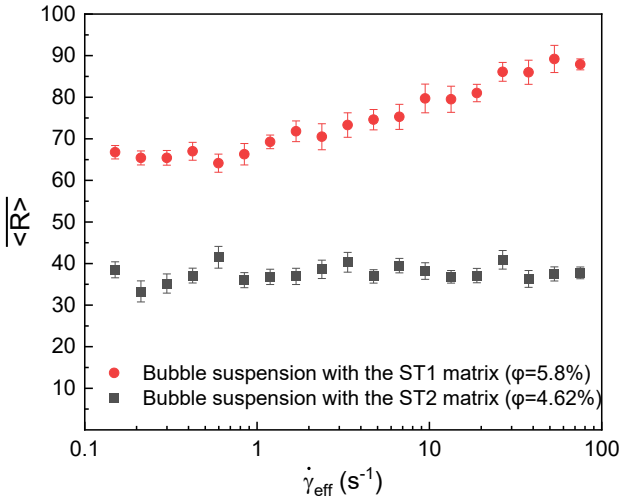

Figure 5.17: Mean volume-weighted average bubble radius (computed through image analysis) as a function of the effective shear rate for a bubble suspension with the ST2 matrix ($\varphi = 4.62\%$) and a bubble suspension with the ST1 matrix ($\varphi = 5.8\%$).

To further compare bubble clustering and alignment phenomena in the ST2 matrix with those observed in the ST1 and Newtonian matrices, the average coverage for the current systems was calculated through image analysis, as described in Sec. 5.3.3. Fig. 5.18 presents the coverage trend for the three visualised bubble suspensions with the ST2 matrix. As shown, the coverage trend follows a similar decreasing pattern as in Newtonian ambient fluids and the ST1 matrix, beginning at effective shear rates around 1 s^{-1}. However, in this case, the decrease in coverage is less pronounced compared to the other two systems. To better highlight the differences among the coverage trends obtained across the different matrices, the data were normalised by the plateau value to remove baseline differences and allow for a direct comparison of the decreasing trends.

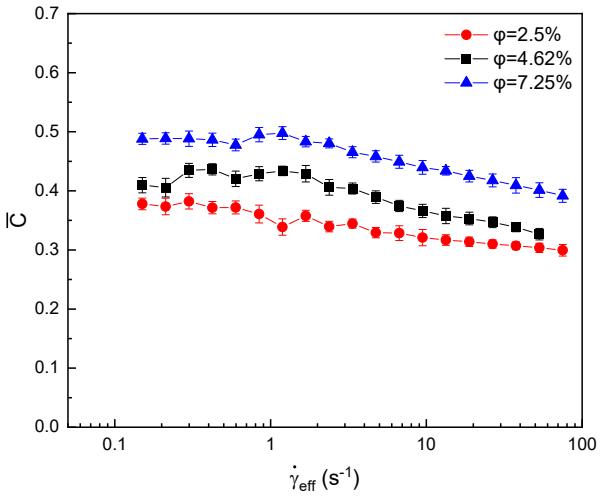

Figure 5.18: Mean coverage as a function of the effective shear rate for bubble suspensions with the ST2 matrix and $\varphi_1 = 2.5\%$, $\varphi_2 = 4.62\%$ and $\varphi_3 = 7.25\%$, respectively.

Fig. 5.19 presents the normalised coverage trends for the ST1 and ST2 matrices, alongside the Newtonian matrix of Chapter 3. Unlike in the ST1 matrix, the coverage trends for the ST2 and Newtonian matrices almost overlap across different bubble volume fractions, indicating that the microstructural changes captured by the coverage trend are driven purely by shear and are not influenced by volume fraction-dependent phenomena, such as coalescence. Moreover, the slope of the coverage trend for the ST2 matrix is less steep than that of the Newtonian matrix, suggesting that while shear-induced bubble clustering occurs in the ST2 matrix, this phenomenon may be weaker compared to Newtonian media.

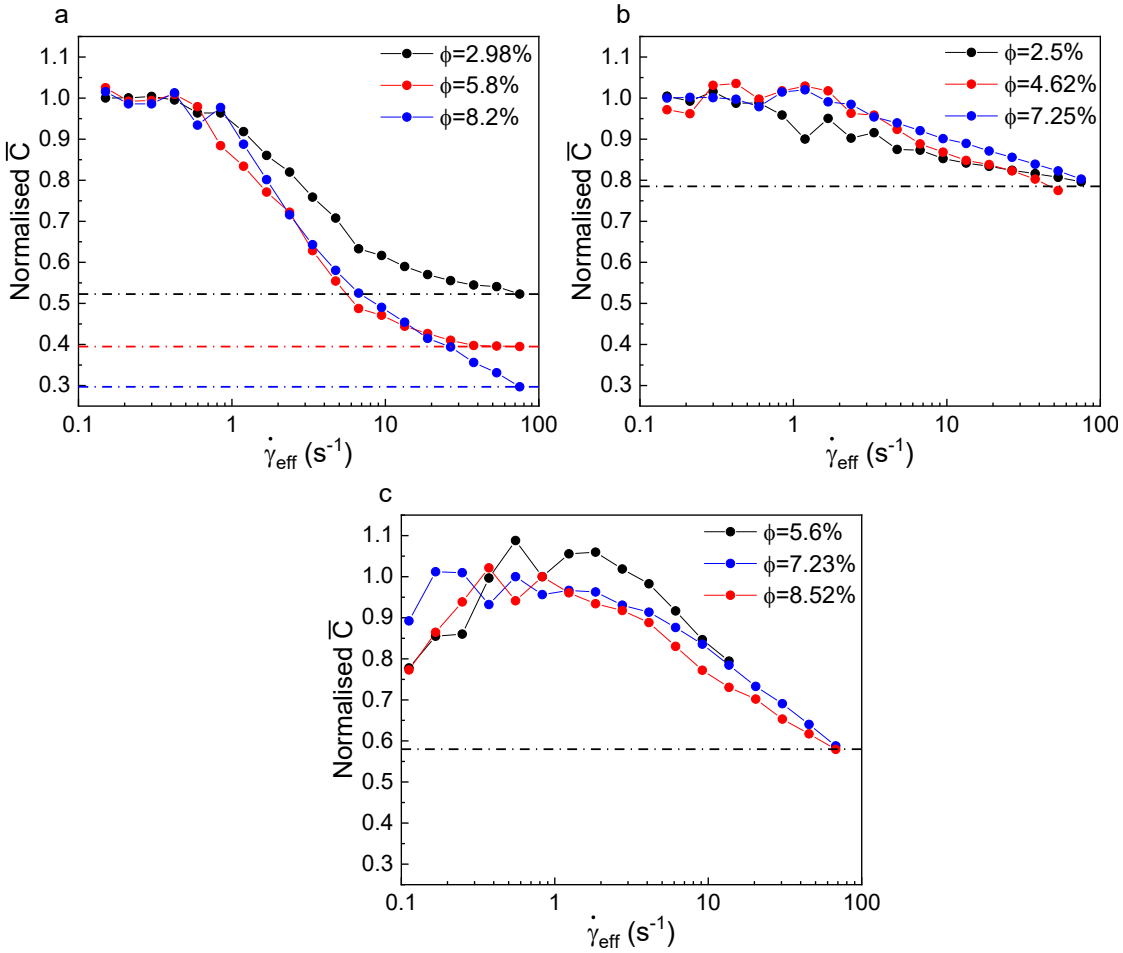

Figure 5.19: Normalised mean coverage trends for (a) the ST1 matrix, (b) the ST2 matrix and (c) the Newtonian matrix studied in Chapter 3. Unlike in the ST1 matrix, the coverage trends for the ST2 and Newtonian matrices almost overlap across different bubble volume fractions, suggesting that the captured microstructural changes are driven purely by shear.

The observed difference in the shear-induced bubble clustering between the ST2 matrix and the Newtonian matrix used in Chapter 3 requires further investigation. A possible explanation for the less pronounced shear-induced clustering observed here lies in the presence of SDS. As mentioned earlier, SDS causes long-range electrostatic repulsions between charged bubbles,

preventing them from coming closer and coalescing. Therefore, it is reasonable to infer that shear-induced clustering could have been mitigated to some extent owing to these electrostatic repulsions. The strong impact of electrostatic repulsions on clustering phenomena has been investigated by Kurz et al. (2021), who reported that the addition of SDS helped disaggregate flocculated droplets in oil/water emulsions.

On the other hand, Span 80, which was used in the Newtonian matrix in Chapter 3, is a non-ionic surfactant that prevents bubble coalescence through steric hindrance and not electrostatic repulsions. The different nature of the surfactants used might explain why addition of Span 80 did not impact shear-induced clustering as SDS did. While this provides a reasonable explanation for the differences in the flow curves and coverage trends of the bubble suspensions with the ST2 matrix, additional mechanisms may also contribute to these trends. It is important to highlight that the suspensions in this study behave as crowded systems with dispersed-phase interactions that potentially impact their behaviour under shear, including clustering/alignment phenomena. Therefore, further experimental work with varying bubble volume fractions and different concentrations of Carbopol and SDS is needed to validate these arguments.

5.5 Conclusions

This chapter explores the effect of matrix rheology on the rheological behaviour of bubble suspensions. To this end, two different shear-thinning inelastic matrices were investigated: (i) a 0.5% wt Carbopol dispersion in a 30/70 wt PEG400/glycerol mixture (ST1 matrix), and (ii) a 0.55% wt Carbopol dispersion in a 30/70 wt PEG400/glycerol mixture containing 35mM SDS (ST2 matrix). Dilute bubble suspensions with these matrices and varying bubble volume fractions were prepared and tested through steady-shear rheological tests and rheo-optical experiments. The viscosity data obtained for both types of bubble suspensions and their respective matrices were fitted to a simplified Carreau-Yasuda equation to assess the impact of bubbles on the shear-thinning behaviour of the matrix. The fitting results indicated that in both cases, the presence of bubbles amplified the shear-thinning behaviour of the matrix, as evidenced by the reduced flow index values of the suspensions. Additionally, the steady-shear rheological tests and rheo-optical experiments provided insights into the effect of matrix composition on the suspension microstructure and the behaviour of bubbles under shear.

Specifically, for the bubble suspensions with the ST1 matrix, the flow curves exhibited the characteristic double decay of relative viscosity, a trend also observed in bubble suspensions with Newtonian ambient fluids. However, in this case, the trend was shifted to average capillary

numbers ($< Ca >$) that were an order of magnitude lower than the $< Ca >$ values at which the double decay was observed in bubble suspensions with Newtonian media. Moreover, the zero-shear viscosities of these suspensions were significantly higher than the predictions of the classic Taylor equation. Instead, the data were well described by the Mooney equation, if one treats the suspensions as having a single dispersed phase with volume fraction equal to the sum of the volume fractions of the swollen Carbopol microgels and of the bubbles. This alignment with the Mooney equation, which accounts for crowding effects and their impact on viscosity, indicates that the suspensions behave as crowded systems with interactions between the two dispersed phases.

To further investigate the shift of the double viscosity decay to smaller $< Ca >$ values and explore potential bubble coalescence, clustering and alignment phenomena, the suspensions were visualised under shear. The visualisation confirmed significant bubble coalescence, which was followed by alignment and clustering of the coalesced bubbles potentially due to wall effects and bubble confinement within the parallel plate gap. These microstructural changes emerged within the shear rate range of approximately 1 s^{-1} to 10 s^{-1} (corresponding to $< Ca >$ values of order of magnitude 0.01), where the first relative viscosity drop was observed. As the shear rate and, in turn, the average capillary number increased further, these phenomena intensified, giving rise to dynamic structures composed of larger, coalesced bubbles that moved collectively under shear. At higher shear rates, toward the upper end of the tested range, deformation of the larger bubbles also became evident. This sequence of interconnected phenomena, including coalescence, the formation of dynamic clusters of coalesced bubbles, and their eventual deformation, was associated with the second viscosity drop, observed at $< Ca >$ values of order magnitude 0.1. The pronounced bubble coalescence phenomena likely stem from the shear-thinning nature of the fluid, which promotes faster drainage of the fluid film between colliding bubbles, and the absence of surfactants, which could otherwise help stabilise bubble interfaces. The causes of earlier bubble deformation at lower capillary numbers (order magnitude 0.l) require further investigation.

The flow curves for the bubble suspensions with the ST2 matrix exhibited distinct differences from those corresponding to the ST1 matrix. Specifically, instead of a double relative viscosity decay, a single decay was observed, occurring over a range of average capillary numbers between approximately 0.01 to 1. This indicates that the addition of SDS significantly altered the bubble-matrix dynamics. Additionally, Carbopol microgels swelled less in the presence of SDS, reducing the effective volume they occupy within the suspension.

Although this reduced swelling likely lessened crowding effects, the zero-shear viscosities of the suspensions remained in good agreement with the predictions of the Mooney equation, indicating that crowding effects and interactions between the two dispersed phases were still present.

To further investigate the absence of the double relative viscosity decay in the bubble suspensions with the ST2 matrix, the suspensions were also visualised under shear. The rheo-optical experiments confirmed that the addition of SDS effectively mitigated coalescence phenomena. As a result, no secondary clustering involving larger, coalesced bubbles were observed, unlike in the ST1 matrix. This marks a key difference in the microstructural evolution of the two systems under shear, which is also reflected in their coverage trends. The trends corresponding to the suspensions with the ST1 matrix exhibited a steeper decrease and a more complex shape compared to those with the ST2 matrix, influenced by the more intricate and interrelated microstructural changes occurring in the former.

Furthermore, rheo-optical observations for the ST2 matrix indicated that at $< Ca >$ values in the range 0.01 to 0.1, where the relative viscosity started to drop, bubbles tended to align or move closer together to form clusters, resembling the shear-induced clustering observed in Newtonian media. No appreciable bubble deformation was observed throughout the course of the rheo-optical experiments, suggesting that this may be the reason why a second drop in relative viscosity was not observed at $< Ca >$ values closer to 1, as in the case of the bubble suspensions with the Newtonian ambient fluid studied in Chapter 3. Statistical image analysis further revealed that shear-induced bubble clustering and alignment in the suspensions with the ST2 matrix were less pronounced than in bubble suspensions with the Newtonian ambient fluid. This difference likely arises from the distinct mechanisms of the surfactants used in the two systems. Specifically, SDS induces electrostatic repulsions that prevent bubbles from getting closer together, thereby reducing shear-induced clustering to some extent. In contrast, Span 80, which was used in the Newtonian matrix of Chapter 3, prevents coalescence through steric hindrance and, therefore, does not affect bubble clustering and alignment.

These findings demonstrate the profound effect of matrix composition on the rheology of bubble suspensions. The presence of an additional dispersed phase (Carbopol microgels) led to crowding effects that had a direct influence of the zero-shear viscosity of the suspensions. Furthermore, the inclusion of a strong anionic surfactant like SDS in the matrix significantly alters the microstructural phenomena under shear and the resulting rheological trends.

Although the experimental results obtained in this study provide a foundation for better understanding the behaviour of bubble suspensions with shear-thinning inelastic matrices, they also highlight that even small changes to matrix composition, such as the addition of surfactant, can significantly impact rheological trends. Therefore, further research with varying matrix compositions is needed to validate the rheological behaviour of these systems and elucidate the intricate interplay between bubbles and the matrix.

Chapter 6

Conclusions and future work

The primary objective of this research was to systematically investigate the influence of bubbles on the rheological properties of matrices with increasing complexity, from simple Newtonian fluids to non-Newtonian shear-thinning matrices relevant to oral health formulations. The study was directly motivated by industrial challenges in the manufacturing of non-aqueous toothpaste formulations, particularly the entrapment of bubbles due to the high-shear mixing process, which has been shown to alter the flow properties of the formulation. The presence of bubbles has been associated with stringiness in the product and inconsistencies in the filling process, ultimately affecting both product quality and manufacturing efficiency. Despite the clear impact of bubbles on formulation behaviour, their influence on the rheology of the matrix remained poorly characterised, necessitating a systematic investigation to quantify their effects and develop a better understanding of the mechanisms governing the rheological behaviour of aerated formulations. Beyond its industrial significance, this research also addresses a critical literature gap in the field of complex fluid rheology, providing reliable experimental data to validate existing rheological models for bubble suspensions. Although prevalent both in nature and industrial applications, the rheology of bubble suspensions has been significantly less explored compared to particle suspensions and emulsions. Key aspects such as the role of polydispersity, the behaviour of suspension microstructure under shear, and the interplay between bubbles and fluid matrix rheology remain poorly understood, making it difficult to predict the behaviour of bubble suspensions in practical applications.

The first aspect was addressed in Chapter 3, which examined the steady-shear viscosity of semi-dilute polydisperse bubble suspensions in a Newtonian ambient fluid consisting of mineral oil and Span 80 (surfactant). The study systematically explored the role of polydispersity in determining suspension viscosity. Theoretical calculations demonstrated that polydispersity has a negligible effect on viscosity unless the bubble size distribution is bimodal, with very small and very large bubbles having comparable volume fractions. In most practical conditions, where bubble sizes follow a gamma-type distribution, polydisperse suspensions can be approximated as monodisperse systems with an equivalent volume-weighted average diameter. To validate these theoretical predictions, steady-shear rheological experiments were performed to obtain the flow curves of the tested suspensions. The results revealed an

unexpected double power-law decay in relative viscosity, spanning a capillary number $< Ca >$ range between 0.01 and 1, a phenomenon that could not be attributed to polydispersity. This indicated that mechanisms other than bubble size distribution were influencing the rheological behaviour of the suspensions. Further investigations using rheo-optical experiments confirmed that the first viscosity drop was associated with the shear-induced formation of bubble clusters and threads, while the second drop was linked to bubble deformation at higher shear rates. These findings highlight the previously unaccounted role of microstructural evolution under shear in defining the viscosity trends of bubble suspensions, revealing a new shear-thinning mechanism that had not been validated experimentally before or considered in theoretical models.

Chapter 4 extended the investigation to the linear viscoelastic properties of semi-dilute polydisperse bubble suspensions in Newtonian matrices, combining small-amplitude oscillatory shear (SAOS) tests with rheo-optical visualisation. This approach allowed for a more reliable assessment of how bubble size distribution and potential measurement artifacts —such as bubble rise, coalescence, and changes in suspension microstructure over time— influence viscoelastic properties. SAOS rheological tests with a pre-shear stage of 3 min at 0.1 s^{-1} showed that at high dynamic capillary number ($< Cd >$) values, the experimental G' values were in good agreement with the predictions of the classic Jeffreys model. However, at lower $< Cd >$ values, deviations emerged, with measured G' exceeding theoretical predictions, suggesting the presence of additional relaxation mechanisms beyond those captured by the model. These discrepancies were more pronounced in denser suspensions, indicating that the underlying phenomena responsible for the observed deviation become more prominent as bubble volume fraction increases. SAOS rheo-optical experiments and image analysis further revealed that the suspension microstructure remained stable during measurements, ruling out potential measurement artifacts, including bubble rise, coalescence, and microstructural evolution during testing, as causes for the observed G' deviations.

Instead, the deviations were linked to bubble fluid dynamic interactions induced by the initial spatial distribution of the bubbles on the rheometer plate before the initiation of the SAOS measurements. These interactions led to complex relaxation phenomena that became evident at longer characteristic flow times. To assess whether stronger and more prolonged pre-shearing could mitigate these effects, additional SAOS measurements were performed using an extended pre-shear stage. The results showed that in dilute suspensions, more intense and prolonged pre-shearing reduced deviations, bringing experimental G' values closer to

theoretical predictions. However, at higher bubble concentrations, pre-shearing had no significant effect on the experimental G' values. Further validation of the bubble fluid dynamic interactions and the associated relaxation phenomena was provided by fitting a multi-mode Jeffreys model to the experimental data. The fitting results confirmed that bubble fluid dynamic interactions induce a complex relaxation process involving multiple relaxation modes, the number of which increases as bubble volume fraction rises. Overall, this study bridged a gap in the literature by providing reliable experimental SAOS data for bubble suspensions in Newtonian media, investigating the effects of potential measurement artifacts on viscoelastic trends, and elucidating the complex relaxation behaviour of these systems.

Building on the findings from Chapters 3 and 4 on the rheology of bubble suspensions with Newtonian matrices, Chapter 5 extended the investigation to non-Newtonian ambient fluids, specifically examining how shear-thinning inelastic matrices influence the flow behaviour of bubble suspensions. Two different matrices were studied: a pure Carbopol dispersion (ST1 matrix) and a Carbopol dispersion containing SDS—an anionic surfactant (ST2 matrix). Steady-shear rheological tests and rheo-optical experiments were conducted to examine how matrix composition affects suspension microstructure under shear and, in turn, the rheological behaviour of these systems. The results showed that in both cases, bubbles amplified the shear-thinning behaviour of the matrix. However, significant differences emerged between the two matrices in terms of bubble coalescence, clustering, and suspension viscosity trends.

For the bubble suspensions generated with the ST1 matrix, the flow curves exhibited a double relative viscosity decay, similar to the trend observed in Newtonian ambient fluids but shifted to an order of magnitude lower capillary numbers ($< Ca >$). Additionally, the zero-shear viscosities of the tested suspensions were significantly higher than those predicted by the classic Taylor equation. Instead, they were well described by the Mooney equation, if one treats the suspensions as having a single dispersed phase with a volume fraction equal to the sum of the volume fractions of the swollen Carbopol microgels and the bubbles. This highlights the influence of crowding effects in the system, suggesting that interactions between the two dispersed phases contribute to the rheological behaviour of the suspensions. Rheo-optical visualisation confirmed significant bubble coalescence, followed by alignment and clustering of the coalesced bubbles, likely due to wall effects arising from the substantial increase in bubble size, to the extent that larger bubbles began experiencing confinement within the parallel plate gap. These microstructural changes started becoming evident at shear rates between 1–10 s^{-1} ($< Ca > \sim 0.01$), aligning with the first viscosity drop. As shear increased

further, these phenomena intensified, leading to the formation of dynamic clusters of coalesced bubbles moving collectively under shear. Toward the upper end of the tested shear rate range, deformation of these larger bubbles also became apparent. This progressive build-up of bubble coalescence, clustering, and eventual deformation contributed to the second viscosity drop, observed at $< Ca >$ values on the order of 0.1. The enhanced bubble coalescence observed in these systems is likely driven by the shear-thinning nature of the matrix, which has been shown to contribute to faster fluid drainage between colliding bubbles, and the absence of surfactants, which could otherwise stabilise bubble interfaces and mitigate such phenomena. Although crowding effects may be linked to the earlier onset of bubble deformation at $< Ca > \sim 0.1$, the precise mechanisms responsible remain unclear and require further investigation.

The flow behaviour of bubble suspensions with the ST2 matrix differed significantly from that of the ST1 systems. Instead of a double relative viscosity decay, a single decay was observed, occurring over $< Ca >$ values of approximately 0.01 to 1, indicating that the presence of SDS significantly altered the microstructural evolution of the suspensions under shear. Additionally, Carbopol microgels swelled less in the presence of SDS, reducing the effective volume they occupied. Although this likely lessened crowding effects compared to the ST1 matrix, zero-shear viscosities remained in good agreement with the Mooney equation, indicating that interactions between bubbles and the dispersed Carbopol microgels were still present. Rheo-optical visualisation revealed that the addition of SDS effectively mitigated bubble coalescence. As a result, no secondary clustering involving larger, coalesced bubbles was observed, unlike in the ST1 suspensions. In the shear rate range of 1–10 s^{-1} ($< Ca > \sim$ 0.01), where the onset of the relative viscosity drop was observed, bubbles tended to align or move closer together due to shear, similar to the behaviour observed in the bubble suspensions with a Newtonian ambient fluid in Chapter 3. No significant bubble deformation was observed throughout the tested shear rate range, suggesting that the observed drop in relative viscosity for the ST2 suspensions can be attributed to shear-induced bubble clustering, and explaining the absence of a second viscosity drop at $< Ca > \approx 0.1$, as observed in the Newtonian system. Further statistical image analysis showed that shear-induced bubble clustering and alignment were less pronounced in the ST2 matrix compared to the Newtonian ambient fluid of Chapter 3. This was attributed to the distinct stabilisation mechanisms of the surfactants used in the two systems. SDS induced electrostatic repulsions, preventing to some extent bubbles from coming closer together and reducing shear-induced clustering, whereas Span 80, used in the Newtonian matrix, stabilised bubbles via steric hindrance but did not inhibit clustering or alignment.

The findings of Chapter 5 highlight the profound effect of matrix composition on the rheology of bubble suspensions. The presence of an additional dispersed phase (Carbopol microgels) introduced crowding effects that strongly influenced suspension viscosity, while the addition of SDS significantly altered microstructural effects under shear, reducing shear-induced bubble clustering and preventing bubble coalescence. This study provides a foundation for understanding the rheology of bubble suspensions with shear-thinning inelastic matrices, but it also underscores the sensitivity of rheological trends to even small changes in matrix composition.

6.1 Future work

While this research has provided valuable insights into the rheological behaviour of bubble suspensions across different fluid matrices, several open questions remain, paving the way for further investigation. Future work should focus on expanding the current findings by further exploring the influence of matrix composition and microstructure on suspension rheology, investigating the linear viscoelastic behaviour of bubble suspensions with more complex non-Newtonian matrices, and building a deeper understanding of shear-induced phenomena and bubble coalescence in flow for both Newtonian and more complex systems through advanced microscopic and rheo-optical techniques.

Effect of matrix composition and microstructure on suspension rheology

The findings of Chapter 5 demonstrated that even small changes in matrix composition can have a significant impact on the rheology of bubble suspensions, highlighting the importance of matrix-specific microstructure. The comparison between two shear-thinning Carbopol matrices—one containing SDS and one without—revealed substantial differences in bubble coalescence, shear-induced clustering/alignment, and the resulting relative viscosity trends. This underscores the need for further investigation into how variations in matrix composition influence suspension behaviour and whether certain rheological trends can be generalised across different shear-thinning systems. Building on these findings, a key avenue for future work would be to systematically investigate the effects of varying Carbopol and SDS concentrations to assess how these fundamental matrix components influence suspension rheology. Increasing Carbopol concentration is expected to induce yield stress and elasticity effects (Migliozzi et al., 2020), introducing behaviours that could fundamentally alter bubble deformation, clustering, coalescence, and consequently, the resulting suspension flow properties. Similarly, since SDS was shown to directly influence shear-induced bubble

clustering and alignment, exploring how the system behaves across different SDS concentrations would provide critical insight into the interplay between surfactant-induced interfacial forces and the evolving suspension microstructure.

Beyond variations in Carbopol and SDS concentrations, a broader exploration of different shear-thinning matrices and surfactant types is also necessary to determine whether the observed flow phenomena are intrinsic to the specific microstructure of the tested matrices or whether they represent more general trends in bubble suspensions with shear-thinning ambient fluids. Understanding how different formulation components influence aerated suspension rheology would aid in developing more robust design principles for complex formulations, ensuring consistent rheological properties across product lines. By systematically disentangling the effects of matrix composition, microstructure, and surfactant properties, future research could provide a more predictive framework for the flow behaviour of bubble suspensions in complex fluids.

Viscoelastic behaviour of bubble suspensions in non-Newtonian matrices

A logical extension of this work would be to investigate the linear viscoelastic properties of bubble suspensions in non-Newtonian matrices, expanding on the steady-shear characterisation conducted in Chapter 5 and complementing the SAOS experiments performed for Newtonian systems in Chapter 4. As demonstrated in Chapter 4, bubble fluid dynamic interactions induced by the spatial distribution of bubbles at the microscale led to complex relaxation phenomena, even in Newtonian matrices. These interactions resulted in multi-mode relaxation behaviour, which became more pronounced as bubble volume fraction increased. Given that non-Newtonian matrices already exhibit intricate relaxation dynamics, the introduction of bubbles adds another level of complexity, potentially leading to interactions between matrix and dispersed phase relaxation mechanisms that cannot be easily predicted. This is further supported by the findings in Chapter 5, where steady-shear rheological experiments revealed that microscale interactions between bubbles and the Carbopol matrix played a critical role in shaping the suspension flow behaviour.

It would therefore be of great interest to investigate how these interactions manifest in the linear viscoelastic regime and whether they give rise to new viscoelastic mechanisms that are absent in Newtonian systems. A systematic study using small-amplitude oscillatory shear (SAOS) tests combined with rheo-optical analysis would provide essential experimental data to address the current gap in the viscoelastic characterisation of bubble suspensions,

particularly in non-Newtonian matrices. While some non-linear viscoelastic data, such as normal stress differences, have been reported for bubble suspensions in non-Newtonian matrices (Torres et al., 2013, 2015), SAOS data remain largely unavailable. However, since SAOS measurements directly capture microstructural relaxation dynamics, which govern flow behaviour under shear, obtaining such data would be invaluable for advancing both theoretical understanding and industrial applications.

Enhancements to the rheo-optical setup for advanced microstructural analysis

Across the different result chapters of this thesis, it became evident that microstructural evolution under shear plays a fundamental role in determining the rheological behaviour of bubble suspensions. Rheo-optical experiments provided valuable insights into bubble coalescence and shear-induced clustering and alignment, revealing complex microstructural rearrangements that directly influenced suspension flow properties. However, the current optical setup presents several limitations that hinder a more detailed and quantitative understanding of these processes. One of the main limitations was slip at the transparent rheometer plate, which led to lower torque measurements compared to those obtained with standard rheometric plates. As a result, simultaneous bulk rheological measurements and direct visualisation of the same sample were not possible, requiring separate experiments for each. Additionally, the resolution of the acquired images was insufficient for advanced image analysis, limiting the ability to track individual bubble clusters, quantify cluster sizes, and fully resolve microstructural evolution in three dimensions.

To overcome these constraints, future work should focus on employing more advanced rheo-optical techniques to gain a comprehensive understanding of microstructural evolution in flow. A key improvement in the current setup would be plasma treatment of the transparent rheometer plate, which could effectively reduce slip phenomena while maintaining optical transparency. Plasma treatment modifies surface properties by generating highly energetic ionised gases that alter surface chemistry and roughness without introducing physical damage. This method has been shown to increase surface roughness, thereby enhancing interfacial friction and minimising wall slip (Ma et al., 2023), allowing for a more accurate assessment of bulk rheological properties while still preserving transparency for real-time microstructural visualisation. Additionally, because plasma treatment is an inert and contamination-free process, it does not introduce any surface residues or reactive compounds that could interfere with suspension microstructure or rheological measurements (Ma et al., 2023).

Beyond transparent plate modifications, the integration of confocal rheometry would provide a direct correlation between local microstructural evolution and bulk rheological response. This technique integrates a laser scanning confocal microscope with a stress-controlled rheometer, enabling high-resolution 3D imaging alongside simultaneous stress and strain measurements (Dutta et al., 2013). By providing real-time, depth-resolved imaging, it allows direct observation of microstructural dynamics—such as bubble clustering, alignment, and coalescence—and their influence on the material's bulk viscosity and elasticity. Confocal rheometry has been successfully applied to study colloidal suspensions and complex fluids (Cheng et al., 2011), and its application here would allow for quantitative microstructural analysis beyond what was possible in this study, including tracking bubble trajectories, measuring cluster size distributions, and analysing structural evolution over time. These enhanced imaging capabilities would provide a more complete picture of the dynamic processes governing bubble suspension microstructure under shear and their impact on the system's rheological response, ultimately improving rheological models for bubble suspensions and aiding the development of more robust, controlled, and scalable industrial formulations.

Appendix A

Supporting Information to Chapter 3

A1. Propeller Aerator Design Schematics

This section presents detailed design schematics of the custom-built aeration device developed in-house for generating the bubble suspensions used in this thesis. The initial design incorporated 10 µm porous ceramic filters, which were later replaced with 2 µm filters to produce smaller bubbles and thereby more stable suspensions.

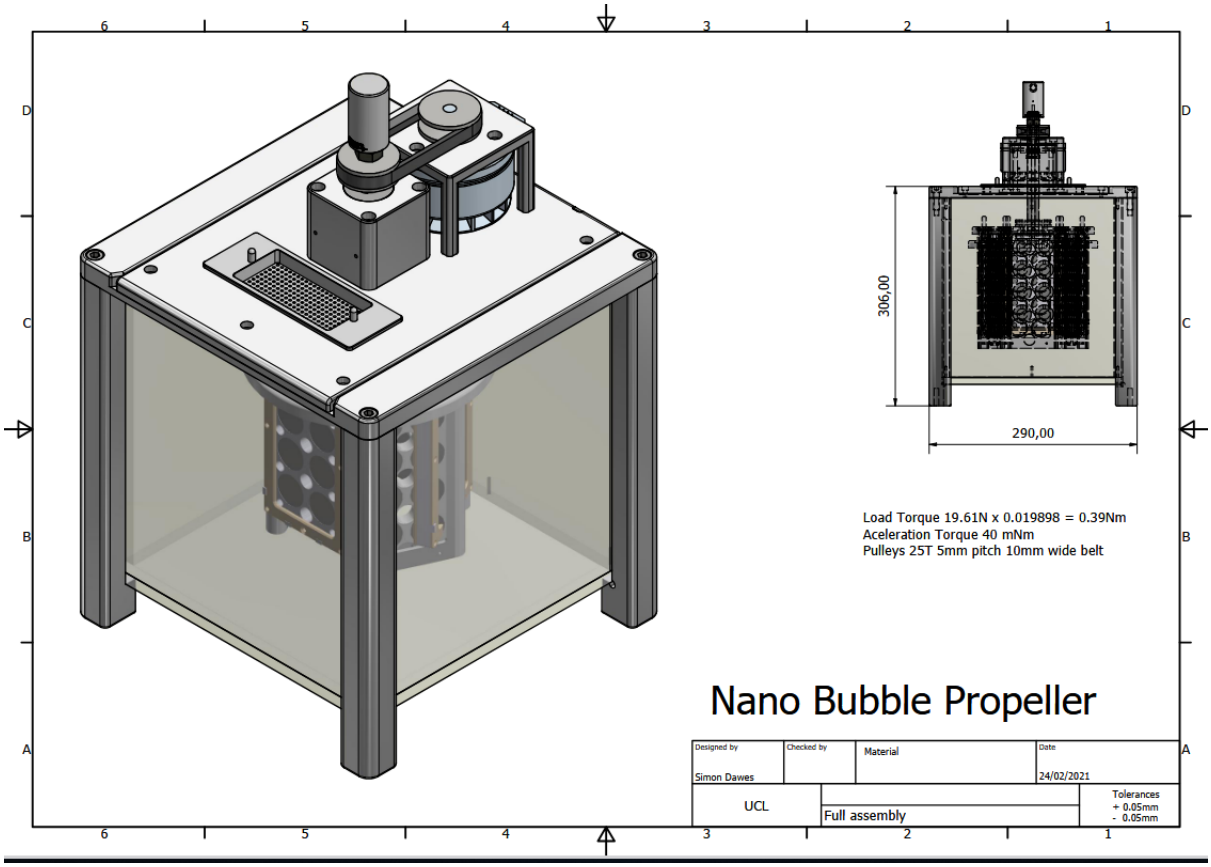

Fig A. 1: 3D design and dimensions of the custom aeration device for bubble suspension generation.

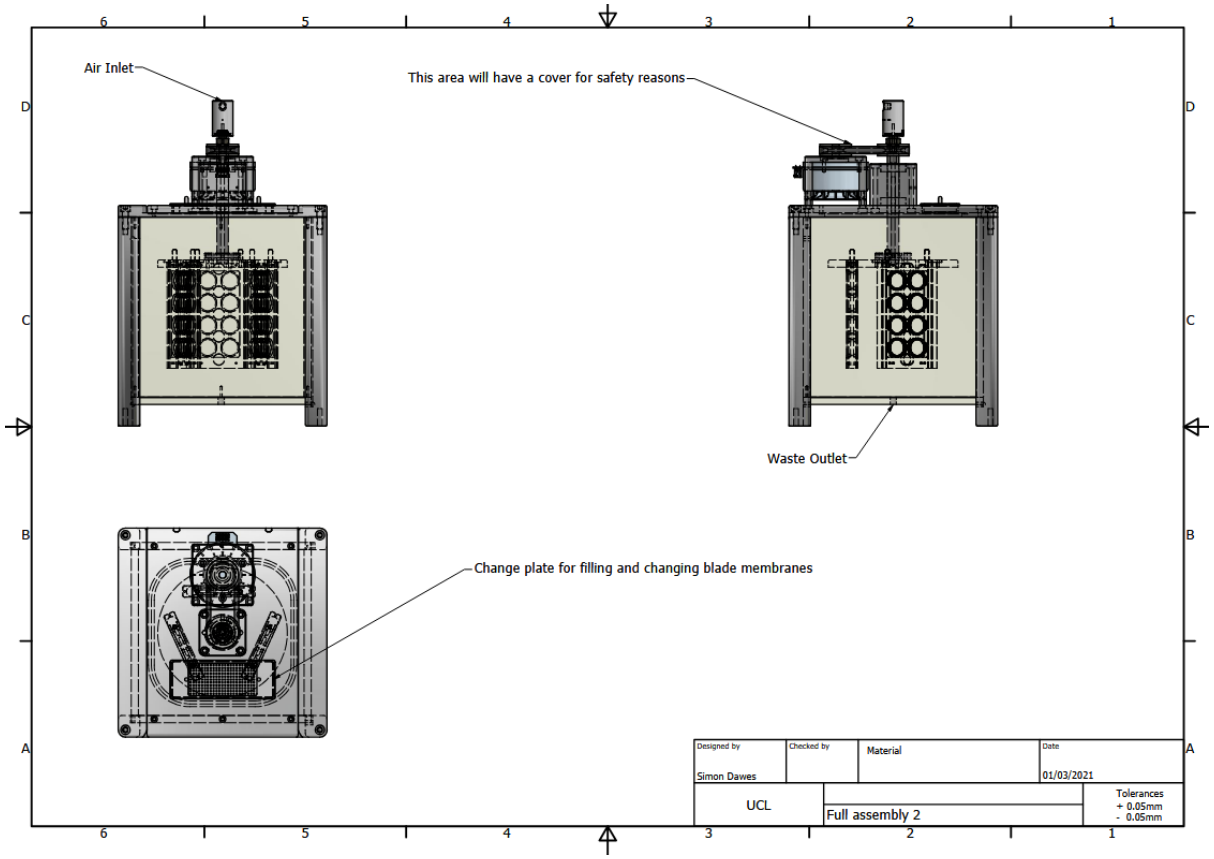

Fig A. 2: Multi-view schematics of the custom aeration system. Front, side, and top views show the location of key components.

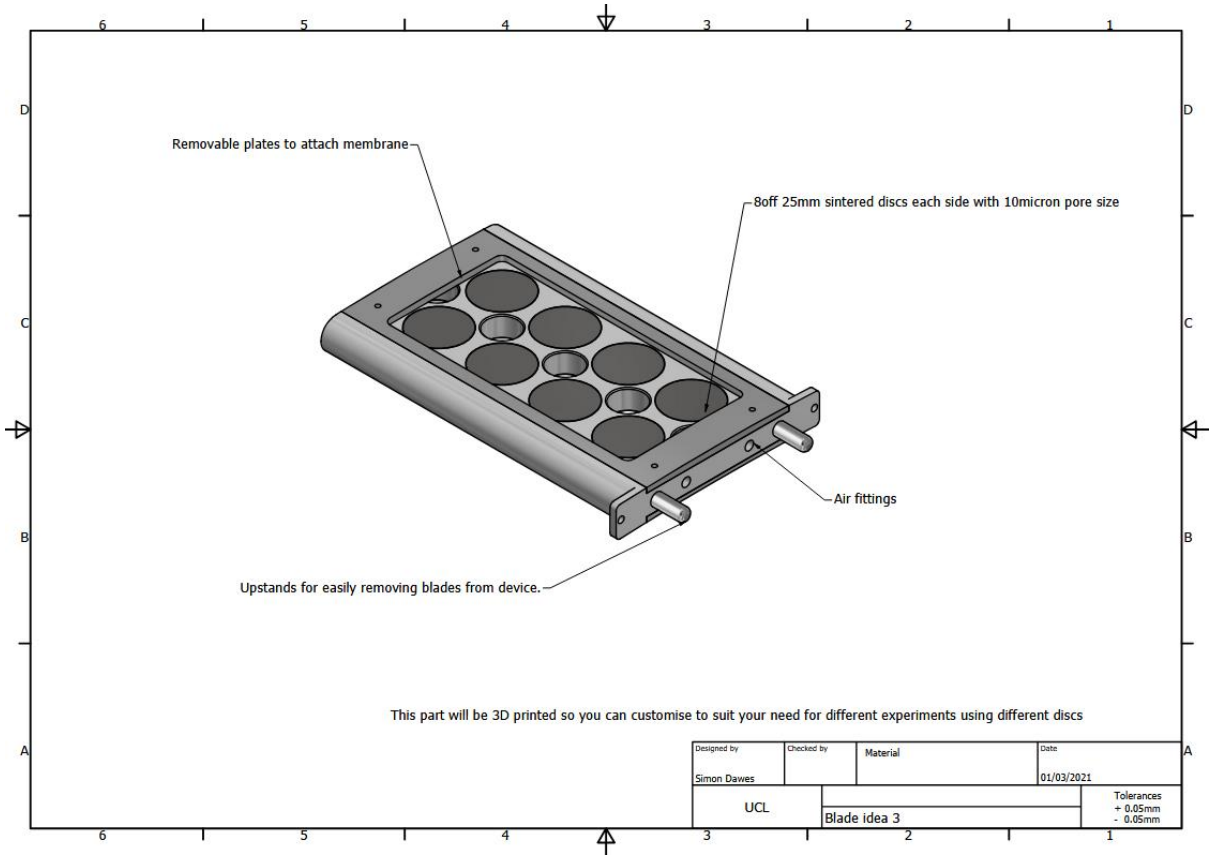

Fig A. 3: Design schematic of the aeration blade used in the custom aeration device. The part was designed for 3D printing to allow customisation with different disc configurations for experimental variations.

A2. Characteristic Microscope Image

This section presents a representative bright-field microscope image of a generated bubble suspension, acquired with a Zeiss Axio Observer 5 microscope (10× Plan-Apochromat objective). The image corresponds to a suspension with a gas volume fraction of φ = 4.2 %, illustrating the typical gamma-type bubble size distribution produced with the custom aeration device.

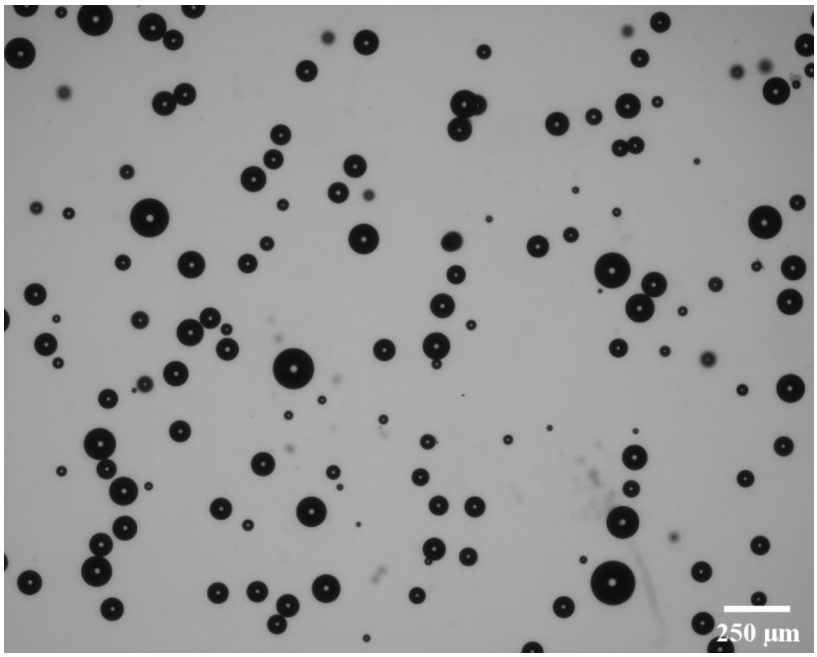

Fig A. 4: Bright-field image (10× magnification) acquired with a Zeiss Axio Observer 5 microscope. The sample corresponds to a suspension with φ = 4.2 %, showing uniformly dispersed bubbles used for rheological testing.

A3. Weissenberg – Rabinowitch Correction

This section describes the Weissenberg-Rabinowitsch correction, applied to the raw steady shear data obtained with a parallel plate rotational rheometer. Let us consider a rotational parallel plate rheometer with diameter R, gap h, and a constant rotational speed Ω.

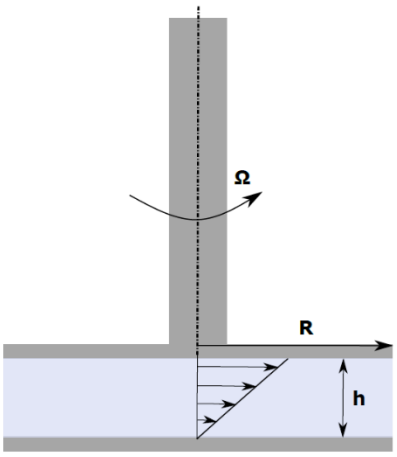

Fig A. 5: Schematic of a parallel plate rheometer.

Regardless of the rheological properties of the fluid between the parallel plates, the shear rate $\dot{\gamma}$ in the fluid volume is not uniform, but changes radially as follows:

$$\dot{\gamma}(r) = \frac{\Omega}{h} r \tag{A1}$$

The torque M required to move the upper plate is the product of the surface integral of the local viscous force exerted on a single fluid element, and its distance r from the centre of the plate (Macosko, 1994).

$$M = \int_0^R 2\pi r dr \tau_{z\theta} \cdot r = \int_0^R 2\pi r^2 \tau_{z\theta} dr = \int_0^R r^2 \eta(r) \dot{\gamma} dr \qquad \text{(A2)},$$

where $\eta(r)$ is the viscosity at any value of r.

Since both $\eta(r)$ and $\dot{\gamma}_r$ are bijective functions of r, the integration variable in Eq. A2 can be changed from r to $\dot{\gamma}$ as follows:

$$r = f(\dot{\gamma}) = \frac{\dot{\gamma} h}{\Omega}\,;\; f'(\dot{\gamma}) = \frac{h}{\Omega} \tag{A3}$$

Substituting Eq. A3 into Eq. A2, we obtain:

$$M = \frac{2\pi R^3}{\dot{\gamma}^3} \int_0^{\dot{\gamma}_E} \dot{\gamma}^3 \eta d\dot{\gamma} \qquad \text{(A4)},$$

where $\dot{\gamma}_E = \frac{\Omega R}{h}$ is the shear rate at the edge of the plate. To eliminate the integral, we differentiate both sides by $\dot{\gamma}_E$ using the Leibnitz rule:

$$\left(\frac{M}{2\pi R^3}\right)\dot{\gamma}^3 = \int_0^{\dot{\gamma}_E} \dot{\gamma}^3 \eta d\dot{\gamma} \tag{A5}$$

$$\frac{d}{d\dot{\gamma}_E}\left[\left(\frac{M}{2\pi R^3}\right)\dot{\gamma}_E{}^3\right] = \int_0^{\dot{\gamma}_E} \frac{\vartheta}{\vartheta\dot{\gamma}_E}(\dot{\gamma}^3\eta)d\dot{\gamma} + \eta(\dot{\gamma}_E)\dot{\gamma}_E^3 \tag{A6}$$

The first term on the right-hand side of Eq. A6 is equal to zero. After rearranging and deriving both terms for $\dot{\gamma}_E$, we obtain Eq. A7 for the steady shear viscosity measured in a parallel-disk rheometer:

$$\eta(\dot{\gamma}_E) = \frac{M\left(3+\frac{dlnM}{d\dot{\gamma}_E}\right)}{2\pi R^3 \dot{\gamma}_E} \tag{A7}$$

Therefore, by plotting the curve of M versus the effective shear rate (i.e the shear rate at the edge) $\dot{\gamma}_E$, we can evaluate the ratio $dlnM/d\dot{\gamma}_E$ as the local slope (n) of the graph plotted in log-log scale, and re-construct the true viscosity curve.

In contrast, if this correction is not applied, the apparent viscosity is overestimated by assuming a uniform shear rate across the plate radius. The fractional error eliminated by the Weissenberg–Rabinowitsch correction can be expressed as $(\eta - \eta_{\text{app}})/\eta = s/(3+s)$, where $s = d\ln M/d\ln \dot{\gamma}_E$ represents the local slope of the log–log torque–shear rate relationship. For the present measurements, the slope ranged from $s = 0.77$–1.00, corresponding to an error reduction of approximately 20–25%. Neglecting the correction would therefore lead to a comparable underestimation of the true viscosity, while applying it ensures accurate evaluation of the shear-dependent viscosity of the bubble suspensions.

Appendix B

Supporting Information to Chapter 4

B1. Rheological characterisation of the ambient fluid

To ensure that the rheology of the ambient fluid did not affect the observed viscoelastic trends, a rheological characterisation of the matrix, i.e., of the mixture of mineral oil and span 80, was conducted. Fig. B.1 presents the flow and viscoelastic curves. As shown, the viscosity remains constant as the shear rate varies. Observing the G' curve, the influence of both inertia effects (at high frequency) and low torque issues (at low frequency) becomes evident. Nonetheless, within the range of reliable G' data, the measured values are consistently three orders of magnitude lower than the corresponding G'' values. This indicates that, within the tested frequency range, the response of the ambient fluid is predominantly viscous. Additionally, Fig. B.2 reports the G' curves of the suspensions detailed in Sec. 4.3.2 in comparison to the G' curve of the matrix. As seen, even for the most dilute bubble suspension, the measured G' values are one order of magnitude larger than those of the matrix. This difference amplifies with increasing bubble volume fraction. Consequently, the elastic contribution of the matrix appears to be negligible and cannot account for the viscoelastic trends observed for the bubble suspensions.

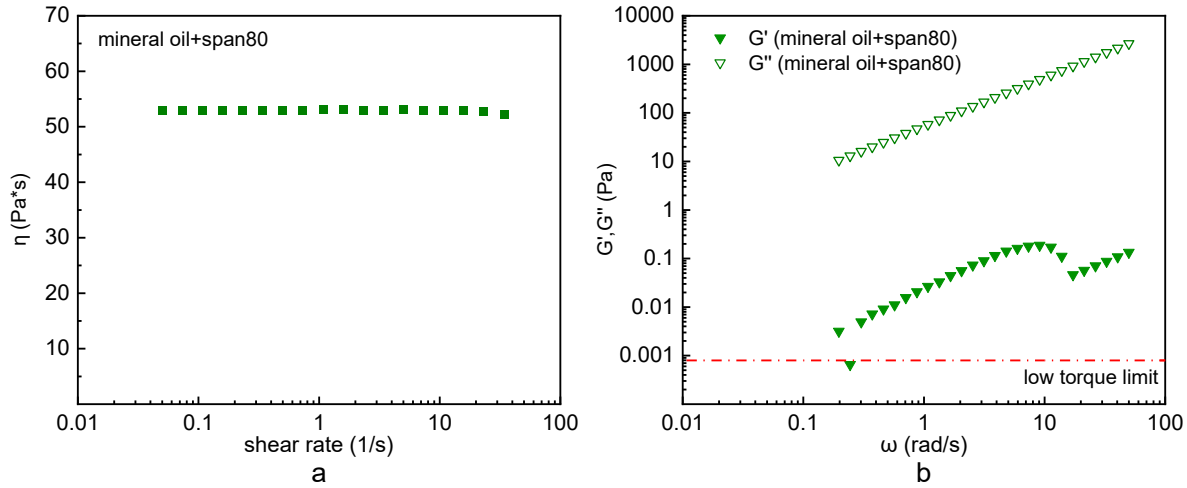

Figure B.6: (a) Viscosity as a function of shear rate. (b) Viscoelastic moduli of the ambient fluid (mixture of mineral oil and span 80).

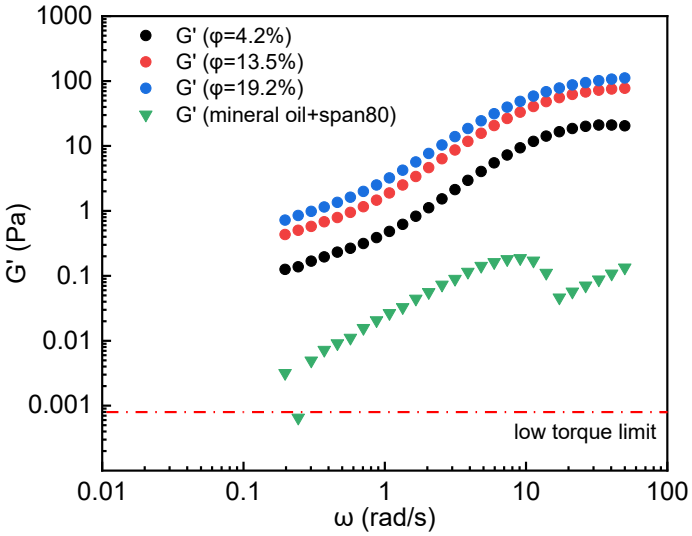

Figure B.7: G' values of the matrix (mixture of mineral oil and span 80) compared to G' values of the tested suspensions.

To determine whether the presence of span 80 in the ambient fluid affected the observed viscoelastic trends, SAOS measurements were conducted using a bubble suspension with pure mineral oil ($\eta = 63.571\ \mathrm{Pa \cdot s}$ at 20 °C) as the ambient fluid. Note that this is not the same mineral oil employed in the mixture, but a more viscous one. The viscoelastic response of the pure mineral oil, depicted in Fig. B.3a, closely resembles that of the mixture of mineral oil and span 80. The measured G'' values once again exceed the corresponding G' values by three orders of magnitude, suggesting that the addition of span 80 does not affect the overall matrix response.

The rationale behind incorporating span 80 into the ambient fluid lies in its ability to reduce the exceptionally high viscosity of the pure mineral oil, which presented challenges in generating bubble suspensions with varying bubble volume fractions. In contrast, the mixture of mineral oil and span 80 offers a suitable viscosity, facilitating the production of stable suspensions with minimal bubble rise during the measurements.

Fig. B.3b shows the viscoelastic curves of a bubble suspension with $\varphi = 9.2\%$ and pure mineral oil ($\eta = 63.571\ \mathrm{Pa \cdot s}$ at 20 °C) as ambient fluid, obtained through SAOS measurements with decreasing oscillation frequency and after 3 min of pre-shear at 0.1 s^{-1}. It is evident that the characteristic G' shoulder at low $\langle Cd \rangle$ values is present regardless of the ambient fluid, indicating that the observed trends are not system-specific.

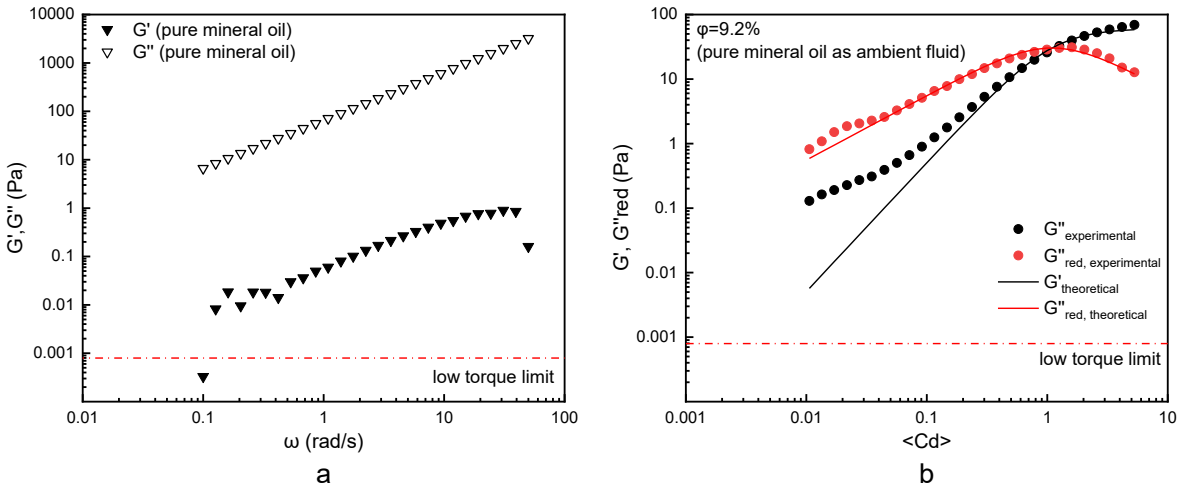

Figure B.8: (a) G', G'' for pure mineral oil (η=63.571 Pa·s at 20 ◦C). (b) G', G''_{red} for a bubble suspension with $\varphi = 9.2\%$ and pure mineral oil (η=63.571 Pa·s at 20 ◦C) as ambient fluid.

Finally, to investigate potential degradations and/or reactions during high-shear mixing that could affect the viscoelastic behaviour of the ambient fluid, the viscoelastic moduli of the aforementioned pure mineral oil were measured before and after aeration. The results, presented in Fig. B.4, indicate that the viscoelastic response of the matrix is unaffected by high-shear mixing. All the findings discussed thus far confirm that the rheology of the matrix is not responsible for the characteristic G' shoulder observed at low $\langle Cd \rangle$ values.

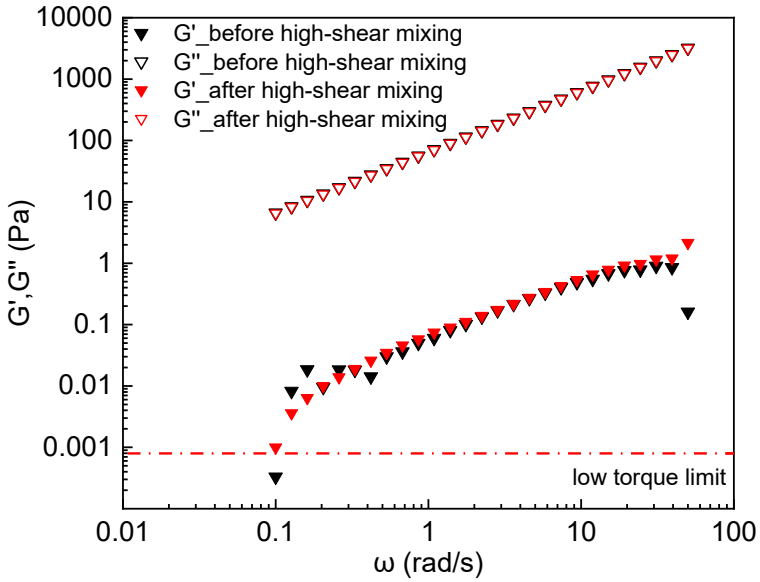

Figure B.9: Viscoelastic curves for pure mineral oil (η=63.571 Pa·s at 20 ◦C) obtained before and after high-shear mixing.

B2. Strain sweep experiments to determine the limits of the linear viscoelastic regime

As mentioned in Sec. 4.2.2, strain sweep experiments were performed to determine the limits of the linear viscoelastic regime. Fig. B.5 presents the G' and G'' curves obtained for a

bubble suspension with $\varphi = 9.5\%$ at $\omega_1 = 0.56$ rad/s, $\omega_2 = 1$ rad/s and $\omega_3 = 10$ rad/s. As seen, both viscoelastic moduli are constant over the examined range of applied strain, suggesting that any strain value within this range is appropriate for the SAOS measurements.

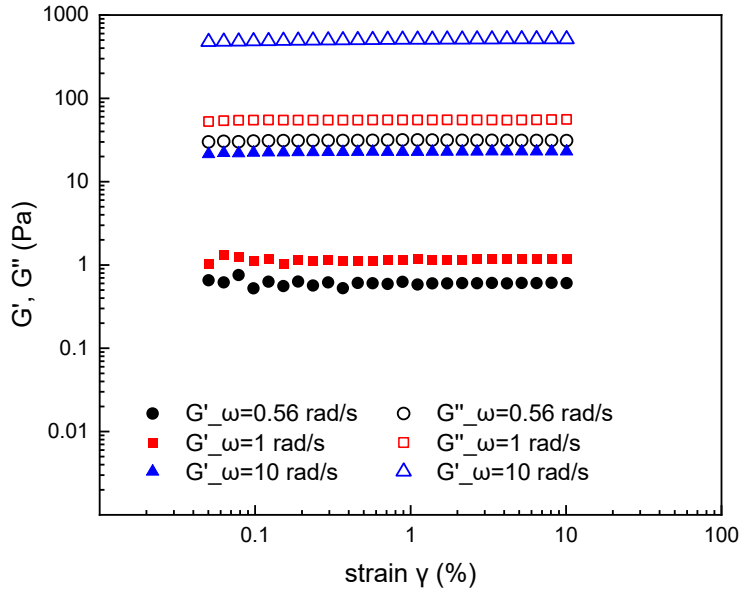

Figure B.10: Strain sweep tests to determine the limits of the linear viscoelastic behaviour.

B3. Reliability of SAOS data at low oscillation frequencies

This section evaluates the reliability of the SAOS data discussed in Sec. 4.3.2.

B3.1 Minimum torque limit

To ensure reliable G' and G''_{red} data in the low oscillation frequency range, it is essential to verify that the measured torque is above a minimum limit. According to (Ewoldt, Johnston and Caretta, 2015), the minimum acceptable G' and G''_{red} values for a material tested in a parallel plate rheometer are given by:

$$G_{min} = \frac{F_\tau \, T_{min}}{\gamma_0} \tag{B.1}$$

where G_{min} refers to either G' or G''_{red}, $F_\tau \equiv \frac{2}{\pi R^3}$, with R being the radius of the plate, T_{min} is the minimum torque in oscillation as specified by the instrument manufacturer, and γ_0 is the strain amplitude.

For the current measurements, which were performed in the Anton Paar MCR302 stress control rheometer, R is equal to 20 mm, T_{min} is equal to 0.5 nN m, and γ_0 is equal to 5%. Substituting these quantities into Eq. 1 yields:

$$G_{min} = 7.96 * 10^{-4} \text{ Pa s} \tag{B.2}$$

The limit of G_{min} has been included in all graphs presenting experimental values of G' and G''_{red}. As shown in Fig. 4.2, all reported measurements are above the G_{min} limit.

B3.2 Phase angle resolution issues at low frequencies

To address potential phase angle resolution issues at low frequencies that could impact the rheological data, the method presented by (Velankar and Giles, 2007) was implemented. A bubble suspension with volume fraction φ equal to 3.1% was generated, and strain sweep tests were performed at different frequencies. For each frequency, the measured values of $\tan\delta$ were plotted as a function of the applied strain amplitude. Fig. B.6 presents indicative results of the strain sweep tests at oscillation frequencies $\omega_1 = 3$ rad/s and $\omega_2 = 0.302$ rad/s. As observed, at sufficiently high strain amplitudes, $\tan\delta$ plateaus. However, for each oscillation frequency, there is a minimum value of the applied strain amplitude, γ_{min}, below which $\tan\delta$ deviates from the plateau, indicating the onset of phase angle resolution issues. This aspect should be investigated, inasmuch as it might lead to inaccuracies during SAOS experiments, where the applied strain amplitude is usually fixed throughout the whole range of the tested frequencies.

In the SAOS experiments reported in Chapter 4, a fixed strain amplitude γ_0 of 5% was used. To ensure that this strain amplitude was appropriate for the lower frequencies considered, the minimum strain amplitude γ_{min} at each frequency was identified from the strain sweep tests. Then, the γ_{min} values were plotted versus the values of the respective oscillation frequencies, generating the diagram reported in Fig. B.7. This graph illustrates the instrumental limitations related to measuring phase angles. As shown, for $\omega = 0.107$ rad/s, γ_{min} is 5%, indicating that the chosen strain amplitude is within the acceptable limits for $\omega \geq 0.107$ rad/s. This suggests that in this frequency range the SAOS data are not influenced by phase angle resolution issues, and that the reported viscoelastic trends (Figs. 4.2 and 4.6) can be trusted.

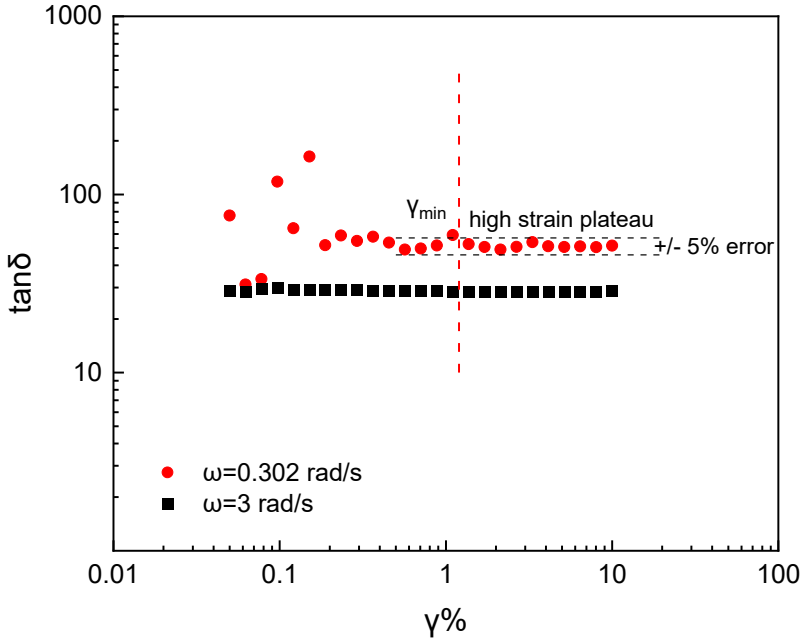

Figure B.11: Strain sweep measurements at two different frequencies. The horizontal dashed lines indicate the high-strain plateau of tanδ at $\omega = 0.302$ rad/s, considering +/- 5% error limits. The vertical dashed line indicates the minimum value of the strain amplitude, γ_{min}, required for reliable phase angle measurements.

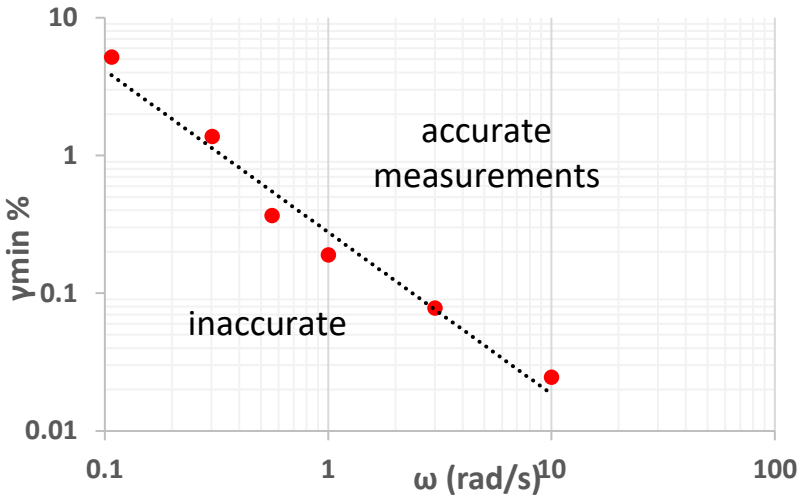

Figure B.12: Minimum strain amplitude, γ_{min}, as a function of the oscillation frequency.

B4. Percent G' deviation versus bubble volume fraction

The deviation of G' observed at lower frequencies in the experiments described in Chapter 4 is not the same for all tested samples. As shown in Fig. 4.3, denser suspensions demonstrate two main effects: (i) a shift of the G' deviation towards higher values of the dynamic capillary number $\langle Cd \rangle$, and (ii) a larger absolute deviation of G' from the theoretical predictions. To further clarify this point, Fig. B.8 presents the percent G' deviation as a function of $\langle Cd \rangle$ for the two extreme bubble volume fractions: $\varphi_1 = 4.2\%$ and $\varphi_2 = 19.2\%$.

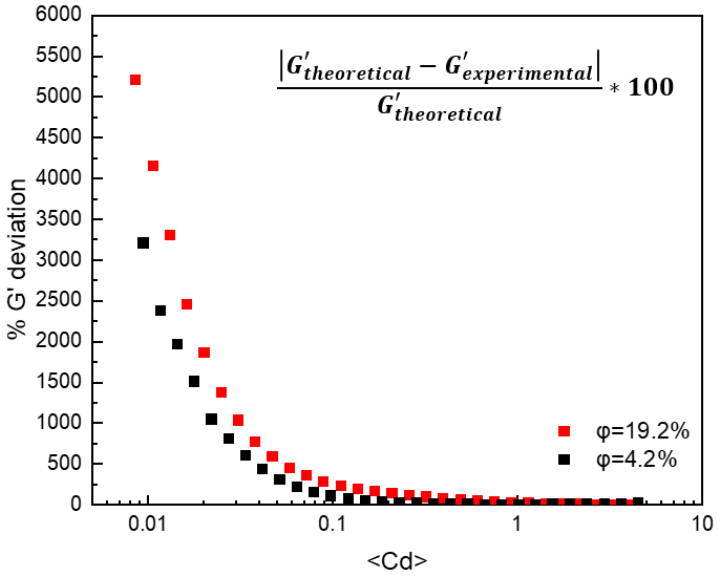

Figure B.13: Percent G' deviation at low dynamic capillary number for $\varphi_1 = 4.2\%$ and $\varphi_2 = 19.2\%$.

As illustrated, within the same low range of $\langle Cd \rangle$, the experimental values of G' deviate more from the theoretical predictions at higher bubble volume fraction, the densest suspension deviating almost twice as much compared to the most dilute one. Additionally, for the smallest volume fraction ($\varphi_1 = 4.2\%$), the findings indicate that applying stronger and more prolonged pre-shearing results in a closer similarity with the theoretical predictions, the percent deviation of G' being almost five times smaller than that at milder pre-shearing. This suggests that – for such a dilute suspension – pre-shearing affects the spatial bubble distribution as well as the average inter-bubble distance, resulting (for stronger/longer pre-shearing) in weaker fluid dynamic interactions and a smaller deviation between experimental data and theoretical predictions.

B5. Theoretical analysis on polydispersity

This section provides a theoretical analysis of the effect of polydispersity on the linear viscoelastic moduli of semi-dilute bubble suspensions. In this analysis, a bubble suspension composed of a mixture of mineral oil and 5% w/w span 80 was considered, with a bubble volume fraction of 4.2% and different bubble sizes. The linear viscoelastic moduli of the suspension were calculated for three different bubble size distributions using the generalised Jeffreys model (Eq. 4.8). The volume fraction φ_i of the i-th bubble class present in the suspension was determined using Eq. 3.5. Below, three theoretical scenarios are presented to examine how different bubble size distributions affect the profiles of the linear viscoelastic moduli of the corresponding suspensions. For each theoretical example, G' and G''_{red} were plotted as functions of the average dynamic capillary number $\langle Cd \rangle$.

B5.1 Scenario 1 - Bimodal distribution ($R_1 = 10\ \mu m$, $R_2 = 500\ \mu m$)

The first scenario examines a bidisperse bubble suspension with bubble radii equal to 10 μm and 500 μm. In this case, the two bubble classes contribute equally to the total bubble volume fraction (that is, each class accounts for 50% of the total bubble volume), so that the volume-weighted average radius is equal to 255 μm. Calculating G' and G''_{red} for this suspension yielded the curves of Fig. B.9.

This example reveals a complex G' trend, consisting of two distinct modes, each of them corresponding to a bubble size class. To better understand the effect of polydispersity on the G' curve, the average dynamic capillary number can be correlated with the dynamic capillary number of each size class, as follows:

$$Cd_i \equiv \frac{\eta_s R_i \omega}{\sigma_{\alpha,\beta}} = \frac{\eta_s \langle R \rangle \omega}{\sigma_{\alpha,\beta}} \frac{R_i}{\langle R \rangle} \equiv \langle Cd \rangle \frac{R_i}{\langle R \rangle} \tag{B.3}$$

which results in:

$$\langle Cd \rangle = \frac{\langle R \rangle}{R_i} Cd_i \tag{A.4}$$

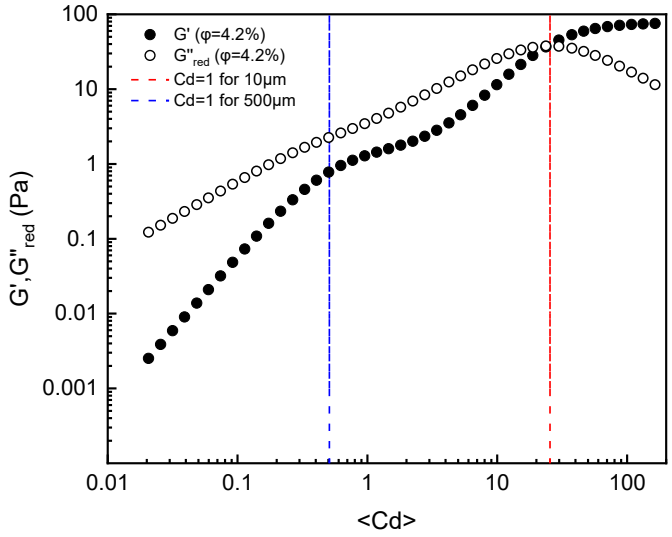

Figure B.14: G' and G''_{red} versus the average dynamic capillary number, for $\varphi = 4.2\%$ and bubble sizes of 10 and 500 microns with $z_1 = z_2 = 0.5$.

For each bubble size class, the transition from viscous to elastic behaviour occurs when the corresponding dynamic capillary number has unit order of magnitude; when this happens, the order of magnitude of the average dynamic capillary number is equal to:

$$\langle Cd \rangle \sim \frac{\langle R \rangle}{R_i} \tag{B.5}$$

According to this, the large bubbles with 500 μm radius will demonstrate their viscoelasticity at $\langle Cd \rangle \approx 0.51$, while for the small bubbles with 10 μm radius, this will happen at $\langle Cd \rangle \approx 25.5$. Examining the G' curve from high to low values of $\langle Cd \rangle$, it can be observed that both bubble size classes behave as elastic inclusions at high $\langle Cd \rangle$ values. At $\langle Cd \rangle \approx 25.5$, the 10 μm bubbles do begin to relax and, as a result, they start behaving as viscous fluids, causing a decrease in G'. For $\langle Cd \rangle$ between 0.51 and 25.5, the curve reflects the combined effect of the viscous response caused by the relaxed 10 μm bubbles and the elastic response originating from the 500 μm bubbles, which have not started relaxing yet. As $\langle Cd \rangle$ decreases below 0.51, the larger bubbles start relaxing as well, leading to a further drop in G' and, in turn, a prevalently viscous behaviour of the dispersed phase.

This example demonstrates that polydispersity can lead to a more complex viscoelastic behaviour that entails different relaxation modes, each associated with a bubble size class (via the associated relaxation time λ_i). In this case, the relaxation process spans a range of average dynamic capillary numbers, instead of happening at $\langle Cd \rangle \sim 1$. In this context, one cannot model the viscoelastic behaviour employing a constitutive equation for monodisperse suspensions and an average bubble diameter, because the different relaxation modes would not appear. Instead, for a semi-dilute bidisperse bubble suspension with very large and very small bubbles having equal bubble volume fractions, one must operate as shown, considering each bubble size class individually, calculating the corresponding viscoelastic moduli (for each bubble size class) by using the constitutive equations for monodisperse suspensions, and then summing the different contributions.

B5.2 Scenario 2 - Bimodal distribution ($R_1 = 10\ \mu m$, $R_2 = 200\ \mu m$)

This scenario pertains to another bidisperse bubble suspension, with a smaller difference between the sizes of the two bubble classes, which are 10 μm and 200 μm. Similar to the previous scenario, the total bubble volume fraction is divided equally between the two bubble classes, so that the volume-weighted average radius is 105 μm. Fig. B.10 shows the theoretical G' and G''_{red} curves for this bidisperse suspension. As seen, also in this case the relaxation process occurs over a wider range of $\langle Cd \rangle$ values compared to a monodisperse bubble suspension. Nevertheless, unlike the first example, the range is smaller, between 10 and 0.5. The first decay of G' happens at $\langle Cd \rangle \approx 10.5$ and reflects the relaxation of the 10 μm bubbles, while the second decay happens at $\langle Cd \rangle \approx 0.525$, reflecting the relaxation of the 200 μm bubbles. The characteristic shape of the G' curve indicates the presence of two relaxation

modes; these, however, are less distinct compared to the previous scenario. This suggests that the effect of polydispersity on the viscoelasticity of bubble suspensions becomes more pronounced as the difference in the sizes of the bubble classes increases.

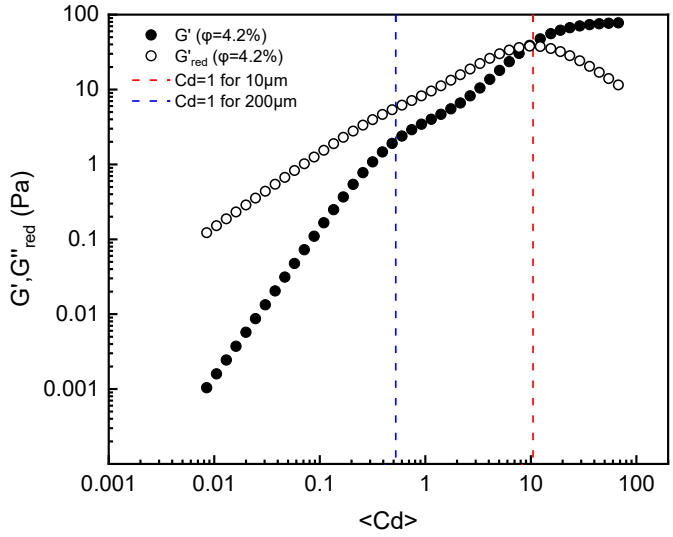

Figure B.15: G', G''_{red} versus average dynamic capillary number, for $\varphi = 4.2\%$ and bubble sizes of 10 and 200 microns, with $z_1 = z_2 = 0.5$.

B5.3 Scenario 3 – Gamma-type distribution (bubble radii between 20 and 120 μm)

This scenario is based on the experimental data from Sec. 4.3.1, where the bubble radii follow a gamma distribution between 20 μm and 120 μm (Fig. B.11a), and the volume-weighted average radius is equal to 61 μm. In this case, the total bubble volume fraction is not equally distributed between small and large sizes, as it was in the first two scenarios. Instead, each size class is assigned a percentage of the total bubble volume fraction. Following the same method as before, the G' and G''_{red} curves of Fig. B.11b (black and hollow points, respectively) were obtained. In contrast to the suspensions previously analysed (scenarios 1 and 2), the cross-over of the two viscoelastic moduli and, in turn, the relaxation of the dispersed phase happen at $\langle Cd \rangle \sim 1$, a behaviour that resembles that of a monodisperse bubble suspension. This finding aligns with what is observed in polymer melts, where a polydisperse molecular weight distribution results in a relaxation time spectrum that can be described by a weighted average relaxation time (Macosko, 1994). To confirm this, the viscoelastic moduli of a monodisperse suspension with bubbles of 61 μm radius and 4.2% volume fraction were calculated employing Eq. 4.7 (Fig. B.11b – black and red curves). As observed, the G' and G''_{red} curves of the two suspensions are almost identical. Therefore, it can be concluded that polydispersity significantly impacts the viscoelastic behaviour of a bubble suspension only if the bubble size distribution is bimodal, with very small and very large bubbles having similar volume fractions

– a condition that is infrequently encountered in applications. Under typical experimental conditions, where bubble sizes follow the gamma distribution, polydispersity has negligible effect and the polydisperse suspension can be regarded as monodisperse with a volume-weighted average bubble radius. This conclusion aligns with the findings on the effect of polydispersity on the steady-shear viscosity of bubble suspensions discussed in Sec. 3.2.

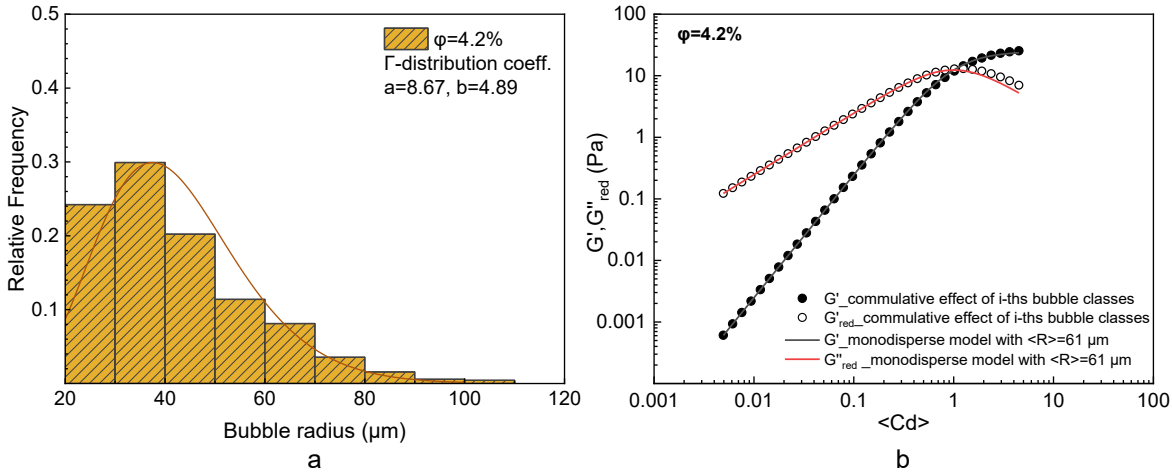

Figure B.16: a) Gamma-type bubble size distribution (20-120 μm). b) G' and G''_{red} versus the average dynamic capillary number for $\varphi = 4.2\%$ and bubble sizes following a gamma distribution between 20 and 120 μm.

B6. Further investigation on bubble rise

To further investigate whether G' increases with time owing to bubble rise, time sweeps were conducted at certain oscillation frequencies, along with SAOS measurements with increasing oscillation frequency. The results are presented below.

B6.1 Time sweep experiments

Fig. B.12 presents the time sweep results for a bubble suspension with $\varphi = 11\%$, tested in the linear regime over 30 minutes at $\omega_1 = 0.5$ rad/s, $\omega_2 = 1$ rad/s and $\omega_3 = 15$ rad/s. As shown, G' is constant over time for $\omega_2 = 1$ rad/s and $\omega_3 = 15$ rad/s. For $\omega_1 = 0.5$ rad/s, an increase of G' was observed over time; however, it was minimal. This suggests that bubble rise had a negligible effect on the experiments, and so it is not responsible for the observed G' shoulder.

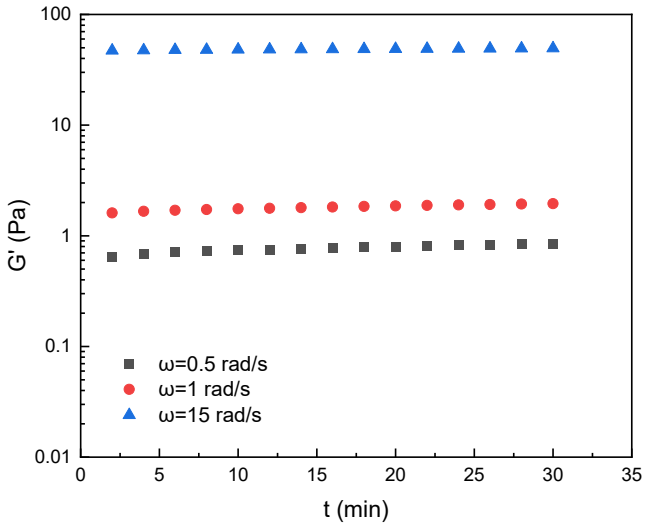

Figure B.17: Time-sweeps of a bubble suspension with $\varphi = 11\%$.

B6.2 SAOS measurements performed by increasing the oscillation frequency

Fig. B.13a presents an example of experimental G' data obtained by both increasing and decreasing the oscillation frequency for a bubble suspension with mineral oil ($\eta = 63.571$ Pa s at 20 °C) as ambient fluid and $\varphi = 9.2\%$. As shown, the characteristic G' deviation is present even in SAOS measurements conducted by ramping up the oscillation frequency – hence without significant influence from bubble rise. As explained in Sec. 4.6, this deviation reflects the collective response of bubbles that are in close proximity due to their spatial distribution after the loading of the samples on the rheometer plate. Fig. B.13b shows an example of the nonuniform spatial distribution of bubbles after sample loading. This sample corresponds to the bubble suspension with $\varphi = 4.2\%$ discussed in Chapter 4.

As expected, when the SAOS measurements are performed inversely (that is, by ramping down the oscillation frequency), more time elapses before recording the low $\langle Cd \rangle$ viscoelastic data. During this time, bubbles tend to rise, leading to a decrease in the average inter-bubble distance. Thus, more bubbles interact with their neighbours, which amplifies the G' deviation. This observation confirms the claim that bubble rise enhances the G' deviation slightly but does not cause it.

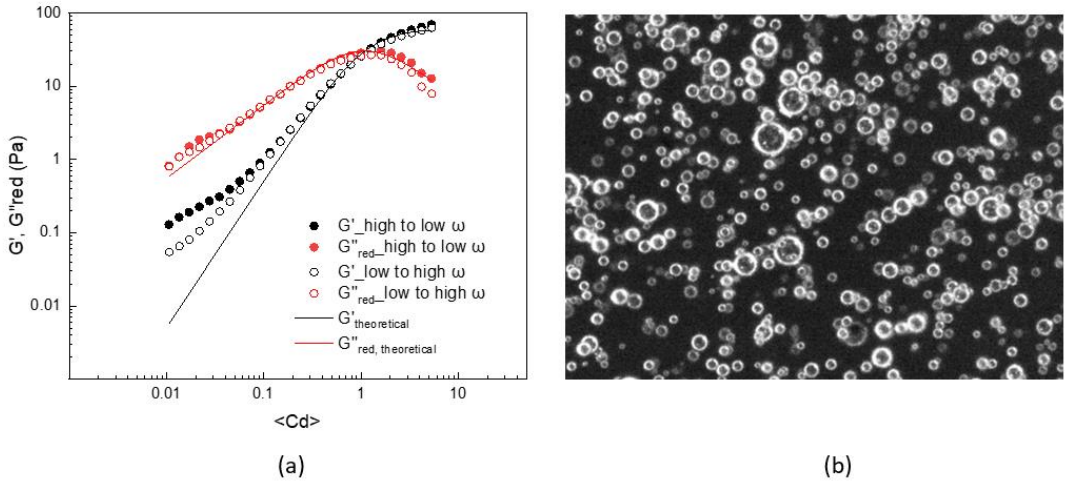

Figure B.18: (a) Experimental G'data obtained by increasing and decreasing the oscillation frequency. (b) Spatial distribution of bubbles after the loading of a sample with $\varphi = 4.2\%$ on the rheometer plate.

B7. Bubble size distributions for different pre-shearing conditions

Fig. B.14 presents the bubble size distributions of the tested suspensions after three minutes of pre-shearing at 0.1 s^{-1} and 33 minutes of pre-shearing at 0.9 s^{-1}. As shown, with stronger and more prolonged pre-shearing, the bubble radii shift to higher values, while still following a gamma type distribution.

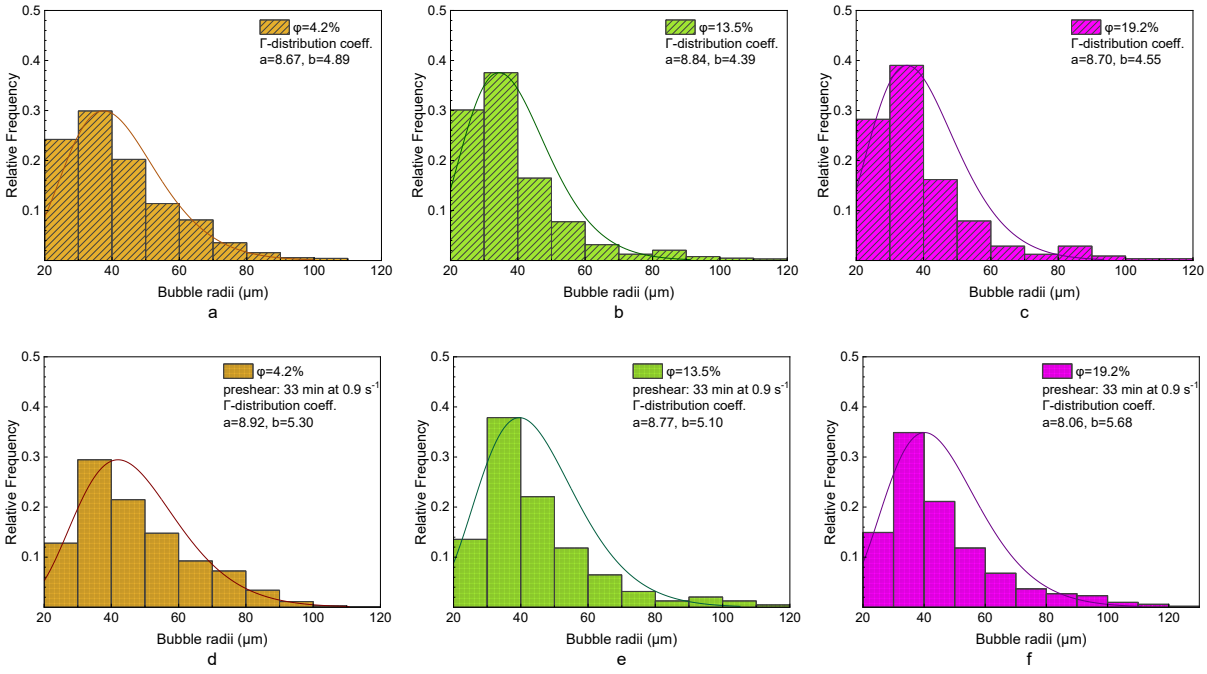

Figure B.19: Bubble size distribution after three minutes of pre-shearing at 0.1 s^{-1} for (a) $\varphi_1 = 4.2\%$, (b) $\varphi_2 = 13.5\%$ and (c) $\varphi_3 = 19.2\%$; bubble size distribution after 33 minutes of pre-shearing at 0.9 s^{-1} for (d) $\varphi_1 = 4.2\%$, (e) $\varphi_2 = 13.5\%$ and (f) $\varphi_3 = 19.2\%$.

B8. Comparison of the Palierne model's predictions to the experimental data

As mentioned in Sec. 4.6, the Palierne model was examined to determine whether it can accurately describe the experimental data, particularly in capturing the characteristic G' shoulder at lower $\langle Cd \rangle$ values. The Palierne model describes the complex modulus of a blend of immiscible fluids, $G^*_{blend}(\omega)$, as follows:

$$G^*_{blend}(\omega) = G^*_m(\omega)\frac{1+3\varphi H(\omega)}{1-2\varphi H(\omega)} \tag{B.6a}$$

with:

$$H(\omega) = \frac{4\left(\frac{\sigma_{\alpha,\beta}}{R}\right)\left[2G^*_m(\omega)+5G^*_i(\omega)\right]+\left[G^*_i(\omega)-G^*_m(\omega)\right]\left[16G^*_m(\omega)+19G^*_i(\omega)\right]}{40\left(\frac{\sigma_{\alpha,\beta}}{R}\right)\left[G^*_m(\omega)+G^*_i(\omega)\right]+\left[2G^*_i(\omega)+3G^*_m(\omega)\right]\left[16G^*_m(\omega)+19G^*_i(\omega)\right]} \tag{B.6b}$$

where $\sigma_{\alpha,\beta}$ is the interfacial tension between the two fluids, R is the volume-weighted radius of the inclusions, $G^*_m(\omega)$ and $G^*_i(\omega)$ are the complex moduli of the matrix and of the inclusions, respectively, while $H(\omega)$ is the relaxation spectrum.

For the systems descripted in Chapter 4, which consist of two Newtonian fluids, these being air as the dispersed phase and a mixture of mineral oil and span 80 as the matrix, the following simplifications can be made:

a) $G^*_i(\omega) = G'_i(\omega) + G''_i(\omega)\, i = 0$, since air is a Newtonian fluid and bubbles can be considered inviscid.
b) $G^*_m(\omega) = G'_m(\omega) + G''_m(\omega)\, i = 0 + (\eta_m\omega)\, i$, since the matrix is a Newtonian fluid with insignificant elasticity and viscosity η_m.

Then, Eq. B.6 becomes:

$$G^*_{blend}(\omega) = G^*_m(\omega)\frac{1+3\varphi H(\omega)}{1-2\varphi H(\omega)} \quad \text{with} \quad H(\omega) = \frac{\left(\frac{\sigma_{\alpha,\beta}}{R}\right)-2G^*_m(\omega)}{5\left(\frac{\sigma_{\alpha,\beta}}{R}\right)+6G^*_m(\omega)} \tag{B.7}$$

Substituting the expression for $H(\omega)$ into $1+3\varphi H(\omega)$ and $1-2\varphi H$, the following expressions are obtained:

$$1+3\varphi H(\omega) = 1+\frac{3\varphi\left[\left(\frac{\sigma_{\alpha,\beta}}{R}\right)-2G^*_m(\omega)\right]}{5\left(\frac{\sigma_{\alpha,\beta}}{R}\right)+6G^*_m(\omega)} = \frac{(5+3\varphi)\left(\frac{\sigma_{\alpha,\beta}}{R}\right)+(1-\varphi)6G^*_m(\omega)}{5\left(\frac{\sigma_{\alpha,\beta}}{R}\right)+6G^*_m(\omega)} \tag{B.8}$$

$$1-2\varphi H(\omega)=1-\frac{2\varphi\left[\left(\frac{\sigma_{\alpha,\beta}}{R}\right)-2G_m^*(\omega)\right]}{5\left(\frac{\sigma_{\alpha,\beta}}{R}\right)+6G_m^*(\omega)}=\frac{(5-2\varphi)\left(\frac{\sigma_{\alpha,\beta}}{R}\right)+(6+4\varphi)G_m^*(\omega)}{5\left(\frac{\sigma_{\alpha,\beta}}{R}\right)+6G_m^*(\omega)} \tag{B.9}$$

Substituting Eqs. B.8, B.9 and $G_m^*(\omega)=(\eta_m\omega)\,i$ into Eq. B.7, the following expression for the complex modulus of the blend is obtained:

$$G_{blend}^*(\omega)=\frac{(5+3\varphi)\left(\frac{\sigma_{\alpha,\beta}}{R}\right)(\eta_m\omega)i-6(1-\varphi)(\eta_m\omega)^2}{(6+4\varphi)(\eta_m\omega)i+(5-2\varphi)\left(\frac{\sigma_{\alpha,\beta}}{R}\right)} \tag{B.10}$$

For brevity, the following quantities are introduced:

$$x\equiv(5+3\varphi)\left(\frac{\sigma_{\alpha,\beta}}{R}\right)(\eta_m\omega)\;;\;y\equiv 6(\varphi-1)(\eta_m\omega)^2$$

$$w\equiv(6+4\varphi)(\eta_m\omega)\;\;;\;\;z\equiv(5-2\varphi)\left(\frac{\sigma_{\alpha,\beta}}{R}\right)$$

and the expression becomes:

$$G_{blend}^*(\omega)=G'_{blend}(\omega)+G''_{blend}(\omega)i$$

$$=\frac{xi+y}{wi+z}=\frac{(xi+y)(-wi+z)}{(wi+z)(-wi+z)}=\frac{(xw+zy)+(xz-yw)i}{w^2+z^2}=\frac{(xw+zy)}{w^2+z^2}+\frac{(xz-yw)}{w^2+z^2}\,i \tag{B.11}$$

Whence, G'_{blend}, G''_{blend} are obtained as follows:

$$G'_{blend}(\omega)=\frac{(xw+zy)}{w^2+z^2}=\frac{80\varphi\left(\frac{\sigma_{\alpha,\beta}}{R}\right)(\eta_m\omega)^2}{\left[(5-2\varphi)\left(\frac{\sigma_{\alpha,\beta}}{R}\right)\right]^2+[(6+4\varphi)(\eta_m\omega)]^2} \tag{B.12a}$$

$$G''_{blend}(\omega)=\frac{(xz-yw)}{w^2+z^2}=\frac{(\eta_m\omega)[(5+3\varphi)(5-2\varphi)\left(\frac{\sigma_{\alpha,\beta}}{R}\right)^2+(6\varphi-6)(6+4\varphi)(\eta_m\omega)^2]}{\left[(5-2\varphi)\left(\frac{\sigma_{\alpha,\beta}}{R}\right)\right]^2+[(6+4\varphi)(\eta_m\omega)]^2} \tag{B.12b}$$

Fig. B.15 compares the experimental profiles of the storage modulus G' (the same reported in Fig. 4.2) with the theoretical predictions obtained from the models of Palierne and Jeffreys for the three volume fractions investigated.

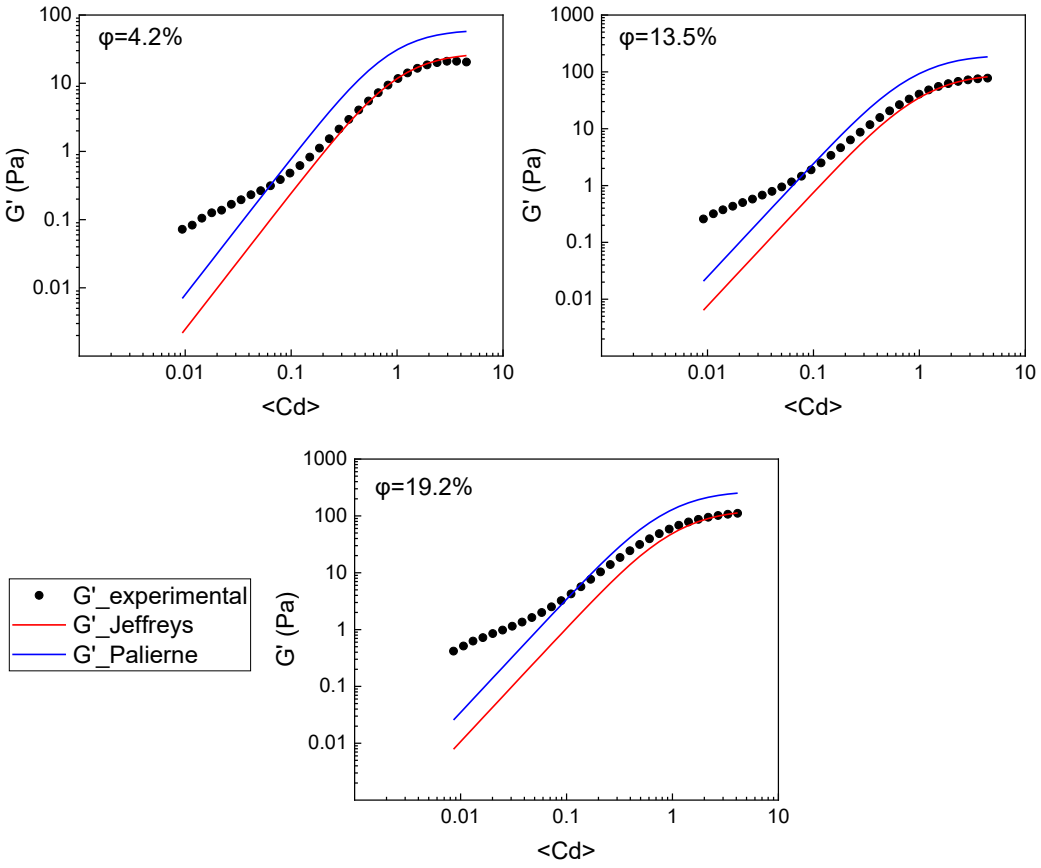

Figure B.20: Experimental values vs theoretical predictions of G'using Jeffreys and Palierne models for polydisperse bubble suspensions with (a) $\varphi_1 = 4.2\%$, (b) $\varphi_2 = 13.5\%$ and (c) $\varphi_3 = 19.2\%$.

As shown, the G' predicted by the Palierne model qualitatively resembles the trend of the Jeffreys model, which predicts only one characteristic relaxation time. Similar to the Jeffreys model, the model of Palierne fails to predict the second G' shoulder at low $\langle Cd \rangle$ values. Furthermore, it does not capture the high $\langle Cd \rangle$ plateau as accurately as the Jeffreys model. As detailed in Sec. 4.6, the inability of the Palierne model to accurately predict the experimental data likely stems from its assumptions regarding the type of droplet interactions.

B9. Effect of bubble shape relaxation

To investigate the effect of bubble shape relaxation on the obtained G' trends, the bubble shape relaxation time in the suspensions reported in Chapter 4 was calculated using the Palierne expression (Graebling et al., 1993), which considers the effect of φ on the shape-relaxation of a single droplet. For bubble suspensions where the ambient fluid is Newtonian, this expression is a modification of the relaxation time given in the Jeffreys model and reads:

$$\lambda_{Palierne} = \left[\frac{4(3+2\varphi)}{(10-4\varphi)}\right]\frac{R\eta_m}{\sigma_{\alpha,\beta}} \tag{B.13}$$

Table 1 reports the shape-relaxation times calculated using the Palierne expression, along with the relaxation times derived from the Jeffreys model for the three suspensions reported in Chapter 4. As shown, the bubble shape-relaxation times predicted by the Palierne model closely align with the relaxation times given by the Jeffreys model (obtained through fitting). Comparing the shape-relaxation times with the results reported in Table 4.5, it becomes evident that, for all tested suspensions, the shape-relaxation times fall between the first and second relaxation times. However, the fitting results revealed the presence of additional relaxation times, which are at least one order of magnitude larger compared with the computed bubble shape-relaxation times. This finding indicates that even if the relaxation mode related to the shape relaxation of the bubbles can be influenced by crowding effects, it cannot be considered responsible for the characteristic deviation of G' at lower $\langle Cd \rangle$ values, which instead is associated with longer relaxation times.

Table B.1: Jeffreys and Palierne relaxation times for the tested suspensions.

$\boldsymbol{\varphi}$ (%)	$\boldsymbol{\lambda_{Jeffreys}}$ (s)	$\boldsymbol{\lambda_{Palierne}}$ (s)
4.2	0.089	0.113
13.5	0.094	0.130
19.2	0.096	0.140

Appendix C

Supporting Information to Chapter 5

C1. Carreau-Yasuda fitting parameters for the bubble suspensions prepared with the ST1 matrix

This section presents the fitting values obtained for the Carreau-Yasuda parameters for the generated bubble suspensions and their corresponding ST1 matrices. As shown in Table C.1, the flow index (n) of the bubble suspensions was consistently lower than that of the matrix, confirming that the presence of bubbles further amplified the shear-thinning behaviour of the matrix. Additionally, the zero-shear viscosity of the suspensions increased with bubble volume fraction as expected.

It's worth noting that the Carreau-Yasuda parameters of the ST1 matrices varied slightly between different suspensions, with these differences becoming more pronounced as the aeration time increased, corresponding to higher bubble volume fractions. As explained in Sec. 5.2.3, the high-shear mixing used during bubble generation likely caused some de-swelling of the Carbopol microgels, leading to variations in the matrix flow curves depending on the duration of exposure. Fig. C1 indicatively presents the flow curves of the ST1 matrices corresponding to the bubble suspensions with $\varphi_1 = 3.85\%$ and $\varphi_4 = 8.7\%$, respectively, confirming this behaviour. To account for this phenomenon, the viscosity of the ST1 matrix was always measured after the rheological tests of each bubble volume fraction to ensure accurate calculation of the suspension's relative viscosity.

Table C.1: Carreau – Yasuda fitting parameters for the bubble suspensions generated with the ST1 as the ambient fluid.

	Carreau – Yasuda parameters				
	a	η_0	λ_c	n	R^2
$\varphi_1 = 3.85\%$	1.183	3.662	0.886	0.869	0.999
ST1 matrix for $\varphi_1 = 3.85\%$	0.965	2.732	0.480	0.883	0.999
$\varphi_2 = 5.12\%$	0.897	3.937	0.522	0.822	0.998
ST1 matrix for $\varphi_2 = 5.12\%$	0.768	2.731	0.259	0.866	0.999
$\varphi_3 = 6.40\%$	0.857	4.092	0.540	0.801	0.998

ST1 matrix for $\varphi_3 = 6.40\%$	0.722	2.610	0.127	0.8503	0.998
$\varphi_4 = 8.70\%$	0.897	4.208	0.469	0.737	0.996
ST1 matrix for $\varphi_4 = 8.70\%$	0.622	2.409	0.144	0.850	0.999

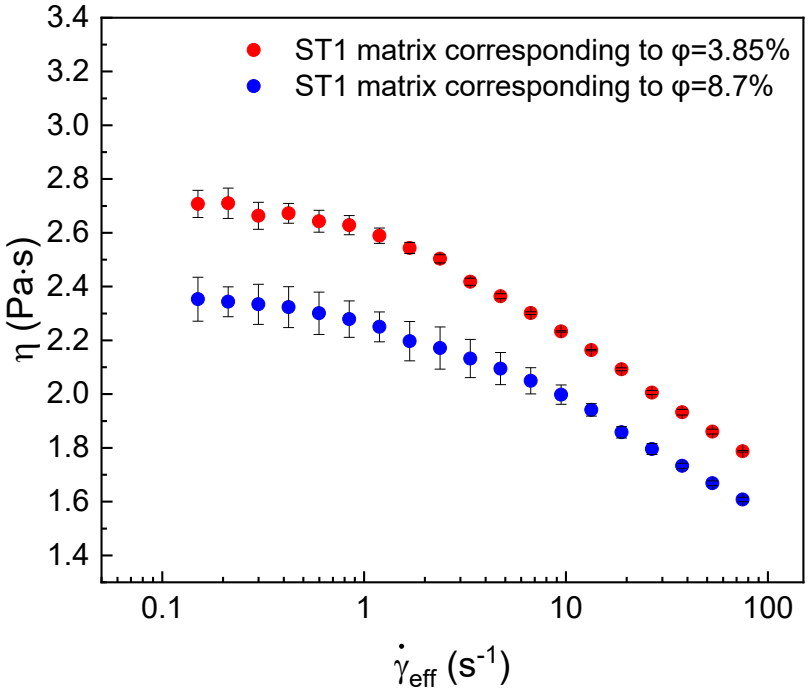

Figure C.1: Flow curves of the ST1 matrices corresponding to bubble suspensions with $\varphi_1 = 3.85\%$ and $\varphi_4 = 8.7\%$.

C2. Carreau-Yasuda fitting parameters for the bubble suspensions prepared with the ST2 matrix

Table C.2 presents the fitting values obtained for the Carreau-Yasuda parameters for both the ST2 matrices and the bubble suspensions generated with them. Similar to above, the presence of bubbles induced additional shear-thinning effects, as evidenced by the lower flow index values of the suspensions compared to their corresponding matrices. The zero-shear viscosity of the suspensions increased with bubble volume fraction (Fig. C.2), consistent with findings in bubble suspensions with the ST1 and Newtonian matrices. Furthermore, the addition of SDS, stabilised Carbopol microgels against high-shear mixing, as evidenced by the almost overlapping matrix flow curves of Fig. C3 and the very similar Carreau-Yasuda fitting values obtained for the matrices of the three tested suspensions, regardless of aeration time.

Table C.2: Carreau – Yasuda fitting parameters for the bubble suspensions prepared with the ST2 matrix.

	Carreau – Yasuda parameters				
	a	η_0	λ_c	n	R^2
$\varphi_1 = 4.95\%$	0.595	2.453	0.155	0.892	0.999
ST2 matrix for $\varphi_1 = 4.95\%$	0.526	1.977	0.126	0.914	1.000
$\varphi_2 = 6.3\%$	0.822	2.494	0.147	0.885	0.999
ST2 matrix for $\varphi_2 = 6.3\%$	0.514	1.987	0.109	0.912	0.999
$\varphi_3 = 8.6\%$	0.662	2.691	0.135	0.859	0.999
ST2 matrix for $\varphi_3 = 8.6\%$	0.491	1.932	0.112	0.910	0.999

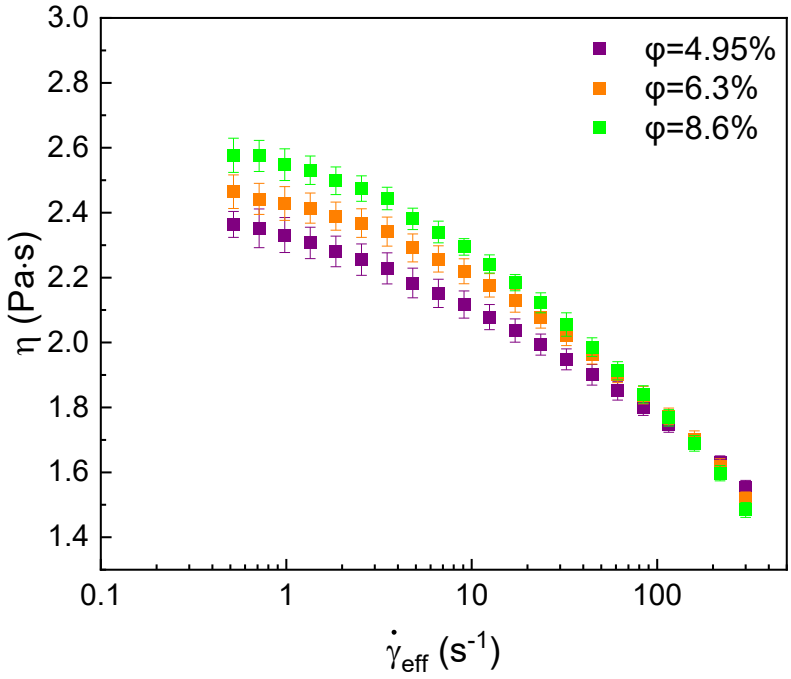

Figure C.2: Flow curves of bubble suspensions generated with the ST2 matrix at bubble volume fractions $\varphi_1 = 4.95\%$, $\varphi_2 = 6.30\%$ and $\varphi_3 = 8.6\%$. The zero-shear viscosity increases with bubble volume fraction.

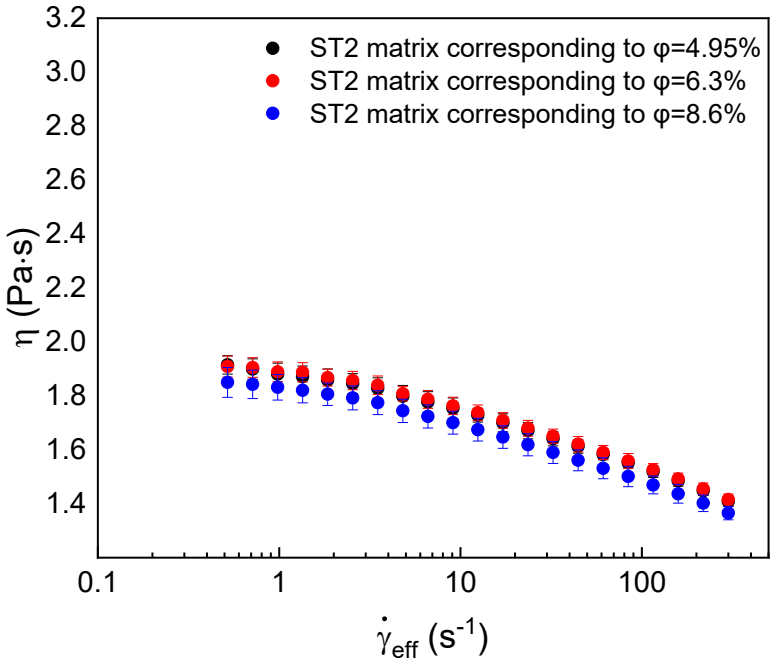

Figure C.3: Flow curves of the ST2 matrices corresponding to bubble suspensions with $\varphi_1 = 4.95\%$, $\varphi_2 = 6.3\%$ and $\varphi_3 = 8.6\%$. The nearly overlapping curves indicate that high-shear mixing had a minimal effect on the deswelling of Carbopol microgels in the presence of SDS.

References

Ahmed, R. M., Takach, N. E., Khan, U. M., Taoutaou, S., James, S., Saasen, A. and Godøy, R. (2009). 'Rheology of foamed cement'. *Cement and Concrete Research*, 39 (4), pp. 353–361. doi: 10.1016/j.cemconres.2008.12.004.

Ahuja, A., Pappas, I. and Potanin, A. (2020). 'Relation between structure and stability of toothpaste with two-step yielding'. *Rheologica Acta*. Springer, 59 (3), pp. 133–145. doi: 10.1007/s00397-019-01183-7.

Ahuja, A. and Potanin, A. (2018). 'Rheological and sensory properties of toothpastes'. *Rheologica Acta*. Springer Verlag, 57 (6–7), pp. 459–471. doi: 10.1007/s00397-018-1090-z.

Bagdassarov, N. S. and Dingwell, D. B. (1992). *A rheological investigation of vesicular rhyolite*. *Journal of Volcanology and Geothermal Research*.

Bagdassarov, N. S. and Dingwell, D. B. (1993). 'Frequency dependent rheology of vesicular rhyolite'. *Journal of Geophysical Research: Solid Earth*. American Geophysical Union (AGU), 98 (B4), pp. 6477–6487. doi: 10.1029/92jb02690.

Bhamla, M. S., Chai, C., Alvarez-Valenzuela, M. A., Tajuelo, J. and Fuller, G. G. (2017). 'Interfacial mechanisms for stability of surfactant-laden films'. *PLoS ONE*, 12 (5), pp. 1–14. Available at: http://arxiv.org/abs/1608.02180.

Bhattacharjee, T., Kabb, C. P., O'Bryan, C. S., Urueña, J. M., Sumerlin, B. S., Sawyer, W. G. and Angelini, T. E. (2018). 'Polyelectrolyte scaling laws for microgel yielding near jamming'. *Soft Matter*. Royal Society of Chemistry, 14 (9), pp. 1559–1570. doi: 10.1039/c7sm01518f.

Bird, R. B., Armostrong, R. C. and Hassanger, O. (1987). *Dynamics of polymer liquids Fluid mechanics (Second ed.)*. John Wiley & Sons, Inc.

Bird, R. B., Stewart, W. E. and Lightfoot, E. N. (2002). *Transport Phenomena (Second ed.)*. New York: John Wiley & Sons, Inc.

Bonacucina, G., Martelli, S. and Palmieri, G. F. (2004). 'Rheological, mucoadhesive and release properties of Carbopol gels in hydrophilic cosolvents'. *International Journal of Pharmaceutics*, 282 (1–2), pp. 115–130. doi: 10.1016/j.ijpharm.2004.06.012.

Boulmedarat, L., Grossiord, J. L., Fattal, E. and Bochot, A. (2003). 'Influence of methyl-β-cyclodextrin and liposomes on rheological properties of Carbopol® 974P NF gels'. in *International Journal of Pharmaceutics*. Elsevier, pp. 59–64. doi: 10.1016/S0378-5173(02)00683-X.

Bousmina, M. and Muller, R. (1993). 'Linear viscoelasticity in the melt of impact PMMA. Influence of concentration and aggregation of dispersed rubber particles'. *Journal of Rheology*. Society of Rheology, 37 (4), pp. 663–679. doi: 10.1122/1.550389.

Campbell, G. M. and Mougeot, E. (1999). 'Creation and characterisation of aerated food products'. *Trends in Food Science & Technology*, 10 (9), pp. 283–296.

Carnali, J.O. and Naser, M.S. (1992). 'The use of dilute solution viscometry to characterize the network properties of carbopol microgels'. *Colloid Polym Sci,* 270, pp. 183–193. doi: 10.1007/BF00652185.

Carreau, P. J., Bousmina, M. and Ajji, A. (1994). 'Rheological properties of blends: Facts and challenges'. in Ghiggino KP (ed.) *Progress in Pacific Science*. New York: Springer-Verlag, pp. 25–40.

Chen, Q., Restagno, F., Langevin, D. and Salonen, A. (2022). 'The rise of bubbles in shear thinning viscoelastic fluids'. *Journal of Colloid and Interface Science*. Academic Press Inc., 616, pp. 360–368. doi: 10.1016/j.jcis.2022.02.043.

Cheng, X., McCoy, J. H., Israelachvili, J. N. and Cohen, I. (2011). 'Imaging the microscopic structure of shear thinning and thickening colloidal suspensions'. *Science*, 333 (6047), pp. 1276–1279. doi: 10.1126/science.1207032.

Chesterton, A., Pereira de Abreu, D., Moggridge, G., Sadd, P. and Wilson, D. (2013). 'Evolution of cake batter bubble structure and rheology during planetary mixing'. *Food and Bioproducts Processing*, 91, pp. 192–206.

Chhabra, R. P. and Richardson, J. F. (2011). *Non-Newtonian flow and applied rheology: engineering applications*. Butterworth-Heinemann.

Choi, S. J. and Schowalter, W. R. (1975). 'Rheological properties of nondilute suspensions of deformable particles'. *Physics of Fluids*, 18 (4), pp. 420–427. doi: 10.1063/1.861167.

Conrad, J. C., Dhillon, P. P., Weeks, E. R., Reichman, D. R. and Weitz, D. A. (2006). 'Contribution of slow clusters to the bulk elasticity near the colloidal glass transition'. *Physical Review Letters*, 97 (26). doi: 10.1103/PhysRevLett.97.265701.

Cross, M. M. (1965). 'Rheology of non-Newtonian fluids: A new flow equation for pseudoplastic systems.' *Journal of Colloid Science*, 20 (5), pp. 417–437.

Daneshi, M. and Frigaard, I. A. (2023). 'Growth and stability of bubbles in a yield stress fluid'. *Journal of Fluid Mechanics*. Cambridge University Press, 957. doi: 10.1017/jfm.2023.27.

Dealy, J. M. (2010). 'Weissenberg and deborah numbers—Their definition and use'. *Rheology Bulletin*, 79, pp. 14–18.

Doi, M. and Ohta, T. (1991). 'Dynamics and rheology of complex interfaces. I'. *The Journal of Chemical Physics*, 95 (2), pp. 1242–1248. doi: 10.1063/1.461156.

Ducloué, L., Pitois, O., Goyon, J., Chateau, X. and Ovarlez, G. (2015). 'Rheological behaviour of suspensions of bubbles in yield stress fluids'. *Journal of Non-Newtonian Fluid Mechanics*. Elsevier, 215, pp. 31–39. doi: 10.1016/j.jnnfm.2014.10.003.

Dutta, S. K., Mbi, A., Arevalo, R. C. and Blair, D. L. (2013). 'Development of a confocal rheometer for soft and biological materials'. *Review of Scientific Instruments*, 84 (6). doi: 10.1063/1.4810015.

Einstein, A. (1911). 'Berichtigung zu meiner Arbeit: „Eine neue Bestimmung der Moleküldimensionen"'. *Annalen der Physik*, 339 (3), pp. 591–592. doi: 10.1002/andp.19113390313.

Ewoldt, R. H., Johnston, M. T. and Caretta, L. M. (2015). 'Ewoldt, R. H., M. T. JohExperimental Challenges of Shear Rheology: How to Avoid Bad Data'. in Spagnolie, S.

(ed.) *Complex Fluids in Biological Systems*. Springer Biological Engineering Series, pp. 207–241.

Fanebust, M., Ozan, S. C. and Jakobsen, H. A. (2021). 'Coalescence of fluid particles with deformable interfaces in non-Newtonian media'. *International Journal of Multiphase Flow*. Elsevier Ltd, 144. doi: 10.1016/j.ijmultiphaseflow.2021.103787.

Feneuil, B., Iqbal, K. T., Jensen, A., Brandt, L., Tammisola, O. and Carlson, A. (2023). 'Experimental and numerical investigation of bubble migration in shear flow: Deformability-driven chaining and repulsion'. *Physical Review Fluids*, 8.

Ferry, J. D. (1980). *Viscoelastic properties of Polymers (3rd ed.)*. New York: John Wiley & Sons, Inc.

Frankel, N. A. and Acrivos, A. (1970). 'The constitutive equation for a dilute emulsion'. *Journal of Fluid Mechanics*, 44 (1), pp. 65–78. doi: 10.1017/S0022112070001696.

Graebling, D., Muller, R. and Palierne, J. (1993). 'Linear viscoelastic behavior of some incompatible polymer blends in the melt. Interpretation of data with a model of emulsion of viscoelastic liquids'. *Macromolecules*, 26, pp. 320–329.

Hadamard, J. S. (1911). 'Mouvement permanent lent d'une sph´ere liquide et visqueuse dans un liquide visqueux.' *C. R. Acad. Sci. Paris*, 152, pp. 1735–1738.

J 0 Sibree. (1934). 'THE VISCOSITY OF FROTH'. *Trans. Faraday SOC*, 30, pp. 325–331.

Jofore, B. D., Erni, P., Vleminckx, G., Moldenaers, P. and Clasen, C. (2015). 'Rheology of microgels in single particle confinement'. *Rheologica Acta*, 54 (7), pp. 581–600.

Joh, S. W., Lee, S. H. and Youn, J. R. (2010). 'Rheological behavior of polydispersed bubble suspensions in shear flows'. *Polymer Engineering and Science*, 50 (1), pp. 128–137. doi: 10.1002/pen.21517.

De Kee', D., Chhabra, R. P. and Dajan, A. (1990). *MOTION AND COALESCENCE OF GAS BUBBLES IN NON-NEWTONIAN POLYMER SOLUTIONS*. *Journal of Non-Newtonian Fluid Mechanics*.

Kogan, M., Ducloué, L., Goyon, J., Chateau, X., Pitois, O. and Ovarlez, G. (2013). 'Mixtures of foam and paste: Suspensions of bubbles in yield stress fluids'. *Rheologica Acta*. Springer Verlag, 52 (3), pp. 237–253. doi: 10.1007/s00397-013-0677-7.

Kudrolli, A., Wolpert, M. and Gollub, J. P. (1997). *Cluster Formation due to Collisions in Granular Material*.

Kurz, F., Reitberger, V., Hengst, C., Bilke-Krause, C., Kulozik, U. and Dombrowski, J. (2021). 'Correlation between physico-chemical characteristics of particulated β-lactoglobulin and its behavior at air/water and oil/water interfaces'. *Foods*. MDPI AG, 10 (6). doi: 10.3390/foods10061426.

Lacroix, C., Aressy, M. and Carreau, P. J. (1997). 'Linear viscoelastic behavior of molten polymer blends: A comparative study of the Palierne and Lee and Park models'. *Rheologica Acta*, 36, pp. 416–428.

Larsen, R. J., Kim, J. W., Zukoski, C. F. and Weitz, D. A. (2010). 'Elasticity of dilatant particle suspensions during flow'. *Physical Review E - Statistical, Nonlinear, and Soft Matter Physics*, 81 (1). doi: 10.1103/PhysRevE.81.011502.

Larson, R. G. (1999). *The Structure and Rheology of Complex Fluids*. New York: Oxford University Press, Inc.

Lavergne, F. A., Sollich, P. and Trappe, V. (2022). 'Delayed elastic contributions to the viscoelastic response of foams'. *Journal of Chemical Physics*. American Institute of Physics Inc., 156 (15). doi: 10.1063/5.0085773.

Lefrançois, P., Ibarboure, E., Payre, B. and Gontier, E. (2015). 'Insights into Carbopol gel formulations: Microscopy analysis of the microstructure and the influence of polyol additives'. *Journal of Applied Polymer Science*, 132 (46), p. 42761.

Lejeune, A. M., Bottinga, Y., Trull, T. W. and Richet, P. (1999). *Rheology of bubble-bearing magmas*. *Earth and Planetary Science Letters*.

Lim, Y. M., Seo, D. and Youn, J. R. (2004). 'Rheological behavior of dilute bubble suspensions in polyol'. *Korea Australia Rheology Journal*, 16 (1), pp. 47–54.

Liu, Z., Liu, L., Zhou, H., Wang, J. and Deng, L. (2015). 'Toothpaste microstructure and rheological behaviors including aging and partial rejuvenation'. *Korea Australia Rheology Journal*. Korean Society of Rheology, 27 (3), pp. 207–212. doi: 10.1007/s13367-015-0021-0.

Llewellin, E. and Manga, M. (2005). 'Bubble suspension rheology and implications for conduit flow'. *Journal of Volcanology and Geothermal Research*, 143 ((1-3)), pp. 205–217.

Llewellin, E. W., Mader, H. M. and Wilson, S. D. R. (2002a). 'The rheology of a bubbly liquid'. *Proceedings of the Royal Society A: Mathematical, Physical and Engineering Sciences*, 458 (2020), pp. 987–1016. doi: 10.1098/rspa.2001.0924.

Llewellin, E. W., Mader, H. M. and Wilson, S. D. R. (2002b). 'The constitutive equation and flow dynamics of bubbly magmas'. *Geophysical Research Letters*. Blackwell Publishing Ltd, 29 (24). doi: 10.1029/2002GL015697.

Loewenberg, M. and Hinch, E. J. (1996). 'Numerical simulation of a concentrated emulsion in shear flow'. *Journal of Fluid Mechanics*, 321, pp. 395–419.

Long, L. (2024). 'Simulation analysis of bubble coalescence behavior characteristics in non-Newtonian fluids based on the phase field method'. in *Journal of Physics: Conference Series*. Institute of Physics. doi: 10.1088/1742-6596/2707/1/012132.

Lopez, W. F., Naccache, M. F. and de Souza Mendes, P. R. (2018). 'Rising bubbles in yield stress materials'. *Journal of Rheology*. Society of Rheology, 62 (1), pp. 209–219. doi: 10.1122/1.4995348.

Ma, C., Nikiforov, A., Hegemann, D., De Geyter, N., Morent, R. and Ostrikov, K. (2023). 'Plasma-controlled surface wettability: recent advances and future applications'. *International Materials Reviews*. Taylor and Francis Ltd., 68 (1), pp. 82–119. doi: 10.1080/09506608.2022.2047420.

Mackenzie, J. K. (1950). 'The elastic constants of a solid containing spherical holes'. *Proceedings of the Physical Society. Section B*, 63 (1), pp. 2–11. doi: 10.1088/0370-1301/63/1/302.

Macosko, C. W. (1994). *Rheology: Principles, Measurements and Applications*. Wiley VCH, Inc.

Mader, H. M., Llewellin, E. W. and Mueller, S. P. (2013). 'The rheology of two-phase magmas: A review and analysis'. *Journal of Volcanology and Geothermal Research*, pp. 135–158. doi: 10.1016/j.jvolgeores.2013.02.014.

Maffettone, P. L. and Minale, M. (1998). 'Equation of change for ellipsoidal drops in viscous flow'. *J. Non-Newtonian Fluid Mech*, 78, pp. 227–241.

Makri, K., Angeli, P. and Mazzei, L. (2019). *Effects of air entrainment on the processing of complex oral healthcare formulations*. London.

Malysa, K. and Lunkenheimer, K. (2008). 'Foams under dynamic conditions'. *Current Opinion in Colloid and Interface Science*, pp. 150–162. doi: 10.1016/j.cocis.2007.11.008.

Manga, M. and Loewenberg, M. (2001). 'Viscosity of magmas containing highly deformable bubbles'. *J. Volcanol. Geophys. Res*, 105, pp. 19–24. Available at: www.elsevier.nl/locate/jvolgeores.

Mckinley, G. H., Byars, J. A., Brown, R. A. and Armstrong, R. C. (1991). *Observations on the elastic instability in cone-and-plate and parallel-plate flows of a polyisobutylene Boger fluid*. *Journal of Non-Newtonian Fluid Mechanics*. Elsevier Science Publishers B.V.

Mckinley, Gareth H, Pakdel, P., Oztekin, A. and Mckinley, G H. (1996). *Rheological and geometric scaling of purely elastic instabilities 1*. *J. Non-Newtonian Fluid Mech*.

Mendoza, C. I. and Santamaría-Holek, I. (2009). 'The rheology of hard sphere suspensions at arbitrary volume fractions: An improved differential viscosity model'. *Journal of Chemical Physics*, 130 (4), pp. 1–22. doi: 10.1063/1.3063120.

Migliozzi, S., Meridiano, G., Angeli, P. and Mazzei, L. (2020). 'Investigation of the swollen state of Carbopol molecules in non-aqueous solvents through rheological characterization'. *Soft Matter*. Royal Society of Chemistry, 16 (42), pp. 9799–9815. doi: 10.1039/d0sm01196g.

Milanović, M., Krstonošić, V., Dokić, L., Hadnacrossed D Signev, M. and Dapčević Hadnacrossed D Signev, T. (2015). 'Insight into the interaction between carbopol® 940 and ionic/nonionic surfactant'. *Journal of Surfactants and Detergents*. Springer Verlag, 18 (3), pp. 505–516. doi: 10.1007/s11743-015-1677-7.

Mitrias, C., Jaensson, N. O., Hulsen, M. A. and Anderson, P. D. (2017). 'Direct numerical simulation of a bubble suspension in small amplitude oscillatory shear flow'. *Rheologica Acta*. Springer Verlag, 56 (6), pp. 555–565. doi: 10.1007/s00397-017-1009-0.

Mitrou, S., Migliozzi, S., Angeli, P. and Mazzei, L. (2023). 'Effect of polydispersity and bubble clustering on the steady shear viscosity of semidilute bubble suspensions in Newtonian media'. *Journal of Rheology*. Society of Rheology, 67 (3), pp. 635–646. doi: 10.1122/8.0000585.

Mooney, M. (1951). ‘The viscosity of a concentrated suspension of spherical particles’. *Journal of Colloid Science*, 6 (2), pp. 162–170.

Morini, R., Chateau, X., Ovarlez, G., Pitois, O. and Tocquer, L. (2019a). ‘Steady shear viscosity of semi-dilute bubbly suspensions’. *Journal of Non-Newtonian Fluid Mechanics*. Elsevier B.V., 264, pp. 19–24. doi: 10.1016/j.jnnfm.2018.12.006.

Morini, R., Chateau, X., Ovarlez, G., Pitois, O. and Tocquer, L. (2019b). ‘Steady shear viscosity of semi-dilute bubbly suspensions’. *Journal of Non-Newtonian Fluid Mechanics*. Elsevier B.V., 264, pp. 19–24. doi: 10.1016/j.jnnfm.2018.12.006.

Ohie, K., Tasaka, Y. and Murai, Y. (2024). ‘Rheology of dilute bubble suspensions in unsteady shear flows’. *Journal of Fluid Mechanics*. Cambridge University Press, 983. doi: 10.1017/jfm.2024.171.

Pal, R. (1992). ‘Rheological properties of emulsions of oil in aqueous non-Newtonian polymeric media’. *Chemical Engineering Communications*, 111, pp. 45–60.

Pal, R. (1996). ‘Viscoelastic properties of polymer-thickened oil- in-water emulsions’. *Chemical Engineering Science*, 51, pp. 3299–3305.

Pal, R. (2003). ‘Rheological behavior of bubble-bearing magmas’. *Earth and Planetary Science Letters*. Elsevier B.V., 207 (1–4), pp. 165–179. doi: 10.1016/S0012-821X(02)01104-4.

Pal, R. (2004). ‘Rheological constitutive equation for bubbly suspensions’. *Industrial and Engineering Chemistry Research*. American Chemical Society, 43 (17), pp. 5372–5379. doi: 10.1021/ie040011r.

Pal, R. (2024). ‘Non-Newtonian behaviour of suspensions and emulsions: Review of different mechanisms’. *Advances in Colloid and Interface Science*. Elsevier B.V. doi: 10.1016/j.cis.2024.103299.

Palierne, J. E. (1990). *Linear rheology of viscoelastic emulsions with interfacial tension*. *Rheologica Acta Rheol Acta*.

Papadopoulou, A., Gillissen, J. J., Wilson, H. J., Tiwari, M. K. and Balabani, S. (2020). ‘On the shear thinning of non-Brownian suspensions: Friction or adhesion?’ *Journal of Non-Newtonian Fluid Mechanics*. Elsevier B.V., 281. doi: 10.1016/j.jnnfm.2020.104298.

Petrović, D., Galić, D., Seifert, D., Lešić, N. and Smolić, M. (2023). ‘Evaluation of Bioactive Glass Treatment for Dentin Hypersensitivity: A Systematic Review’. *Biomedicines*. Multidisciplinary Digital Publishing Institute (MDPI). doi: 10.3390/biomedicines11071992.

Piau, J. M. (2007). ‘Carbopol gels: Elastoviscoplastic and slippery glasses made of individual swollen sponges. Meso- and macroscopic properties, constitutive equations and scaling laws’. *Journal of Non-Newtonian Fluid Mechanics*. Elsevier, 144 (1), pp. 1–29. doi: 10.1016/j.jnnfm.2007.02.011.

Ponce-Torres, A., Acero, A. J., Herrada, M. A. and Montanero, J. M. (2018). ‘On the validity of the Jeffreys (Oldroyd-B) model to describe the oscillations of a viscoelastic pendant drop’.

Journal of Non-Newtonian Fluid Mechanics. Elsevier B.V., 260, pp. 69–75. doi: 10.1016/j.jnnfm.2018.06.008.

Poole, R. J. (2012). 'The Deborah and Weissenberg numbers'. *Bulletin of the British Society of Rheology*, 53, pp. 32–39.

Rust, A. C. and Manga, M. (2002). *Effects of bubble deformation on the viscosity of dilute suspensions*. *J. Non-Newtonian Fluid Mech*.

Rybczynski, M. W. (1911). 'On the translatory motion of a fluid sphere in a viscous medium.' *Bull. Acad. Sci. Cracovie*, 40, pp. 40–46.

Seo, D. and Youn, J. R. (2005). 'Constitutive Equations for Dilute Bubble Suspensions and Rheological Behavior in Simple Shear and Uniaxial Elongational Flow Fields'. *Fibers and Polymers*, pp. 131–138.

Shaqfe, S. G. (1996). *PURELY ELASTIC INSTABILITIES IN VISCOMETRIC FLOWS*. *Annu. Rcv. Fluid. Mech*. Available at: www.annualreviews.org.

Sikorski, D., Tabuteau, H. and de Bruyn, J. R. (2009). 'Motion and shape of bubbles rising through a yield-stress fluid'. *Journal of Non-Newtonian Fluid Mechanics*, 159 (1–3), pp. 10–16. doi: 10.1016/j.jnnfm.2008.11.011.

Stein, D. J. and Spera, F. J. (1992). *Rheology and microstrncture of magmatic emulsions: theory and experiments*. *Journal of Volcanology and Geothermal Research*.

Stein, D. J. and Spera, F. J. (2002). *Shear viscosity of rhyolite-vapor emulsions at magmatic temperatures by concentric cylinder rheometry*. *Journal of Volcanology and Geothermal Research*. Available at: www.elsevier.com.

Sunartio, D., Ashokkumar, M. and Grieser, F. (2007). 'Study of the Coalescence of Acoustic Bubbles as a Function of Frequency, Power, and Water-Soluble Additives'. *Journal of American Chemical Society*, 129 (18), pp. 6031–6036.

Sura, V. M. and Panda, P. C. (1990). *Viscosity of Porous Glasses*. *J Am Cerom SOC*.

Tasaka, Y., Kimura, T. and Murai, Y. (2015). 'Estimating the effective viscosity of bubble suspensions in oscillatory shear flows by means of ultrasonic spinning rheometry'. *Experiments in Fluids*. Springer Verlag, 56 (1), pp. 1–13. doi: 10.1007/s00348-014-1867-5.

Taylor, G. I. (1932). 'The Viscosity of a Fluid Containing Small Drops of Another Fluid'. *Proceedings of the Royal Society A*, 138, pp. 41–48.

Thuy Linh, N., Ducloue, L., Ovarlez, G. and Chateau, X. (2013). 'Overall prop erties of a soft porous material: Surface tension e ects'. *Poromechanics V: Proceedings of the Fifth Biot Conference on Poromechanics*, pp. 1895–1902.

Torres, M. D., Gadala-Maria, F. and Wilson, D. I. (2013). 'Comparison of the rheology of bubbly liquids prepared by whisking air into a viscous liquid (honey) and a shear-thinning liquid (guar gum solutions)'. *Journal of Food Engineering*, 118 (2), pp. 213–228. doi: 10.1016/j.jfoodeng.2013.04.002.

Torres, M. D., Hallmark, B. and Wilson, D. I. (2015). 'Determination of the shear and extensional rheology of bubbly liquids with a shear-thinning continuous phase'. *Rheologica Acta*. Springer Verlag, 54 (6), pp. 461–478. doi: 10.1007/s00397-014-0832-9.

Tzounakos, A., Karamanev, D. G., Margaritis, A. and Bergougnou, M. A. (2004). 'Effect of the surfactant concentration on the rise of gas bubbles in power-law non-Newtonian liquids'. *Industrial and Engineering Chemistry Research*. American Chemical Society, 43 (18), pp. 5790–5795. doi: 10.1021/ie049649t.

Velankar, S. S. and Giles, D. (2007). 'How do I know my phase angles are correct?' *Rheology Bulletin*, 76, pp. 8–20.

Vélez-Cordero, J. R. and Zenit, R. (2011). 'Bubble cluster formation in shear-thinning inelastic bubbly columns'. *Journal of Non-Newtonian Fluid Mechanics*, 166 (1–2), pp. 32–41. doi: 10.1016/j.jnnfm.2010.10.003.

Whitaker, K. A., Varga, Z., Hsiao, L. C., Solomon, M. J., Swan, J. W. and Furst, E. M. (2019). 'Colloidal gel elasticity arises from the packing of locally glassy clusters'. *Nature Communications*. Nature Publishing Group, 10 (1). doi: 10.1038/s41467-019-10039-w.

WHO. (2020). *Fact Sheet- Oral health*. Available at: https://www.who.int/news-room/fact-sheets/detail/oral-health (Accessed: 27 April 2025).

Yang, Y., Oztekin, A., Neti, S. and Mohapatra, S. (2012). 'Particle agglomeration and properties of nanofluids'. *Journal of Nanoparticle Research*. Kluwer Academic Publishers, 14 (5). doi: 10.1007/s11051-012-0852-2.

Yokozeki, T., Schulz, S., Buschhorn, S. and Schulte, K. (2012). 'Investigation of shear thinning behavior and microstructures of MWCNT/epoxy and CNF/epoxy suspensions under steady shear conditions'. *European Polymer Journal*, 48, pp. 1042–1049.

Zenit, R. and Feng, J. J. (2018). 'Hydrodynamic Interactions Among Bubbles, Drops, and Particles in Non-Newtonian Liquids'. *The Annual Review of Fluid Mechanics is online at*, 50, pp. 505–539. doi: 10.1146/annurev-fluid-122316.